JULIUS-MAXIMILIANS-UNIVERSITÄT WÜRZBURG

DISSERTATION

The life of an exciton: From ultrafast nonradiative relaxation to high quantum yield fluorescence

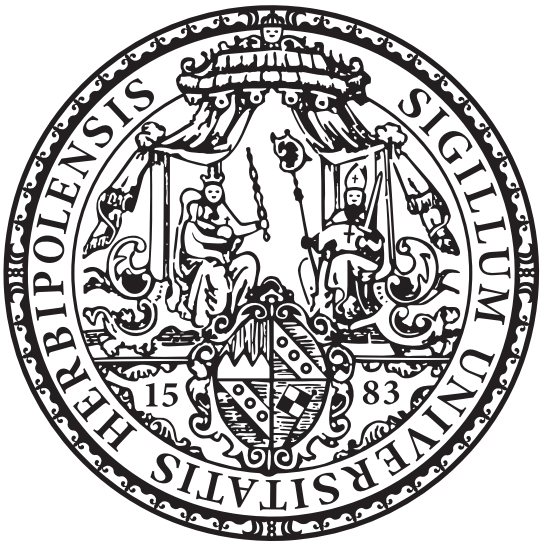

Dissertation zur Erlangung des naturwissenschaftlichen Doktorgrads
an der Fakultät für Chemie und Pharmazie der
Julius-Maximilians-Universität Würzburg

vorgelegt von

Joscha Hoche

aus Herzberg am Harz

Würzburg, 2023

Eingereicht bei der Fakultät für Chemie und Pharmazie am

20.02.2023

Gutachter der schriftlichen Arbeit

1. Gutachter: Prof. Dr. Roland Mitric

2. Gutachter: Prof. Dr. Volker Engel

Prüfer des öffentlichen Promotionskolloquiums

1. Prüfer: Prof. Dr. Roland Mitric

2. Prüfer: Prof. Dr. Volker Engel

3. Prüfer: Prof. Dr. Ingo Fischer

4. Prüfer: Prof. Dr. Christoph Lambert

5. Prüfer: Prof. Dr. Frank Würthner

Datum des öffentlichen Promotionskolloquiums

12.05.2023

Doktorurkunde ausgehändigt am

List of Publications

This thesis is based on the following references:

[1] R. Einsele, **J. Hoche**, R. Mitric
Long-range Corrected Fragment Molecular Orbital Density-Functional Tight-binding Method for Excited States in Large Molecular Systems
J. Chem. Phys., **158**, 044121 (2023)

[2] **J. Hoche**, M. I. S. Röhr, C. Lambert, R. Mitric
Polarisation-Anisotropy and Nonadiabatic Dynamics Simulations in pyrene-BODIPY conjugates
in preparation (2023).

[3] E. Titov, T. Kopp, **J. Hoche**, A. Humeniuk, R. Mitric
(De)localization dynamics of molecular excitons: comparison of mixed quantum-classical and fully quantum treatments
Phys. Chem. Chem. Phys., **24**, 12136–12148 (2022)

[4] L. J. Patalag, **J. Hoche**, R. Mitric, D. B. Werz, B. L. Feringa
Transforming Dyes Into Fluorophores: Exciton-Induced Emission with Ethylene-Bridged Oligo-BODIPYs
Angew. Chem., **61**, e202116834 (2022)

[5] **J. Hoche**, M. Flock, X. Miao, L. N. Philipp, M. Wenzel, I. Fischer, R. Mitric
Excimer formation in the isolated tetracene dimer
Chem. Sci., **10**, 11965–11975, (2021)

[6] L. J. Patalag[†], **J. Hoche**[†], M. Holzapfel, A. Schmiedel, R. Mitric, C. Lambert, D. B. Werz
Ultrafast Resonance Energy Transfer in Ethylene-Bridged BODIPY Heterooligomers: From Frenkel to Förster Coupling Limit
J. Am. Chem. Soc., **143**, 7414–7425 (2021), [†]contributed equally and are considered co-first authors

[7] C. Lambert, **J. Hoche**, M. H. Schreck, M. Holzapfel, A. Schmiedel, J. Selby, A. Turkin, R. Mitric
Ultrafast Energy Transfer Dynamics in a Squaraine Hetero-Triad
J. Phys. Chem. A, **125**, 2504–2511, (2021)

[8] H.-C. Schmitt, I. Fischer, L. Ji, J. Merz, T. B. Marder, **J. Hoche**, M.I.S. Röhr, R. Mitric
Isolated 2-hydroxypyrene and its dimer: a frequency-and time-resolved spectroscopic study
New J. Chem., **33**, 14949–14956 (2021)

[9] A. Humeniuk, M. Buzancic, **J. Hoche**, J. Cerezo, F. Santoro, V. Bonačić-Koutecký, R. Mitric
Predicting fluorescence quantum yields for molecules in solution: A critical assessment of the harmonic approximation and the choice of the lineshape function
J. Chem. Phys. 152, 054107 (2020)

[10] **J. Hoche**, A. Schulz, L. Dietrich, A. Humeniuk, M. Stolte, D. Schmidt, T. Brixner, F. Würthner, R. Mitric
The Origin of the Solvent Dependence of Fluorescence Quantum Yields in Dipolar Merocyanine Dyes
Chem. Sci., **10**, 11013–11022 (2019)

[11] N. Auerhammer, A. Schulz, A. Schmiedel, M. Holzapfel, **J. Hoche**, M.I.S. Röhr, R. Mitric, C. Lambert
Dynamic Exciton Localisation in a pyrene-BODIPY-pyrene dye conjugate
Phys. Chem. Chem. Phys. 21, 9013–9025 (2019)

Additional Publications

[12] M.I.S. Röhr, H. Marciniak, **J. Hoche**, M.H. Schreck, H. Ceymann, R. Mitric, C. Lambert
Exciton Dynamics from Strong to Weak Coupling Limit Illustrated on a Series of Squaraine Dimers
J. Phys. Chem. C 122, 8082-–8093 (2018)

[13] **J. Hoche**, H.C. Schmitt, A. Humeniuk, I. Fischer, R. Mitrić, M.I.S. Röhr
The mechanism of excimer formation: An experimental and theoretical study on the pyrene dimer
Phys. Chem. Chem. Phys. 19, 25002–25015 (2017)

The journal articles [2], [4], [5], [6], [7], [10], and [11] were used in this cumulative dissertation. The table below summarizes to which extent material from these publications has been reused in text passages of this thesis. Permissions to reproduce copyright material were obtained from the corresponding journals, as stated below.

Publication	**Use**	**Thesis**
Ref. [2]	text reproduced, figures adapted in part and modified, SI ommited	pp. 87–98
Ref. [4]	text and figures reproduced, SI partly ommited	pp. 139–158
Ref. [5]	text and figures reproduced, SI ommited	pp. 99–118
Ref. [6]	text and figures reproduced, SI ommited	pp. 33–52
Ref. [7]	text and figures reproduced, SI ommited	pp. 53–66
Ref. [10]	text and figures reproduced, SI adapted in part and modified	pp. 20–32, pp. 119–138
Ref. [11]	text and figures reproduced, SI ommited	pp. 67–86

Permissions to reproduce copyrighted work in this thesis

Contents

Chapter 1

Introduction

The interaction between light and matter forms the basis of technological applications such as organic light-emitting diodes (OLEDs),[14–16] photovoltaics[17,18] or wearable technologies,[19] and fundamental processes such as photosynthesis or photocatalysis.[20–23] However, the characteristics of a material are not given simply by the sum of the properties of individual molecular components. Both intermolecular interactions and environmental effects can have a strong influence on the macroscopic features of organic materials.[10,24,25] For example, aggregation of molecules can change the optical absorption and emission properties significantly.[24,26,27] Interaction with solvents can strongly affect the potential energy surfaces of molecules, shifting absorption and emission to significantly lower or higher wavelengths (solvatochromism).[28] Changing the environment's polarity or viscosity makes it possible to modify non-radiative relaxation channels that allow switching the molecular emission on or off.[10]
Developing new efficient and accurate theoretical methods for predicting molecular properties and their environment is increasingly important,[29] as new compounds need to be produced in sophisticated syntheses before their functionalities can be determined by physical measurements. Only after this enormous time-, labor- and chemical-intensive synthesis it is possible to assess whether the molecules are suitable for specific applications or not.[30,31] That is why research and development of new functional materials are slow and costly.[32] Theoretical and computational methods can significantly accelerate this trial-and-error-based chemistry by predicting molecules' optical properties and deciding which compounds are the most suitable for synthesis.[30]

The motivation of this thesis is to identify the processes that take place in chromophores after the excitation of electronic states and to determine their influence on the optical properties of the molecular systems. In particular, the effect on the spontaneous emission of light (luminescence) was investigated in this work from various points of view. In the case of luminescence, factors such as emission energy, decay time, photoluminescence quantum yield (PLQY), the type of emission (fluorescence vs. phosphorescence), and possible loss channels play a crucial role in the suitability of a molecule for technological applications.[14,15] The emission energy of molecules can be simulated with reasonable accuracy, and the electrostatic influence of the solvent on the emission can also be well described.[33] However, this is often much more difficult in (hetero)-oligomers or even complex aggregates since critical processes precede the luminescence, which can strongly influence the emission properties.[6,24,25]

For example, excitation energy transfer is a key process in the understanding of luminescence, as it allows that the emission occurs from different molecular units than where the absorption takes place.[6] This can lead to major shifts in the emission wavelength and in the fluorescence quantum yields. Often this phenomenon is described using Förster's resonance energy transfer theory (FRET)[34,35], which assumes localized electronic states on individual molecules or molecular subunits that undergo excitonic coupling. This theory works particularly well for weakly coupled chromophores such as biological light-harvesting systems.[20,36] However, in the case of optoelectronic devices that consist of densely stacked molecules or covalently bound oligomers that interact substantially stronger, experimental data did not meet predictions based on FRET.[6,12,37,38] Therefore, the chapters 2 to 5 in this thesis will address the following questions that are based on the excitation energy transfer: How can this process be efficiently modelled and explicitly visualized? How do excitation energy and exciton coupling disorder influence the energy transfer rates and how can the disorders be modified by chemical substitutions? How can simulated excitation energy transfer be directly linked to experimental measurements?

Clearly, the energy transfer is only one of several important aspects influencing the luminescence. Another process that has gained a lot of interest, especially in recent years[5,13,39,40], is the excimer formation. Although this phenomenon has been known for about 60 years[41], its role as a loss channel for many optical applications as well as approaches how to prevent it are not yet fully understood.[42–45] The formation of the excimer is characterized by a strong interaction of two molecules in the excited state that leads to a significant stabilization of the electronic state. Usually the molecules obey a strongly stacked conformation with parallel orientation to maximize the orbital overlap.[5,13] This energetic lowering of the excited state can often result in a trapping of the dimer in this state, due to a deep minimum on the potential energy surface. Furthermore, the short intermolecular distance and large orbital overlap cause the trap state to have a significant charge-transfer character with weak oscillator strength.[13] These properties make an excimer a very undesirable phenomenon for a wide variety of optical applications.[43] For this reason, the dynamics and structural rearrangement during the excimer formation has been extensively studied as part of this thesis and the simulations have also been supported by experimental measurements in a collaborative effort. Not only was it investigated how the excimer forms within a few picoseconds and how the electronic character of the states evolves over time, but also how it influences the formation of singlet-correlated triplet pair states that form the basis for the singlet-fission process[46].

Besides the excimer formation there is another important and common loss channel that is caused by the presence of conical intersections between the electronic ground state and the first excited state. It was often thought that fluorescent molecules are characterized by rigid, conjugated molecular structures that have a stable excited

state minimum,[47,48] while on the other hand non-fluorescent compounds have reactive excited states and decay to the ground state on an ultrafast time scale (e.g. due to the presence of conical intersections).[49–51] Although this classification is often true, there is also a regime between these two extremes, so that, for example, relaxation through conical intersections, which are only thermally accessible through a barrier, occurs on a similar time scale as radiative processes.[10] A similar effect can also be observed in phosphorescent triplet emitters, where a reactive metal-centered state can be thermally accessed from the emissive metal-to-ligand charge transfer state.[52] This dichotomy of rigid, emissive compounds on the hand and reactive, non-emissive ones on the other hand is also reflected in the methods to simulate these phenomena. While approaches based on the harmonic approximation and Fermi's golden rule are usually employed to simulate radiative relaxation rates,[9] different methods like non-adiabatic molecular dynamics are used to study the relaxation through conical intersections.[53,54] However, the latter is usually only possible on a time scale up to a few picoseconds and is not able to quantitatively simulate rates on the nanosecond time scale.[55,56] In contrast, models based on the harmonic approximation are not able to describe relaxation via conical intersections, as this is a strongly anharmonic phenomenon.[9,51] For this reason, as part of this thesis, a new model was developed to extend the rate description based on the harmonic approximation by the relaxation across a barrier thus including relaxation through conical intersections. In addition, this new model also takes into account the electrostatic as well as the frictional effects of solvents on the barriers. It has been successfully used to describe the solvent dependence of the PLQYs of merocyanine dyes.[10] By extension to intersystem crossing processes, the model also allowed to characterize all relaxation channels in different series of BODIPY oligomers.[4]

Structure of this Thesis

This thesis is based on peer-reviewed publications, and the following will briefly introduce which articles and topics are covered in the chapters.
The beginning sections 1.1, 1.2 and 1.3 introduce the concepts of semi-classical dynamics, exciton theory and relaxation rate modeling to the reader and serve as a theoretical background for the following chapters in this thesis. While the first section presents a brief introduction to semi-classical dynamics, the second section compares different approaches to simulate the Coulomb interaction in molecular aggregates. The third section of the introduction derives the fluorescence rate and the energy gap law based on Fermi's Golden Rule. The in-depth description of the theoretical approaches and introduction to the particular scientific questions are given in the corresponding chapters.
Starting with Chapter 2, the thesis elucidates the different aspects of light-matter interaction in molecular systems. Specifically, this means that the first four chapters deal with various phenomena that occur within the first few hundred femtoseconds after light excitation of multichromophoric systems. In particular, they cover topics

like excitation energy transfer and exciton localization. In addition the disorder of site energies and excitonic couplings as well as the connection with experimental quantities play an essential role in these chapters.
Chapter 2 reports on a joint theoretical and experimental investigation of BODIPY heterooligomers which consist of one terminal red-emitting unit and one to three green-emmitting BODIPY units. Two series are considered which differ only in the presence or absence of ethyl groups. These molecular systems exhibited one of the fastest excitation energy transfer processes observed to date in the literature with a lifetime of 39 fs. Light-induced dynamics simulations revealed that the ethyl groups strongly influence the disorder of the excited state energy levels. Moreover, they allowed us to explain the trends in energy transfer lifetimes in detail.
In **Chapter 3** the excitation energy transfer in a squaraine heterotriad consisting of three different covalently linked squaraine chromophores was investigated. A combination of femtosecond transient absorption spectroscopy and light-induced dynamics simulations revealed an ultrafast energy transfer from one terminal squaraine unit to the other within less than 40 fs. The simulations showed that the energy transfer is closely related to the internal conversion process even though the heterotriad is only weakly excitonically coupled.
Chapter 4 examines the photophysics of a molecular triad consisting of a BODIPY dye and two pyrene chromophores. While steady-state measurements indicate only moderate chromophore interactions within the triad, time-resolved measurements show that an initially delocalized excited state localizes onto the BODIPY chromophore upon pyrene excitation. Using light-induced dynamics simulations, it was possible to reveal an oscillatory behavior where the excitation hops between the pyrene units and the BODIPY dye several times until it finally becomes localized on the BODIPY chromophore within 100 fs. Moreover, the simulations show that this is accompanied by an ultrafast non-radiative relaxation within the excitonic manifold mediated by the nonadiabatic coupling.
The same molecular triad as in chapter 4 and a similar dyad, with only a single pyrene unit, were investigated in **Chapter 5** with light-induced dynamics simulations. This chapter shows how the exciton localization and energy transfer lifetime are mediated by the presence of the second pyrene substitution. Furthermore, it was possible to directly connect the energy transfer process to polarization-anisotropy spectroscopy in both molecular systems.
In **Chapter 6**, compared to the previous chapters, not only was a new system and phenomenon studied, but also the time scale after excitation was extended to several tens of picoseconds. On this time scale, it was possible to investigate the mechanism of excimer formation and its interplay with the singlet-correlated triplet pair state ^{1}(TT) in the tetracene dimer. Furthermore, the inclusion of doubly excited states in non-adiabatic dynamics and their diabatization allowed us to observe a transient population of the ^{1}(TT) state, which, however, gets depopulated on a timescale of 8 ps, leading finally to the trapping in the excimer minimum.
The following two chapters, **7** and **8**, extend the time scale and the processes studied

once again and examine all relaxation processes that happen after light excitation up to the ns and even μs scale. The focus here is to investigate whether radiative or non-radiative relaxation channels are preferred by the molecules and to understand photoluminescence quantum yields (PLQYs) both qualitatively and quantitatively.
In **Chapter 7** the photochemistry of a merocyanine dye in various solvents is studied. Initially, the PLQYs seemed to contradict the energy gap law[57]. However, simulations allowed us to to identify a barrier to conical intersections which is very sensitive to solvent polarity and serves as a temperature dependent relaxation channel. The conical intersection is characterized by a twisted geometry which allows subsequent photoisomerization. Developing a model that combines Kramers rate theory[58] with Jortner's energy gap law[57] allowed us to simulate the PLQY in good agreement with experimental values. Moreover, transient absorption measurements confirmed the formation of a photoisomer, while the measurements of fluorescence quantum yields at low temperatures demonstrated the existence of an activation energy barrier.
In the final **Chapter 8**, many of the previously studied aspects and processes are combined in one work. Here, it was presented to which extent exciton formation can amplify fluorescence based on a series of oligo-BODIPYs. The non-radiative deactivation channels — internal conversion (IC) and intersystem crossing (ISC), also combined with an upstream reductive Photoelectron Transfer (rPET) — were identified at the monomeric state, and the evolution of fluorescence and (non-)radiative decay rates predicted along the oligomeric series. It was possible to show that a significant fluorescence enhancement is not limited to sterically induced motional restrictions but can be solely achieved by excitonic coupling of chromophores.
The thesis concludes with a summary and outlook in chapter 9 and 10.

1.1 Semi-classical Dynamics

Molecular quantum mechanics provides a theoretical framework for describing dynamical processes in molecular systems. However, solving the quantum mechanical equations of motion required for such simulations is computationally expensive or even infeasible because the computational cost grows exponentially with the number of degrees of freedom. Fully quantum mechanical calculations are therefore limited to small molecules, and efficient approximations are necessary in most cases. One such approximation was developed by Born and Oppenheimer and is based on the idea of separating the electronic from the nuclear motion.[59] The approximation is motivated by the electron mass being much lower than the mass of the nuclei. The Born-Oppenheimer approximation models the nuclei as wave packets moving in the mean potential generated by the presence of the electrons. For the solution of the electronic part of the wavefunction, the nuclear coordinates can be assumed to be stationary, which leads to the electronic time-independent Schrödinger equation,

$$\hat{H}_{\mathrm{el}}(\mathbf{r};\mathbf{R})\psi_i(\mathbf{r};\mathbf{R}) = E_{\mathrm{el},i}(\mathbf{R})\psi_i(\mathbf{r};\mathbf{R}), \tag{1.1}$$

for an electronic wavefunction ψ_i which depends only parametrically on the nuclear configuration $\mathbf{R}$.
The electronic Hamiltonian is given by

$$\hat{H}_{\mathrm{el}}(\mathbf{r};\mathbf{R}) = \hat{T}_{\mathrm{e}}(\mathbf{r}) + \hat{V}_{\mathrm{ee}}(\mathbf{r}) + \hat{V}_{\mathrm{en}}(\mathbf{r};\mathbf{R}) + \hat{V}_{\mathrm{nn}}(\mathbf{R}), \tag{1.2}$$

where $\hat{T}_{\mathrm{e}}(\mathbf{r}) = -\sum_{i=1}^{N} \frac{1}{2}\nabla_i^2$ is the kinetic energy operator for the electrons and $\hat{V}_{\mathrm{ee}}(\mathbf{r}) = \sum_{i=1}^{N}\sum_{j>i}^{N} \frac{1}{|\mathbf{r}_i - \mathbf{r}_j|}$ represents the Coulomb interaction between the electrons. $\hat{V}_{\mathrm{en}}(\mathbf{r};\mathbf{R}) = -\sum_{i,A} \frac{Z_A}{|\mathbf{r}_i - \mathbf{R}_A|}$ accounts for the attraction between electrons and nuclei and the last term $\hat{V}_{\mathrm{nn}}(\mathbf{R}) = \sum_{A<B} \frac{Z_A Z_B}{\mathbf{R}_A - \mathbf{R}_B}$ represents the repulsion of the nuclei. The electronic Hamiltonian is only parametrically dependent on the nuclear coordinates and does not contain the kinetic energy of the nuclei. The eigenenergies $E_{\mathrm{el},i}(\mathbf{R})$ on the right-hand side of Eq. 1.1 play the role of potentials for the nuclear motion and represent the potential energy surfaces (PES) of a given electronic wavefunction ψ_i. The eigenfunctions ψ_i provide an orthonormal basis into which the total electron-nuclear wavefunction can be expanded as a linear combination of electronic eigenstates

$$\Psi(\mathbf{r};\mathbf{R}) = \sum_i \vartheta_i(\mathbf{R})\psi_i(\mathbf{r};\mathbf{R}). \tag{1.3}$$

The expansion coefficients ϑ_i that depend only on the nuclear coordinates represent the nuclear wavefunctions. Substituting this ansatz into the time-independent Schrödinger equation leads to a coupled set of equations that only involve nuclear

wavefunctions,

$$\left[\hat{T}_{\mathrm{n}} + E_{\mathrm{el},i}(\mathbf{R})\right] \vartheta_i(\mathbf{R}) - \sum_j \hat{B}_{ij}\vartheta_j(\mathbf{R}) = E\vartheta_i(\mathbf{R}), \tag{1.4}$$

where $\hat{B}_{ij}$ describes the nonadiabatic coupling of the electronic and nuclear degrees of freedom which is given by:

$$\hat{B}_{ij} = \sum_A^M \frac{1}{2m_A}\left[2\left\langle\psi_i(\mathbf{r};\mathbf{R})\,|\,\nabla_{R_A}\,|\,\psi_j(\mathbf{r};\mathbf{R})\right\rangle\nabla_{R_A} + \left\langle\psi_i(\mathbf{r};\mathbf{R})\,\middle|\,\nabla^2_{R_A}\,\middle|\,\psi_j(\mathbf{r};\mathbf{R})\right\rangle\right] \tag{1.5}$$

The Born-Oppenheimer approximation neglects the couplings $\hat{B}_{ij}$ and allows one to express the total wavefunction as a simple product of the electronic and nuclear wavefunction

$$\Psi(\mathbf{r};\mathbf{R}) = \vartheta_i(\mathbf{R})\psi_i(\mathbf{r};\mathbf{R}). \tag{1.6}$$

The set of Eqs. 1.4 is then replaced by uncoupled equations of the form

$$\left[\hat{T}_n(\mathbf{R}) + E_{\mathrm{el},i}(\mathbf{R}) - \hat{B}_{ii}\right]\vartheta_i(\mathbf{R}) = E\vartheta_i(\mathbf{R}). \tag{1.7}$$

for each electronic state. Neglection of the nonadiabatic couplings works well for energetically separated electronic states, which is e.g., the case for processes that only occur in the electronic ground state. However, the Born-Oppenheimer approximation fails if the coupling plays a substantial role as it is the case in photochemistry or optoelectronic materials.
The effort required to fully describe the dynamics of a system using a quantum dynamics grows exponentially with the number of degrees of freedom of the system. Furthermore, knowledge of the potential governing the nuclear motion is necessary over the entire coordinate space relevant to the dynamics to accurately represent the electronic energy of the system. Therefore, the second approximation replaces the nuclear wavepackets with an ensemble of classical trajectories. The nuclear motion of a molecule which resides in its i-th electronic state is then represented by a classical point particle $\mathbf{R}_i(t)$, whose movement follows Newton's equations

$$\mathbf{F} = \mathbf{m}\frac{\mathrm{d}^2\mathbf{R}(t)}{\mathrm{d}t^2} = \mathbf{m}\ddot{\mathbf{R}}(t) = -\nabla_{\mathbf{R}}E_{\mathrm{el},i}(\mathbf{R}). \tag{1.8}$$

The diagonal matrix $\mathbf{m}$ defines the nuclear masses and the negative gradient of the PES $E_i(\mathbf{R})$ determines the force $\mathbf{F}$. For simulations, numerical integration of Newton's equation of motion is required to obtain coordinates and velocities at specific time steps. Different algorithms exist for this integration; the Verlet algorithm[60] is one of the most prominent, which expands the nuclear coordinates after a time step

Δt in a Taylor series around the current time step t

$$\mathbf{R}(t+\Delta t) = \mathbf{R}(t) + \mathbf{v}(t)\Delta t - \frac{\mathbf{F}(t)}{2\mathbf{m}}\Delta t^2 + \frac{\mathrm{d}^3\mathbf{R}(t)}{\mathrm{d}t^3}\frac{\Delta t^3}{6} + \mathscr{O}\left(\Delta t^4\right). \tag{1.9}$$

The same Taylor expansion can be used for negative time steps $-\Delta t$

$$\mathbf{R}(t-\Delta t) = \mathbf{R}(t) - \mathbf{v}(t)\Delta t - \frac{\mathbf{F}(t)}{2\mathbf{m}}\Delta t^2 - \frac{\mathrm{d}^3\mathbf{R}(t)}{\mathrm{d}t^3}\frac{\Delta t^3}{6} + \mathscr{O}\left(\Delta t^4\right), \tag{1.10}$$

and the general form of the Verlet algorithm can be obtained by addition of equation 1.9 and 1.10

$$\mathbf{R}(t+\Delta t) = 2\mathbf{R}(t) - \mathbf{R}(t-\Delta t) - \frac{\mathbf{F}(t)}{\mathbf{m}}\Delta t^2 + \mathscr{O}\left(\Delta t^4\right). \tag{1.11}$$

Neglecting the fourth order term on the right-hand side allows obtaining new coordinates with an error of the order Δt^4. The time steps Δt should be shorter than the time-scale of the fastest nuclear motion to ensure that neglecting higher-order terms is a good approximation. In organic materials, the C−H stretching modes usually have the shortest oscillation period and determine the timestep to be roughly 1 fs. However, numerical propagation also requires velocities that the Verlet algorithm does not provide directly. The velocity Verlet algorithm offers this possibility by evaluating the coordinates, velocities, and forces at the current time step

$$\begin{aligned} \mathbf{R}(t+\Delta t) &= \mathbf{R}(t) + \mathbf{v}(t)\Delta t - \frac{\mathbf{F}(t)}{2\mathbf{m}}\Delta t^2 \\ \mathbf{v}(t+\Delta t) &= \mathbf{v}(t) + \frac{\mathbf{F}(t) - \mathbf{F}(t+\Delta t)}{2\mathbf{m}}\Delta t^2 \end{aligned} \tag{1.12}$$

The error of the velocity Verlet variant[61] is on the fourth order, too, and the energy conservation of both algorithms is ensured by the invariance under the transformation $\Delta t \to -\Delta t$, also known as the time-reversibility.
The forces of the adiabatic potential energy surfaces are determined *on the fly* by an electronic structure calculation for the current nuclear geometry $\mathbf{R}$.

1.1.1 Nonadiabatic Dynamics

Two approaches are commonly employed for simulating non-adiabatic events in molecular dynamics, which are of fundamental importance in photochemistry. Tully's surface hopping is a stochastic method in which transitions between electronic states that corresponds to the switch of a trajectory to another potential energy surface.[55] A trajectory is restricted to moving on one PES at a time. However, surface hops to other states can occur, according to a probability that is calculated based on quantum electronic state populations. In contrast, the mean-field Ehrenfest dynamics method propagates a trajectory on a linear combination of electronic states, forming

an effective potential energy surface.[62] Since only the surface hopping approach was used in this work, the discussion below will be limited to this method.
Expansion of the total electronic wavefunction in terms of the eigenfunctions of the electronic Hamiltonian at the current nuclear geometry is given by

$$|\Psi_{\mathrm{el}}(\mathbf{r};\mathbf{R}(t))\rangle = \sum_j c_j(t)\,|\psi_j(\mathbf{r};\mathbf{R}(t))\rangle\,, \tag{1.13}$$

where the products of the complex-valued coefficients are the elements of the density matrix $\rho_{ij}(t) = c_i(t)c_j^*(t)$. The time-dependent population of each electronic state $|\psi_j(\mathbf{r};\mathbf{R}(t))\rangle$ is given by the corresponding diagonal element of the density matrix ρ_{jj}. Inserting Eq. 1.13 into the time-dependent Schrödinger equation and projection onto the i-th electronic state gives a set of coupled equations for the time-dependent expansion coefficients

$$i\hbar\frac{\partial}{\partial t}c_i(t) = E_i(\mathbf{R})c_i(t) - i\hbar\sum_j \underbrace{\langle\psi_i(\mathbf{r};\mathbf{R}(t))\,|\,\nabla_R\psi_j(\mathbf{r};\mathbf{R}(t))\rangle}_{\mathbf{d}_{ij}}\cdot\mathbf{v}(t)\cdot c_j(t). \tag{1.14}$$

where the abbreviation $\mathbf{d}_{ij}$ is used for the non-adiabatic coupling vector between states i and j that mediates the transitions between states. If the population (the diagonal element of the density matrix) on a different electronic state increases, the trajectory may switch from its current state. Te probability of a trajectory changing its electronic state is dependent on the time derivative of the density matrix

$$\frac{\mathrm{d}}{\mathrm{d}t}\rho_{ij} = \dot{\rho}_{ij} = \frac{i}{\hbar}\left(E_j - E_i\right)\rho_{ij}(t) - \sum_{k\neq i}\left(\mathbf{v}(t)\left(\mathbf{d}_{ik}\rho_{kj} + \mathbf{d}_{jk}\rho_{ik}\right)\right) \tag{1.15}$$

$$\frac{\mathrm{d}}{\mathrm{d}t}\rho_{ii} = \dot{\rho}_{ii} = \sum_{k\neq i} b_{ik} = -2\sum_{k\neq i}\mathrm{Re}\left(\mathbf{v}(t)\mathbf{d}_{ik}\rho_{ki}\right). \tag{1.16}$$

The probability of jump between two electronic states consists of two parts[63]; the chance to depopulate the actual state i

$$P_{i,\mathrm{depopulation}} = \Theta(-\dot{\rho}_{ii})\frac{-\dot{\rho}_{ii}}{\rho_{ii}}\Delta t, \tag{1.17}$$

and the chance to populate the specific state j among all states the population of which is increasing:

$$P_{j,\mathrm{population}} = \Theta(\dot{\rho}_{jj})\frac{\dot{\rho}_{jj}}{\sum_k \Theta(\dot{\rho}_{kk})\dot{\rho}_{kk}}, \tag{1.18}$$

where the Heaviside step function Θ is one for positive arguments and zero otherwise, ensuring a zero hopping probability if the current state population increases and/or the population of the target state j decreases. The transition probability from a state

i to a state j between two consecutive times $t_{n+1} - t_n = \Delta t$ is given by the product of the population and depopulation probability

$$P_{i\to j} = P_{i,\text{population}} P_{j,\text{depopulation}} \tag{1.19}$$

$$= \Theta(-\dot{\rho}_{ii})\Theta(\dot{\rho}_{jj}) \frac{-\dot{\rho}_{ii}}{\rho_{ii}} \frac{\dot{\rho}_{jj}}{\sum_k \Theta(\dot{\rho}_{kk})\dot{\rho}_{kk}} \Delta t. \tag{1.20}$$

Whether a hop between electronic states occurs is determined by drawing a random number $0 \leq \xi \leq 1$ and if $0 < \xi < \sum_{j\neq i} P_{i\to j}$, a switch to another state is appropriate. On an ensemble level with a large number of trajectories the relative amount of trajectories in an electronic state should approach the quantum population probability

$$\frac{N_i(t)}{N(t)} \to \rho_{ii}(t). \tag{1.21}$$

If a jump from one state i to another state j occurs, then the potential energy changes, and it has to be compensated by the kinetic energy of the trajectory if the energy conservation has to be satisfied. Tully suggested that the velocities are rescaled along the direction of the non-adiabatic coupling vector according to[55]

$$\mathbf{v}(t + \mathrm{d}t) = \mathbf{v}(t) - \xi \mathbf{d}_{ij}, \tag{1.22}$$

where the rescaling factor ξ_{ij} tries to hold the equality

$$E_{\text{kin}}(\mathbf{v}(t)) + E_i(\mathbf{R}(t)) = E_{\text{kin}}(\mathbf{v}(t)) + E_j(\mathbf{R}(t)) \tag{1.23}$$

In cases where the increase in potential energy exceeds the available kinetic energy, the energy conservation can not be fulfilled, and the hop is forbidden.

1.1.2 Field-induced surface hopping method

Tully's surface hopping method allows the description of transitions between electronic states, but we have yet to discuss the occupation of the initial states. From an experimental point of view, two different conditions can be distinguished. One is photoexcitation and the other is electrical excitation. The first is used mainly in studying molecular properties, e.g., in solvent, film, or gas phase. In contrast, the latter is used in optoelectronic devices and stacks of different materials. Since we focus in this work on the properties of molecules and their aggregates, especially in solution and gas phase, we will discuss only photoexcitation in the following. Excitation by an electric field leads to the occupation of states that are optically allowed, which is determined by their transition dipole moment,

$$\boldsymbol{\mu}_{ij}(\mathbf{R}(t)) = \langle \psi_i(\mathbf{r}; \mathbf{R}(t)) | (q\mathbf{r}) | \psi_j(\mathbf{r}; \mathbf{R}(t)) \rangle \,, \tag{1.24}$$

where the charge is given by q and the position operator by $\mathbf{r}$. The coupling between transition dipole moment and electric field $\mathbf{E}(t)$ is given

$$-\boldsymbol{\mu}_{ij}(\mathbf{R}(t)) \cdot \mathbf{E}(t) \tag{1.25}$$

The field-induced surface hopping (FISH) method[56] introduces this coupling in Eq. 1.14 as

$$i\hbar\frac{\partial}{\partial t}c_i(t) = E_i(\mathbf{R})c_i(t) - i\hbar\sum_j \left(\mathbf{d}_{ij} \cdot \mathbf{v}(t) - \boldsymbol{\mu}_{ij} \cdot \mathbf{E}(t)\right) c_j(t) \tag{1.26}$$

and the time derivatives of the density matrix elements become

$$\begin{aligned}\frac{\mathrm{d}}{\mathrm{d}t}\rho_{ij} =& \dot{\rho}_{ij} = i\left(E_j - E_i\right)\rho_{ij}(t) \\ &- \sum_k \left(\mathbf{v}(t) \cdot \left(\mathbf{d}_{ik}\rho_{kj} - \mathbf{d}_{jk}\rho_{ik}\right) + \left(\boldsymbol{\mu}_{kj}\rho_{ik}\mathbf{E}(t) - \boldsymbol{\mu}_{ik}\rho_{kj}\mathbf{E}(t)\right)\right)\end{aligned} \tag{1.27}$$

$$\frac{\mathrm{d}}{\mathrm{d}t}\rho_{ii} = \dot{\rho}_{ii} = -2\sum_k \left(\mathrm{Re}\left(\mathbf{v}(t)\mathbf{d}_{ik}\rho_{ki}\right) + \mathrm{Im}\left(\boldsymbol{\mu}_{ij}\rho_{ki}\mathbf{E}(t)\right)\right). \tag{1.28}$$

The probability of a jump to a different electronic state is calculated in the same way as in Tully's surface hopping approach. During the laser pulse, the energy is not conserved, but once the pulse has ceased, the energy conservation will be upheld again.
As shown, the field-induced surface hopping method not only describes the transitions between electronic states during the nonradiative-relaxation but also considers the initial state population given by the photoexcitation. This makes it possible to simulate light-induced dynamics in complex chromophores and aggregates efficiently.

1.2 Exciton Theory

Understanding and predicting the excited states and the corresponding relaxation dynamics of conjugated organic molecules are increasingly crucial for developing functional materials, such as display solutions or organic electronics.[6,12,21,24–27,64,65] For over 60 years, this has inspired many studies to create an understanding of the electronic excitations and intermolecular interactions in organic aggregates and films.[24] These investigations were motivated initially by the independent discovery of Jelley[66] and Scheibe[67] in the 1930s. They observed that aggregation of pseudoisocyanine (PIC) chloride leads to an intensified, narrowed, and bathochromically-shifted absorption spectrum and that these effects are reversible upon heating and cooling the solution. In his seminal work, Scheibe correctly attributed the spectral changes to the polymerization/aggregation of PIC[67]. Nowadays, dye aggregates acting in this way are called Scheibe- or J-aggregates (J after Jelley).[24] Supramolecular systems

with hypsochromically shifted absorption bands are called H-aggregates (H denotes hypsochromic).
The exciton theory is based on the Born-Oppenheimer approximation, which provides a separation of electronic and nuclear degrees of freedom. We consider the simplest possible case, two molecules A and B in a vacuum at a fixed distance having fixed nuclear coordinates. Furthermore, we assume that we know the exact eigenstates of monomer A and B, which each form an orthonormal basis in the Hilbert space of A and B,

$$\left\{\left|\psi_k^A\right\rangle, \quad k = 1, \cdots, N_A\right\} \quad \text{and} \quad \left\{\left|\psi_l^B\right\rangle, \quad l = 1, \cdots, N_B\right\}, \tag{1.29}$$

where N_A (N_B) denotes the number of eigenvectors of A (B). The basis in the Hilbert space of the dimer ($A + B$) can be formed as a direct product of the basis of A and B

$$\left\{\left|\psi_k^A\right\rangle \otimes \left|\psi_l^B\right\rangle, \quad \{k = 1, \cdots, N_A \quad l = 1, \cdots, N_B\right\}. \tag{1.30}$$

This allows writing the eigenstates of the dimer in the new basis as

$$|\psi_{AB}\rangle = \sum_{k=1}^{N_A}\sum_{l=1}^{N_B} c_{kl} \left|\psi_k^A\right\rangle \otimes \left|\psi_l^B\right\rangle. \tag{1.31}$$

The expansion coefficients can be determined by inserting the eigenstates in the Schrödinger equation,

$$\hat{H} \sum_{k=1}^{N_A}\sum_{l=1}^{N_B} c_{kl} \left|\psi_k^A\right\rangle \otimes \left|\psi_l^B\right\rangle = E \sum_{k=1}^{N_A}\sum_{l=1}^{N_B} c_{kl} \left|\psi_k^A\right\rangle \otimes \left|\psi_l^B\right\rangle, \tag{1.32}$$

and projecting on the individual basis functions $\left|\psi_i^A\right\rangle \otimes \left|\psi_j^B\right\rangle$

$$\sum_{k=1}^{N_A}\sum_{l=1}^{N_B} c_{kl} \underbrace{\left(\left\langle\psi_i^A\right| \otimes \left\langle\psi_j^B\right|\right) \hat{H} \left(\left|\psi_k^A\right\rangle \otimes \left|\psi_l^B\right\rangle\right)}_{H_{ij,kl}} = E \sum_{k=1}^{N_A}\sum_{l=1}^{N_B} c_{kl} \underbrace{\left(\left\langle\psi_i^A\right| \otimes \left\langle\psi_j^B\right|\right) \left(\left|\psi_k^A\right\rangle \otimes \left|\psi_l^B\right\rangle\right)}_{S_{ij,kl}} \tag{1.33}$$

It is now possible to denote the eigenvalue problem as

$$\sum_{k=1}^{N_A}\sum_{l=1}^{N_B} H_{ij,kl} c_{kl} = E \sum_{k=1}^{N_A}\sum_{l=1}^{N_B} S_{ij,kl} c_{kl}. \tag{1.34}$$

Since we assert that the basis of A and B are orthonormal, we can simplify the overlap

matrix elements as:

$$\begin{aligned} S_{ij,kl} &= \left(\left\langle \psi_i^A \right| \otimes \left\langle \psi_j^B \right|\right) \left(\left| \psi_k^A \right\rangle \otimes \left| \psi_l^B \right\rangle\right) \\ &= \left\langle \psi_i^A \mid \psi_k^A \right\rangle \left\langle \psi_j^B \mid \psi_l^B \right\rangle \\ &= \delta_{ik}\delta_{jl} \end{aligned} \tag{1.35}$$

Now we take a closer look at the Hamiltonian operator of the dimer. We can construct the Hamiltonian as,

$$\hat{H} = \hat{H}_A + \hat{H}_B + \hat{V}, \tag{1.36}$$

where $\hat{H}_A$ ($\hat{H}_B$) is the Hamiltonian of monomer A (B) and $\hat{V}$ is the electrostatic interaction between A and B. Therefore, the matrix element $H_{ij,kl}$ is defined by

$$\begin{aligned} H_{ij,kl} =& \left(\left\langle \psi_i^A \right| \otimes \left\langle \psi_j^B \right|\right) \hat{H} \left(\left| \psi_k^A \right\rangle \otimes \left| \psi_l^B \right\rangle\right) \\ =& \left(\left\langle \psi_i^A \right| \otimes \left\langle \psi_j^B \right|\right) \left[\hat{H}_A + \hat{H}_B + \hat{V}\right] \left(\left| \psi_k^A \right\rangle \otimes \left| \psi_l^B \right\rangle\right) \\ =& \left\langle \psi_i^A \left| \hat{H}_A \right| \psi_k^A \right\rangle \left\langle \psi_j^B \mid \psi_l^B \right\rangle + \left\langle \psi_i^A \mid \psi_k^A \right\rangle \left\langle \psi_j^B \left| \hat{H}_B \right| \psi_l^B \right\rangle + \left\langle \psi_i^A \right| \otimes \left\langle \psi_j^B \left| \hat{V} \right| \psi_k^A \right\rangle \otimes \left| \psi_l^B \right\rangle \\ =& E_k^A \delta_{ik}\delta_{jl} + E_l^B \delta_{ik}\delta_{jl} + \left\langle \psi_i^A \right| \otimes \left\langle \psi_j^B \left| \hat{V} \right| \psi_k^A \right\rangle \otimes \left| \psi_l^B \right\rangle . \end{aligned} \tag{1.37}$$

Inserting this expression back into the eigenvalue problem, we get:

$$(E_i^A + E_j^B)c_{ij} + \sum_{k=1}^{N_A}\sum_{l=1}^{N_B} \left[+ \left(\left\langle \psi_i^A \right| \otimes \left\langle \psi_j^B \right|\right) \hat{V} \left(\left| \psi_k^A \right\rangle \otimes \left| \psi_l^B \right\rangle\right)\right] c_{kl} = E c_{ij} \tag{1.38}$$

To further simplify the problem, we assume that each monomer only contributes two electronic states, the electronic ground state, and one singlet excited state. Since those two states in which exactly one monomer is excited while the other is in the ground state will mix the most because their energetic distance is the smallest, we can make an additional approximation and neglect all interactions except this one. This gives us a simple expression for the electronic ground state and the doubly excited state of the dimer

$$\begin{aligned} E_0 &= E_g^A + E_g^B + \left\langle \psi_g^A \psi_g^B \left| \hat{V} \right| \psi_g^A \psi_g^B \right\rangle \rightarrow |\psi_{gg}\rangle = \left| \psi_g^A \right\rangle \otimes \left| \psi_g^B \right\rangle \\ E_3 &= E_e^A + E_e^B + \left\langle \psi_e^A \psi_e^B \left| \hat{V} \right| \psi_e^A \psi_e^B \right\rangle \rightarrow |\psi_{ee}\rangle = \left| \psi_e^A \right\rangle \otimes \left| \psi_e^B \right\rangle . \end{aligned} \tag{1.39}$$

Moreover, it reduces the eigenvalue problem for the two singly excited exciton states to a dimension of 2x2:

$$\begin{bmatrix} E_g^A + E_e^B + \left\langle \psi_g^A \psi_e^B \left| \hat{V} \right| \psi_g^A \psi_e^B \right\rangle & \left\langle \psi_g^A \psi_e^B \left| \hat{V} \right| \psi_e^A \psi_g^B \right\rangle \\ \left\langle \psi_e^A \psi_g^B \left| \hat{V} \right| \psi_g^A \psi_e^B \right\rangle & E_e^A + E_g^B + \left\langle \psi_e^A \psi_g^B \left| \hat{V} \right| \psi_e^A \psi_g^B \right\rangle \end{bmatrix} \begin{bmatrix} c_{ge} \\ c_{eg} \end{bmatrix} = E \begin{bmatrix} c_{ge} \\ c_{eg} \end{bmatrix} \tag{1.40}$$

We now introduce two abbreviations and assume that all involved wavefunctions are real:

$$\begin{aligned} J_{ge} &\equiv \left\langle \psi_g^A \psi_e^B \left| \hat{V} \right| \psi_e^A \psi_g^B \right\rangle = \left\langle \psi_e^A \psi_g^B \left| \hat{V} \right| \psi_g^A \psi_e^B \right\rangle \\ D_{ge} &\equiv \left\langle \psi_g^A \psi_e^B \left| \hat{V} \right| \psi_g^A \psi_e^B \right\rangle = \left\langle \psi_e^A \psi_g^B \left| \hat{V} \right| \psi_e^A \psi_g^B \right\rangle . \end{aligned} \tag{1.41}$$

This allows us to write the 2x2 eigenvalue problem as,

$$\begin{bmatrix} E_g^A + E_e^B + D_{ge} & J_{ge} \\ J_{ge} & E_g^A + E_e^B + D_{ge} \end{bmatrix} \begin{bmatrix} c_{ge} \\ c_{eg} \end{bmatrix} = E \begin{bmatrix} c_{ge} \\ c_{eg} \end{bmatrix}, \tag{1.42}$$

and the eigenvalues of the two exciton states are given by:

$$E_\pm = \frac{1}{2}\left(E_g^A + E_e^A + E_g^B + E_e^B\right) + D_{ge} \pm \frac{1}{2}\sqrt{\left(E_g^A - E_g^B + E_e^A - E_e^B\right)^2 + 4J_{ge}^2}. \tag{1.43}$$

1.2.1 Exciton Coupling

In the following, we will take a closer look at the interaction part of the Hamiltonian. This electrostatic interaction is often called excitonic coupling

$$J_{ge} = \left\langle \psi_g^A \psi_e^B \left| \hat{V} \right| \psi_e^A \psi_g^B \right\rangle \tag{1.44}$$

and contains the following four electrostatic interaction terms:

- electrons of A with electrons of B: $\hat{V}_{e_A,e_B}$
- electrons of A with nuclei of B: $\hat{V}_{e_A,Z_B}$
- electrons of B with nuclei of A: $\hat{V}_{e_B,Z_A}$
- nuclei of A with nuclei of B: $\hat{V}_{Z_A,Z_B}$

However, due to the orthogonality of the eigenstates of A and B only the Coulomb electron-electron interaction term is non-zero:

$$\begin{aligned} J_{ge} = &\left\langle \psi_g^A \psi_e^B \left| \hat{V}_{e_A,e_B} \right| \psi_e^A \psi_g^B \right\rangle + \left\langle \psi_e^B \left| \hat{V}_{e_B,Z_A} \right| \psi_g^B \right\rangle \underbrace{\left\langle \psi_g^A \middle| \psi_e^A \right\rangle}_{=0} \\ &+ \left\langle \psi_g^A \left| \hat{V}_{e_A,Z_B} \right| \psi_e^A \right\rangle \underbrace{\left\langle \psi_e^B \middle| \psi_g^B \right\rangle}_{=0} + V_{Z_A,Z_B} \left\langle \psi_g^A \mid \psi_e^A \right\rangle \underbrace{\left\langle \psi_e^B \middle| \psi_g^B \right\rangle}_{=0} \end{aligned} \tag{1.45}$$

The Coulomb interaction between the two excited states of the chromophores is given by

$$\begin{aligned} J_{ge} &= \frac{1}{4\pi\epsilon}\sum_{i=1}^{n_A}\sum_{j=1}^{n_B}\left\langle \psi_g^A\psi_e^B\left|\frac{1}{r_{ij}^{AB}}\right|\psi_e^A\psi_g^B\right\rangle \\ &= \frac{1}{4\pi\epsilon}\int \mathrm{d}\mathbf{x}_1^A\mathrm{d}\mathbf{x}_1^B \underbrace{n_A\int \mathrm{d}\mathbf{x}_2^A\cdots d\mathbf{x}_N^A\psi_g^A\left(\mathbf{x}_1^A,\cdots\right)\psi_e^A\left(\mathbf{x}_1^A,\cdots\right)}_{\rho_{ge}^A(\mathbf{x}_1^A)}\frac{1}{r_{11}^{AB}}\underbrace{n_B\int \mathrm{d}\mathbf{x}_2^B\cdots\mathrm{d}\mathbf{x}_N^B\psi_g^B\left(\mathbf{x}_1^B\cdots\right)\psi_e^B\left(\mathbf{x}_1^B,\cdots\right)}_{\rho_{ge}^B(\mathbf{x}_1^B)} \end{aligned} \tag{1.46}$$

where n_A (n_B) denote the number of electrons and ρ_{ge}^A (ρ_{ge}^B) is the transition density between the ground state and the first excited state of the monomer A (B). This allows writing the coupling as

$$J_{ge} = \frac{1}{4\pi\epsilon}\int d\mathbf{r}d\mathbf{r}'\frac{\rho_{ge}^A(\mathbf{r})\rho_{ge}^B(\mathbf{r}')}{|\mathbf{r}-\mathbf{r}'|} \tag{1.47}$$

If we introduce the electrostatic potential that is created by the transition density of monomer B

$$V(\mathbf{r}) = \frac{1}{4\pi\epsilon}\int d\mathbf{r}'\frac{\rho_{ge}^B(\mathbf{r}')}{|\mathbf{r}-\mathbf{r}'|} \tag{1.48}$$

then we can rewrite the coupling as

$$J_{ge} = \int d\mathbf{r}V(\mathbf{r})\rho_{ge}^A(\mathbf{r}). \tag{1.49}$$

Transition density cube method

A method for accurately calculating the Coulombic coupling between monomers was introduced by Scholes et al.[37] and is called the transition density cube (TDC) method. In this method, the transition density is constructed on a three-dimensional grid of finite-sized volume elements (cells) which make up the cube,

$$\rho_{eg}(x,y,z) = \frac{1}{V_\delta}\int_z^{z+\delta_z}\int_y^{y+\delta_y}\int_x^{x+\delta_x}\psi_e\psi_g\mathrm{d}x'\mathrm{d}y'\mathrm{d}z' \tag{1.50}$$

here δ_α define the grid size of the density cube, and V_δ is the element volume ($V_\delta = \delta_x\delta_y\delta_z$). Inserting Eq. 1.50 into Eq. 1.47 leads to the working equation of the TDC method

$$J_{ge} = \frac{1}{4\pi\epsilon}\sum_{i,j}\frac{\rho_{eg}^A(i)\rho_{eg}^B(j)}{r_{ij}}, \tag{1.51}$$

where $\rho_{eg}^A(i)$ and $\rho_{eg}^B(j)$ are TDC elements i and j for monomer A and B and r_{ij} is their separation. The only approximation involved here is in the finite size of the grid

over which the numerical summation is carried out.

Transition charge method

Since the TDC method often requires many grid points and integration over six dimensions can be numerically very expensive, it can often be useful to simplify the calculation of the coupling further. The idea is to represent the potential generated by the transition density (see Eq. 1.48) by atom-centered transition charges. This approach corresponds to the tight-binding approximation widely used in quantum chemistry to approximate the two-electron Coulomb integrals. This simplifies the expression for the coupling to

$$V = \sum_{i,j} \frac{q^{\mathrm{A}}_{\mathrm{eg},i}, q^{\mathrm{B}}_{\mathrm{eg},j}}{\left|\mathbf{R}^A_i - \mathbf{R}^{\mathrm{B}}_j\right|}, \tag{1.52}$$

where i and j denote the atom indices on monomer A and B, respectively. However, we have not yet defined how to calculate these transition charges. A variety of different methods have been described in the literature. In tight-binding quantum chemistry methods, the Mulliken population analysis is usually employed to compute transition charges from the product of the transition density and the overlap matrix. Another popular approach is to fit the transition charges to the electrostatic potential created by the transition density, as presented by Renger et al.[68] Compared to the TDC method, the main advantage is that the summation only has to be performed over the atoms of the two monomers instead of over all grid points. This simplification allows calculating the excitonic couplings very efficiently. Although the transition charge method is often quite accurate, there may be problematic cases when it is not suitable. By only summing over products of charges located on atoms, it cannot account for the parts of the transition density that are localized elsewhere. For example, a state may be localized perpendicular to a molecular plane, but this would not be reflected at all by atom-centered transition charges.

Point-dipole approximation

The multipole expansion formula allows expanding the electrostatic potential around the center of charge density[69]

$$V(\mathbf{r}) = \frac{1}{4\pi\epsilon} \times \left[\underbrace{\frac{1}{r} \int \rho_{eg}\left(\mathbf{r}'\right) d\mathbf{r}'}_{\text{monopol}} + \underbrace{\frac{1}{r^2} \int \rho_{eg}\left(\mathbf{r}'\right) \cos\theta r' d\mathbf{r}'}_{\text{dipole}} + \underbrace{\frac{1}{r^3} \int \rho_{eg}\left(\mathbf{r}'\right) \left(\frac{3}{2}\cos^2\theta - \frac{1}{2}\right) r'^2 d\mathbf{r}' + \cdots}_{\text{quadrupole}} \right]. \tag{1.53}$$

Due to the orthogonality of the eigenstates, the leading monopol term is always zero. The second term contains the transition dipole moment

$$\boldsymbol{\mu}_{eg} \equiv \int \rho_{eg}\left(\mathbf{r}'\right) \mathbf{r}' d\mathbf{r}'. \tag{1.54}$$

If the multipole expansion is only done up to the dipole term, one gets the following approximation for the electrostatic potential:

$$V(\mathbf{r}) = \frac{\boldsymbol{\mu}_{eg} \cdot \mathbf{r}}{4\pi\epsilon} \times \frac{1}{r^3} \tag{1.55}$$

Inserting this into Eq. 1.49 and doing another multipole expansion of the appearing $\frac{1}{|\mathbf{R}_{AB}+\mathbf{r}''|^3}$ term leads to

$$\begin{aligned} J_{ge} = & \frac{\boldsymbol{\mu}_{eg}^{A} \cdot \mathbf{R}_{AB}}{4\pi\epsilon R_{AB}^{3}} \underbrace{\int \rho_{eg}^{B}\left(\mathbf{r}''\right) d\mathbf{r}''}_{=0} \\ & + \frac{\boldsymbol{\mu}_{eg}^{A}}{4\pi\epsilon R_{AB}^{3}} \cdot \underbrace{\int \mathbf{r}'' \rho_{eg}^{B}\left(\mathbf{r}''\right) d\mathbf{r}''}_{\boldsymbol{\mu}_{eg}^{B}} - 3 \times \frac{\boldsymbol{\mu}_{eg}^{A} \cdot \mathbf{R}_{AB}}{4\pi\epsilon R_{AB}^{5}} \mathbf{R}_{AB} \cdot \underbrace{\int \mathbf{r}'' \rho_{eg}^{B}\left(\mathbf{r}''\right) d\mathbf{r}''}_{\boldsymbol{\mu}_{eg}^{B}} \\ & - 3 \times \frac{\boldsymbol{\mu}_{eg}^{A}}{4\pi\epsilon R_{AB}^{5}} \cdot \underbrace{\int \mathbf{r}'' \left(\mathbf{R}_{AB} \cdot \mathbf{r}''\right) \rho_{eg}^{B}\left(\mathbf{r}''\right) d\mathbf{r}''}_{\approx 0} \end{aligned} \tag{1.56}$$

Since the first term cancels and the last term will be negligible, we can write the Coulomb coupling in the point dipole approximation as

$$J_{ge} = \frac{1}{4\pi\epsilon} \left(\frac{\boldsymbol{\mu}_{eg}^{A} \cdot \boldsymbol{\mu}_{eg}^{B}}{R_{AB}^{3}} - 3 \frac{\left(\boldsymbol{\mu}_{eg}^{A} \cdot \mathbf{R}_{AB}\right)\left(\mathbf{R}_{AB} \cdot \boldsymbol{\mu}_{eg}^{B}\right)}{R_{AB}^{5}} \right) \tag{1.57}$$

which can be further simplified by using the geometric relations that are shown in Figure 1.1.
So that the Coulomb coupling can be written as[70]

$$V^{\text{Coulomb}} = \frac{\left|\boldsymbol{\mu}_{eg}^{A}\right| \left|\boldsymbol{\mu}_{eg}^{B}\right|}{4\pi\epsilon \boldsymbol{R}_{AB}^{3}} \underbrace{\left(\cos\left(\Phi - 3\right) \cos\Theta_A \cos\Theta_B\right)}_{\kappa} \tag{1.58}$$

with $\cos\Phi = \frac{\boldsymbol{\mu}_{eg}^{A} \cdot \boldsymbol{\mu}_{eg}^{B}}{\left|\boldsymbol{\mu}_{eg}^{A}\right| \cdot \left|\boldsymbol{\mu}_{eg}^{B}\right|}$, $\cos\Theta_A = \frac{\boldsymbol{\mu}_{eg}^{A} \cdot R_{AB}}{\left|\boldsymbol{\mu}_{eg}^{A}\right| \cdot |R_{AB}|}$ and $\cos\Theta_B = \frac{\boldsymbol{\mu}_{eg}^{B} \cdot R_{AB}}{\left|\boldsymbol{\mu}_{eg}^{B}\right| \cdot |R_{AB}|}$.

Comparison of methods

Now that we have presented the different methods for calculating the excitonic coupling let us compare them in their accuracy. A boron-dipyrromethene (BODIPY)

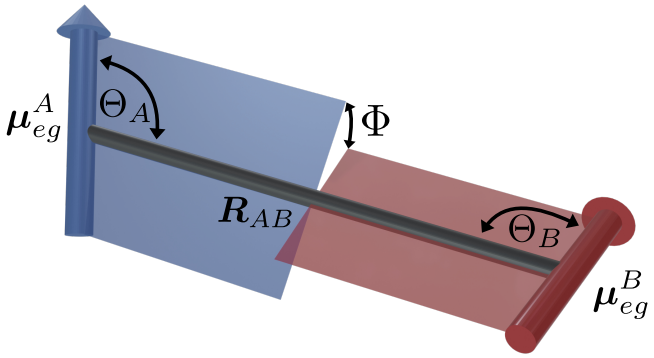

Figure 1.1: Transition dipole moment vectors of monomer A (blue arrow) and monomer B (red arrow) together with their distance vector (black cylinder). The angles Θ_A, Θ_B and Φ are highlighted.

unit was used as a test system since BODIPY was intensively investigated in this thesis. In addition, this is an excellent model system since it has a very bright first excited state, which is separated from the higher excited states. Thus, the above approximations in the framework of exciton theory should apply to this system.

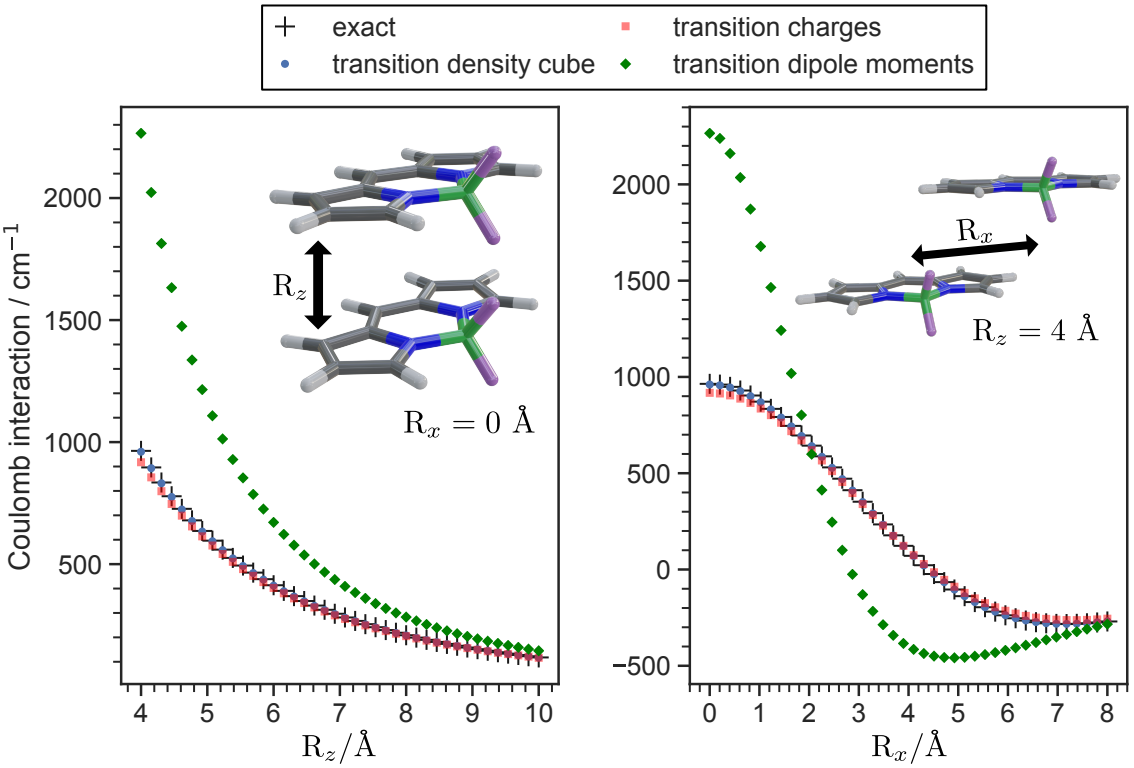

Figure 1.2: Comparison of excitonic couplings using four different methods for a distance and longitudinal scan of a BODIPY dimer. The exact method refers to the analytical calculation of the 2-electron Coulomb integrals, while the other three methods are presented in detail in the text. The grid spacing for the TDC method is 0.15 Angstrom. The transition charges were rescaled to match the transition dipole moment in magnitude.

For this comparison, the monomer's electronic ground and first excited state were calculated using (TD)-DFT (wB97XD[71]/def2SVP[72]). Then, the couplings were calculated using the presented methods for a scan along the z-axis, which is perpendicular to the BODIPY plane, and the longitudinal axis (x). In addition, the 2-electron Coulomb integrals were calculated analytically, and these data will be referred to as *exact* in the following. As can be seen in Figure 1.2, the results of the TDC, as well as the transition charge method, agree very well quantitatively with the exact coupling energies. When using the transition dipole moments, one sees a substantial overestimation of the coupling at short distances in the case of the scan along the z-axis. This deviation is in good agreement with Ref. 37 and 68.
Moreover, in the case of the longitudinal scan, the coupling is not only overestimated at small displacements, but even the sign is wrong at displacements of about 3-4 Å. These two examples show that using transition dipole moments for excitonic coupling is only appropriate if the distance between the two chromophores is large, so the approximations are valid.

1.3 Relaxation rates based on Fermi's Golden Rule

For the rational design of new emitters, reliable predictions of transition rates would be of great help. The usefulness of luminescent molecules depends directly on the photoluminescence quantum yield, which is defined by the competition of the radiative relaxation (fluorescence or phosphorescence) to all other non-radiative relaxation channels. In the following sections, the radiative rate expression and the energy gap law[57] are derived.

1.3.1 Fluorescence Rates

In the Born-Oppenheimer approximation, the wave function of the initial and final states can be separated into an electronic and vibrational part

$$|i\rangle = |\Psi_i\rangle|\Theta_i\rangle \quad |f\rangle = |\Psi_f\rangle|\Theta_f\rangle, \tag{1.59}$$

with Ψ being the electronic wave function and Θ the vibrational one.
The potential energy surfaces of the S_0 and S_1 states are approximated to be harmonic and have the same frequencies ω_i and normal modes. The only difference is a horizontal shift of the equilibrium geometry ΔQ_i for each mode $i = 1, \ldots, N$ in normal mode coordinates and a vertical shift to higher energy by the adiabatic excitation energy ΔE.
We assume that the initial state for all transitions is always the lowest vibrational level in S_1 and that contributions from higher vibrational levels and higher excited states can be neglected (This is equivalent to setting the temperature to $T = 0$ K). In the initial vibrational wave function, therefore all oscillators are in the ground state:

$$|\Theta_i\rangle = |\mathbf{0'}\rangle = |0'_1\rangle \otimes |0'_2\rangle \otimes \cdots \otimes |0'_N\rangle \tag{1.60}$$

The apostrophe indicates that the harmonic oscillator wavefunctions on S_1 are shifted relative to those on S_0, i.e. $\phi'(Q_i) = \phi(Q_i - \Delta Q_i)$. The final vibrational state on S_0 is

$$|\Theta_f\rangle = |\boldsymbol{m}\rangle = |m_1\rangle \otimes |m_2\rangle \otimes \cdots |m_N\rangle. \tag{1.61}$$

The vector $\boldsymbol{m}$ gives the number of phonons in each mode. Only those final states are allowed where the vibrational energy $E_{\boldsymbol{m}} = \sum_{i=1}^{N} m_i\omega_i$ is smaller than the adiabatic excitation energy ΔE, since otherwise no photon can be emitted.
The overlap squared between the vibrational ground state on S_1 and the final vibrational state with $\boldsymbol{m}$ phonons on S_0 is given by the product of the Franck-Condon

factors for each mode,

$$|\langle 0_i'|m_i\rangle|^2 = \left|\int_{-\infty}^{+\infty} \phi_0(Q_i - \Delta Q_i)\phi_m(Q_i)dQ_i\right|^2 \tag{1.62}$$

$$= \frac{S_i^{m_i} e^{-S_i}}{m_i!}, \tag{1.63}$$

where we have defined the Huang-Rhys factor for mode i in terms of the displacement ΔQ_i as

$$S_i = \frac{1}{2}\Delta Q_i^2 \omega_i. \tag{1.64}$$

The product of Franck-Condon factors gives the overlap between the initial and final vibrational wavefunctions:

$$F_{\boldsymbol{m}} = |\langle \mathbf{0}'|\boldsymbol{m}\rangle|^2 = \prod_{i=1}^{N} \frac{S_i^{m_i} e^{-S_i}}{m_i!} \tag{1.65}$$

The radiative rate increases as the third power of the emission energy and second power of the transition dipole moment $\boldsymbol{\mu}_{eg}$:

$$k_{\mathrm{rad}} = u_{\mathrm{rad}}|\boldsymbol{\mu}_{eg}|^2 \sum_{\boldsymbol{m}} \left(\Delta E - E_{\boldsymbol{m}}\right)^3 F_{\boldsymbol{m}} \Theta\left(\Delta E - E_{\boldsymbol{m}}\right) \tag{1.66}$$

The Heaviside function $\Theta(\cdot)$ ensures that the energy difference between the initial and final states is positive so that a photon can be emitted. The factor $u_{\mathrm{rad}} = 2.142 \times 10^{10}\mathrm{s}^{-1}$ converts the rates from atomic units to s^{-1} [1]. Summing over all vibrational states $\boldsymbol{m}$ is a complex combinatorial problem since the number of states grows exponentially with the number of atoms. We follow the procedure proposed in Ref. 74 and group the vibrational states into classes depending on the number of simultaneously excited modes. Limiting the sum to the first few classes $C_1, C_2, \ldots, C_{n_{\max}}$ the computational effort can be kept low while including those states that contribute most to the radiative rate. The convergence is monitored via the sum of Franck-Condon factors, $\sum_{\boldsymbol{m}} F_{\boldsymbol{m}}$, which should equal one if the sum is complete.
If the vibrational structure does not change at all between the S_0 and S_1 minima, only the 0-0 vibrational transition has non-vanishing Franck-Condon factors, $F_{\boldsymbol{m}} = \delta_{\boldsymbol{m},\mathbf{0}}$, and Eq. 7.5 simplifies to Einstein's expression for the spontaneous emission rate, $k_{\mathrm{rad}}^{\mathrm{Einstein}} = u_{\mathrm{rad}}|\boldsymbol{\mu}_{eg}|^2 \Delta E^3$.

[1] The physical constants that make up the prefactor can be found in Eq. 4.18 of Ref. 73

1.3.2 Internal Conversion Rates - Time-Independent

Non-adiabatic transitions are mediated by the operator $\mathscr{T}$ for the nuclear kinetic energy

$$\begin{aligned} V_{if} &= \langle\Psi_i|\langle\Theta_i|\mathscr{T}|\Psi_f\rangle|\Theta_f\rangle \\ &\approx -\sum_{j=1}^{N}\langle\Psi_i|\frac{\partial\Psi_f}{\partial Q_j}\rangle\langle\Theta_i|\frac{\partial\Theta_f}{\partial Q_j}\rangle \end{aligned} \tag{1.67}$$

where terms like $\langle\Psi_i|\frac{\partial^2}{\partial Q_j^2}\Psi_f\rangle$ have been neglected. The electronic derivative coupling vector is computed in Cartesian coordinates x, so we need to transform it to normal mode coordinates, $\langle\Psi_i|\frac{\partial\Psi_f}{\partial Q_j}\rangle = \sum_k\langle\Psi_i|\frac{\partial\Psi_f}{\partial x_k}\rangle\frac{\partial x_k}{\partial Q_j}$.
For non-radiative transitions, we also need the nuclear part of the non-adiabatic coupling vector, i.e.

$$\langle\Theta_i|\frac{\partial\Theta_f}{\partial Q_j}\rangle = \prod_{\substack{k=1,\\k\neq j}}^{N}\langle 0'_k|m_k\rangle\langle 0'_j|\frac{\partial}{\partial Q_j}|m_j\rangle, \tag{1.68}$$

which is derived in Appendix A. After defining the scalar product between the electronic and the nuclear non-adiabatic coupling vectors as

$$\begin{aligned} N_{\boldsymbol{m}} &= \sum_{j=1}^{N}\langle\Psi_i|\frac{\partial\Psi_f}{\partial Q_j}\rangle\cdot\frac{\langle 0'_j|\frac{\partial}{\partial Q_j}|m_j\rangle}{\langle 0'_j|m_j\rangle} \\ &= \sum_{j=1}^{N}\langle\Psi_i|\frac{\partial\Psi_f}{\partial Q_j}\rangle\sqrt{\omega_j}\left(\frac{m_j}{\sqrt{2S_j}}-\sqrt{\frac{S_j}{2}}\right) \end{aligned} \tag{1.69}$$

the harmonic part of the internal conversion rate can be expressed as

$$k_{\mathrm{ic}}^{\mathrm{harm}} = u_{\mathrm{ic}}\sum_{\boldsymbol{m}}F_{\boldsymbol{m}}N_{\boldsymbol{m}}^2\delta\left(\Delta E - E_{\boldsymbol{m}}\right). \tag{1.70}$$

The factor $u_{\mathrm{ic}} = 2.598\times10^{17}\mathrm{s}^{-1}$ converts the rate to s^{-1} when all other quantities are given in atomic units.
The δ-function enforces energy conservation. Only transitions to states with the same energy are allowed. These are highly excited vibrational states with vibrational energies close to the adiabatic excitation energy, $E_{\boldsymbol{m}} \approx \Delta E$. Because of the discrete nature of the vibrational states, exact alignment of initial and final vibrational states would be required to satisfy energy conservation. However, interaction with the environment leads to energetic broadening so that transitions are allowed within a narrow window of energy. To account for this, we replace the delta function with a

Gaussian of finite width Γ:

$$\delta(\Delta E - E_{\boldsymbol{m}}) \approx \frac{1}{\sqrt{2\pi\Gamma^2}} \exp\left(-\frac{1}{2}\left(\frac{\Delta E - E_{\boldsymbol{m}}}{\Gamma}\right)^2\right) \tag{1.71}$$

The width of the energy window is taken as the average spacing between vibrational levels, $\Gamma = \frac{1}{N}\sum_i \omega_i$.
Reaching convergence is much more difficult for the internal conversion rate than the radiative rate since the states that contribute most lie at high energies where the density of states is enormous. There is no criterion such as the sum of Franck-Condon (FC) factors for radiative rates for assessing the convergence of IC rates. To extend the summation to high classes C_n, we must cull the number of states within each class. To this end, we select those normal modes with either larger non-adiabatic couplings (the so-called promoting modes) or significant Franck-Condon factors. The normal modes are sorted this way, and the number of modes is reduced until the number of integrals that must be considered falls below a manageable threshold. Since all rates are positive numbers, the rates obtained for a reduced subset of vibrational states are only a lower bound. In this way, one can increase the maximum number of classes C_n, and the number of integrals per class until the IC rate stops changing significantly.

1.3.3 Internal Conversion Rates - Time-Dependent

The sum-over-states or time-independent approach of the previous section converges only very slowly. Therefore time-dependent approaches have been developed[75–77], where the infinite sums can be performed analytically at the expense of having to propagate in time. A discrete Fourier transformation then obtains the rate for internal conversion. For the adiabatic shift model - initial and final states only differ in the equilibrium geometry - the time-dependent formalism takes a simple form, which is presented here for completeness.
The δ-function for enforcing energy conversion in Eq. 1.70 can be expressed by its Fourier transform

$$\delta(\Delta E - E_{\boldsymbol{m}}) = \frac{1}{2\pi}\int_{-\infty}^{+\infty} dt \exp(\imath(\Delta E - E_{\boldsymbol{m}})t), \tag{1.72}$$

so that the non-radiative rate becomes

$$k_{\mathrm{ic}}^{\mathrm{harm}} = \frac{1}{2\pi}\int_{-\infty}^{\infty} e^{\imath\Delta E t}\left\{u_{\mathrm{ic}}\sum_{\boldsymbol{m}} F_{\boldsymbol{m}} N_{\boldsymbol{m}}^2 e^{-\imath E_{\boldsymbol{m}} t}\right\} dt \tag{1.73}$$

Now we introduce the abbreviations

$$A_j = \langle \Psi_i | \frac{\partial \Psi_f}{\partial Q_j} \rangle \sqrt{\frac{\omega_j}{2S_j}} \tag{1.74}$$

$$B_j = -\langle \Psi_i | \frac{\partial \Psi_f}{\partial Q_j} \rangle \sqrt{\frac{\omega_j S_j}{2}} \tag{1.75}$$

so that Eq. 1.69 can be written as

$$N_{\boldsymbol{m}} = \sum_j (A_j m_j + B_j) \tag{1.76}$$

The Fourier transform of the non-radiative rate becomes then

$$\begin{aligned} \tilde{k}_{\mathrm{ic}}(t) &= u_{\mathrm{ic}} \sum_{\boldsymbol{m}} F_{\boldsymbol{m}} N_{\boldsymbol{m}}^2 e^{-\imath E_{\boldsymbol{m}} t} \\ &= u_{\mathrm{ic}} \sum_{\boldsymbol{m}} \prod_{k=1}^{N} \frac{1}{m_k!} S_k^{m_k} e^{-S_k - \imath \omega_k t m_k} \sum_{i=1}^{N} (A_i m_i + B_i) \sum_{j=1}^{N} (A_j m_j + B_j) \end{aligned} \tag{1.77}$$

We introduce the abbreviation

$$G_m^{(i)} = e^{-S_i} \frac{1}{m!} \left(S_i e^{-\imath \omega_i t} \right)^m, \tag{1.78}$$

write out the sum over vibrational quantum numbers

$$\sum_{\boldsymbol{m}} = \sum_{m_1=0}^{\infty} \sum_{m_2=0}^{\infty} \cdots \sum_{m_i=0}^{\infty} \cdots \sum_{m_N=0}^{\infty} \tag{1.79}$$

and group the factors $G_{m_i}^{(i)}$ with their respective sums. This gives

$$
\begin{aligned}
\tilde{k}_{\mathrm{nr}}(t) = u_{\mathrm{ic}} & \sum_{i=1}^{N} \sum_{j\neq i}^{N} \sum_{m_1=0}^{\infty} G_{m_1}^{(1)} \dots \\
& \sum_{m_{i-1}=0}^{\infty} G_{m_{i-1}}^{(i-1)} \sum_{m_i=0}^{\infty} G_{m_i}^{(i)} (A_i m_i + B_i) \sum_{m_{i+1}=0}^{\infty} G_{m_{i+1}}^{(i+1)} \dots \\
& \sum_{m_{j-1}=0}^{\infty} G_{m_{j-1}}^{(j-1)} \sum_{m_j=0}^{\infty} G_{m_j}^{(j)} (A_j m_j + B_j) \sum_{m_{j+1}=0}^{\infty} G_{m_{j+1}}^{(j+1)} \dots \\
& \sum_{m_N=0}^{\infty} G_{m_N}^{(N)} \\
+ u_{ic} & \sum_{i=1}^{N} \sum_{m_1=0}^{\infty} G_{m_1}^{(1)} \dots \\
& \sum_{m_{i-1}=0}^{\infty} G_{m_{i-1}}^{(i-1)} \sum_{m_i=0}^{\infty} G_{m_i}^{(i)} (A_i m_i + B_i)^2 \sum_{m_{i+1}=0}^{\infty} G_{m_{i+1}}^{(i+1)} \dots \\
& \sum_{m_N=0}^{\infty} G_{m_N}^{(N)}.
\end{aligned}
\tag{1.80}
$$

The double sums over i and j were split into sums where $i \neq j$ and $i = j$. We introduce the abbreviation

$$
X_i(t) = S_i e^{-\imath\omega_i t} \tag{1.81}
$$

The sums over m are performed by recognizing the Taylor expansion of the exponential function, $\sum_{m=0} x^m/m! = e^x$, $\sum_{m=0} m/m! x^m = x e^x$ and $\sum_{m=0} m^2/m! x^m = (x^2 + x)e^x$ for $x = S e^{-\imath\omega t}$:

$$
\sum_{m=0}^{\infty} G_m^{(i)} = e^{-S_i} \sum_{m=0}^{\infty} \frac{1}{m!} X_i^m = e^{-S_i + X_i} \tag{1.82}
$$

and similarly

$$
\begin{aligned}
& \sum_{m=0}^{\infty} G_m^{(i)} (A_i m + B_i) \\
& \quad = e^{-S_i} \left\{ A_i \sum_{m=0}^{\infty} \frac{m}{m!} X_i^m + B_i \sum_{m=0}^{\infty} \frac{1}{m!} X_i^m \right\} \\
& \quad = e^{-S_i + X_i} (A_i X_i + B_i)
\end{aligned}
\tag{1.83}
$$

and

$$\begin{aligned}
&\sum_{m=0}^{\infty} G_m^{(i)}(A_i m + B_i)^2 \\
&\quad = e^{-S_i} \sum_{m=0}^{\infty} \frac{X_i^m}{m!} \left\{ A_i^2 m^2 + 2A_i B_i m + B_i^2 \right\} \\
&\quad = e^{-S_i + X_i} \left\{ A_i^2 X_i^2 + (2A_i B_i + A_i^2) X_i + B_i^2 \right\}
\end{aligned} \tag{1.84}$$

Substituting Eqs. 1.82, 1.83 and 1.84 into 1.80 gives finally

$$\begin{aligned}
\tilde{k}_{\mathrm{ic}}(t) = u_{\mathrm{ic}} &\left(\prod_{k=1}^{N} e^{-S_k + X_k(t)} \right) \\
&\times \left\{ \sum_{i=1}^{N} \sum_{j=1}^{N} (A_i X_i(t) + B_i)(A_j X_j(t) + B_j) + \sum_{i=1}^{N} A_i^2 X_i(t) \right\}
\end{aligned} \tag{1.85}$$

Since vibrational energy levels are discrete, energy conservation would require perfect energetic alignment of the initial and final vibrational states. Initial and final states will only accidentally have the same energy when the vibrational frequencies are commensurable. Therefore we need to relax energy conservation a little by replacing the δ-function with the Gaussian broadening function of Eq. 1.71. The physical justification is that the coupling to an environment broadens the vibrational levels and allows transitions between close levels so that their line shape functions overlap. Using the Fourier transform of a Gaussian, the broadened line shape function can be expressed as

$$\delta(\Delta E - E_{\boldsymbol{m}}) \approx \frac{1}{2\pi} \int_{-\infty}^{\infty} dt \exp\left(-\frac{1}{2} \Gamma^2 t^2 \right) \exp(\imath(\Delta E - E_{\boldsymbol{m}})t). \tag{1.86}$$

If we use this definition instead of the δ-function in Eq. 1.73 the non-radiative rate as a function of the excitation energy becomes

$$k_{\mathrm{ic}}^{\mathrm{harm}}(\Delta E) = \frac{1}{2\pi} \int_{-\infty}^{\infty} e^{\imath \Delta E t} \left\{ e^{-\frac{1}{2}\Gamma^2 t^2} \tilde{k}_{ic}(t) \right\} dt. \tag{1.87}$$

$\tilde{k}_{\mathrm{ic}}(t)$ is evaluated on an equidistant grid covering the interval $[-T, T]$ and the non-radiative rate at the given excitation energy ΔE is then obtained by interpolating the discrete Fourier transform in Eq. 1.87. The time-dependent formalism is much more efficient than the time-independent one at the cost that the information about which vibrational levels contribute most to the rate is lost. Except for the discretization error, both formalisms, if converged, give the same results (see Fig. 1.3).

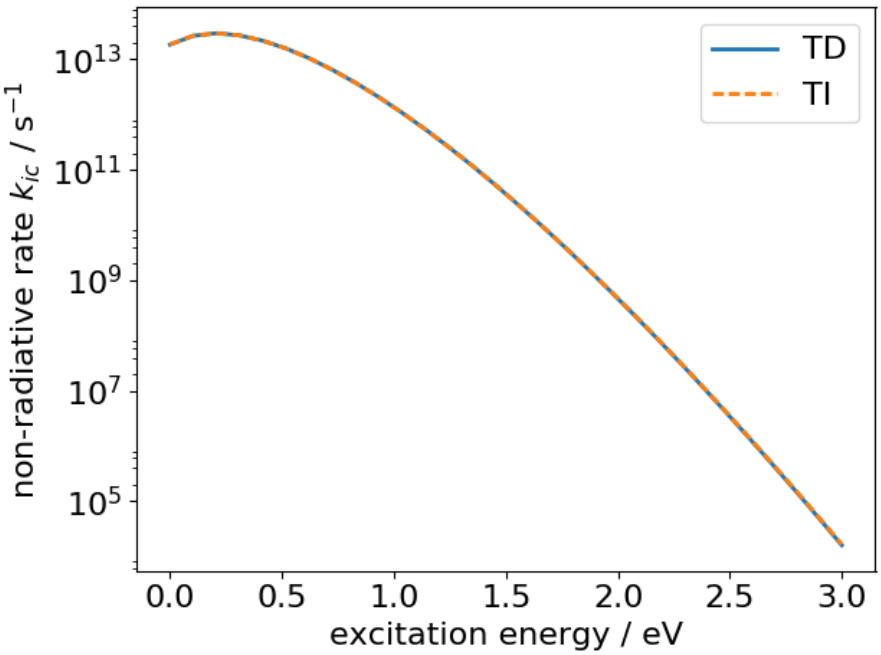

Figure 1.3: Comparison of non-radiative rates k_{ic} as functions of excitation energy computed with the time-dependent (TD) and time-independent (TI) formalism for a fictitious system with three vibrational modes. The frequencies, Huang-Rhys factors and non-adiabatic couplings of the model were set to $\omega_1 = 1000$ cm^{-1}, $\omega_2 = 1111$ cm^{-1}, $\omega_2 = 2100$ cm^{-1}; $S_1 = 0.1$, $S_2 = 0.01$, $S_3 = 0.5$; $\langle\Psi_i|\partial\Psi_f/\partial Q_1\rangle = -0.01$, $\langle\Psi_i|\partial\Psi_f/\partial Q_2\rangle = 0.03$, $\langle\Psi_i|\partial\Psi_f/\partial Q_3\rangle = 0.005$. The parameters for the discrete Fourier transform were, $N_t = 2^{16}$ sample points and a maximum propagation time of $T = 4000$ fs. At an excitation energy of 1 eV the rate amounts to $k_{\text{ic}}^{\text{harm}} = 1.36 \times 10^{12}$ s^{-1}. The small discrepancy between TD and TI formalism at high energies is due to the finite energy resolution of the discrete Fourier transform.

1.3.4 Energy gap law

To derive an energy gap law from Eq. 1.73 some simplifying assumptions need to be made: (1) The frequencies and Huang-Rhys factors of all modes are replaced by their average values, $\omega_{\text{eff}} = \sum_{i=1}^{N} \omega_i \frac{C_i}{\sum_{j=1}^{N} C_j}$ is the effective vibrational mode and $S = N^{-1} \sum_{i=1}^{N} S_i$. (2) The $P < N$ modes with non-vanishing non-adiabatic couplings are called promoting modes. The coupling per mode is replaced by the average value, so that the total length of the non-adiabatic coupling vector remains unchanged: $\left|\langle\Psi_i|\frac{\partial\Psi_f}{\partial Q}\rangle\right|^2_{\text{avg}} = P^{-1} \sum_{i=1}^{P} \left|\langle\Psi_i|\frac{\partial\Psi_f}{\partial Q_i}\rangle\right|^2$. Substituting Eq. 1.85 into Eq. 1.73 and using

the averaged quantities, the non-radiative rate becomes

$$\begin{aligned} k_{\mathrm{ic}}^{\mathrm{harm}} = \frac{u_{ic}}{4\pi} \left| \langle \Psi_i | \frac{\partial \Psi_f}{\partial \boldsymbol{Q}} \rangle \right|^2 \omega_{\mathrm{eff}} \\ \times \Big\{ PS \int_{-\infty}^{\infty} \exp\left(\imath \Delta E t + NS(e^{-\imath \omega_{\mathrm{eff}} t} - 1) \right) dt \\ - (2PS - 1) \int_{-\infty}^{\infty} \exp\left(\imath [\Delta E - \omega_{\mathrm{eff}}] t + NS(e^{-\imath \omega_{\mathrm{eff}} t} - 1) \right) dt \\ + PS \int_{-\infty}^{\infty} \exp\left(\imath [\Delta E - 2\omega_{\mathrm{eff}}] t + NS(e^{-\imath \omega_{\mathrm{eff}} t} - 1) \right) dt \Big\} \end{aligned} \tag{1.88}$$

The three integrals all have the form

$$\int_{-\infty}^{\infty} \exp(f(t)) dt \tag{1.89}$$

with

$$f(t) = \imath \varepsilon t + NS(e^{-\imath \omega_{\mathrm{eff}} t} - 1) \tag{1.90}$$

for $\varepsilon = \Delta E, \Delta E - \omega_{\mathrm{eff}}, \Delta E - 2\omega_{\mathrm{eff}}$. Integrals of this type can be approximated by saddle point integration (see chapter 10.5 in Ref. 78). The largest contribution to the integral comes from the region around the stationary points of $f(t)$ (where $f'(t_0) = 0$). After expanding the exponent to quadratic order around the stationary point, the resulting Gaussian integral can be solved:

$$\begin{aligned} \int_{-\infty}^{\infty} e^{f(t)} dt &\approx \int_{-\infty}^{\infty} \exp\left(f(t_0) + \underbrace{f'(t_0)}_{=0} (t - t_0) + \frac{1}{2} f''(t_0)(t - t_0)^2 \right) dt \\ &\overset{x = t - t_0}{=} e^{f(t_0)} \int_{-\infty}^{\infty} \exp\left(-\frac{1}{2} [-f''(t_0)] x^2 \right) dx \\ &= e^{f(t_0)} \sqrt{\frac{2\pi}{(-f''(t_0))}} \end{aligned} \tag{1.91}$$

The derivatives of $f(t)$ are

$$f'(t) = i\varepsilon - \imath \omega_{\mathrm{eff}} NS e^{-\imath \omega_{\mathrm{eff}} t} \tag{1.92}$$

$$f''(t) = -\omega_{\mathrm{eff}}^2 NS e^{-\imath \omega_{\mathrm{eff}} t} \tag{1.93}$$

$f'(t)$ has a single root at

$$\imath t_0 = \frac{1}{\omega_{\mathrm{eff}}} \log\left(\frac{\omega_{\mathrm{eff}} NS}{\varepsilon} \right) \tag{1.94}$$

which corresponds to a maximum since

$$f''(t_0) = -\omega_{\text{eff}}\varepsilon \quad < 0. \tag{1.95}$$

The value of the exponent at the maximum $t = t_0$ is

$$f(t_0) = -\frac{\varepsilon}{\omega_{\text{eff}}}\left(\log\left(\frac{\varepsilon}{\omega_{\text{eff}}NS}\right) - 1\right) - NS. \tag{1.96}$$

Putting everything together, the saddle point approximation for our integral reads:

$$\int_{-\infty}^{\infty} e^{f(t)}dt \approx \exp\left(-\frac{\varepsilon}{\omega_{\text{eff}}}\left(\log\left(\frac{\varepsilon}{\omega_{\text{eff}}NS}\right) - 1\right) - NS\right)\sqrt{\frac{2\pi}{\omega_{\text{eff}}\varepsilon}} \tag{1.97}$$

Using this approximation to evaluate the three integrals in Eq. 1.88 we obtain the non-radiative rate in the saddle point approximation:

$$\begin{aligned} k_{\text{ic}}^{\text{harm}} = \frac{u_{ic}}{2\sqrt{2\pi}}\left|\langle\Psi_i|\frac{\partial\Psi_f}{\partial \boldsymbol{Q}}\rangle\right|^2 e^{-NS} \\ \times PS\left\{I\left(\frac{\Delta E}{\omega_{\text{eff}}}\right) - (2 - \frac{1}{PS})I\left(\frac{\Delta E}{\omega_{\text{eff}}} - 1\right) + I\left(\frac{\Delta E}{\omega_{\text{eff}}} - 2\right)\right\} \end{aligned} \tag{1.98}$$

where the function $I(x)$ of dimensionless argument x is defined as:

$$I(x) = \sqrt{\frac{1}{x}}\exp\left(-x\left[\log\left(\frac{x}{NS}\right) - 1\right]\right) \tag{1.99}$$

According to Eq. 1.98, the non-radiative rate is proportional to the electronic non-adiabatic coupling matrix element. It decreases exponentially with the displacement between ground and excited state minima (because of the exponential factor e^{-NS} the relation $S = \frac{1}{2}\Delta Q^2\omega_{\text{eff}}$). Moreover, it has a seemingly complex dependence on ΔE because of the interference between the three I-functions at slightly shifted arguments. For adiabatic excitation energies that are large relative to the average vibrational frequency, $\Delta E \gg \omega_{\text{eff}}$, one recognizes in Eq. 1.98 a term that is similar to a finite difference approximation for the second derivative of I,

$$I(x) - 2I(x-1) + I(x-2) \approx I''(x-1) \qquad \text{for } \; x \gg 1, \tag{1.100}$$

so that Eq. 1.98 simplifies to

$$\begin{aligned} k_{\text{ic}}^{\text{harm}} \approx \frac{u_{ic}}{2\sqrt{2\pi}}\left|\langle\Psi_i|\frac{\partial\Psi_f}{\partial \boldsymbol{Q}}\rangle\right|^2 \\ \times e^{-NS} \times \left\{I\left(\frac{\Delta E}{\omega_{\text{eff}}} - 1\right) + PS\; I''\left(\frac{\Delta E}{\omega_{\text{eff}}} - 1\right)\right\} \end{aligned} \tag{1.101}$$

This is the energy gap law (cf. Ref. 79) at $T = 0$ K. For large adiabatic excitation energies the non-radiative rate decreases faster than exponentially, because of the behaviour of $I(x)$ for $x \to \infty$.
Fig. 1.4 shows the energy dependence of the non-radiative rate according to the energy gap for the merocyanine dye.
Eqn. 7.6 is similar to the energy gap law derived by Englman and Jortner (eqn. 5.4 in Ref. 57) in the weak coupling limit for $T = 0$ K, which in our notation would read

$$k_{\mathrm{ic}}^{\mathrm{harm}} \approx \frac{u_{\mathrm{ic}}}{2\sqrt{2\pi}} \left| \langle \Psi_i | \frac{\partial \Psi_f}{\partial \boldsymbol{Q}} \rangle \right|^2 e^{-NS} I\left(\frac{\Delta E}{\omega_{\mathrm{eff}}}\right) \tag{1.102}$$

Our result differs from theirs primarily by the second derivative of $I(x)$. This additional term arises because we consider the scalar product between the electronic and nuclear non-adiabatic coupling vectors in Eq. 1.69, while Englman and Jortner make the approximation $N_{\boldsymbol{m}}^2 \propto C^2$, lumping the contributions of different vibrational states to the non-adiabatic coupling into a single constant C. This simplifies their problem so that they can use tricks originally developed to calculate the shape of absorption curves[80,81] to derive the non-radiative rate at non-zero temperature (Eq. (5.12) in Ref. 57). The more complicated nature of Eq. 1.69 precludes us from using the same techniques. However, a back-of-the-envelope calculation shows that temperature effects on the non-radiative rate in the harmonic approximation are likely negligible compared to the errors introduced by the harmonic approximation itself. At room temperature the thermal energy amounts to $\beta^{-1} = k_B \times 300\ K = 209\ \mathrm{cm}^{-1}$ compared to the energy of a C=C stretch vibration (a typical promoting mode) in the range $\hbar\omega_{\mathrm{eff}} = 1400 - 1600\ \mathrm{cm}^{-1}$, which gives $\beta\hbar\omega_{\mathrm{eff}} \approx 7$. The probability that the promoting mode in the initial state is excited at room temperature is negligible:

$$\begin{aligned} p(n \geq 1) = \sum_{n=1}^{\infty} p(n) &= \frac{\sum_{n=1}^{\infty} e^{-\beta\hbar\omega_{\mathrm{eff}}(n+\frac{1}{2})}}{\sum_{n=0}^{\infty} e^{-\beta\hbar\omega_{\mathrm{eff}}(n+\frac{1}{2})}} = e^{-\beta\hbar\omega_{\mathrm{eff}}} \\ &\approx 0.0009, \end{aligned} \tag{1.103}$$

Vibrational modes with lower frequencies can be excited thermally, but their contribution to the non-adiabatic coupling vector is smaller than that of the promoting modes.

1.3.5 Nonadiabatic Couplings

Here we derive the expression for the non-adiabatic coupling between displaced harmonic oscillator eigenfunctions in terms of the Huang-Rhys factors. The indices labeling the vibrational modes are suppressed for clarity. The action of the momentum

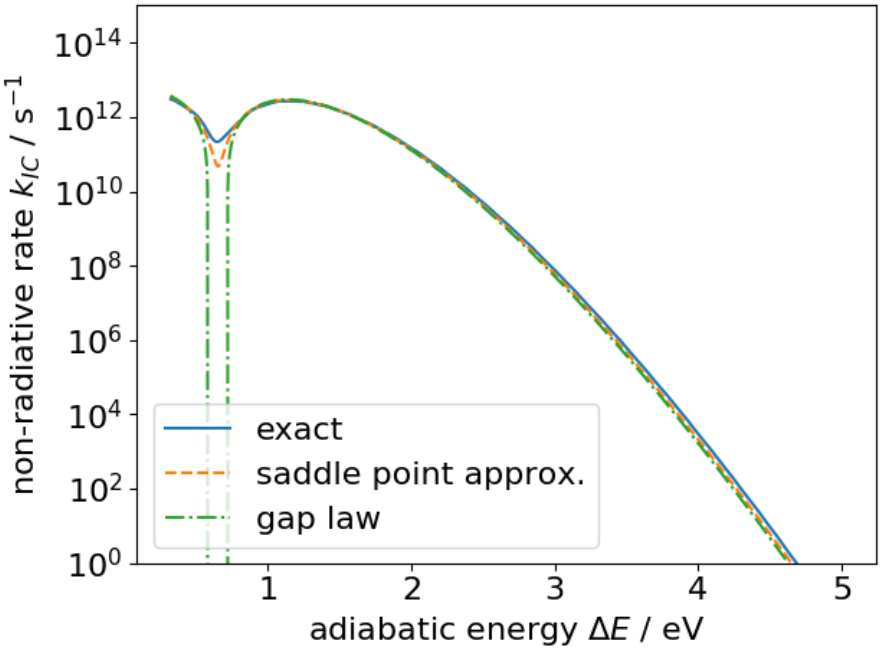

Figure 1.4: Energy gap law for non-radiative rates. Average frequencies and Huang-Rhys factors from the merocyanine dye were used. Non-radiative rates are shown for different approximations: numerically exact integrals by Fourier transformation according to Eq. 1.88 (solid blue), convolved with a Gaussian of exponent $\Gamma = \frac{1}{2}\omega_{\text{eff}}$), saddle point approximation according to Eq. 1.98 (dashed orange) and the energy gap law according to Eq. 7.6 (dotted green). Interestingly there is a dip at ≈ 0.8 eV where k_{ic} has a local minimum.

operator $\mathscr{P}$ on an eigenstate of the harmonic oscillator is given by[82]

$$-\imath\frac{d\phi_m(Q)}{dQ} = \mathscr{P}\phi_m \tag{1.104}$$

$$= \imath\sqrt{\frac{\omega_{\text{eff}}}{2}}\left(\sqrt{m+1}\phi_{m+1}(Q) - \sqrt{m}\phi_{m-1}(Q)\right) \tag{1.105}$$

Therefore the derivative coupling can be expressed in terms of overlap integrals to states with $m-1$ and $m+1$ phonons:

$$\begin{aligned}\langle 0'|\frac{\partial}{\partial Q}|m\rangle &= \int_{-\infty}^{\infty}\phi_0(Q-\Delta Q)\frac{d\phi_m}{dQ}(Q)dQ \\ = -\sqrt{\omega_{\text{eff}}}&\left(\sqrt{\frac{m+1}{2}}\int_{-\infty}^{\infty}\phi_0(Q-\Delta Q)\phi_{m+1}(Q)dQ\right. \\ &\left.-\sqrt{\frac{m}{2}}\int_{-\infty}^{\infty}\phi_0(Q-\Delta Q)\phi_{m-1}(Q)dQ\right)\end{aligned} \tag{1.106}$$

Using the definition of the Franck-Condon factors in Eq. 1.63 we obtain the coupling

expressed via the Huang-Rhys factors:

$$\begin{aligned}\langle 0'|\frac{\partial}{\partial Q}|m\rangle &= \sqrt{\omega_{\text{eff}}}\left(\sqrt{\frac{m}{2}}\sqrt{\frac{S^{m-1}e^{-S}}{(m-1)!}} - \sqrt{\frac{m+1}{2}}\sqrt{\frac{S^{m+1}e^{-S}}{(m+1)!}}\right) \\ &= \langle 0'|m\rangle\sqrt{\omega_{\text{eff}}}\left(\frac{m}{\sqrt{2S}} - \sqrt{\frac{S}{2}}\right)\end{aligned} \tag{1.107}$$

Chapter 2

Ultrafast Resonance Energy Transfer in Ethylene-Bridged BODIPY Heterooligomers: From Frenkel to Förster Coupling Limit

---

A series of distinct BODIPY heterooligomers (dyads, triads, and tetrads) comprising a variable number of typical green BODIPY monomers and a terminal red-emitting styryl-equipped species acting as an energy sink was prepared and subjected to computational and photophysical investigations in solvent media. An ethylene tether between the single monomeric units provides a unique foldameric system, setting the stage for a systematic study of excitation energy transfer processes (EET) on the basis of nonconjugated oscillators. The influence of stabilizing β-ethyl modulated substituents on conformational space and the disorder of site S_2 exciton state energies and electronic couplings was addressed. In this way, both the strong (Frenkel) and the weak (Förster) coupling limit could be accessed within a single system: the Frenkel limit within the strongly coupled homooligomeric green donor subunit and the Förster limit at the terminal heterosubstituted ethylene bridge. Femtosecond transient-absorption spectroscopy combined with mixed quantum-classical dynamic simulations demonstrate the limitations of the Förster resonance energy transfer (FRET) theory and provide a consistent framework to elucidate the trend of increasing relaxation lifetimes at higher homologous, revealing one of the fastest excitation energy transfer processes detected to date with a corresponding lifetime of 39 fs.

2.1 Introduction

Energy transfer is of fundamental importance in various biological systems that interact with (sun)light to achieve signal processing or conversion of light energy into charge gradients and chemical energy.[36,83,84] The channeling of excitation energy toward a reaction center as exploited by the photosynthetic apparatus takes advantage of intermolecular aggregation (J-aggregation) of chromophores in which delocalized excitons may form and diffuse over larger distances.[20,85,86] The interactions within these aggregates are often approximated by Coulomb coupling of localized transition dipole oscillators. The discovery of intermolecularly J-aggregating cyanine dyes[66,67,87] provided a useful experimental data basis for the description of these phenomena by quantum-mechanical approaches, the most prominent being Kasha's exciton coupling theory.[26,88] However, tailor-made molecular frameworks derived from discrete oligomers[89] are generally better suited for defined optoelectronic purposes as applied in OLEDs and organic photovoltaics.[90] Even though the degrees of freedom are reduced in such oligomers and the mutual alignment of transition dipole oscillators is to some extent (computationally) predictable,[91] a sensitivity toward environmental influences (solvent, temperature, additives, etc.) as well as to subtle structural manipulations remains[92–94] and can even be beneficially exploited. Scholes et al. have investigated quantum coherence dynamics in the intermediate coupling regime with conjugated poly(phenylenevinylene) polymers as a function of solvent polarity[95] revealing coherent intrachain but not interchain excitation energy transfer (EET). Some of us have demonstrated that the choice of solvent is able to force squaraine polymers to switch between coiled and zigzag superstructures, triggering ultrafast intrachain energy transfer events between these coexistent morphologies on a time scale of $\approx$ 70 fs.[96] Several dye scaffolds were involved in similar studies on EET rates[97] with either flexible tethers between the donor-acceptor pair,[98–100] a more rigid connectivity (alkynyl,[11,101,102] sp^2–sp^2,[103–105] stiff aliphatic linker,[106] metal center[107]), or even orthogonally aligned units.[108–110] In many cases, especially in the short-range regime, experimental data did not meet theoretical predictions, which led to further improvements of the theory, such as refined calculations of electronic couplings,[37,38] the introduction of electron-nuclear coupling effects (e.g., shared vibrational modes[111]), the involvement of through-bond/exchange interactions,[112] and the consideration of quantum coherence.[113–116] Another important question however is whether the rate of intramolecular EET processes is dependent on the aggregation modes, coupling strengths, and the extent of energetic disorder within the interacting donor and acceptor units, respectively. BODIPY motifs, which are predominantly known for serving as powerful fluorescent tags and sensing platforms in life sciences,[117–121] also entered the field of supramolecular chemistry and profit from a toolbox of versatile postfunctionalizations.[122–125] While a range of different conjugation modes was introduced, most of them suffer from either a conformational space that is too restricted (methylene tether)[126,127] or detrimental π-overlap (direct sp^2–sp^2,[128,129] alkynyl[130,131]) to enable defined alignments. However, such

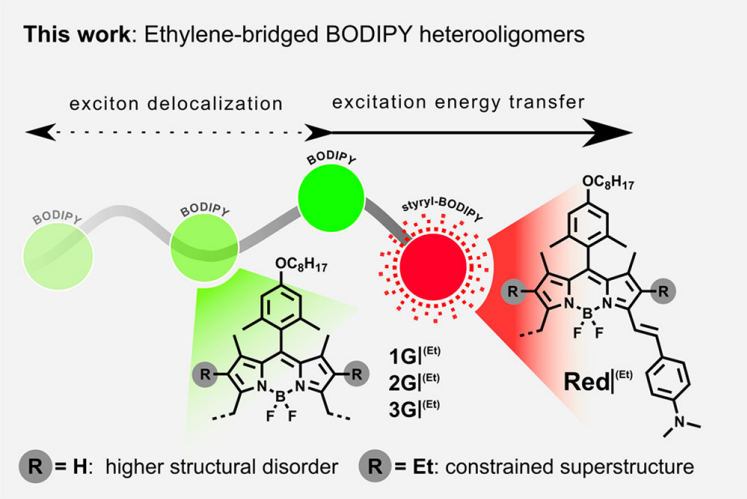

Figure 2.1: Conceptual ideas of the presented work.

alignments would be necessary to achieve narrowed absorption/emission profiles as consequence of J-aggregation with delocalized excitons. Recently, we introduced a straightforward approach to transform α-methyl groups of various BODIPY dyes into ethylene bridges that link a number of chromophores to form linear, oligo-BODIPY arrays.[132] Depending on the substitution pattern of the BODIPY core, absorption and emission profiles were gradually narrowed along the growing chain length and brought close to resonant coalescence, a clear indication for efficient exciton delocalization.

In this work we address the question to what extent excitonic coupling conditions present in a green oligo-BODIPY subunit of variable length (monomer to trimer, **1G** to **3G**, emission in the green spectral region) influence energy transfer toward a single, integrated, terminal BODIPY acceptor unit (Figure 2.1). The latter acts as an energy sink because of its lower lying S_1 state (**Red**, emission in the red spectral regime). For this purpose, we designed a series of dyads, triads, and tetrads, in which an ethyl group at the β-positions (R = Et) of the individual BODIPY cores (called EtDM = ethyldimethylpyrrole series) was introduced to achieve a tight, locked-in superstructure. In contrast, an analogous series of dyads, triads, and tetrads with R = H (called DM = dimethylpyrrole series) allows for a wider conformational space with higher structural flexibility. Both series were then investigated by steady state optical spectroscopy in toluene solution and the obtained experimental data complemented by femtosecond transient-absorption spectroscopy and mixed quantum-classical nonadiabatic dynamic simulations to explore the photoinduced dynamics in these series. We will demonstrate that while the interaction between the green BODIPYs is in the strong coupling regime, thus forming delocalized excitons (Frenkel coupling limit), the interaction to the red BODIPY is much weaker (Förster coupling limit). On the basis of this categorization, however, we show that the interpretation of experimentally observed energy transfer rates requires a theoretical approach beyond standard

Förster theory.

2.2 Results and Discussion

2.2.1 Synthesis of Oligo-BODIPYS

For the synthesis of the BODIPY heterooligomers we applied and improved our recently developed strategy to couple α-methyl-substituted BODIPY motifs by oxidative dimerization at the methyl groups, thereby forming the desired ethylene linker. To be more specific, we replaced iodine monochloride by $CuCl_2$ as oxidant after a preceding deprotonation of an α-methyl proton with LDA at $-78°C$. The base selectively deprotonates α-methyl groups of *meso*-aryl-substituted BODIPY scaffolds and is able to form intermediate lithium organyls. We assume that $CuCl_2$ afterward abstracts one electron and releases α-methyl radical species, which quickly recombine. This approach also facilitated a hetero-dimerization between unsubstituted BODIPY dimers and styryl-equipped derivatives, giving the triad compounds **2G-Red** and **2G-Red**$|^{Et}$ in yields of ca. 30 % (Figure 2.2).

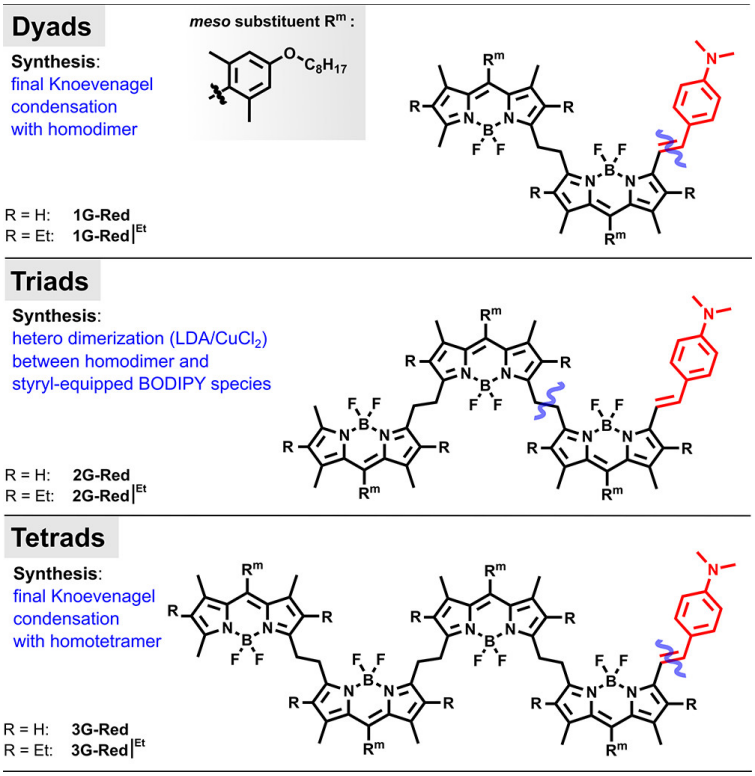

Figure 2.2: Final structures and nomenclature of the prepared dyad, triad, and tetrad species as well as description of the synthetic access. For detailed procedures see Supporting Information of Ref. 6.

Since this reaction inherently gives rise to a statistically controlled range of byprod-

ucts, dyad (**1G-Red** and **1G-Red**$|^{\mathrm{Et}}$) and tetrad congeners (**3G-Red** and **3G-Red**$|^{\mathrm{Et}}$) were synthesized alternatively by final Knoevenagel condensations on homooligomers with satisfying yields ($\sim$ 50 %) under careful reaction control to avoid 2–fold condensation products.

2.2.2 Computational Study of Structural Properties

Owing to the difficulty to obtain crystal structures of our heterooligomers and the indications that solid state geometries might drastically differ from the ones found in solution, we performed a thorough computational analysis in order to assign photophysical data to structural origins. Assuming a nearest-neighbor approximation, we focused on homodimeric and heterodimeric substructures first and studied them separately. The *meso*-substituent $\mathrm{R^m}$ (Figure 2.2) does not interfere in the crucial aggregation sphere at the ethylene bridge and thus plays only a minor role in the adopted microstructure, which was also photophysically proven in our previous work.[133] $\mathrm{R^m}$ was thus omitted for simplicity and savings of computational costs. A preluding, force-field-based Monte Carlo sampling restricted the conformational space predominantly to the subspace of the ethylene bridge (Figure 2.3A). Both antiperiplanar (*AP*) and synclinal (*SC*) conformations give rise to further *trans* and *cis* alignments of the dye scaffold, respectively. While an *AP-trans* structured dimer possesses C_i symmetry, *AP-cis* and *SC-trans* analogues are C_2 symmetric conformers. *SC-cis* has the lowest symmetry (C_1) and can only give phenotypically distorted higher homologues. Furthermore, *AP-cis* suffers from significant steric and Coulomb repulsion due to the close proximity of the *cis*-oriented dye moieties and their stationary dipole moments. From this simplified viewpoint, *AP-cis* and *SC-trans* conformations appear as the most suitable candidates for global minimum superstructures and lead to staggered (*AP-cis*) and saddle-like (*SC-trans*) geometries. With these preconsiderations in hand we performed initial geometry optimizations of homo- and heterodimers at the DFT level and refined resulting geometries with single-point computations engaging the double-hybrid functional DSD-BLYP-D3[134] (Figure 2.3B). Even though the more flexible dimers (R = H) as well as their constrained counterparts (R = Et) both clearly disfavor *cis* orientations (*AP-cis* and *SC-cis*) by ca. 3–8 kcal/mol, a clearcut discrimination between the saddle and the staggered geometry is difficult to detect in either case. It is important to note that in the saddle geometry the dihedral angle γ_{D} strongly deviates from the ideal 60° in the case of β unsubstituted dimers ($\mathrm{R = H}, \gamma_{\mathrm{D}} \approx$ ca. 34°), presumably because the looser linkage allows for additional energy gain by partial intramolecular $\pi - \pi$ stacking. This leads to a nearly perfect linear alignment of the long axes of adjacent dipyrrin moieties ($\gamma_{\mathrm{Ax}} \approx 0°$), whereas in the β-ethyl-substituted case (R = Et) a slight curvature promotes a helical superstructure. The computational ambiguity prompted us to compute also all final oligomeric species. Based on the tendency toward a saddle geometry in the terminal hetero-unit the alignment was kept fixed at that linking unit, and staggered as well as saddle arrangements respectively were computed at the remaining ethylene bridges

of the corresponding homo green subunit. Despite a weak discrimination, we found a minor, yet consistent dominance of the all-saddle superstructure in both series and for all heterooligomers. This tendency is more pronounced when the β-substituent (R = Et) is present, which underlines its stabilizing contribution and its constraining effect on the conformational space. On the basis of these results we assume, however with some caution, that the structural equivalent to our photophysical data is the *all-saddle* conformation in all three cases (dyad, triad, and tetrad) for the DM as well as for the EtDM series.

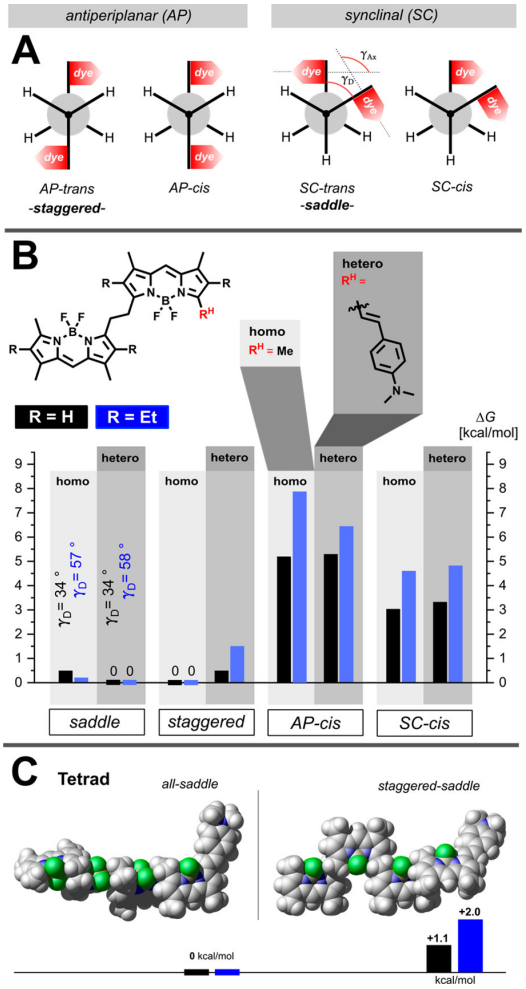

Figure 2.3: (A) Outlined conformational space of the ethylene bridge. (B) Energetic ranking (Gibbs free energy) of different conformations of homo- and heterodimeric substructures in toluene. Geometry/thermochemistry: M052X-D3/def2-TZVPP/toluene (PCM), single-point: DSD-BLYP-D3/def2-TZVPP/toluene (SMD). *Meso* substituent Rm (Figure 2.2) was omitted. (C) Two competing tetrad geometries, exemplarily shown for the β-unsubstituted series (R = H), and their energetic ranking; see SI for full data. Geometry: M052X-D3/def2-TZVP/toluene (PCM), single-point: DSD-BLYP- D3/def2-TZVPP/toluene (SMD).

2.2.3 Optical Spectroscopy

The steady state absorption and emission spectra of the DM and EtDM heterooligomer series are depicted in Figure 2.4. Panels A and C visualize the data of the DM- and EtDM-derived dyads, respectively, together with their two monomeric parent compounds. In both cases the absorption spectrum is characterized by two main bands, which resemble the signatures of the native, *green* BODIPY monomer and its *red* styryl-equipped congener in shape and energy. While the *green* peak at ca. 19800 cm^{-1}(**1G-Red**) and 18900 cm^{-1}(**1G-Red**$|^{Et}$) undergoes no significant shift compared to the corresponding peaks of the *green* monomers G$|^{(Et)}$, the low-energy (*red*) main absorption peak of the dyads is slightly red-shifted by 220 cm^{-1}(**1G-Red**) and 200 cm^{-1} (**1G-Red**$|^{Et}$). The absorption spectra of the longer heterooligomers are similar to the ones of **1G-Red** and **1G-Red**$|^{Et}$ and also show two strong bands. When comparing the heterooligomers within one series (Figure 2.4B/D), the low-energy *red* band, corresponding to S_1, slightly increases in intensity but remarkably undergoes no further red-shift, although the distance between the centers of the terminal *red* BODIPY and the *green* subunit increases along the series. In contrast to that, the *green* band is strongly red-shifted when BODIPY units are added, accompanied by a pronounced increase in intensity. This shift is very similar to the values recently observed for corresponding homooligomers and directly allows gauging the excitonic coupling energy V_{GG} within the *green* subunit. More precisely, compared to the dyad **1G-Red** the *green* peak of the triad **2G-Red** is displaced by 600 cm^{-1} and by 930 cm^{-1} for **3G-Red**. Very similar shifts are present in the EtDM series (**2G-Red**$|^{Et}$: 620 cm^{-1}, **3G-Red**$|^{Et}$: 1010 cm^{-1}), which already proved to show strong exciton delocalization and narrowed absorption bandwidths in related homooligomers in contrast to DM-derived species.[132] The widely isoenergetic absorption bands of heterooligomers (*green* peak) and their *green* building blocks suggest that the *green* subunit can be treated as a discrete and strongly coupled entity within the heterooligomers. However, when comparing the intensities of the respective *green* bands in the heterooligomer series, a significant mismatch with the corresponding intensities of monomeric *green* BODIPY species $\left(\mathbf{G}, \mathbf{G}|^{Et}\right)$ appears. To evaluate this relative decrease for the dyads quantitatively and to avoid spectral contaminations by the adjacent *red* unit, the absorption spectrum of the corresponding styryl-equipped monomer Red$|^{Et}$ was subtracted from the dyad spectrum and the remaining *green* intensity integrated. From this integral we calculated the squared transition dipole moment (μ^2 = dipole strength) by eq S1 of Ref. 6. For **1G-Red** the squared *green* transition dipole moment decreases by ca. 18 % from 34 D^2 (single monomer G) to 28 D^2, whereas in the case of **1G-Red**$|^{Et}$ this effect is approximately twice as strong with a decrease of 37 % from 35 D^2 to 22 D^2. This loss of absorption intensity in both dyads is a direct consequence of excitonic coupling assigning the second *green* band to an S_2 excited state with a hetero-pair of out-of-phase coupled oscillators as depicted in Figure 2.5. The intensity of the corresponding *red* band is consistently amplified, which results in total squared transition dipole moments that are sums of their monomeric building blocks, respectively (Table 2.1).

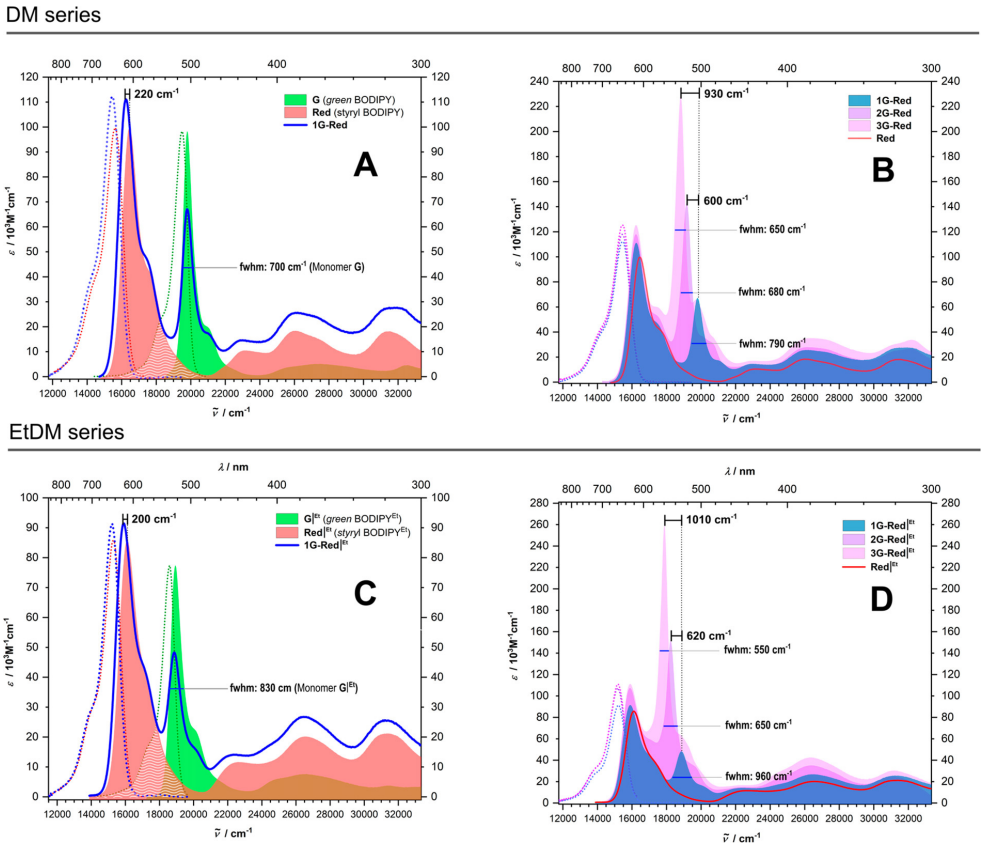

Figure 2.4: Steady state absorption and emission spectra of all final dyads, triads, and tetrads in toluene at room temperature. Emission spectra (dashed) are normalized and shown in the same color as the corresponding absorption. (A and B) β-Unsubstituted series (DM); (C and D) β-ethyl-substituted one (EtDM). The spectra of monomers **G**/**G**$|^{\mathrm{Et}}$ and Red/Red$^{\mathrm{Et}}$ are also included.

$$V^2 = \left(\frac{\delta E}{2}\right)^2 - \left(\frac{\Delta E_{\mathrm{G-Red}}}{2}\right)^2 \tag{2.1}$$

Exciton coupling is based on a coherent excitation event, which in many cases is manifested in vibronically decoupled absorption bands of small line width (exchange narrowing).[134,135] Indeed, in the case of the EtDM series the *green* absorption line width (fwhm) decreases from 963 cm^{-1} (**1G-Red**$|^{\mathrm{Et}}$) to 649 cm^{-1} (**2G-Red**$|^{\mathrm{Et}}$) and eventually to 548 cm^{-1} (**3G-Red**$|^{\mathrm{Et}}$), while in the DM series the decrease is much less pronounced (Figure 2.4D). The ethyl substituents provide a rather fixed alignment between adjacent oscillators, reducing the extent of diagonal (= site energy) disorder and leading to a stronger coupling. Similar narrowing effects have been found for the S_1 state of other J-type aggregates but, to the best of our knowledge, not for the S_2 state of the exciton manifold.

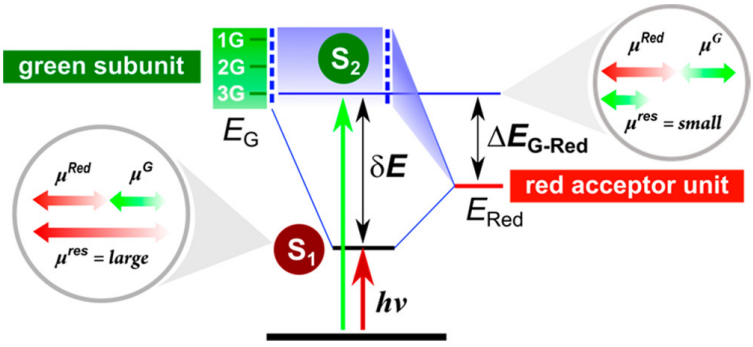

Figure 2.5: Exciton coupling diagram adjusted to our molecular setup (the S_2 state of the heterooligomers and the unperturbed S_1 states of the *green* homooligomers coincide in energy, visualized as one blue energy level.) Simplified derivation of the S_2 state exemplarily shown for tetrad 3G-Red.

Thus, on the basis of Kasha's exciton coupling theory, both bands correspond to two accessible exciton states, S_1 and S_2.
For the dimers **1G-Red** and **1G-Red**$|^{\mathrm{Et}}$, their coupling can be quantified using eq 2.1, in which δE denotes the splitting of the two spectral peaks and $\Delta E_{\text{G-Red}}$ the energy difference of the S_1 states of the parent monomeric building blocks. Since an increasing $\Delta E_{\text{G-Red}}$ entails a growing δE, large energy differences between the coupling partners can still result in high coupling energies despite low shifts of the involved absorption peaks.
The excitonic coupling energies $V_{\text{G-Red}}$ of both dyads turned out to be similar. They amount to ca. -550 cm^{-1} (**1G-Red**) and ca. -490 cm^{-1} (**1G-Red**$|^{\mathrm{Et}}$). While the higher value in the case of **1G-Red** might be a consequence of a stricter parallel alignment of coupled transition moments initiated by the smaller dihedral angle γ_D (Figure 2.3A), the negative sign results from J-aggregate behavior, that is, a head-to-tail arrangement of transition dipoles.
In a first attempt to evaluate the coupling of the longer heterooligomer series we made the assumption that the two/three *green* BODIPYs are so strongly coupled that they form a single chromophore unit whose S_1 state couples with the S_1 state of the red BODIPY (**Red** and **Red**$^{\mathrm{Et}}$). This approach is corroborated by our recent investigation of *green* BODIPY homooligomers[132] as well as by the qualitative categorization of coupling strengths according to $\left|\frac{V}{\Delta E_{\text{AB}}}\right| \cdot$ [12] With the rough estimation $V = V_{\text{GG}} \approx -500$ cm^{-1} (see Table 2.1) and $\Delta E_{\text{AB}} = \Delta E_{\text{GG}} \approx 0$ cm^{-1} the quotient gives $\left|\frac{V}{\Delta E_{\text{AB}}}\right| > 1$, which refers to a strong coupling case addressing the Frenkel coupling limit of this study. Upon application of eq 2.1 for a dyad structure, the coupling constants $V_{\text{G-Red}}$ stay within a narrow window for an entire series as mentioned above (Table 2.1). With $V = V_{\text{G-Red}} \approx -500$ cm^{-1} and $\Delta E_{\text{AB}} = \Delta E_{\text{G-Red}} \approx 3000$ cm^{-1} the quotient results in $\left|\frac{V}{\Delta E_{\text{AB}}}\right| \approx 0.17 < 1$, which classifies the coupling in the intermediate range and thus closer to the Förster limit where $\left|\frac{V}{\Delta E_{\text{AB}}}\right| \ll 1$ is expected.
Above, we treated the exciton coupling in the heterotriads and tetrads as effective

Table 2.1: Spectroscopic Data of Prepared Compounds in Toluene at RT[a]

BODIPY	λ_A^a /cm^{-1}(nm)	fwhm[b] /cm^{-1}	λ_F^c /cm^{-1}(nm)	$\Delta\tilde{\nu}^d$ /cm^{-1}	ϵ^e /10^{3}M^{-1} cm^{-1}	Φ_F^f (rt)	τ_F^g /ns	k_F^h /10^{8}s^{-1}	$\mu^{2\ i}$ /D^2	$V_{\mathrm{G-Red}}(V_{\mathrm{GG}})^j$ /cm^{-1}
G (Mon.)	19800 (505)	700	19490 (513)	310	98	0.88	4.63	1.90	34	-
Red (Mon.)	16450 (608)	n.d.	15620 (640)	820	100	0.83	3.41	2.43	73	-
1G-Red	19760 (506) 16230 (616)	960	15460 (647)	770	113/69	0.85	3.33	2.56	111$^{\mathrm{tot}}$ $\underline{28}^{1G}$ | *83*$^{\mathrm{Red}}$	-550
2G-Red	19160 (522) 16210 (617)	680		750	118/143	0.82	3.16	2.59	146$^{\mathrm{tot}}$ $\underline{57}^{2G}$ | *89*$^{\mathrm{Red}}$	-580[k] (-650)
3G-Red	18830 (531) 16230 (616)	650		770	125/228	0.82	3.00	2.73	188$^{\mathrm{tot}}$ $\underline{94}^{3G}$ | *94*$^{\mathrm{Red}}$	-520[k] (-650)
G|Et (Mon.)	18900 (529)	830	18590 (538)	310	77	0.87	5.17	1.68	35	-
Red|Et (Mon.)	16100 (621)	n.d.	15290 (654)	810	86	0.80	3.72	2.15	71	-
1G-Red|Et	18870 (530) 15900 (629)	960	15220 (657)	680	91/48	0.78	3.64	2.14	99$^{\mathrm{tot}}$ $\underline{22}^{1G}$ | *77*$^{\mathrm{Red}}$	-490
2G-Red|Et	18250 (548) 15870 (630)	650		650	107/151	0.83	3.47	2.39	149$^{\mathrm{tot}}$ $\underline{62}^{2G}$ | *87*$^{\mathrm{Red}}$	-510[k] (-660)
3G-Red|Et	17860 (560) 15870 (630)	550		650	111/259	0.85	3.37	2.52	186$^{\mathrm{tot}}$ $\underline{96}^{3G}$ | *90*$^{\mathrm{Red}}$	-430[k] (-660)

[a] Energy of main BODIPY absorption bands. [b] Full width at half-maximum of green absorption bands.
[c] Energy of main emission band. [d] Stokes shift referring to lowest energy absorption band.
[e] Extinction coefficient of main absorption band. First value: low-energy (red) band; second value, if noted, high-energy green band.
[f] Absolute fluorescence quantum yield. [g] Experimental fluorescence lifetime (TCSPC).
[h] Fluorescence rate constant according to Φ_F/τ_F [i] Squared transition dipole moment according to eq S1 of Ref. 6; underlined values refer to the green low-energy absorption band after subtraction of the monomeric Red and Red$|^{\mathrm{Et}}$ absorption spectrum, respectively. Values in italics are the difference between the total transition dipole moment and the green one; they correspond to the lowest exciton state.
[j] Exciton coupling energy; values in parantheses refer to the coupling

two-state systems. While an analytical evaluation of the coupling in the case of the heterodimer is straightforward, the full treatment considering all three/four states of the heterotriad and the tetrad is more complicated. Thus, in a second approach we resume with a numerical solution of the corresponding secular determinant, which describes the excitonic coupling V between the localized diabatic eigenstates E of the oligomers, eq 2.2.

$$\begin{vmatrix} E_{\mathrm{G}}-\varepsilon & V_{\mathrm{GG}} & 0 & 0 \\ V_{\mathrm{GG}} & E_{\mathrm{G}}-\varepsilon & V_{\mathrm{GG}} & 0 \\ 0 & V_{\mathrm{GG}} & E_{\mathrm{G}}-\varepsilon & V_{\mathrm{G-Red}} \\ 0 & 0 & V_{\mathrm{G-Red}} & E_{\mathrm{Red}}-\varepsilon \end{vmatrix} = 0 \qquad (2.2)$$

Here the orange entries refer to the **1G-Red**$|^{\mathrm{Et}}$ heterodyad (2×2 matrix), the red entries together with the orange entries (3×3 matrix) to **2G-Red**$|^{\mathrm{Et}}$, and the full 4×4 matrix to **3G-Red**$|^{\mathrm{Et}}$. For E_{G} we used the absorption energy of **G**$|^{(\mathrm{Et})}$ and for E_{Red} we used **Red**$^{(\mathrm{Et})}$ (Table 2.1). Focusing exemplarily on the DM case we took -550 cm^{-1} for $J_{\text{G-Red}}$ as evaluated above. Then we diagonalized the 3×3 part of the matrix, which yields the eigenvalues (= absorption energies) of **2G-Red** (Table 2.2).

We varied the input V_{GG} until we obtained a reasonable agreement of the two lowest energy eigenvalues with the observed S_1 and S_2 state energies. This procedure yielded $V_{\mathrm{GG}} = -540$ cm^{-1}. In the same way, we obtained $V_{\mathrm{GG}} = -610$ cm^{-1} for **3G-Red** after diagonalizing the 4×4 matrix. The discrepancy between these two input couplings reflects the crudeness of this approximation as we omit any couplings between

Table 2.2: Exciton Coupling Values, Relative Eigenvalues, and Squared Transition Moments from Eq 2.2

BODIPY	J_{GG}/cm^{-1}	J_{G-Red}/cm^{-1}	rel eigenvalues/cm^{-1}	μ^2/D^2
1G-Red		–550	90	20.3
			–3440	86.5
2G-Red	–540	–550	580	0.4
			–490	51.8
			–3440	90.3
3G-Red	–610	–550	881	1.4
			44	0.5
			–835	82.8
			–3441	92.2
1G-Red|Et		–490	85	19.4
			–2885	86.5
2G-Red|Et	–560	–490	596	0.4
			–510	49.0
			–2886	90.3
3G-Red|Et	–660	–490	950	1.4
			42	0.6
			–904	81.0
			–2888	92.2

non-nearest-neighbors. In practice, only the two lowest energy absorptions S_1 and S_2 are visible in the experimental spectra, but these proved to be sufficient to fit V_{GG} in the described way. We also obtained the eigenvectors of the respective matrices (Table 2.2), which show in all cases that the S_1 state is predominantly formed by the localized **Red** wave function (coefficient > 0.98). Multiplying the eigenvector components with the localized individual squared transition moments of the *green* and *red* BODIPYs taken from Table 2.1 as 34 D^2 and 73 D^2, respectively, gave the squared transition moments of the S_1 and S_2 states in all heterooligomer cases, which are in reasonable agreement with the experimentally estimated values from integration of the bands (Table 2.2). For example, exciton theory gives $(\mu_{S2})^2 / (\mu_{S1})^2 = 20/87$ D^2 for **1G-Red**, 52/90 D^2 for **2G-Red**, and 83/92 D^2 for **3G-Red**. This is in line with the experimental observation of intensity borrowing from the *green* to the *red* unit. For the EtDM series of heterooligomers we made essentially the same observations. When exciting the heterooligomers at the S_2 band, no emission from the S_2 state was detected in any of the heterooligomer cases in the solvent systems studied (DCM, THF, and toluene), proving complete energy transfer from S_2 to S_1. In contrast, we observed emission from S_1 (see Figure 2.4) with the band shape being the mirror image of the lowest energy absorption band and a very small Stokes shift. The quantum yield of fluorescence for both series in toluene is very similar to the values obtained for the *red* building blocks **Red** and $\mathbf{Red}^{Et}$ ($\Phi_F \approx 0.8$). However, in DCM and THF

the DM series shows a dramatically decreased red fluorescence ($\Phi_F \approx 0.01 - 0.1$), while the EtDM series still maintains a reasonable emission in THF ($\Phi_F \approx 0.3$; see SI). This might indicate a delicate geometrical reorganization as a function of solvent polarity, which might lead to conical intersections as the source of a direct nonradiative pathway and underpins the foldameric nature of our heterooligomers.

2.2.4 Transient Absorption Spectroscopy

In order to probe the photoinduced dynamics of the above mentioned energy transfer process at all heterooligomers, we performed transient absorption (TA) spectroscopy with fs-time resolution in fluid toluene. We excited the oligomers by 30 fs pulses from a NOPA at 20600 cm^{-1}, which is at the blue flank of the *green* BODIPY absorption. Here, the ratio of *green* BODIPY absorption to *red* BODIPY absorption is maximal, which ensures that we excite predominantly the *green* BODIPYs (S_2 of the oligomer). The transient spectra were probed by a white-light continuum between 12500 and 25000 cm^{-1}, which was delayed in logarithmic steps up to ca. 8 ns relative to the pump pulse. Because all six oligomers behave very similarly, we discuss here only the TA spectra of **3G-Red**$|^{Et}$. The spectra of all oligomers can be found in the Supporting Information of Ref. 6 (Figures S26-S31). The TA spectra of **3G-Red**$|^{Et}$ in toluene are presented in Figure 2.6A, for three consecutive time frames. At early times (bottom panel), a sharp negative signal is rising with the instrument response function at 18000 cm^{-1}. This signal decays quickly within ca. 100 fs and gives rise to TA spectra that consist of several positive signals (excited state absorption) between 16500 and 22000 cm^{-1} and a prominent negative signal between 13000 and 16500 cm^{-1} (ground state bleaching and stimulated emission). The described process can easily be seen in the time trace at 17900 cm^{-1} (Figure 2.6B, bottom panel). After ca. 100 fs, the TA spectra only slightly change their spectral shape (Figure 2.6A, middle and upper panel).

To gain a more detailed insight, the TA spectra were analyzed by a global deconvolution using GLOTARAN software,[136] which also was used to treat the coherent artifact and to correct the white-light dispersion. This global deconvolution yields decay-associated difference spectra (DADS) and evolution-associated difference spectra (EADS). The former represents a parallel kinetic model, in which the DADS are amplitude spectra that are associated with an exponential decay. The latter represents a consecutive kinetic model, in which the first EADS rises with the instrument response and decays monoexponentially. The second EADS rises with the lifetime of the former and so on. DADS and EADS of **3G-Red**$|^{Et}$ are shown in Figure 2.6C. EADS in general are composed of negative signals that result from ground state bleaching (GSB) and stimulated emission (SE) and positive signals that are caused by excited state absorption (ESA). In the first component of the EADS of **3G-Red**$|^{Et}$ we observe a strong GSB at ca. 18000 cm^{-1}, which coincides with the absorption peak of the *green* BODIPYs (S_2 of the oligomer). At the blue side there is an ESA at ca. 18500 cm^{-1}, which is caused by an excitation into a two-exciton state.[23] At ca.

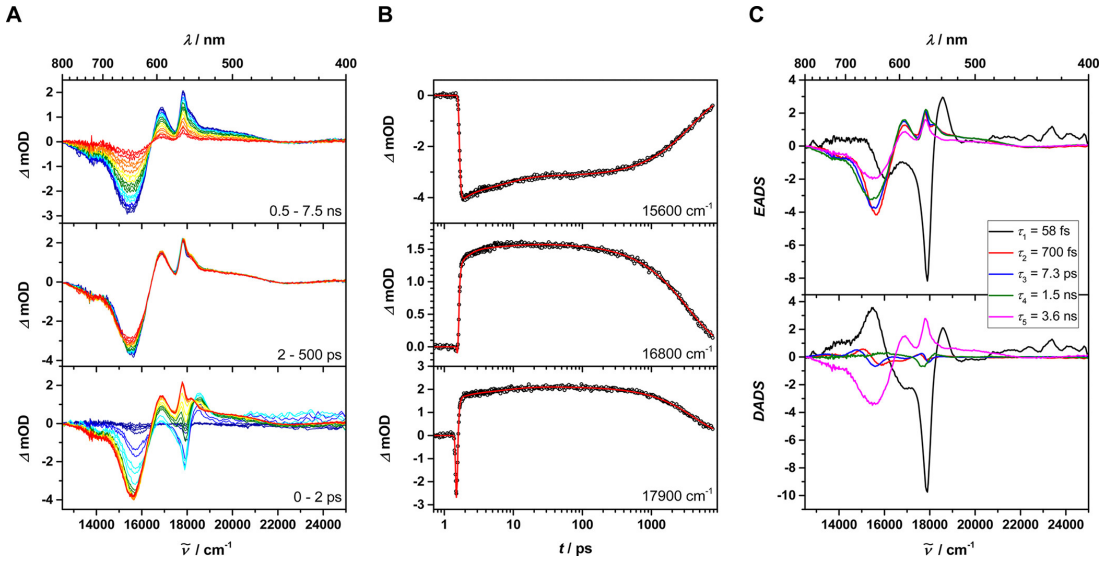

Figure 2.6: (A) Chirp and stray light corrected transient spectra of **3G-Red**$|^{\mathrm{Et}}$ in toluene excited at 485 nm. Early spectra are given in blue; late spectra in red. (B) Time scans and global fit at selected wavenumbers. (C) Evolution-associated difference spectra (top) and decay-associated difference spectra (bottom) of a global fit using GLOTARAN software.

16100 cm^{-1} we observe also a GSB, which is associated with population of the *red* BODIPY (S_1 of the oligomer) due to the fact that we cannot exclusively excite the S_2 state of the oligomer. This EADS has a lifetime of 58 fs and is followed by a series of EADS which are distinctly different from the former. These very similar EADS possess ESA at ca. 17000 and 18000 cm^{-1} and a broad GSB+SE at 15500 cm^{-1}. These spectral features clearly prove excitation of the *red* BODIPY, that is, the S_1 state of the oligomer. In the DADS, the components with 700 fs and 7.3 ps show a sigmoidal shape, which indicates a shift in the GSB+SE band, which is most likely caused by solvent relaxation of toluene.[137] The longer component of 1.5 ns together with that of 3.6 ns represent ground-state recovery and reflect the inhomogeneity of the oligomer because of various possible conformers. Thus, the fs component of 58 fs represents the internal conversion from S_2 to S_1 within the heterotetrad. As these states are predominantly localized at the *green* subunit and the *red* BODIPY, respectively, this lifetime refers to the ultrafast energy-transfer process between the two moieties. In Table 2.3 we collected all lifetimes from the TA measurement of all oligomers. While the lifetimes associated by the solvent dynamics (ca. 1 and 7 ps) and ground-state recovery (ca. 3-4 ns) are very similar for all oligomers, the energy-transfer component shows a distinct trend. Within one series of oligomers, this lifetime increases on going from **1G-Red** (45 fs) over **2G-Red** (71 fs) to **3G-Red** (89 fs). The lifetime increases similarly, but is consistently shorter for the EtDM-series: **1G-Red**$|^{\mathrm{Et}}$ (39 fs), **2G-Red**$|^{\mathrm{Et}}$ (42 fs), **3G-Red**$|^{\mathrm{Et}}$ (58 fs).
In a first approach to interpret the measured energy transfer rates, we employed Förster's theory in the formulation of Fermi's golden rule.[36] The latter allows cir-

Table 2.3: Experimental (TA) and Theoretical (Förster Theory/FT) Lifetimes and Energy Transfer Rates

	τ/fs		k/ps^{-1} [a]	
BODIPY	TA (exptl)	FT/eq 2.3 (theoretical)	TA (exptl)	FT/eq 2.3 (theoretical)
1G-Red	45	36/36[b]	22	28/28[b]
2G-Red	71	22/24[b]	14	46/41[b]
3G-Red	89	22/19[b]	11	46/52[b]
1G-Red$\|^{\mathrm{Et}}$	39	27/29[b]	26	37/35[b]
2G-Red$\|^{\mathrm{Et}}$	42	22/25[b]	24	45/40[b]
3G-Red$\|^{\mathrm{Et}}$	58	24/19[b]	17	42/52[b]

[a]Energy transfer rates and lifetimes obtained via $\tau = 1/k$, respectively.
[b]Assuming a constant excitonic coupling constant for all heterooligomers within one series (DM: $V_{\mathrm{G-Red}} = -550$ cm^{-1}, EtDM: $V_{\mathrm{G-Red}} = -480$ cm^{-1}), averaged from Table 2.1.

cumventing the structural parameter input of the commonly utilized equation by estimating the coupling conditions only from spectral information by applying eq 2.3. With that approach we intended to bypass the challenging evaluation of orientation factors κ and distance ratios at our heterostructures and to provide a more comprehensive treatment of the coupling input V, which is restricted to a Coulomb interaction in traditional Förster resonance energy transfer (FRET) theory. In Fermi's golden rule expression V denotes the excitonic coupling constant corresponding to $V_{\mathrm{G-Red}}$, for which we used the average of couplings from Table 2.1, while c is the speed of light and ρ the density of initial and final states.

$$k_{\mathrm{FT}} = 4\pi^2 c V^2 \rho(\tilde{\nu}) \tag{2.3}$$

The density of states ρ can be approximated directly from photophysical data via the following integral.

$$\rho(\tilde{\nu}) \approx \int I_{\mathrm{F}}(\tilde{\nu})\tilde{\nu}^{-1} \cdot \varepsilon(\tilde{\nu})\tilde{\nu}^{-3} d\tilde{\nu} \tag{2.4}$$

The integral quantifies the spectral overlap of donor and acceptor unit by combining reduced and area-normalized absorption and emission spectra, respectively (emission spectra of the donor unit are taken from monomers $\mathbf{G}|^{(Et)}$ or respective homooligomers $\mathbf{2G}|^{(\mathrm{Et})}$ and $\mathbf{3G}|^{(\mathrm{Et})}$). We want to stress that despite the widespread use of eq 2.3 the expression is still based on a number of assumptions: first, we treat the *green* BODIPY arrays as a single, strongly coupled donor entity ($V_{\mathrm{GG}} \approx -600$ to -700 cm^{-1}; see Table 2.1), which appears justified as reasoned above in the context of the spectroscopically supported exciton coupling analysis. The second assumption is the applicability of perturbation theory in the present case as the interaction between the *green* donor subunit and the *red* BODIPY acceptor moiety might be too strong for using an equation based on perturbation theory. This coupling is on the

order of $V_{\mathrm{G-\ Red}} \approx -400$ to $-600\ \mathrm{cm}^{-1}$ (see Table 2.1); however, the strong difference between the energy levels of donor and acceptor still leads to localized wave functions (see above). The third and perhaps most critical aspect is to model the density of states in eq 2.4 by using fluorescence spectra of relaxed excited states. Since the ultrafast energy transfer occurs in the femtosecond regime, it cannot be expected that vibrational and solvent relaxation processes are fully completed. Thus, the excitation event induced by an ultrashort pump pulse exciting the system does not lead to the population of the excited state vibronic levels that correspond to the steady-state spectra. Therefore, results from Fermi's golden rule expression can only be considered as a rough upper bound. Table 2.3 represents the energy transfer rates obtained via eq 2.3 in comparison with measured counterparts from transient absorption spectroscopy. Presumably, owing to the inaccuracy of the density of states, which becomes unrealistically high by using fluorescence spectra of vibrationally relaxed states, and which increase on going from dyads to tetrads, energy transfer rates are on the right order of magnitude, yet overestimated by eq 2.3.
While the density of states is a challenging parameter to account for spectroscopically in systems where energy transfer occurs in the short-range regime, the electronic coupling V in eq 2.3 can be quite correctly derived from optical spectra as we did above. In Förster's original formulation, V is the pure Coulomb coupling evaluated from the donor fluorescence transition dipole moment and acceptor absorption transition moment. In alternative formulations, the fluorescence transition moment is replaced by that of the donor absorption, as it is done in Kasha's exciton coupling theory. Scholes et al. have shown that more accurate values of the Coulomb coupling could be obtained by replacing the point dipole approximation made in the original Förster formulation by transition densities whose interaction is calculated by numerical integration on a spatial grid.[37] In this way, the shape of the donor and acceptor chromophores is taken into account. The values of the Coulomb coupling calculated using different approaches are given in the Supporting Information of Ref. 6. While all methods gave Coulomb couplings on the same order of magnitude as those estimated by the energy splitting above, they show a much more pronounced decreasing trend on going from the dyads to the tetrads. The reason for this discrepancy could be that the experimentally determined couplings (see Table 2.1) not only include Coulomb interactions but also to some extent exchange interactions. While the former is negative for the J-type alignment of the BODIPY chromophores, the latter is always positive and thus may compensate part of the Coulomb coupling. We assume that the exchange coupling may indeed be significant, as the ethylene linkers are likely to arrange a direct contact of adjacent π-systems, especially in the saddle geometry (Figure 2.3C). In order to estimate the short-range contribution to the overall coupling, we have used the approach introduced by Scholes et al.[138] as outlined in the Supporting Information of Ref. 6 where also the different contributions are given in Table S3 and Figure S34. Both the Coulomb as well as the exchange coupling decrease with the number of *green* chromophores, while their sum remains almost constant owing to the opposite signs of the two coupling terms. This is consis-

tent with the coupling values obtained from the experimental spectra. Therefore, we wish to point out that in the heterooligomers investigated in this study the exchange coupling is not negligible, but has values that are a factor of $\sim 2-3$ smaller than those of the Coulomb couplings.

2.2.5 Nonadiabatic Dynamics Simulations

Both exciton coupling analyses undertaken above as well as the application of Fermi's golden rule are based on a static picture of wave functions imposing severe limitations to a realistic treatment of the present EET processes. In the nonadiabatic simulations that follow, we consider the dynamic evolution of wave functions; that is, couplings and state energies are now time dependent variables that correlate with molecular motions. We performed light-induced dynamics simulations at all six systems to identify the excited state relaxation and exciton transfer dynamics after applying a laser pulse resonant to the second absorption band S_2. Since the rise and fall of the state populations show the same qualitative picture for all of the oligomers, we will focus here only on the state populations of **3G-Red**$|^{\mathrm{Et}}$ (see SI in Ref. 6 for full data set).
The time-dependent excited state populations are shown in the top of Figure 2.7. Due to the large spectral bandwidth of the pulse, which is on the order of 1000 cm^{-1}, and the relatively high number of close-lying electronic states, the pulse populates all four exciton states to some extent.
Within a short time of about 50 fs the trajectories leave all higher electronic states and the population is transferred to the S_1 state, reflecting the energy transfer rate to the *red* BODIPY acceptor unit. The rise of the S_1 population was fitted with a mono exponential function and gave the corresponding time constant of 57 fs for **3G-Red**$|^{\mathrm{Et}}$.
In the bottom of Figure 2.7 the time-dependent exciton localization is visualized by calculating the fraction of transition density matrix (FTDM),

$$\mathrm{FTDM}_X^N = \frac{\sum_{\mu\in X}\sum_{\nu\in X} P^2_{\mu\nu,N}}{\sum_{\mu\in \text{ tetrad }}\sum_{\nu\in \text{ tetrad }} P^2_{\mu\nu,N}} \tag{2.5}$$

which shows the partitioning of excitation between individual fragments. Here $P^2_{\mu\nu,N}$ are the transition density matrix elements of the atomic orbital μ or ν between the ground state and the N th excited state. The symbol X denotes the monomer and may take the value **Red**, $\mathbf{G}_1$, $\mathbf{G}_2$, or $\mathbf{G}_3$ (for the different *green* BODIPY monomeric units, with $\mathbf{G}_1$ being the closest one to the *red*). The interaction with the laser pulse leads to a distribution of the excitation that resides with 70 % mainly on the *green* BODIPYs (especially on the terminal *green* one ($\mathbf{G}_3$)). The electronic relaxation leads to an exciton transfer from *green* units to the *red* terminus within 100 fs. Since the localization on the outer *green* unit $\mathbf{G}_3$ is highest at the beginning and lowest at the end, we can conclude that the exciton transfer is mediated by the connecting *green* BODIPY units along the linking ethano tethers. The exciton relaxation time

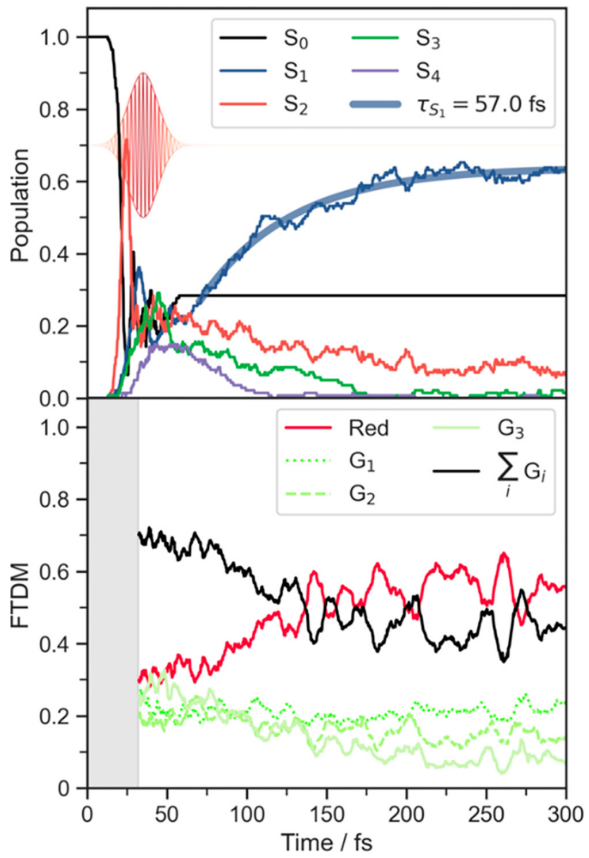

Figure 2.7: (Top) Electronic state populations of an ensemble of 150 trajectories during the field-induced surface-hopping simulation dynamics of **3G-Red**$|^{\mathrm{Et}}$. The bold blue line shows the fit of the S_1 population to a monoexponential fit function. (Bottom) Ensemble averaged fraction of transition density matrix (FTDM) time evolution for the individual fragments (Red: *red* BODIPY, $\mathbf{G}_1$: *green* BODIPY adjacent to *red* one, $\mathbf{G}_2$: middle *green* BODIPY, $\mathbf{G}_3$: terminal *green* BODIPY) and the sum of the *green* subunit (black curve).

constant of 57 fs for **3G-Red**$|^{\mathrm{Et}}$ is in excellent agreement with the lifetime of 58 fs obtained by the TA experiments. Furthermore, the simulations nicely reflect the evolution of lifetimes (with one exception) along the growing homologues: for the EtDM series the lifetime increases going from **1G-Red**$|^{\mathrm{Et}}$ (35 fs), to **2G-Red**$|^{\mathrm{Et}}$ (36 fs), and finally reaching 57 fs for **3G-Red**$|^{\mathrm{Et}}$. In the case of the DM series we similarly observe an increase in relaxation lifetimes starting from **1G-Red** (36 fs) to 2G-Red (43 fs). However, the **3G-Red** oligomer exhibits a shorter lifetime of 33 fs, which is opposite to the trend in the experimental observation. To further investigate and explain these trends, we computed the fluctuations of the monomeric site and excitonic coupling energies between the *red* acceptor and a discrete *green* subunit along the trajectories. To this end, the heterooligomers were cut into two parts and structurally saturated with hydrogens, and the S_1 energies as well as the excitonic couplings were computed with 2 fs steps. In this way, we obtained quasi diabatic matrix elements together with their standard deviations, which allow the comparison

of fluctuations for all heterooligomers (Figure 2.8).

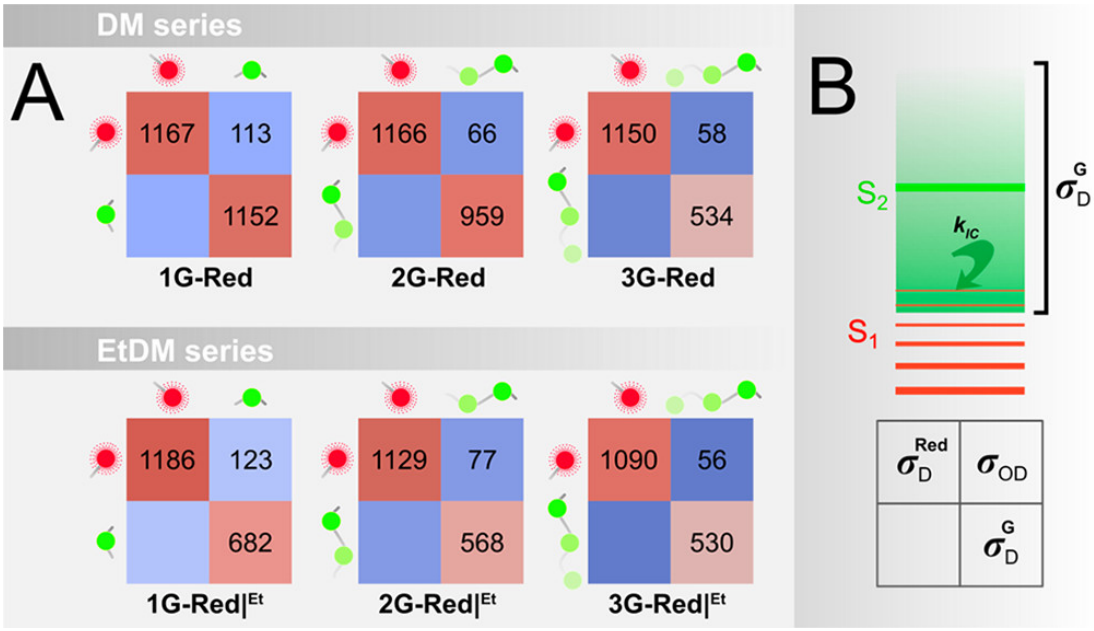

Figure 2.8: (A) Standard deviations (in cm^{-1}) of the quasi diabatic diagonal σ_D and off-diagonal σ_{OD} matrix elements obtained from the light-induced dynamics simulations. (B) Illustrated impact of higher standard deviations on the energy transfer rate k_{IC} and legend for the explanation of the graphic.

The diagonal disorders of the *red* BODIPY (upper left squares) show only a negligible, decreasing trend by going from the dyads to the tetrads within both series. However, in the case of the *green* subunit this trend is clearly more pronounced and the EtDM series shows systematically lower fluctuations in these matrix elements, reflecting the increased stiffness compared to the DM series as a consequence of stabilizing β-ethyl groups. In addition, we observe a clear trend in the off-diagonal disorders, which are also depicted in Figure 2.8A (upper right squares). The fluctuations in the excitonic couplings decrease continuously along the series from dyad to the tetrad, consistently for DM and EtDM species with slightly larger standard deviations in the latter one. In contrast to the outcome of Fermi's golden rule expression the light-induced dynamic simulations are able to reproduce the experimental trend of decreasing energy transfer rates at larger heterooligomers. Figure 2.8B illustrates the relation between the fluctuation of the *green* site energy σ_D^G and the transfer rate, which can be regarded also as an internal conversion (IC) process within the strong coupling limit. Owing to the inherent exponential dependence of IC (energy gap law) rate, negative deviations have a higher impact on the increase of the rate than positive ones, rendering the modulus of the standard deviation itself crucial for the rate of the process. Thus, we conclude that the exciton bandwidth caused by site-energy disorder effects can lead to the increase of the energy transfer rate, which cannot be accounted for by a simple Forster theory approach.

2.3 Conclusion

We submitted two distinct series (dyad, triad, and tetrad) of ethylene-bridged BODIPY heterooligomers, differing in their BODIPY substitution pattern, to a profound study of individual energy transfer and localization processes employing a tandem of femtosecond transient absorption spectroscopy and computational dynamic simulations. The easily accessible molecular frameworks consist of a green subunit of strongly coupled BODIPY monomers (S_2 state, Frenkel limit) and a styryl-equipped red BODIPY acceptor unit as terminal energy sink (S_1 state). Both series (DM: β-unsubstituted, EtDM: β-ethyl group) show a trend of decreasing energy transfer rates at higher homologues, a fs-spectroscopic observation that cannot be understood in the frame of the simple energy transfer theory based on Fermi's golden rule. Mixed quantum-classical dynamic simulations were able to link the induced conformational stability of β-ethyl groups in the EtDM series to standard deviations of diagonal disorder matrix elements. The same underpin an enhanced lifetime of the S_2 state at growing green subunits in both series, providing a theoretical confirmation for the decreasing ultrafast EET rates obtained from transient absorption spectroscopy. Higher energy transfer rates in shorter heterooligomers are thus caused by higher diagonal disorders and a consequently promoted IC mechanism, as governed by the Englman-Jortner's energy gap law.[79] While in the DM case the corresponding relaxation lifetimes gradually increase from 45 fs (dyad) to 89 fs (tetrad), the dyad of the EtDM series exhibits a lifetime of 39 fs, corresponding to one of the fastest EET processes discovered to date. The easily integrable ethylene bridge thus proves to be a highly efficient linker to allow for high coupling strengths between local oscillators without making use of a commonly employed π-conjugational connectivity. We believe that this study will provide new impulses for economic molecular designs that focus on light-harvesting, exciton transfer, and injection processes involved in the development of novel organic optoelectronic devices.

Chapter 3

Ultrafast Energy Transfer Dynamics in a Squaraine Heterotriad

---

A squaraine heterotriad consisting of three different covalently linked squaraine chromophores was synthesized, and its absorption spectra were interpreted in terms of Kasha's exciton coupling theory. Using the exciton couplings derived from model dyads (ca. 700 cm^{-1}) as the input, we were able to predict the exciton state energies of the heterotriad. Transient absorption spectroscopy with femtosecond time resolution showed that excitation of the highest exciton state populates a state mainly localized at one terminal squaraine chromophore, and energy transfer to the lowest exciton state localized at the other terminal squaraine occurs within 30 fs. Field-induced surface hopping dynamics simulations support the assumption of ultrafast energy transfer. Moreover, they show the close relationship between internal conversion and energy transfer in the intermediate to weak coupling regime. The latter is a consequence of excitation localization caused by molecular vibrations.

3.1 Introduction

Tuning the optical properties according to the needs is one of the major tasks when designing chromophores for optoelectronic applications. Choosing an appropriate parent chromophore and attaching suitable substituents is one of the popular ways to achieve this goal. An alternative is to arrange several chromophores in space in a suitable manner to allow for excitonic interactions, which leads to either hypsochromic (H-type) or bathochromic (J-type) shifts of lowest energy absorption bands. A suitable arrangement can be induced either by supramolecular assembly or by covalent linking of chromophores.[65] In most cases, the excitonic ensemble is built up from chemically identical chromophores.[139–143] However, some studies report on heteroaggregates,[144] heterooligomers,[12,145] or heteropolymers[11,146,147] where two different chromophores with different absorption energies are employed. Generally, this leads to smaller shifts of the absorption maxima compared to the monomeric components. The reason is that for a given exciton coupling strength the splitting of, for example, dyad eigenstates δE scales as

$$\delta E = 2\sqrt{\Delta E^2 + J^2} \tag{3.1}$$

where ΔE is half the energy difference of the monomer eigenstates and J is the exciton coupling energy.[23] Thus, the larger ΔE is, the more similar are the dyad eigenstates to those of the monomers. The ratio $J/\Delta E$ may be used to assign the regimes of strong ($\gg 1$), intermediate (≈ 1), and weak ($\ll 1$) exciton coupling. However, besides shifting absorption energies, exciton coupling may also influence the intensity of transitions. Thereby, for J-type aggregates, the lowest exciton eigenstate carries the largest oscillator strength while it is the upper exciton state for an H-type aggregate.[87] Thus, coupling of two different chromophores may change the shape of absorption spectra considerably concerning the relative intensities of exciton states. In this work we investigate the excitonic interactions in a triad **tSQABC** built up from three different squaraine dyes whose absorption energy decreases from **SQA** over **SQB** to **SQC**. We chose squaraine dyes as they possess narrow absorption bands in the red to near-infrared spectral region, which eases the analyses of their ensemble spectra in terms of exciton coupling. Furthermore, squaraine dyes usually show strong fluorescence with high quantum yield which promotes application in biomedicine and optoelectronics.[145,148–162] We will compare the steady-state optical properties with those of the monomers and with those of two heterodyads **SQAB** and **dSQBC** that constitute subunits of the triad. The former dimer was recently investigated and turned out to be in the weakly coupled regime because of the –on time average – relatively high site energy difference ΔE. We will also address the question, what is the consequence for energy transfer processes between the different chromophore units within the triad when either squaraine **SQA** or **SQB** is excited? The latter aspect was investigated by transient absorption spectroscopy with femtosecond time resolution. Applying light-induced nonadiabatic dynamics simulations using the field-induced surface-hopping (FISH) method,[56,163] we modeled the static and dynamic

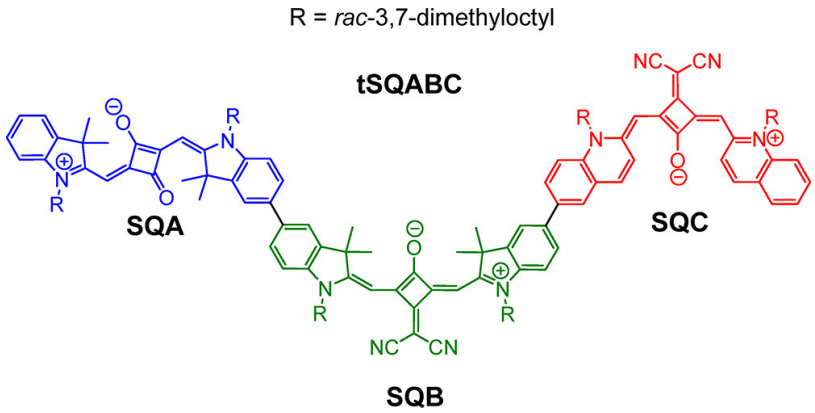

Figure 3.1: Molecular Formula of the Heterotriad **tSQABC** R = rac-3,7-dimethyloctyl

optical properties of the heterotriad to gain more insight into the time evolution of the involved energy transfer processes.

3.2 Results and Discussion

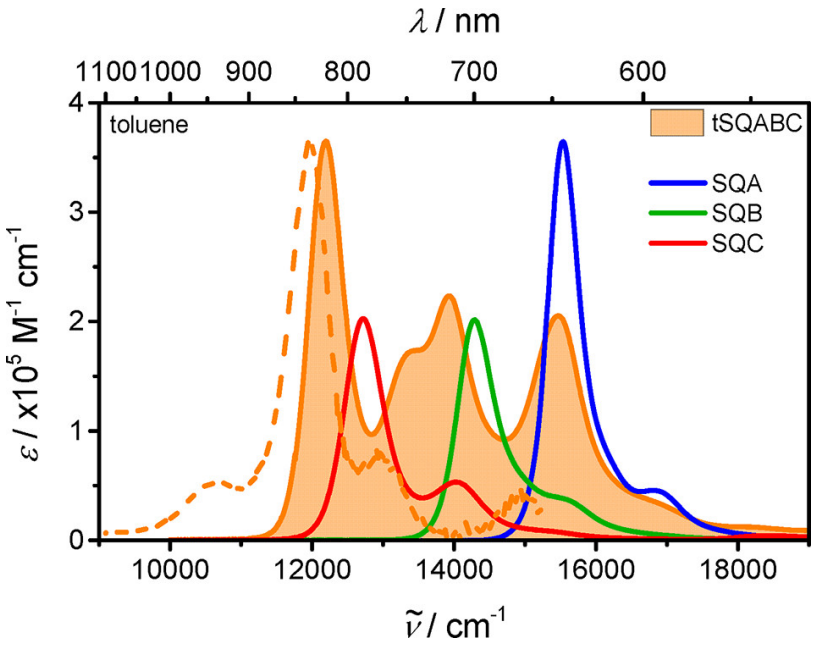

Figure 3.2: Absorption spectra of **SQA**, **SQB**, **SQC** (solid lines), and tSQABC (filled spectrum) and the normalized fluorescence spectrum of **SQABC** (dashed line), excited at 15500 cm^{-1} in toluene.

3.2.1 Steady-State Optical Spectroscopy

The syntheses of the squaraine triad and dyads is described in the Supporting Information of Ref. 7. The absorption spectra of the **tSQABC** triad is displayed in Figure 3.2 together with those of the corresponding monomers. The latter show the typical narrow absorption spectra with a small vibronic peak at the high-energy side. For the triad, we can identify essentially three maxima which, besides a more or less pronounced red-shift, correspond to the absorption maxima of the monomers. Even stronger deviations are found for the extinction coefficients. While **SQA** possesses the highest extinction coefficient and those of **SQB** and **SQC** are almost equal, the lowest energy peak of **SQABC** shows the highest extinction coefficient and those of the higher energy peaks are almost equal. These observations clearly indicate that the three chromophores are electronically coupled in the **tSQABC** triad. We used Kasha's exciton coupling theory[23,87] to analyze this coupling by solving the determinant eq 3.2 for the eigenvalues ε.

$$\begin{vmatrix} E_{\mathrm{A}} - \varepsilon & J_{\mathrm{AB}} & 0 \\ J_{\mathrm{AB}} & E_{\mathrm{B}} - \varepsilon & J_{\mathrm{BC}} \\ 0 & J_{\mathrm{BC}} & E_{\mathrm{C}} - \varepsilon \end{vmatrix} = 0 \tag{3.2}$$

$$\mu_i^2 = \left(c_i^{\mathrm{A}} \mu^{\mathrm{A}} + c_i^{\mathrm{B}} \mu^{\mathrm{B}} + c_i^{\mathrm{C}} \mu^{\mathrm{C}} \right)^2 \tag{3.3}$$

In this determinant E_i are the diabatic eigenstate energies of the isolated monomers i, and J_{ij} are the respective couplings between these states. Here, we neglect interactions between squaraines **SQA** and **SQC** (nearest-neighbor approximation) as well as all vibronic effects.[164]

Table 3.1: Experimental Absorption Maxima and Exciton Coupling Energies of Squaraine Heterodyads and the Heterotriad in Toluene

	$\tilde{\nu}_{\mathrm{abs1}}/\mathrm{cm}^{-1}$	$\tilde{\nu}_{\mathrm{abs2}}/\mathrm{cm}^{-1}$	$\tilde{\nu}_{\mathrm{abs3}}/\mathrm{cm}^{-1}$	J/cm^{-1}
dSQAB	13670	15580	$-^a$	−740
dSQBC	12250	14290	$-^a$	−650
tSQABC	12200	13940	15470	$-^a$

[a] Not determined.

It should be noted that this is one of the simplest possible models, and more elaborate models[26] that account for vibronic effects and are based on the Holstein Hamiltonian[165] were derived by Fulton and Gouterman[166] and Witkowski and Moffitt.[167] As the input for eq 3.2 we used the dyad coupling energies $|J_{\mathrm{AB}}| = 740\ \mathrm{cm}^{-1}$ and $|J_{\mathrm{BC}}| = 650\ \mathrm{cm}^{-1}$ given in Table 3.1 derived from the two dyads **dSQAB** and dSQBC by using eq 3.1. Then, solving eq 3.2 for the eigenvalues of the heterotriad yields $\varepsilon_1 = 12447\ \mathrm{cm}^{-1}, \varepsilon_2 = 14173\ \mathrm{cm}^{-1}$, and $\varepsilon_3 = 15878\ \mathrm{cm}^{-1}$ which, after shifting by

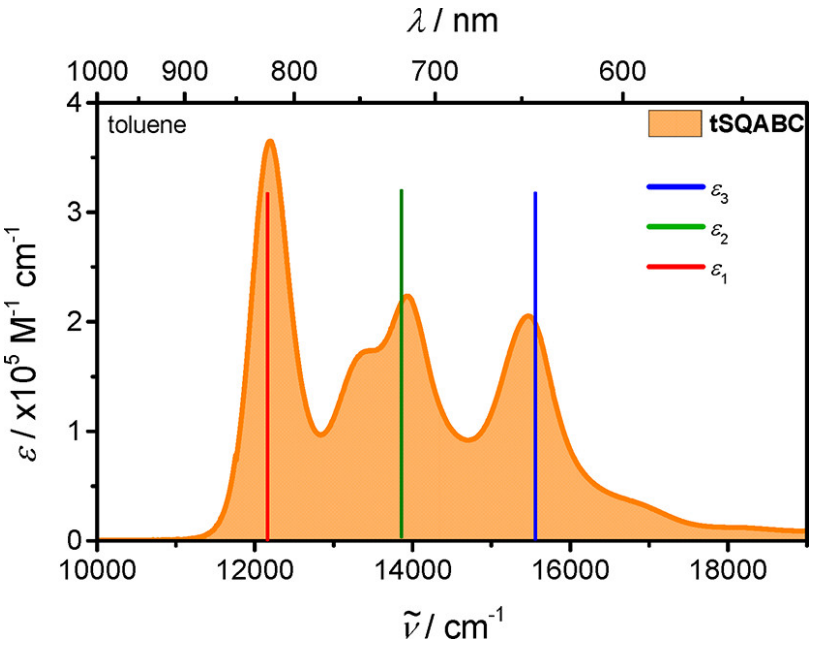

Figure 3.3: Absorption spectrum of **SQABC** in toluene and exciton coupling eigenvalues obtained from eq 3.2 after shifting by -300 cm^{-1} (solid sticks).

-300 cm^{-1}, agree very nicely with the experimental spectrum (see Figure 3.3). The shift is necessary as Kasha's exciton coupling theory provides relative energies only. The good agreement shows the applicability of the simple Kasha model and the nearest neighbor approximation for the heterotriad. Furthermore, it shows that excitations in the heterotriad are at least partially delocalized. As mentioned above, a further hint toward excitonically coupled chromophores is the increase of transition dipole strength for the lowest-energy peak and the decrease of the dipole strength of the highest-energy peak compared to the respective monomers.
In the case of an ideal J-aggregate of three identical chromophores, where the transition dipole moments are in a head-to-tail arrangement, one would expect that all transition strength is almost exclusively collected in the lowest-energy exciton state. This is not the case here for several reasons. First, the dipole strength for the i-th eigenvalue is given by eq 3.3, where μ^{A}, μ^{B}, and μ^{C} are the transition moment vectors of the localized diabatic states of chromophore A, B, and C, and c_i are the respective components of the eigenvectors of eq 3.2. In the case of three different chromophores, these eigenvector components are generally not equal and are not related by any symmetry. Therefore, all states will possess a nonzero transition dipole strength. Second, because of the banana bent shape of **SQB** and **SQC** and because several rotamers around the biaryl axes will exist, there will be no exact head-to-tail arrangement of transition moment vectors, and the upper exciton states gain some dipole strength as well. Nevertheless, because the lowest energy absorption possesses the highest dipole strength, one can assume that the couplings J are negative. The monomers **SQA** and **SQB** show strong fluorescence with high quantum yields (0.62 and 0.75, respec-

Table 3.2: Absorption Maxima, Extinction Coefficients, Dipole Strength, Fluorescence Maxima, Fluorescence Quantum Yields, Fluorescence Lifetimes (Amplitudes in Parentheses), and Average Values of Fluorescence Lifetimes of Squaraine Monomers, Dyads, and the Triads in Toluene

	$\tilde{\nu}_{\mathrm{abs}}/\mathrm{cm}^{-1}$	$\epsilon_{\max}/M^{-1}\ \mathrm{cm}^{-1}$	$\mu_{\mathrm{eg}}^2/\mathrm{D}^2$	$\tilde{\nu}_{\mathrm{em}}/\mathrm{cm}^{-1}$	Φ_{fl}	$\tau_{\mathrm{fl}}^b/\mathrm{ns}$	$\bar{\tau}_{\mathrm{fl}}^c/\mathrm{ns}$
SQA[d]	15500	3.65×10^5	127	15300	0.62	0.07 (0.03) 0.20 (0.10) 1.72 (0.87)	1.52
SQB[d]	14300	2.02×10^5	92.7	14000	0.75	3.45	3.45
SQC	12700	2.03×10^5	111	12500	–[a]	0.04	0.04
dSQAB	13700	3.13×10^5	248	13400	0.69	1.80 (0.51) 2.41 (0.49)	2.14
dSQBC	12300	3.22×105	237	12100	–[a]	0.08	0.08
tSQABC	12200	3.65×10^5	398	12000	–[a]	–[a]	–[a]

[a] Not determined. [b] (Multi)exponential fit of fluorescence decay measured by TSCPC; excitation at 15200 cm^{-1}(656 nm). [c] $\bar{\tau}_{\mathrm{fl}} = a_1\tau_1 + a_2\tau_2$; see ref[168]. [d] see ref[155].

tively) and little Stokes shift upon excitation. Much to our surprise **SQC** shows only weak fluorescence — too weak to determine the quantum yield accurately (for spectra, see Figure S1 in Ref. 7). This is due to fast nonradiative decay as proved by the very short lifetime (0.04 ns) compared to those of **SQA** (1.52 ns) and **SQB** (3.45 ns) (see Table 3.2). We suspect that in **SQC** a strong out-of-plane motion of the naphthyl rings leads to a conical intersection with the ground-state potential, thereby enhancing nonradiative decay.[169] The fluorescence of the heterodyads is a mirror image of their lowest-energy absorption peak (see Figure S2 in Ref. 7). The heterodyad **dSQAB** also possesses a high fluorescence quantum yield (0.69) and a long lifetime (2.14 ns), but **dSQBC** shows negligible fluorescence with a very short lifetime (0.08 ns). Also, the triad **tSQABC** displays only very little fluorescence; thus, neither quantum yield nor lifetime could be determined. When excited at the highest-energy absorption peak at 15500 cm^{-1}, the fluorescence spectrum is a mirror image of the lowest-energy absorption peak, but we also see smaller emission peaks at 13000 and 15000 cm^{-1}, which correspond to the two higher energy absorption peaks (see Figure 3.2). Thus, although the three squaraines are coupled by a high exciton coupling J, which leads to the exciton manifold observed in the absorption spectrum, fluorescence is emitted not only from the lowest exciton state but also from the higher exciton states.

3.2.2 Femtosecond-Time-Resolved Optical Spectroscopy

The aforementioned observations prompted us to investigate the heterotriad by transient absorption (TA) spectroscopy with femtosecond time resolution. Here, we excited the triad in toluene solution at three different wavenumbers matching the three

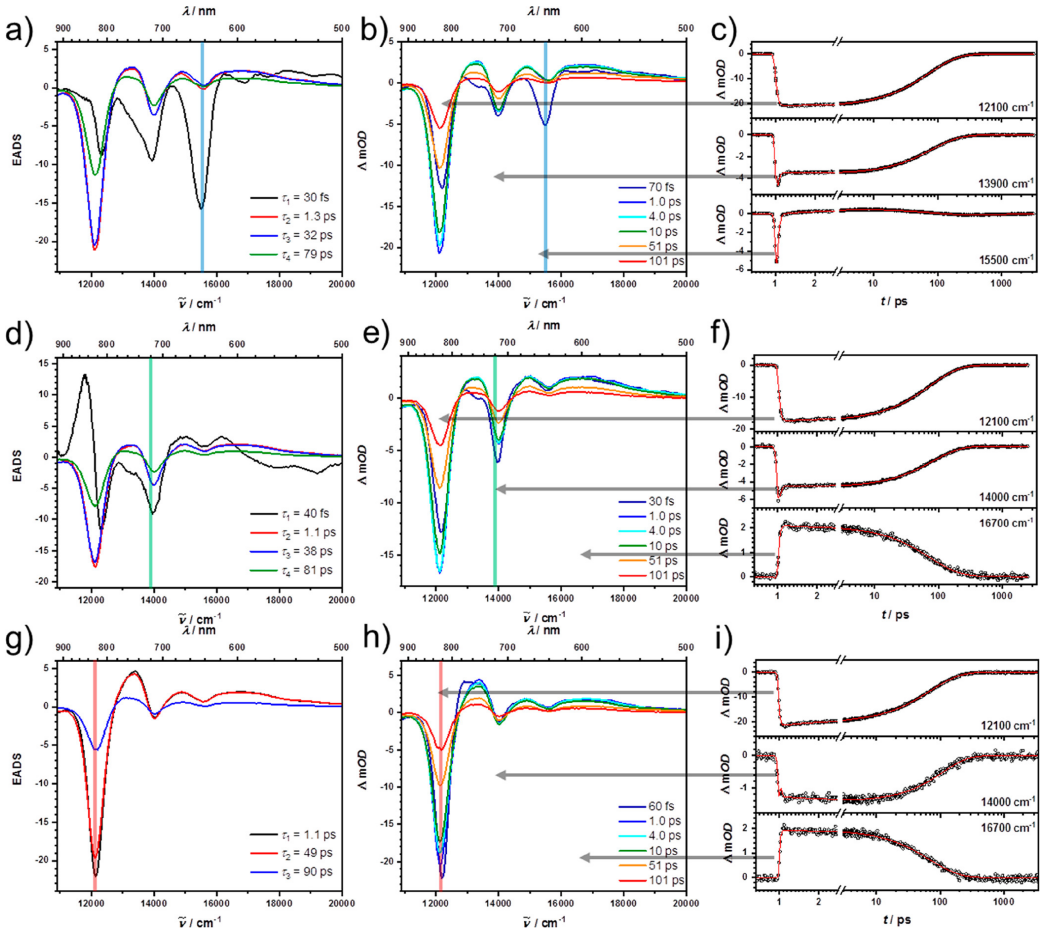

Figure 3.4: Transient absorption spectra of **tSQABC** in toluene. First row: excitation at 15600 cm^{-1}; second row: excitation at 13900 cm^{-1}; third row: excitation at 12200 cm^{-1}. The colored vertical bars indicate the excitation wavenumber. First column: EADS derived from a global deconvolution; second column: TA spectra at selected delay times; third column: time traces and fits at selected wavenumbers which are indicated by gray horizontal arrows.

main absorption peaks in the steady-state absorption spectrum. Probing was done with white light in the range $10900 - 20000$ cm^{-1}($500 - 920$ nm) under magic angle conditions.

In Figure 3.4 in the middle panels, the TA spectra of **tSQABC** for three different excitation wavenumbers are displayed, while on the right-hand side, time traces referring to the maximum bleaching signals together with a global multiexponential fit [136] are given. On the left-hand side, the evolution associated difference spectra (EADS) are shown, which result from a global fit of the transient spectral data assuming a consecutive multiexponential model. In general, the TA spectra consist of a (negative) ground-state bleaching (GSB) signal which results from depopulation of the ground-state signals, of (negative) stimulated emission (SE) signals, and of (positive) excited-state absorption (ESA) signals.

We will first discuss the TA spectra for excitation of the triad at the lowest energy absorption peak at 12200 cm^{-1}. The TA spectra in Figure 3.4h show a very prominent GSB at that energy and much smaller GSB contributions at ca. 14000 cm^{-1} and a weak dip at 15600 cm^{-1}. Positive peaks at ca. 14500, 15000, and 17000 cm^{-1} indicate that the GSB is overlaid by a broader ESA signal. SE is not visible as a separate signal, but may be suspected to be at the low-energy flank of the GSB at 12000 cm^{-1}. The global deconvolution (Figure 3.4g) results in three spectrally very similar components with lifetimes of ca. 1, 50, and 90 ps. The latter two are rather short because of fast ground-state recovery from the inhomogeneous ensemble, which is the reason for the obviously rather low fluorescence quantum yield. The components between 1 and several 10 ps may also be attributed to solvent relaxation and slow molecular relaxation as often observed in the context of squaraine excited-state relaxation.[106]

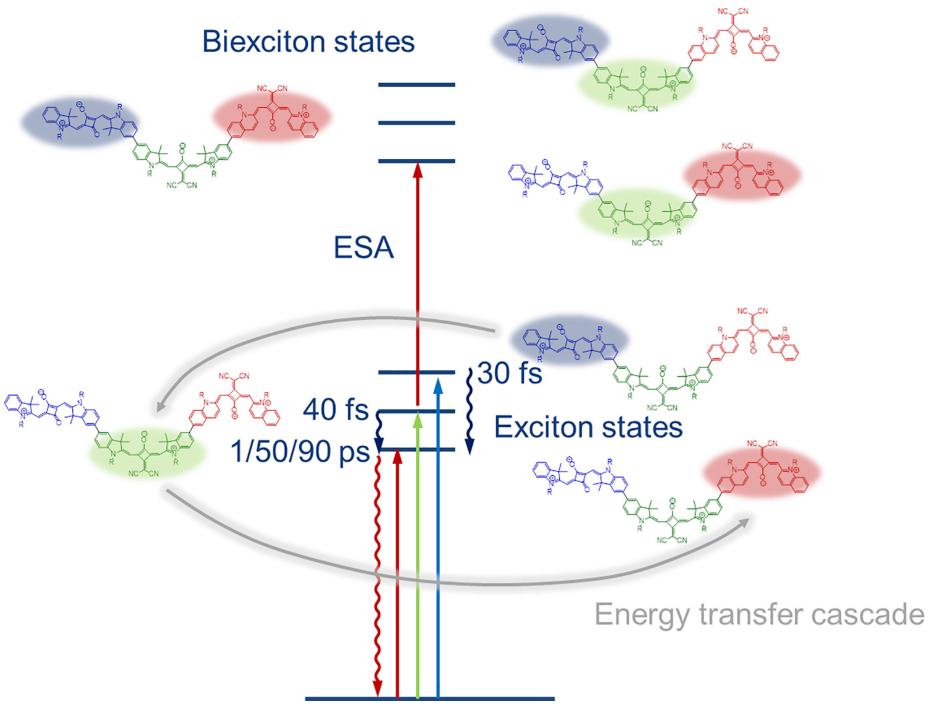

Figure 3.5: Schematic energy state diagram of exciton and two-exciton states in the diabatic basis. The inserted relaxation times refer to the EADS of the femtosecond transient absorption experiments.

When exciting the triad at the energy of the highest exciton state at 15600 cm^{-1}, we observed a prominent GSB at ca. 12200 cm^{-1}. But compared to the spectrum in Figure 3.4h a stronger GSB occurs at 14500 cm^{-1} and particularly at 15500 cm^{-1} The latter shows a very fast decay which can also nicely be seen in the time traces at 15500 cm^{-1} (Figure 3.4c). Besides three EADS with lifetimes almost identical with those of the excitation experiment at 12000 cm^{-1}, the global deconvolution yields an additional short-lived component with $\tau = 30$ fs (Figure 3.4a). This EADS possesses

three negative peaks; two of them coincide with those of the absorption spectrum at 15500 and 14000 cm^{-1}. The third one at 12300 cm^{-1} is shifted to slightly higher energies. This suggests that it is superimposed by a positive ESA at the low-energy side. Such an ESA is expected for the excitation from the highest exciton state to a two-exciton state.[12,106,170] However, despite this discrepancy, the intensities of the GSB spectrum do not match that of the absorption spectrum at all. In the EADS with $\tau = 30$ fs, the negative peak at 15500 cm^{-1} is by far the most intense. This points toward a localization of excitation in the **SQA** chromophore. Such a localization has been observed by us in squaraine dyads before and is caused by a time fluctuation of transition density between the different chromophores within a given dyad.[12,106] In the heterotriad, on average, the transition density is more often localized on **SQA** in the highest exciton state which causes the more intense GSB at this wavenumber. This localization effect can also be seen by semiempirical CIS calculations presented below.
Excitation of the middle exciton state of the triad at 13900 cm^{-1} yielded TA spectra similar to the ones before, but the fast decaying peak at 15500 cm^{-1} is missing. Global deconvolution again gives three components with almost identical lifetimes as for the two experiments before and a fourth additional component with $\tau = 40$ fs. This EADS shows a negative GSB at 14000 and 12300 cm^{-1} and an ESA at 11700 cm^{-1}. The latter is probably caused by excitation into a two-exciton state (see Figure 3.5). The negative peak at 14000 cm^{-1} is again interpreted as being caused by excitation localization, in that case in the **SQB** chromophore moiety. Thus, we interpret the two short lifetimes in the second and the third excitation experiment as being caused by fast interband relaxation processes. A schematic energy state diagram which collects the measured data is given in Figure 3.5.

3.2.3 Computational Results on tSQABC

In order to substantiate the experimental results and to get a closer insight into the excitation localization and the associated dynamic processes within the triad, we performed quantum chemical calculations.
For the simulation of the thermally broadened ensemble absorption spectrum of **tQABC**, we sampled the ground-state canonical harmonic Wigner distribution at $T = 300$ K using a semiempirically parametrized PM3 Hamiltonian. To this end, 140 geometries were generated. The electronic absorption spectrum for each individual structure has been computed at the PM3-CIS level of theory (see Figure 3.6a). The stick spectra have been convoluted by Lorentzians using a width of 200 cm^{-1} to generate the continuous curve (see Figure 3.6a). It should be noted that absorption spectra based on Wigner distributions describe the spectral broadening due to all vibrational degrees of freedom in a semiclassical way. Therefore, transitions between individual vibrational quantum states are not explicitly accounted for, but the envelope of the energy transfer cascade spectrum is correctly described. The first band is located at 11900 cm^{-1} and is in good agreement with the experimental absorption

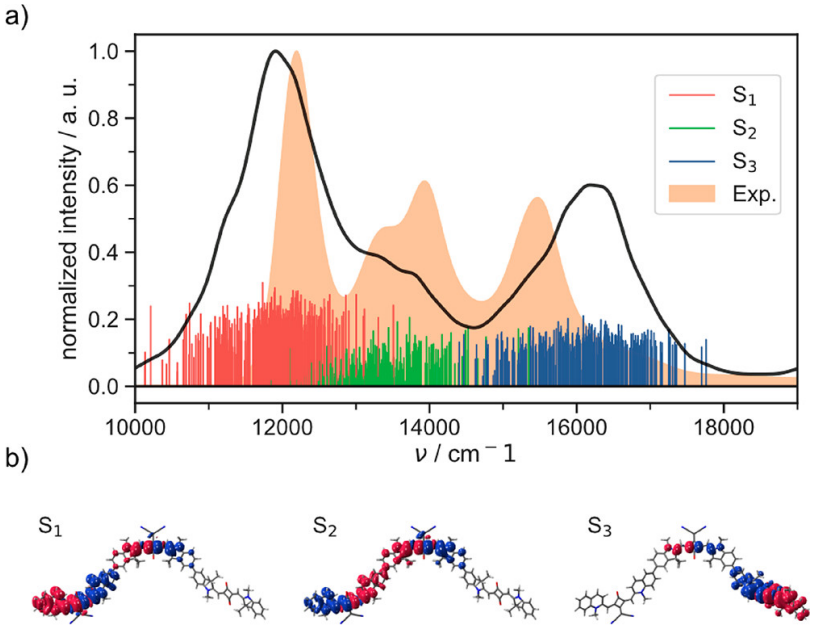

Figure 3.6: (a) Ensemble absorption spectrum of **tSQABC** simulated at the PM3-CIS level of theory using a Wigner ensemble of nuclear geometries generated at $T = 300$ K (black curve). The spectrum has been generated by convoluting the individual transitions of each geometry (red, green, and blue sticks) with a Lorentzian function using a width of 200 cm^{-1}. The experimental absorption spectrum in toluene is shown as an orange curve in the background. (b) Transition densities between the ground state and the first three excited states.

band at 12200 cm^{-1}. The corresponding S_0−S_1 transition is localized on the **SQC** fragment and to some extent on the **SQB** unit, as can be seen from the transition densities (TDs) in Figure 3.6b. The second band, caused by the S_0−S_2 transition and localized almost equally on the **SQB** and **SQC** fragment, starts around 13000 cm^{-1}. In comparison to the experimental absorption spectrum, the position of the **SQB** localized transition is shifted by about 1000 cm^{-1} due to the inadequate description of the monomer absorption at the PM3-CIS level which also leads to the weaker computed intensity of this transition. This has been already observed in our previous study of squaraine dyads.[12] The third absorption band located at 16150 cm^{-1} is in good agreement with the experimental absorption band at around 15500 cm^{-1}. At the top of Figure 3.6b the transition densities at the ground-state geometry between the S_0 and the corresponding excited state are shown. Despite the relatively high excitonic coupling of several hundred wavenumbers, a quite strong localization of the third excited states on the **SQA** monomer can be seen.
To reveal the mechanism of exciton transfer after excitation of the highest exciton state, we have performed field-induced surface hopping dynamics simulations. The central wavelength of the applied laser pulse was set to 16130 cm^{-1} to match the maximum of the absorption band of the S_3 state. The relative populations of the electronic states are shown in Figure 3.7. The interaction with the laser field leads to

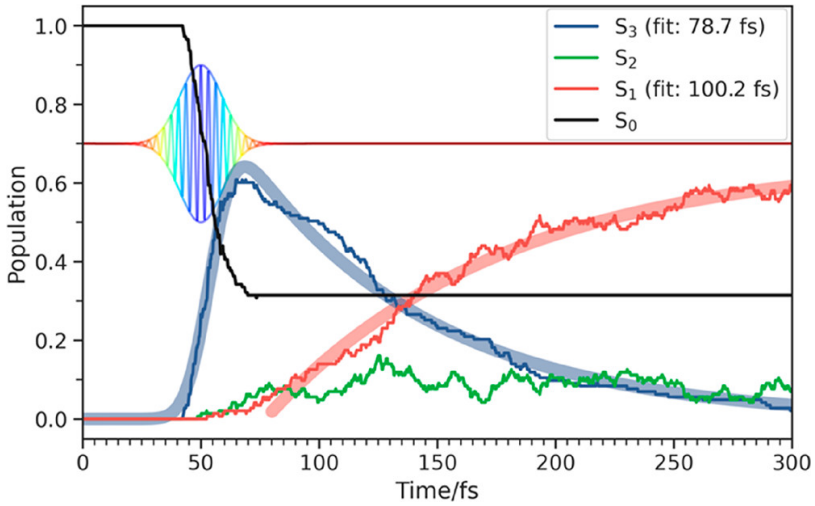

Figure 3.7: Time-dependent electronic state populations for an ensemble of 140 trajectories during the field-induced surface hopping simulations of **tSQABC**. The bold blue line shows the fit of the S_3 populations to the following fit function: $G(t) = A\exp\left[-\left(t-t_0\right)/\tau\right]\exp\left(b^2/4\sigma^2\right)\left[1+\mathrm{erf}\left(\left(t-t_0-b^2\right)/2\sigma\right)/b\right]$. The red bold line shows the fit of the S_1 population to the fit function $F(t) = -A\exp\left(-\left(t-t_0\right)/\tau\right)+B$. In both functions τ is the time constant for the population decay/rise. The values of the time constants are shown in the inset, and the time evolution of the laser pulse is shown in the background.

strong population transfer from the ground state (S_0) to the third exciton state (S_3). After 70 fs a large part of the ensemble is excited, and ultrafast relaxation to the lower two excited states follows. The time constant for this decay is about 79 fs. However, the second exciton state (S_2) is only transiently populated, and there is a very fast transition to the first one (S_1). On a time scale of about 100 fs the whole population is transferred into the S_1. But it should be mentioned that the time constants from the simulation are probably too high since the energetic separation of S_2 and S_3 in the dynamics simulations is overestimated by about 1000 cm^{-1}($\sim$ 0.12 eV). This slows down the population transfer from S_3 to S_2 significantly because the rate of internal conversion is strongly dependent on the energy gap. The fact that the decay time of S_3 is shorter than the rise of S_1 shows that S_2 is a transient state. The time dependent populations cannot be fitted by a simple $S_3 \rightarrow S_2 \rightarrow S_1$ kinetic scheme. A closer look at the probability distributions of transfer events (see Figures S4 and S5 in Ref. 7) shows that besides direct $S_3 \rightarrow S_1$ steps, there are also frequent back processes from $S_2 \leftarrow S_1$.

To analyze the exciton dynamics, we have monitored the fragment transition densities on the monomeric units along the trajectories by calculating the fraction of transition density matrix (FTDM) (as discussed in the computational details of Ref. 7). The resulting functions are presented in Figure 3.8, showing the distribution of the excitation on the given monomer at ensemble level. It can be seen that, initially, the excitation is almost completely localized on the **SQA**. Because of the ultrafast

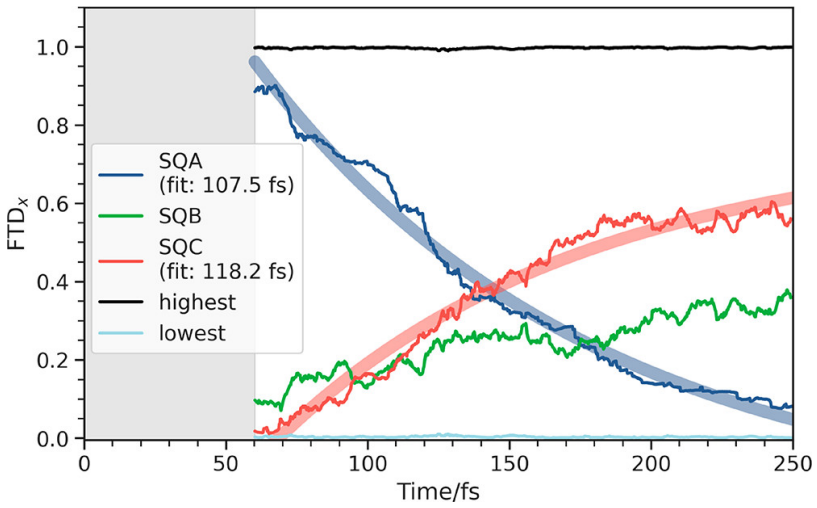

Figure 3.8: Ensemble-averaged FTDM on the three squaraine monomers (**SQA**, **SQB**, and **SQC**) along the light-induced dynamics simulations of **tSQABC**. The bold blue and red lines show the fit of the **SQA** and **SQC** FTDM following the fit function $F(t) = -A \exp\left[-\left(t - t_0\right)/\tau\right] + B$. In both functions τ is the time constant for the population decay/rise. The values of the time constants are shown in the inset. The first 60 fs of the curves are not shown because the excitation by the laser pulse is completed at this time, and the trajectories are starting in the electronic ground state.

internal conversion from the S_3 state to the lower excited states, an exciton transfer from **SQA** to the **SQB** and **SQC** unit takes place within 100 fs. Over the whole simulation time, the localization of the excitation on both the **SQB** and **SQC** increases further. So that finally a ratio of about 60 % : 40 % (**SQC** : **SQB**) is achieved. This corresponds to the stationary TDM distribution of the S_1 as shown in Figure 3.6b.

3.3 Conclusions

In conclusion, the excellent agreement of exciton states calculated by using Kasha's exciton coupling theory with those of the experimentally observed absorption spectra of **tSQABC** triad demonstrates that using exciton coupling values extracted from subunits, in our case, dyads, is a useful way to predict the eigenstates of a larger system, here a heterotriad.
Transient absorption spectroscopy experiments with femtosecond time resolution show that excitation of the heterotriad at the highest energy exciton state S_3 is followed by internal conversion to the middle (S_2) and the lowest exciton state (S_1). The latter is populated with a time constant of 30 fs. Similarly, when the middle exciton state is directly excited, IC populates S_1 within 40 fs. The IC rate for the energy transfer between **SQA** and **SQB** in a similar dyad where the two squaraines are bridged by a phenylene spacer was recently determined to be $(30\ \text{fs})^{-1}$.[171,172] The IC rate in **dSQAB** was also recently estimated to be $(54\ \text{fs})^{-1}$ and $(30\ \text{fs})^{-1}$, respec-

tively.[12,172] Both agree nicely with the findings in the heterotriad. The intensities of ground-state bleaching of the three exciton states can be used to estimate the relative population in time (for a comparison of the EADS and the negative absorption spectrum, see Figure S3 in Ref. 7). This qualitative picture is corroborated by quantum chemical calculations. Here, we showed by calculating the transition densities that while S_3 is largely localized at the **SQA** moiety, S_2 is delocalized between **SQB** and **SQC**, but S_1 again is mainly localized at **SQC**. Fitting of the electronic state populations gave IC times of 70 fs ($S_3 \rightarrow S_2$) and 100 fs ($S_2 \rightarrow S_1$), which are somewhat longer than the experimental values but still in rather good agreement considering that the S_2 state is computed to be at too low energy. Thus, despite the sizable exciton coupling between the three chromophore units (J ca. -700 cm^{-1}), the IC processes can be conceived as an ultrafast energy transfer cascade in the intermediate to weak coupling regime[36,70,95] in this heterotriad because the heterogeneous nature of the triad leads — on the time average — to (partial) localization of excited states on the respective chromophore moiety.

Chapter 4

Dynamic exciton localisation in a pyrene-BODIPY-pyrene dye conjugate

---

The photophysics of a molecular triad consisting of a BODIPY dye and two pyrene chromophores attached in 2-position are investigated by steady state and fs time-resolved transient absorption spectroscopy as well as by field-induced surface hopping (FISH) simulations. While steady state measurements indicate moderate chromophore interactions within the triad, the time-resolved measurements show upon pyrene excitation a delocalised excited state which localises onto the BODIPY chromophore with a time constant of 0.12 ps. This could either be interpreted as an internal conversion process within the excitonically coupled chromophores or as an energy transfer from the pyrenes to the BODIPY dye. The analysis of FISH-trajectories reveals an oscillatory behaviour where the excitation hops between the pyrene units and the BODIPY dye several times until finally they become localised on the BODIPY chromophore within 100 fs. This is accompanied by an ultrafast nonradiative relaxation within the excitonic manifold mediated by the nonadiabatic coupling. Averaging over an ensemble of trajectories allowed us to simulate the electronic state population dynamics and determine the time constants for the nonradiative transitions that mediate the ultrafast energy transfer and exciton localisation on BODIPY.

4.1 Introduction

Whether an ensemble of two or more different chromophores is excited by light of certain energy as a whole, or whether only one of these chromophores is excited and energy transfer to other chromophores occurs as a possible follow-up process is one of the most fundamental issues in photophysics of complex chromophores. If the latter scenario applies, the rate of excitation energy transfer processes may span a range from several ns to several tens of fs. On the slower time scale an incoherent energy transfer from an excited energy donor to a farther apart situated energy acceptor often described by Förster's resonance energy transfer (FRET) is operative. Here, donor and acceptor are so weakly coupled that they retain the spectroscopic characteristics of the isolated components, but other issues such as orientation of transition moments and spectral overlap of donor fluorescence with acceptor absorption are important parameters governing the rate of the process.[35,65,173–178] On the other extreme, two or more chromophores may be coupled so strongly that the eigenstates of the newly formed super-chromophore deviate dramatically from those of its constituents. Often, these new eigenstates can be constructed using exciton coupling theory and energy transfer between the constituents is coherent until dephasing and relaxation take place.[21,23,88,164,179–181] The latter can be viewed as an internal conversion process. However, the intermediate coupling regime is also often found and has attracted much attention in recent years.[95,182] Quite recently we addressed the exciton dynamics in a series of covalently linked squaraine dimers spanning the range from weak to intermediate to the strong coupling regime.[12] In another work we described the optical properties of some dye conjugates consisting of *trans*-indolenine squaraine and BODIPY dyes linked by alkyne spacers.[145] Those dye conjugates are in the strong coupling regime where the exciton coupling energy exceeds 1000 cm^{-1}. In this paper, we concentrate on triad systems where a BODIPY chromophore is combined with two pyrene molecules attached *via* an alkyne spacer to each end of the chromophore. In principle, in this case the pyrene may act as the energy donor and the BODIPY dye as the acceptor. Here the eigenstates of the unperturbed chromophore constituents are energetically much farther apart, as in the case of the BODIPY-squaraine conjugates mentioned above. Pyrene was chosen as the formal energy donor as it possesses several special electronic properties making it an attractive chromophore for energy transfer purposes. Pyrene has a high molar extinction coefficient in the UV region and the absorption spectrum is dominated by the transition to the S_2 state (polarised along the long molecular axis (x), often called L_a band) because the S_1 state (y-polarised, L_b band) is almost forbidden.[183,184] Because internal conversion from S_2 to S_1 is ultrafast (75−85 fs),[185,186] fluorescence is emitted from the S_1 state, leading to an exceptionally high apparent Stokes shift. Due to the low oscillator strength, the S_1 lifetime is rather long (several hundred nanoseconds) which makes pyrene useful for non-radiant energy transfer.[185,187] Keeping these properties in mind it is not surprising that pyrene has been used as a chromophore in numerous studies for optical applications.[188] However, the above-mentioned symmetry proper-

ties of pyrene excited states may only have an influence on photophysical processes if pyrene is attached to other energy acceptors *via* its 2− or 7−position and the (local) symmetry is preserved. Binding pyrene at its 2− or 7−position also leaves the typical pyrene properties almost undisturbed because both HOMO and LUMO possess a nodal plane along the long molecular axis going through the 2− and 7−position. However, if pyrene is substituted at the typically employed 1-position, the molecular symmetry is distorted. Even though the substitution of pyrene in 2- and 7-position has been facilitated by using Ir-catalysed reactions by Marder *et al.* a decade ago, only a few studies that use this substitution pattern are known to the best of our knowledge.[189,190] To expand the photophysical studies of the 2, 7−substituted pyrene chromophores we have synthesised the dye conjugate $\mathbf{Py_2B}$ (see Fig. 4.1) to investigate the influence of the pyrene excited states on possible excitonic interactions with — or energy transfer to the BODIPY[191] chromophore. BODIPY[192,193] dyes usually possess C_{2v} molecular symmetry (for molecular structure see Fig. 4.1) and display a high and rather narrow absorption band, distinctly red-shifted from pyrene, as well as high to medium fluorescence quantum yields. The lowest energy band is polarised perpendicular to the C_2 axis, that is, along the long molecular axis (x). For S_2 and S_3 the situation is less clear as they overlap strongly. One of those is polarised parallel to S_1, the other perpendicular.[193] Especially the BODIPY chromophore is an ideal building block in energy transfer arrays from a synthetic as well as photophysical point of view. For this reason, it has been extensively used in energy transfer research because it can easily be substituted at various positions; it has a high absorption coefficient in the visible as well as a high fluorescence quantum yield, and it shows a very low tendency to form triplet excited states.[194,195] Several of the energy transfer studies with BODIPY as the energy acceptor also include pyrene as the donor, which, however, was exclusively linked at the 1−position.[112,194–207] The most widely used substitution pattern for connecting pyrene to BODIPY is the substitution at the boron centre.[194,196,197,201,203,204,208] Harriman *et al.* reported two simple triads, one consisting of a BODIPY dye with two pyrene chromophores connected to the BODIPY boron atom *via* an alkyne bridge, and the other one being a mixed triad with pyrene and perylene as energy donors. Energy transfer has also been investigated by Ziessel *et al.*[200] for species where pyrene is attached either directly or *via* bridges to the BODIPY at the methine carbon atom between the two pyrrole rings. By comparison of excitation and absorption spectra the authors estimated an effective energy transfer from pyrene to BODIPY in excess of 90 % with a calculated energy transfer rate (by Förster theory) of $(1.5\ \text{ps})^{-1}$ when the pyrene is directly attached to the BODIPY, and $(27\ \text{ps})^{-1}$ when it is separated by an ethynylphenyl spacer. Vauthey *et al.* quite recently reported on a pyrene-BODIPY dyad in which the pyrene is attached at its 1−position *via* a phenylene spacer to the *meso*-position of the BODIPY dye. Here, excitation into the pyrene initiates energy transfer with $\tau = 0.4$ ps to the BODIPY chromophore followed by internal conversion (IC) with $\tau < 0.1$ ps.[207] No example of a dye conjugate where a pyrene is linked to the pyrrole units of a BODIPY chromophore is known to us. However, Burgess *et al.*[209] investi-

gated the energy transfer in dyads consisting of BODIPY and anthracene with diverse substitution positions. They found efficient energy transfer in all compounds, but the energy transfer rate was fastest when the anthracene was attached at the 2−position of the BODIPY. To shed light onto the dynamic light-induced processes in the $\mathbf{Py_2B}$ dye conjugate, we perform here transient absorption (TA) measurements with fs time resolution to follow the ultrafast processes expected after excitation into the pyrene S_2 state. These experimental studies are supported by theoretical simulations of the light-induced nonadiabatic dynamics which have been performed in the frame of the field-induced surface hopping (FISH) method.

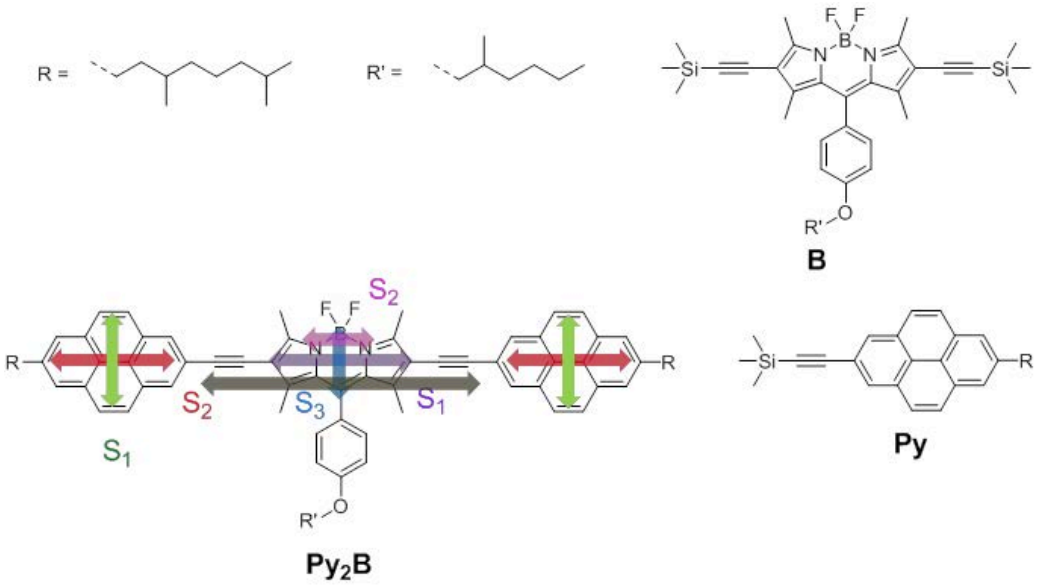

Figure 4.1: Symmetrical pyrene–BODIPY–pyrene conjugate and its parent compounds. The inserted arrows mark the estimated chromophore-localised transition moment direction.

4.2 Results and Discussion

The $\mathbf{Py_2B}$ triad was synthesised by coupling the appropriate monomers *via Sonogashira* reactions. For detailed information see supporting information of Ref. 7.

4.2.1 Steady state UV-vis absorption and fluorescence spectra

The triad absorption spectra were measured in dichloromethane (DCM) at room temperature and compared with those of its parent compounds $\mathbf{B}$[47] and the pyrene derivative $\mathbf{Py}$ (see Fig. 4.2).
The absorption spectrum of $\mathbf{Py_2B}$ covers a broad wavenumber range with one intense band originating from the BODIPY $S_1 \leftarrow S_0$ excitation around 17200 cm^{-1}. This band is clearly more diffuse (fwhm = 1790 cm^{-1}) and also redshifted by 900 cm^{-1}

Table 4.1: Steady-state optical spectroscopic properties of the pyrene-BODIPY-pyrene triad and the corresponding parent compounds in dichloromethane at r.t.

	$\tilde{\nu}_{abs}/cm^{-1}$	$\epsilon/M^{-1}cm^{-1}$	$fwhm_{abs}/cm^{-1}$	μ^2_{abs} /D^2	ν_{fl}	$fwhm_{fl}/cm^{-1}$	μ^2_{fl} /D^2	ϕ_{fl}	$\tilde{\nu_{ex}}/cm^{-1}$
Py	29400	33200	–	0.98	25180	–	26.2	0.10	–
B	18100	83200	1080	48.4	17600	1030	44.1	0.84	–
Py$_2$B	17200	69600	1790	58.7	16300	1350	79.3	0.72	18900

than the one of the reference compound **B** (fwhm = 1080 cm^{-1}). A weaker and broader band in the spectrum of **Py$_2$B** between 22000-27000 cm^{-1} stems from the overlapping BODIPY $S_2 \leftarrow S_0$ and $S_3 \leftarrow S_0$ excitation.[193] The low anisotropy in the fluorescence excitation anisotropy measurements in poly-THF (see Supporting Information of Ref. 11) indicates that the S_2 state is polarised perpendicular to the S_1 state, but the S_3 state is again polarised parallel to the S_1 state. At the blue edge of the spectrum, the typical vibrational progression associated with the pyrene $S_2 \leftarrow S_0$ absorption (see Fig. 4.2) is visible. The two BODIPY bands in **Py$_2$B** are shifted to lower energy compared to the parent **B** chromophore. In contrast, the peaks of pyrene in **Py$_2$B** remain at the same spectral position, but are distinctly more diffuse, and their intensities deviate from the expected doubled intensity of **Py**. This indicates that there is an additional band between 29000-33000 cm^{-1}, which is caused by the interaction of the BODIPY dye and pyrene and which overlaps with the pyrene absorption peaks. The high anisotropy (ca. 0.33) in the fluorescence excitation anisotropy (see SI of Ref. 11) shows that the pyrene S_2 band and the overlapping band possess the same polarisation direction as that of the BODIPY $S_1 \rightarrow S_0$ band, that is, polarisation along the long molecular axis (x).

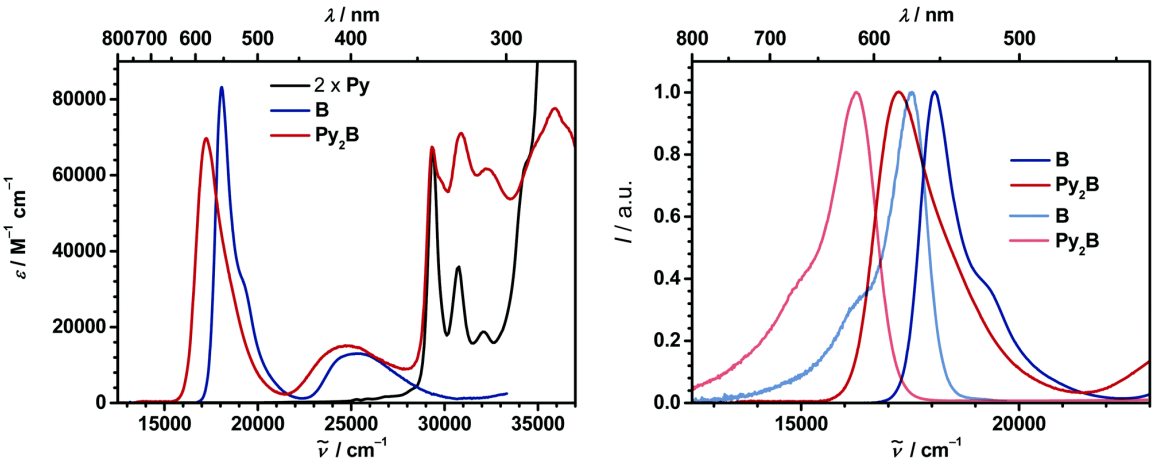

Figure 4.2: (a) Absorption spectra and (b) normalised absorption and fluorescence spectra of **Py$_2$B**, **B** and **Py** in dichloromethane at r.t. For the emission spectra, the excitation of **Py$_2$B** was at 29400 cm^{-1}.

In the triad **Py$_2$B** the shift and fwhm of the lowest energy BODIPY dye band

indicate moderate interaction with the pyrene π–system in the ground and in the lowest excited state, which therefore appears to be largely localised at the BODIPY chromophore. This conclusion is drawn from the fact that the absorption features (band energies and band shapes) resemble those of the parent chromophores. On the other hand, exciton coupling theory predicts that even a strong coupling would lead to vanishing shifts of transitions in the coupled super-chromophore if the eigenstates of the monomer chromophores are energetically very far apart; that is, small shifts are no indication for the absence of electronic couplings.[145] The squared transition moments of the lowest energy absorption band in $\mathbf{Py_2B}$ as determined by eq. 4.1 is only about 21 % higher than that of the isolated parent dye **B**, which also indicates that the original electronic character of this transition is retained in the ground state and Franck–Condon state in the triad (see Table 4.1).

$$\mu_{\mathrm{abs}}^2 = \frac{3hc\varepsilon_0 \ln 10}{2000\pi^2 N_{\mathrm{AV}}} \frac{9n}{(n^2+2)^2} \int \frac{\varepsilon}{\tilde{\nu}} \mathrm{d}\tilde{\nu} \tag{4.1}$$

Direct excitation of a $\mathbf{Py_2B}$ solution in DCM into the pyrene $S_2 \leftarrow S_0$ absorption band at 29400 cm^{-1} results in strong BODIPY type fluorescence at 16300 cm^{-1} (see Fig. 4.2), which has a Stokes shift of 900 cm^{-1}. This BODIPY emission of $\mathbf{Py_2B}$ has a more pronounced structure with a smaller fwhm (1350 cm^{-1}) whereas the absorption spectrum is distinctly more diffuse (fwhm = 1790 cm^{-1}). This hints towards a more flexible ground state geometry with a flat hypersurface (possibly rotation around the CC triple bonds) than in the excited state where all components of the triad are coplanar.[210] The fluorescence quantum yield of $\mathbf{Py_2B}$ ($\Phi_{\mathrm{fl}} = 0.72$) is slightly lower than that of **B** ($\Phi_{\mathrm{fl}} = 0.84$) beyond the experimental error of ca. 5 %.

Table 4.2: Time resolved optical data from time correlated single photon counting (TCSPC) and transient absorption spectroscopy (TA) of the $\mathbf{Py_2B}$ triad and reference compounds in dichloromethane at r.t.

	τ_{fl}/ns (TCSPC)	$\tilde{\nu}_{\mathrm{ex}}$ /cm^{-1}	$\tilde{\nu}_{\mathrm{em}}$ /cm^{-1}	τ/ps (TA)	$\tilde{\nu}_{\mathrm{ex}}$ /cm^{-1}
Py	34.8	31650	25200	–	–
B	4.93	23920	17570	–	–
$\mathbf{Py_2B}$	3.03 (3.05)	23920 (31650)	16290	0.12, 1.6, 22, 460, 3100	30800

4.2.2 Computed absorption spectra and electronic states of Py_2B

In order to simulate the thermally broadened absorption spectrum of $\mathbf{Py_2B}$ we sampled the ground state canonical harmonic Wigner distribution at $T = 300$ K. Overall, 300 normal mode displacements and momenta were generated and converted back to Cartesian coordinates. The electronic absorption spectra for each individual structure from the ensemble have been calculated at the AM1-CIS and TD-CAM-B3LYP

levels of theory and all stick spectra have been convoluted by Lorentzians in order to generate the continuous curve. The resulting thermally broadened absorption spectra are presented in Fig. 4.3 together with the experimental spectrum. The theoretical spectra at both levels reproduce the experimental absorption bands well. In particular, the splitting between the first and the third absorption band is in excellent agreement, and the second band is much broader than the first one, also in agreement with the experiment.

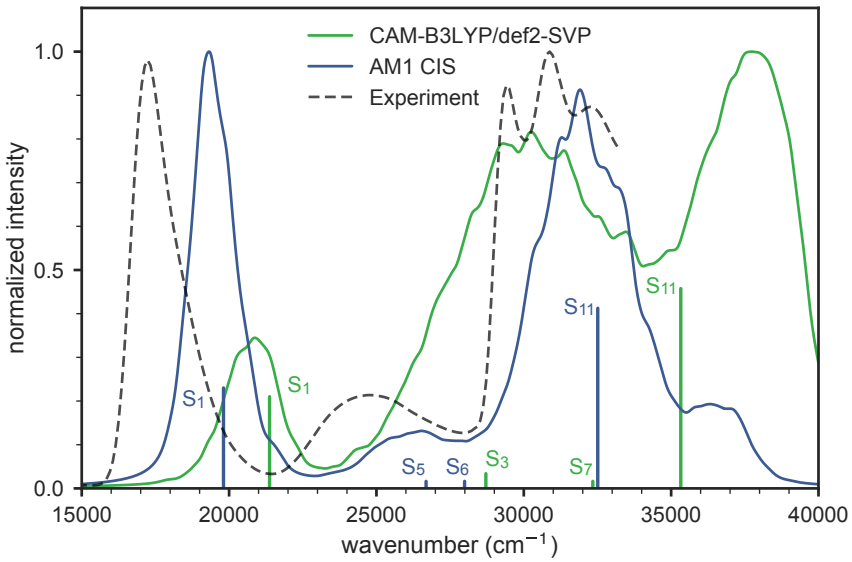

Figure 4.3: Comparison between the simulated spectra at the level of AM1 CIS and TD-CAM-B3LYP/def2SVP and experimental absorption spectrum of $\mathbf{Py_2B}$. The vertical transition from the ground state are shown as sticks with the notation of the corresponding excited state. The simulated individual transitions have been convolved by a Lorentzian function with a width of 500 cm^{-1}.

In Fig. 4.4 we present transition densities and natural transition orbitals of the dominant optically active electronic excited states calculated at the AM1-CIS level, which will be used to carry out nonadiabatic dynamics simulations, and at the TD-CAM-B3LYP level of theory. The character of the dominant electronic transitions is in perfect agreement between both employed methods. In the following, we will discuss the AM1-CIS results while the detailed comparison between the electronic states at the AM1-CIS and TDDFT level is given in the supporting information of Ref 7. As can be seen from Fig 4.4a, the S_1 state is mainly localised on the BODIPY-unit and its transition moment is oriented along the molecular longitudinal axis. The S_5 and S_6 states have a much weaker oscillator strength. The S_5 exhibits a strong localisation on the pyrene unit while the S6 is partly localised on the BODIPY-unit. The second intense absorption peak at around 32000 cm^{-1} is dominated by the S_{11}-state, which is delocalised over the whole system. The delocalisation arises due to the "J-type“ coupling between the longitudinally polarised pyrene-states and the corresponding

BODIPY-state. In the case of transversally polarised pyrene transitions, the states remain uncoupled and are thus fully localised on the pyrene unit (*cf.* dark S_2, S_3, S_9, and S_{10}-states in between the bright ones in Fig. S3 and S4 of Ref. 11). These findings are in very good agreement with the qualitative picture obtained from the experimental absorption spectra.

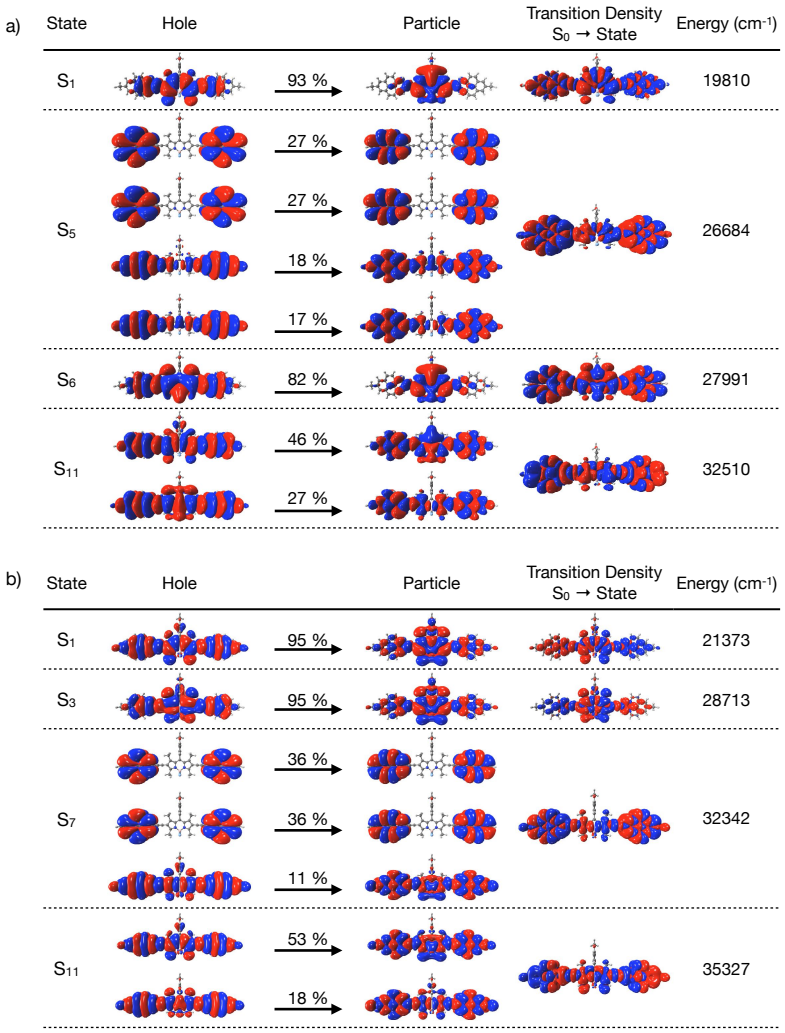

Figure 4.4: (a) Natural transition orbitals (NTOs) of the dominant excited states, the resulting transition densities (TDs), energies and the polarisation in braces at the AM1 CIS level. (b) NTOs of the dominant excited states, TDs and energies (polarisation) at the TDDFT level. Only contributions with eigenvalues > 0.1 are shown.

In order to investigate the presence of charger-transfer (CT)-states and the composition of the excited states, we have partitioned the transition densities into natural transition orbitals (NTOs, *i.e.* orbital representation which diagonalizes the transition density matrix). In the S_1- and S_2-state the electrons will be excited from a

delocalised configuration to the one localised at the BODIPY-unit. These two excitations only differ in the sign of the hole so that in the case of the S_1 this leads to constructive overlap with the particle but in the S_2 the overlap is almost destructive and only a small transition moment remains (see Supporting Information of Ref. 11). The S_5-state is composed of two kinds of transitions and each consists of two different combinations of particles and holes. Of course, the combination of three chromophores leads to deviations of the electronic character of the triad excited states from those of the individual dyes because states with mixed character are generated by configuration interaction. Thus, the AM1-CIS computed S1 state clearly refers to the BODIPY $S_1 \leftarrow S_0$ excitation around 17200 cm^{-1}, the dark AM1 S_2–S_4 states and the bright S_6 state are *y*-polarised combinations of the (two) pyrene S_1 and BODIPY S_2 states. The AM1 S_5 state refers to an *x*-polarised combination of the two *x*-polarised pyrene S_2 states, as is the very intense AM1 S_{11} state.

4.2.3 Fluorescence lifetime measurements

The fluorescence lifetime of the triad was measured by time-correlated single photon counting (TCSPC, see Table 4.2) in DCM. When exciting the lowest energy band of the $\mathbf{Py_2B}$ triad, we measured a lifetime of 3.03 ns, much shorter than that of **B** with 4.93 ns. When excited at 31650 cm^{-1} the pyrene S_2 state the triad also shows fluorescence with the same lifetime as when excited at the lowest energy state of the BODIPY chromophore. Using these lifetimes and the fluorescence quantum yields the squared transition moment of the fluorescence μ_{fl}^2 can be calculated *via* the Strickler–Berg equation:[47]

$$k_{fl} = \frac{16 \cdot 10^6 \pi^3}{3h\varepsilon_0} \frac{n\left(n^2+2\right)^2}{9} \left\langle \tilde{\nu}_{fl}^{-3} \right\rangle_{av}^{-1} \mu_{fl}^2 \tag{4.2}$$

where $\left\langle \tilde{\nu}_{fl}^{-3} \right\rangle_{av}^{-1} = \int I_{fl} d\tilde{\nu} / \int I_{fl} \tilde{\nu}^{-3} d\tilde{\nu}$ is the average cubic fluorescence energy and $k_{fl} = \Phi_{fl}/\tau_{fl}$ is the radiative rate constant. For the parent chromophore **B** the thereby evaluated (input from Table 4.1) fluorescence transition dipole moment is in reasonable agreement (within ca. ±10 %) with those of the absorption spectra, which indicates no major changes of the electronic/geometrical nature in the lowest energy excited state. For the triad, the situation is distinctly different; that is, the squared fluorescence transition moment is enhanced by ca. 35 % compared to that of the absorption. This effect is even more impressing when comparing the squared fluorescence transition moments of **B** with those of $\mathbf{Py_2B}$. Here the latter is 80 % larger. A preliminary explanation for this observation is that the excited states of the triad undergo a structural rearrangement (possibly flattening) which results in an increased electronic coupling of the pyrene and BODIPY chromophore leading to an enhanced squared transition moment of the fluorescence process.[211] This is also supported by the different band shapes of the BODIPY absorption in $\mathbf{Py_2B}$ and **B**.

4.2.4 Femtosecond pump probe spectroscopy

The steady-state photophysical properties of the $\mathbf{Py_2B}$ triad give first hints about the interactions in the pyrene-substituted BODIPY dye conjugate, but no information about its photoinduced dynamics. Therefore, transient absorption (TA) measurements with fs time resolution were performed to distinguish between a dynamic energy transfer after excitation into the pyrene S_2 state or the formation of delocalised excitonic states with subsequent internal conversion processes. The symmetric triad was measured in DCM at r.t. and excited at the energy (30800 cm^{-1}) of the 01-band of the pyrene S_2 state. This allows following the pyrene S_2 state dynamics by looking at the 00–band without problems caused by excitation stray light. At this wavenumber, pyrene is primarily excited, but because of band overlap, a state that is formed by the interaction of pyrene with the BODIPY chromophore is excited, too.
Excitation of $\mathbf{Py_2B}$ at the 01-transition of the pyrene S_2 state also excites a state resulting from the interaction of pyrene and BODIPY significantly. The resulting TA spectra, which rise within instrument response (ca. 100 fs) show a strong ground state bleaching (GSB) below ca. 19000 cm^{-1} and excited state absorption (ESA) with the maxima at ca. 20500 and 28700 cm^{-1}. Global analysis of the TA spectra with the minimum number of exponential functions gives decay associated difference spectra (DADS, amplitude spectra of species which evolve parallel in time) and the equivalent evolution associated difference spectra (EADS, spectra of species which evolve sequentially with increasing lifetimes) (Fig. 4.5) with $\tau = 0.12, 1.6, 22, 460$ and 3100 ps. The first EADS with $\tau = 0.12$ ps shows strong GSB at the spectral position of the lowest energy absorption of the BODIPY chromophore, but no concomitant stimulated emission (SE) at lower energy, and GSB at the 00–transition of the pyrene S_2 state at 29300 cm^{-1}. This can also nicely be seen in comparison with the absorption spectrum of $\mathbf{Py_2B}$ (red spectrum, see Fig. 4.6a) and shows that the $\mathbf{Py_2B}$ is excited and the resulting transition density is distributed over all triad constituents. However, this state is not the lowest energy state because otherwise one would expect SE arising at ca. 16000 cm^{-1}. The EADS with longer time constants represent relaxation processes (see also DADS in Fig. 4.5c) and the last one with $\tau = 3100$ ps ground state recovery is in excellent agreement with the TCSPC lifetime. Just for comparison, direct excitation of the lowest energy state of $\mathbf{Py_2B}$ at 17200 cm-1 yielded very similar TA spectra and the global analysis gives similar EADS and time constants with the exception of the ultrafast component, which is missing (see Fig. S2 in Ref. 11). We now compare the last EADS with $\tau = 3100$ ps with the sum of emission and absorption spectra of $\mathbf{Py_2B}$ yielding the ESA contribution (blue spectrum, see Fig. 4.6b). This constructed ESA shows a strong absorption peak at 29300 cm^{-1} which appears to be unreasonably strong. This peak indicates that using the triad absorption spectrum to simulate the GSB was not appropriate and that the transition density of the lowest energy excited state of $\mathbf{Py_2B}$ is, on average, not entirely spread over the BODIPY and both pyrene chromophores, because otherwise one would expect that the absorption spectrum including all features of the triad constituents matches the GSB. In other words, localisation of excitation must have

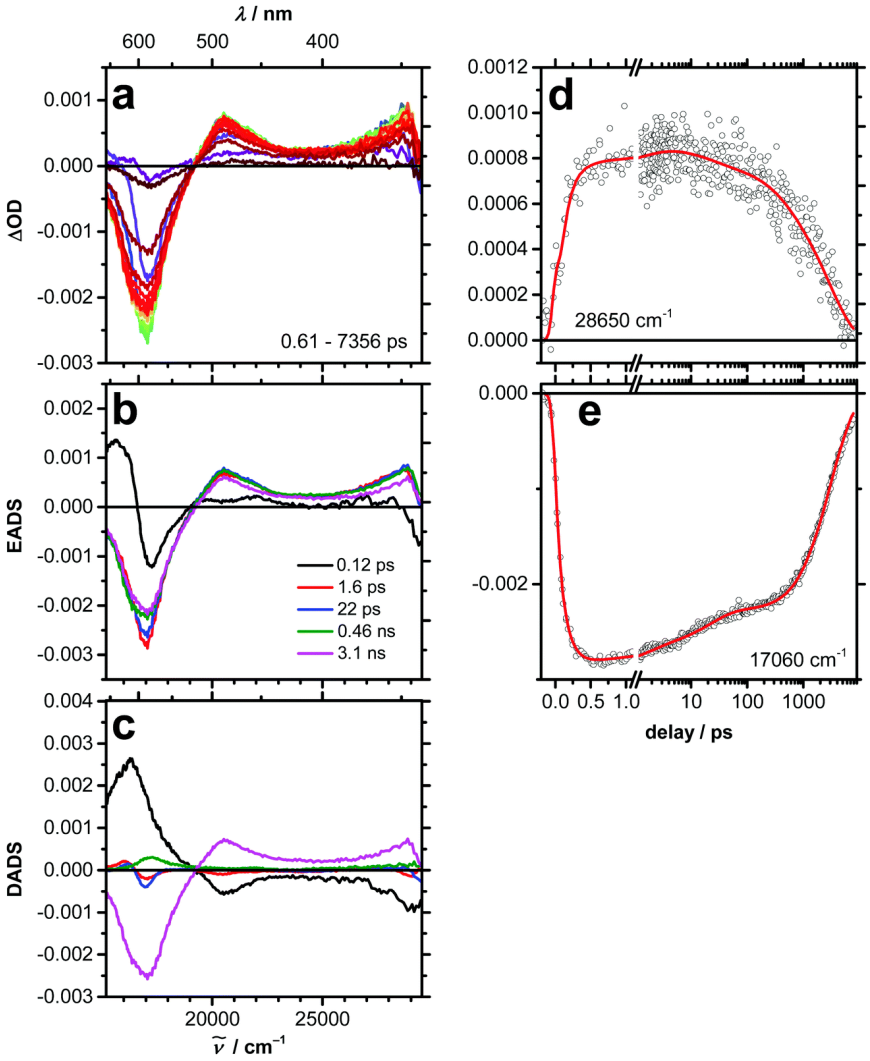

Figure 4.5: Chirp corrected transient spectra of $\mathbf{Py_2B}$ (a) in dichloromethane at 30800 cm^{-1} excitation. (b) Evolution associated difference spectra from global fit of the TA data. (c) Decay associated difference spectra from global fit of the TA data. (d and e) Transient decay profiles (black circles) at selected wavenumbers and global fit (red line).

been occurred, at least to some extent. This somewhat conflicting result shall be elucidated by using computational methods, which allow looking on the electronic processes of a single molecule and not only on the average of an ensemble as in our experiments.

4.2.5 Light-induced nonadiabatic dynamics simulations

In order to investigate the dynamical processes induced in the $\mathbf{Py_2B}$ triad after photoexcitation computationally, the nonradiative relaxation of the molecule has been simulated using the field-induced surface hopping (FISH) method[56] that allows to

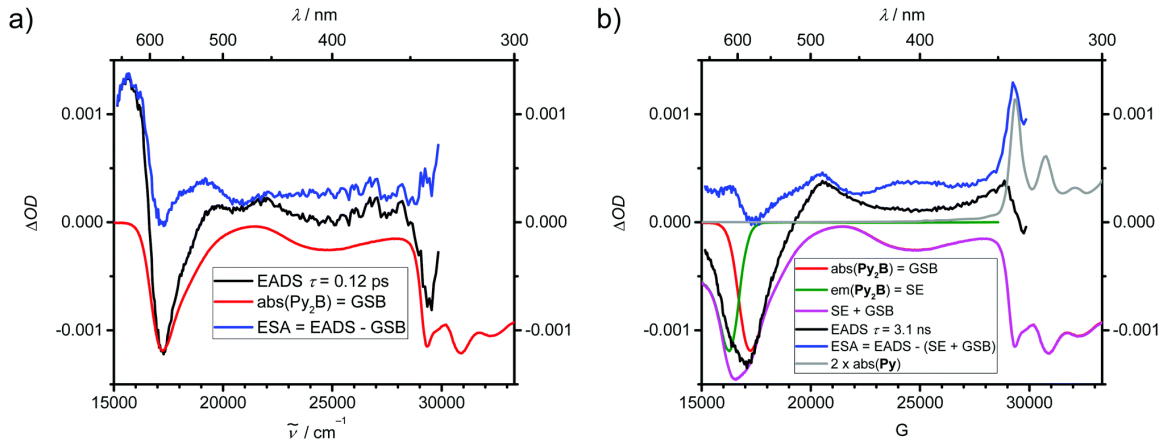

Figure 4.6: Reconstruction of ESA spectra (in blue) of **Py$_2$B** from EADS (a) with τ = 0.12 ps and (b) with τ = 3.1 ns using steady-state absorption and emission spectra.

treat the excitation by laser fields and nonadiabatic transitions on an equal footing. The above described Wigner ensemble used to simulate the absorption spectrum has also been employed to generate 150 initial conditions for the FISH simulations. An ensemble of trajectories has been propagated for 500 fs in a manifold of 20 electronic states. For excitation, a Gaussian shaped laser pulse resonant to the second broad absorption band has been used, whose full width at half maximum (fwhm) was 21 fs, and the field amplitude was maximal at 50 fs. The parameters were chosen to be similar to the experimental ones. The resulting electronic state population dynamics is shown in Fig. 4.7, where we have grouped several excited states together. The laser pulse leads to significant population of the higher lying excited state. We have summed the population of the S_4 up to the S_{20} state due to the fact that these states show a very similar population decay. Within a short time interval of about 50 fs, most of the trajectories leave the higher lying states and the S_2– and S_3 states are populated (see green line in Fig. 4.7). However, the population of these states rises only up to 35 %, since some of the trajectories relax directly into the first excited state. The decay of the second and third excited state has a time constant of 97 fs and leads to the population increase of the S_1 state with a very similar time constant of 99 fs. No transitions to the ground state take place within the simulation time, which is consistent with the experimentally observed fluorescence lifetime of ca. 3 ns. In order to elucidate the time dependent orientation of the transition moment between the ground state and the actual state populated in the surface hopping simulations, we have performed an averaging at every time step over the whole ensemble of trajectories. After excitation with the laser pulse, a transition dipole moment of about 1.2 D along the x-axis to the actual state can be observed, which decays on a time scale less than 50 fs to 0.7 D (see Fig. 4.8). During this time, the dipole along the short molecular axis increases to about 0.3 D, with the maximum amplitude located at 80 fs. Within 150 fs the transition moment along the y-axis decreases to almost zero and the x-component moment increases up to 4.0 D.

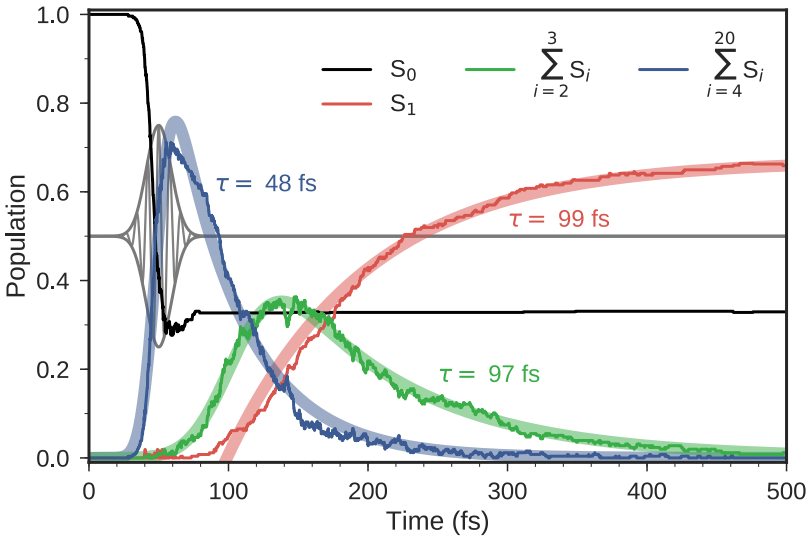

Figure 4.7: Population of an ensemble of 150 trajectories of the electronic states during the field induced surface hopping dynamics of $\mathbf{Py_2B}$. The bold red line shows the fit of the S_1 population to the following fit function: $F(t) = -A\exp\left(-\frac{t-t_0}{\tau}\right) + B$. The blue and green bold lines show the fit of the summed populations to the following function: $G(t) = A\exp\left(-\frac{t-t_0}{\tau}\right)\exp\left(\frac{b^2}{4\sigma^2}\right)\left[1+\mathrm{erf}\left(\frac{t-t_0-\frac{b^2}{2\sigma}}{b}\right)\right]$, which is chosen to describe the population increase induced by a laser pulse and simultaneous exponential decay.

The observed time-dependence of the transition dipole moment is in good agreement with experimentally obtained changes in the polarisation of the transition, which are shown on top of the state diagrams in Fig. 4.12 and refers to the intermediate population of the AM1-CIS computed S_2–S_4 and S_6 state with y-polarisation. The time constant for the decrease in the longitudinal orientation with 35 fs is of the same order of magnitude as the experimental constant for the switch from the longitudinal to the transversal polarisation (75 fs) of the S_2–S_1 internal conversion in pyrene. Furthermore, the subsequent increase in the longitudinal direction within 99 fs refers to the S_1 population and is in perfect accordance to the experimentally obtained lifetime, with a value of 120 fs, for step **A** in the state diagram that is rate determining for the corresponding process.

4.2.6 Analysis of the exciton localisation dynamics

In order to analyse the exciton dynamics, the adiabatic electronic states along the trajectories have been decomposed into the diabatic basis with excitations localised on individual monomers. We have monitored the population of these diabatic states along the trajectories by integrating the square of the electronic transition density (TD) for the adiabatic state which is populated at the given time step over the volume

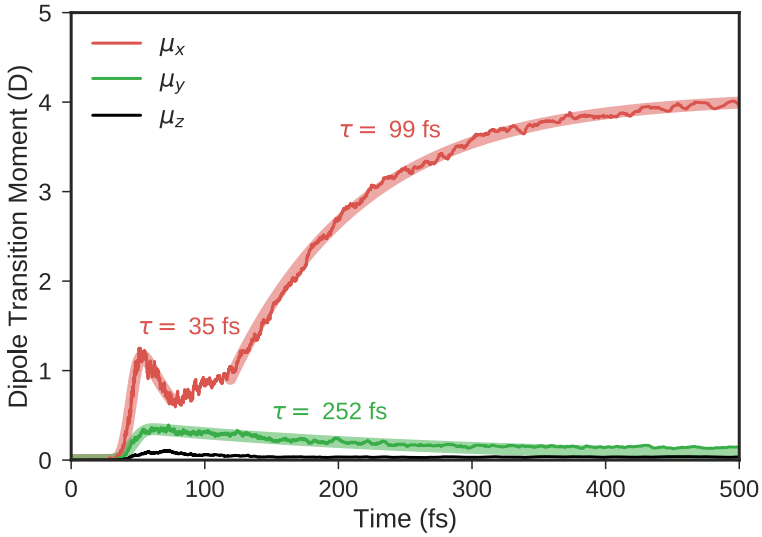

Figure 4.8: Transition dipole moment of the actual populated electronic state of the whole ensemble. The y-direction and the first 80 fs of the x-direction are fitted with the bold line to the following fit function: $G(t) = A \exp\left(-\frac{t-t_0}{\tau}\right) \exp\left(\frac{b^2}{4\sigma^2}\right) \left[1 + \mathrm{erf}\left(\frac{t-t_0-\frac{b^2}{2\sigma}}{b}\right)\right]$. The bold red line of the x-direction between 120 fs and 500 fs shows the fit to $F(t) = -A \exp\left(-\frac{t-t_0}{\tau}\right) + B$

corresponding to each subunit and normalised the square of the whole transition density. This delivers two functions presented in Fig 4.9a for two representative trajectories (see also Fig. 4.10 for a pictorial representation) as well as the average of both functions over the whole ensemble which is presented in Fig. 4.9b. The value of 1.0 corresponds to the complete exciton localisation on the respective unit, while for the value of 0.5, the TD is equally distributed over the whole system. The excitation leads to a short transient exciton localisation-delocalisation dynamics over the whole molecular system and after 150 to 200 fs the exciton is strongly localised on the BODIPY subunit and resides there. On an ensemble level, a very short transient exciton localisation on the 4–alkoxyphenyl group is observed which is accompanied by a decay, resulting in a coherent delocalisation within 10 fs. This delocalisation lasts for more than 100 fs and is followed by strong localisation on the BODIPY subunit within another 100 fs.

In order to gain a further insight into the localisation dynamics, we have calculated a 2D map of the transition densities between the electronic ground state and current state by integrating the transition density along the axis perpendicular to the molecular plane for the whole ensemble. The result is shown for selected time steps in Fig. 4.11 and the full animation is provided in the Supporting information of Ref. 11. A superposition of the ensemble geometries at a given time step are shown in the bottom of each figure. The analysis of the exciton localisation shows a transient

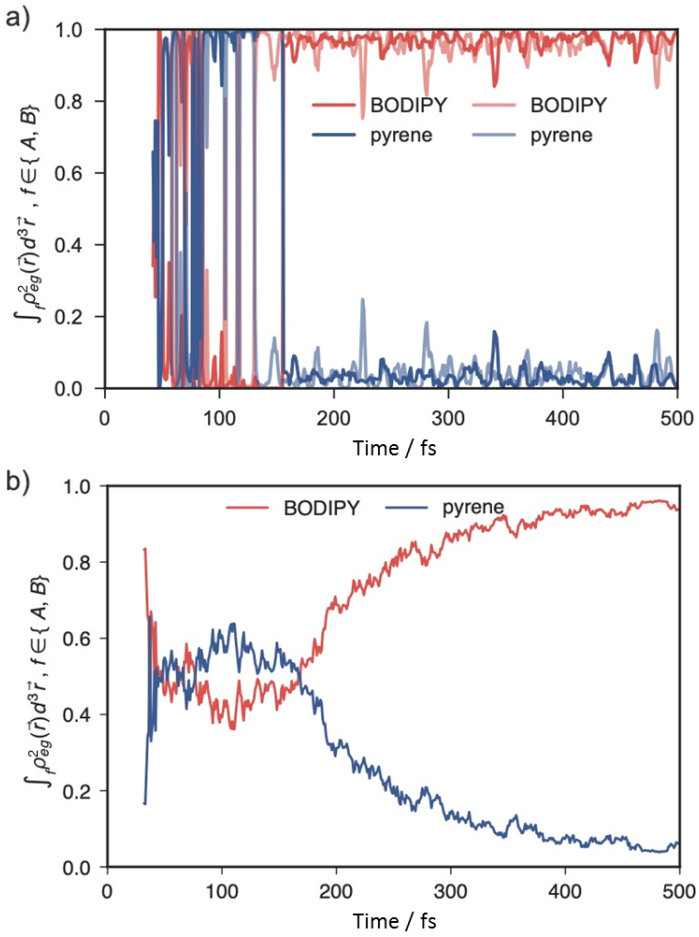

Figure 4.9: Integrated transition density on a given subunit (red, BODIPY; blue, pyrene units) for two single trajectories (a) and averaged over the whole ensemble (b).

localisation/delocalisation within the first 60 fs of the dynamics simulation on ensemble level. This is followed by a delocalisation over all subunits which lasts for around 100 fs. Afterwards, the exciton localises on the BODIPY unit and remains there for the rest of the simulation time. During the time duration of the FISH simulations, the structures do not undergo any pronounced structural deformation but exhibit only relatively low amplitude vibrations.

4.3 Discussion and Conclusions

With the above collected information at hand, we can construct a state diagram for the photoinduced processes in $\mathbf{Py_2B}$, which is displayed in Fig. 4.12. At this point we stress that we assign the diverse states with labels, which describe the electronic character of the excited state best without any assumption, whether we deal with a more localised or a more delocalised state that may also involve other molecular

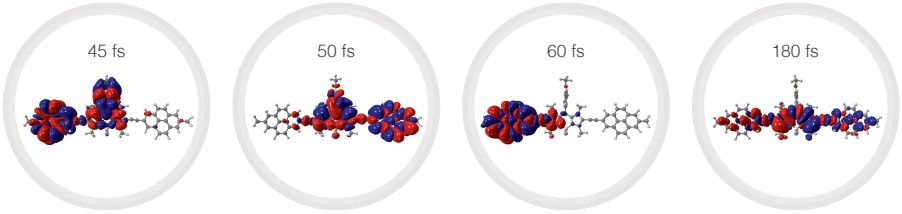

Figure 4.10: Transition densities between electronic ground state and current state on a single trajectory level. The depicted transition densities correspond to the integrated values shown in dark colours in Fig. 4.9a

units than those indicated in the label. From the TA experiments it appears that the rate determining step for the population of the lowest energy BODIPY state after excitation of the pyrene S_2 and concomitantly the B-Py state is process A between the pyrene S_1 state and the BODIPY S_3 state with $\tau = 0.12$ ps, assuming ultrafast IC between BODIPY S_3 and S_2/S_1. The FISH simulations corroborate this interpretation as they predict a ca. 100 fs time constant for the population of the S_1 state from a state which has predominantly pyrene S_2 character, although this state is the AM1 S_2 state. However, from the time resolved experiments alone it is not quite clear whether we deal here with internal conversion within an excited superchromophore comprising the two pyrene units and the BODIPY dye or with energy transfer between one of the pyrene units and the BODIPY dye. The comparison of TA spectrum and steady-state absorption spectrum in Fig. 4.6a shows a very strong GSB at 29300 cm^{-1} comparable to the pyrene absorption at this energy and, at the same time, a pronounced GSB at the BODIPY absorption energy. This hints towards a sizable electronic coupling between the BODIPY and the pyrenes in the excited state although, the excited state has a spectroscopically strong S_2 character of pyrene. While the former observation speaks for an IC process, the latter argues for an energy transfer process of almost decoupled chromophores. Likewise, in the final excited state (Fig. 4.6b), the GSB at 29300 cm^{-1} indicates an electronic coupling between the BODIPY excited state and pyrene but the intensity of the GSB is much less than one would expect. Thus, phenomenologically it appears that we deal with an intermediate case where the electronic coupling is strong enough to allow excitation of the whole triad but weak enough to retain most of the spectroscopic character of either BODIPY or pyrene states. The latter may be due to the fact that the S_2 transition moment is oriented along the long axis of pyrene thus minimising excitonic interactions with the nearby lying S_3/S_2 states of BODIPY or squaraine.
As we have recently shown in a quantum-dynamical study in case of a dyad built up from two different squaraine dyes, the transition density of an individual molecule not only hops between the two excitonically coupled S_1/S_2 states but also between the two squaraine chromophores within the first several 100 fs after excitation into S_2. Thus, a site energy difference between the dyad chromophore constituents may lead to a dynamic behaviour but finally to localisation of excitation in the lower energy chromophore. This situation may also apply to the $\mathbf{Py_2B}$ triad here, that is, fast

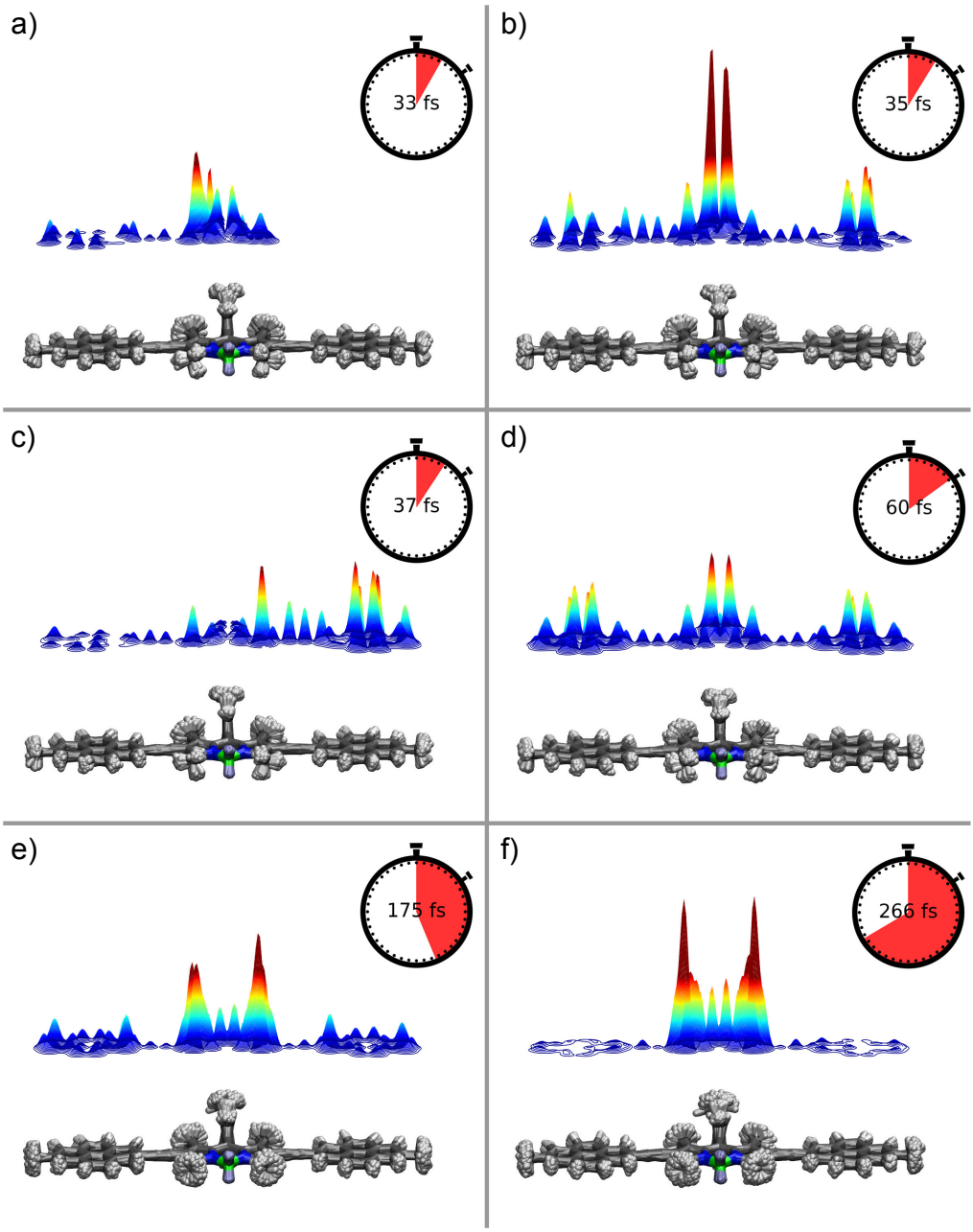

Figure 4.11: Transition densities between electronic ground state and current state after integration along the axis which is perpendicular to the molecular plane and averaging over the whole ensemble of trajectories (top). Superposition of the molecular structures at the given time frame (bottom). The numbers in the clock correspond to the simulation time (top right corner).

hopping of transition density between BODIPY and pyrene may lead to a macroscopic ensemble in which on average there is more BODIPY excited than pyrene. This would lead to a GSB signal which does not reflect the steady state absorption

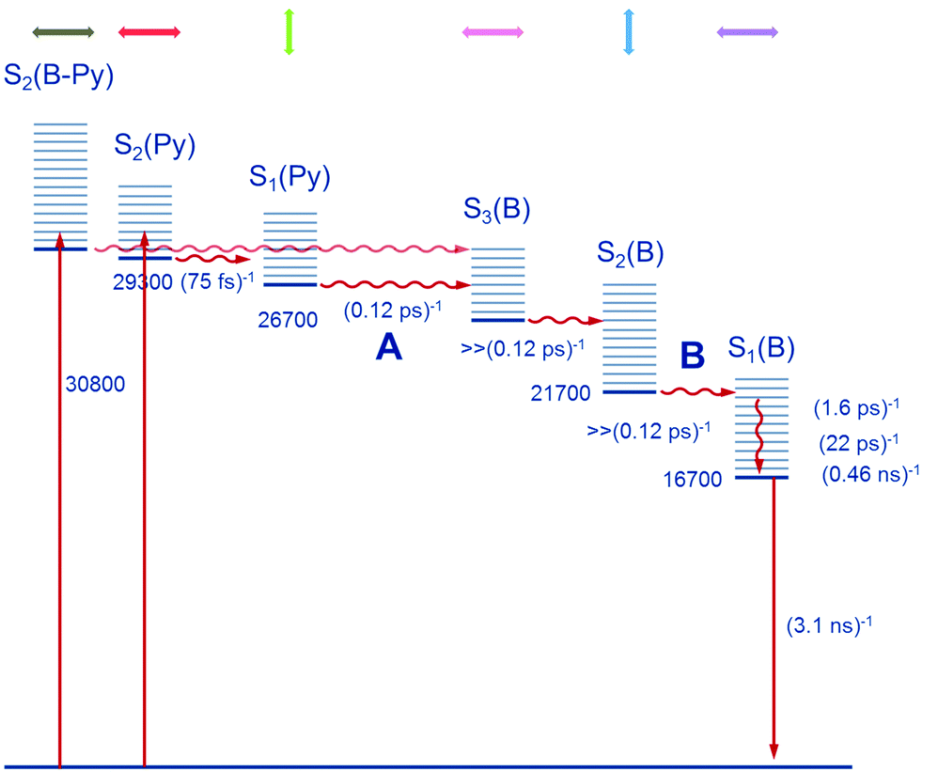

Figure 4.12: State diagrams for the photophysical processes in $\mathbf{Py_2B}$. The assignment is made for the local chromophore states, as abbreviated in parentheses. The 00-state energies of the diverse states were estimated as follows: for $S_2(\mathbf{Py})$ from the most intense absorption peak. For $S_1(\mathbf{Py})$ from the highest energy peak of the fluorescence spectrum. For $S_2(\mathbf{B})$ from the intersection of a tangent to the lowest energy flank of the corresponding absorption spectrum with the x axis. For $S_1(\mathbf{B})$ from the intersection of absorption and emission spectra. The energy of the partially delocalised $S_2(\mathbf{B\text{-}Py})$ states is estimated. For $\mathbf{Py_2B}$ the polarisation direction of each transition is given on top of the graph.

spectrum in intensity. Again, the FISH simulations shed light onto the dynamics. Looking at a single trajectory tells us that after pyrene excitation the excitation density hops several times over the two pyrene units and the BODIPY chromophore until it gets trapped onto the BODIPY chromophore (Figs. 4.9a and 4.10). However, on averaging the transition density of many trajectories, and that is what we observe experimentally, it appears that an initially delocalised triad state comprising all three components is populated until localisation of excitation at the BODIPY occurs after ca 200 fs (Figs. 4.9b and 4.11). The latter process agrees excellently with the experimentally observed 120 fs for the population of S_1. Thus, excitation of $\mathbf{Py_2B}$ may be best described by neither IC nor energy transfer but by what we would like to call "dynamic exciton localisation" which clearly represents the bridge between the both extreme scenarios[39] and also may involve symmetry-breaking.[106,212–214]

4.4 Experimental

The synthesis of the triad is described in the Supporting Information of Ref. 11.

4.4.1 Optical spectroscopy

Steady-state absorption measurements were carried out in 1 cm quartz cuvettes from Hellma in dichloromethane (Uvasol from Merck) at r.t. using a Jasco V670 spectrometer. The pure solvent was used as a reference. Fluorescence spectra were measured in 1 cm quartz cuvettes with Uvasol® solvents from Merck using an Edinburgh Instruments FLS980 spectrometer. The dissolved samples were purged with argon for 15 min before the measurement. Fluorescence quantum yields were determined using optically dense samples in an integrating sphere following the method of Bardeen *et al.*[215] to correct for self-absorption. Fluorescence lifetimes were measured by time-correlated single-photon counting (TCSPC) with the FLS980 spectrometer using pulsed laser diodes at 15200 cm^{-1} or 19650 cm^{-1} or a pulsed light emitting diode at 31250 cm^{-1} as excitation source. The instrumental response was determined with a scatterer solution consisting of colloidal silicon in deionised water. All spectra were recorded under magic angle conditions using a fast PMT detector (H10720). Lifetimes were determined by deconvolution of the experimental decay (4096 channels) with the instrument response function and by fitting the decay curves with an exponential decay function using the FAST software (version 3.4.2).

4.4.2 Femtosecond transient absorption spectroscopy

All experiments were performed in quartz cuvettes from Spectrocell (Oreland, PA) with an optical path length of 0.2 mm equipped at r.t. All samples were dissolved in DCM, filtered and degassed for 30 min. The optical density was adjusted to ca. 0.2 at the corresponding excitation wavenumber. The transient absorption spectra were performed with a Newport-Spectra-Physics Solstice one-box amplified ultrafast Ti:Sapphire laser system with a fundamental wavenumber of 12500 cm^{-1} (800 nm), a pulse length of 100 fs and a repetition rate of 1 kHz. The output beam from the Solstice amplifier was split into two parts. One part was focussed onto a vertically oscillating CaF_2 crystal to produce a white light continuum between 11800 cm^{-1} (850 nm) and 28600 cm^{-1} (350 nm). The resulting beam, which was polarised horizontally was used as the probe pulse. The second pulse was used to pump an optical parametric amplifier (TOPAS-C) from Light Conversion to generate the pump pulse with a pulse length of 140 fs at the appropriate excitation wavelength. By using a wire grid (Moxtek), the polarisation axis of the pump pulse was set to magic angle relative to the probe pulse. The pump pulse (50 nJ, ⌀ ca. 0.4 mm) and the probe pulse (⌀ ca. 0.1 mm) met at an angle of 6^o vertically in the cuvette. The probe pulse was measured by means of an CMOS sensor (Ultrafast Systems, Helios) in the range of 11900 cm^{-1} (840 nm) to 29400 cm^{-1} (340 nm) with an intrinsic resolution of 1.5 nm. To compensate for white light intensity fluctuations, a reference beam was

split off and detected with an identical spectrograph. Every second probe pulse was blocked by a mechanical Chopper (500 Hz) to measure the ratio of I and I_0. The computer-controlled stage (retro reflector in double pass setup) set the time difference between pump and probe pulse in 20 fs intervals from 0 fs to 4 ps and 4 ps to 8 ns in logarithmic steps with a maximum of 200 ps. Before data analysis, the raw transient data were corrected for stray light and white light dispersion (chirp). The chirp was corrected by fitting a polynomial to the cross phase modulation signal of the pure solvent under otherwise experimental conditions. The evolution associated difference spectra (EADS) and the species associated difference spectra (SADS) were obtained from the corrected data by a global analysis using GLOTARAN[136,216] software.

4.4.3 Computational Details

For the simulation of absorption spectra of the studied system, the structure has been first optimised in the frame of the semiempirical AM1 parametrisation[217,218] and we calculated the vibrational modes to sample 150 structures from a phase space Wigner distribution at 300 K. The excited states properties have been calculated in the framework of parametrised Configuration Interaction Singles (CIS). After performing extensive benchmark calculations on the energetics and characters of the excited states on the considered energy range, we have chosen an active space of 15 occupied and 15 virtual orbitals. The calculated stick absorption spectra were convolved with a Lorentzian function in order to obtain better comparability with the experimental data. Furthermore, to validate the applicability of AM1 for the studied system, we have also calculated the optical absorption spectra, natural transition orbitals[219] and transition densities at the TDDFT level, using the long-range corrected CAM-B3LYP[220] functional and the def2-SVP[221] basis set as implemented in the Gaussian16 quantum chemical software package[222] (see Supporting Information of Ref. 11). The light-induced nonadiabatic dynamics simulations have been performed using the field-induced surface hopping (FISH) methodology. This allows for realistic modeling of the excitation process induced by an ultrashort laser pulse as well as the description of the nonradiative transitions which are mediated by the nonadiabatic couplings.[56,63,163] The laser fields employed in the simulations were parametrised in the time domain as Gaussian pulses. The full width at half-maximum (fwhm) for all applied pulses was 21 fs, and the field amplitude was maximal at 50 fs. The parameters were chosen to be similar to the experimental ones. For this purpose, the nonadiabatic dynamics simulations were performed in the manifold of the electronic ground and up to 20 excited electronic states. The nuclear degrees of freedom were propagated by solving the classical Newtonian equations using the velocity Verlet algorithm with a time step of 0.1 fs for a total number of 5000 steps.

Chapter 5

Polarisation-Anisotropy and Nonadiabatic Dynamics Simulations in pyrene-BODIPY conjugates

Excitation energy transfer (EET) is of fundamental importance in natural and artificial light-harvesting systems as it influences the functional performance of photovoltaic and organic electronic devices. Here, we present a theoretical study of the exciton transfer dynamics in a covalently linked pyrene-BODIPY donor-acceptor dyad and triad. For this purpose, we employ field-induced surface-hopping (FISH), allowing for an explicit description of the initial excitation induced by a short laser pulse as well as of the subsequent cascade of nonradiative transitions that are induced by the nonadiabatic coupling between the excited electronic states. We elucidate the detailed mechanism leading to the exciton transfer from the pyrene unit to the BODIPY unit on a time scale of 100 fs. The ultrafast energy transfer between the donor and acceptor states is mediated by a sequence of nonradiative transitions involving dynamic localisation and delocalisation of the exciton. We show how this can be connected to polarisation-anisotropy spectroscopy.

5.1 Introduction

Understanding excitation energy transfer (EET) is a key step for developing artificial light-harvesting systems that can facilitate solar energy conversion[21,178,223] or the development of novel fluorescence-based sensors.[224,225] Multichromophoric systems played a fundamental role in understanding these transfer processes and were subject to numerous experimental and theoretical studies.[3,6,10,12,24,27,109,226–233] Intermolecular EET has been frequently described by the Förster resonance energy transfer (FRET), where the underlying process is interpreted as an incoherent hopping of a localised photoexcitation from one monomer or subunit to the neighbouring one.[34,35] This approach requires that donor and acceptor exhibit localized electronic states that are weakly coupled, and the donor fluorescence spectrum and the acceptor absorption spectrum should possess spectral overlap. Scholes and Fleming revised this approach[22] to take the delocalized character of the electronic states into

account, which leads to distinct acceleration of the energy transfer. However, in cases of strongly coupled aggregates, these theories are not applicable and coherent, wave-like energy transfer is observed.[182,234–236] Therefore these two mechanisms can be considered as two limiting cases of exciton transfer.
BF_2-chelated dipyrromethene (**BODIPY**) compounds are a very promising class of molecules in the development of artificial photosynthetic systems as they exhibit high absorption coefficients and high emission quantum yields that can easily be adjusted by substitution at several positions.[117,206,229,237] Recently, Lambert *et al.* reported a tuning of spectral properties by linking squaraine chromophores to BODIPY to exploit the best features of both dyes.[64]
Here, we aim to investigate the energy transfer dynamics in a **BODIPY** dye linked to pyrene units that serve as the energy donors. Several previous works reported energy transfer processes between these two chromophores, but they all share that pyrene is linked at the 1- or 4-position.[194–197,201,202,204,205,207] We recently investigated the light-induced dynamics in the triad system in an experimental and theoretical study[11]. Therefore, we focus on the differences between the exciton dynamics in a symmetrical dye conjugate (triad) and an unsymmetrical one (dyad). These two systems are studied in detail by employing mixed quantum-classical methods for the simulation of the excitation energy transfer and internal conversion process. Recently, it was shown that this methodology is applicable to investigate energy transfer in donor-acceptor systems[238] and exciton dynamics in multichromophoric dyes.[12,13,103,239,240] We provide a comprehensive picture of the energy transfer processes in these systems by employing FISH simulations[54,163,241] and an extensive analysis of the exciton dynamics. In this context, polarisation-anisotropy spectroscopy has been used in many recent studies to probe the exciton dynamics and to connect the theoretical simulations directly to an experimental observable.[239,242–249] Here, we show that the dynamic exciton localisation in the pyrene-BODIPY conjugates strongly correlates to the time-dependent polarisation-anisotropy, which should stimulate further time-resolved experimental studies on these systems.

5.2 Theoretical methods

5.2.1 Structural properties and stationary absorption spectra

The optimized structures of the **PyB'**-dyad and **Py_2B**-triad were calculated in the framework of the semiempirically parameterized AM1 method.[250]
The excited state properties have been calculated by employing the configuration interaction with singles (CIS) method within the same parameterization. The active space has been restricted to 15 occupied and 15 virtual orbitals for efficiency reasons. Comparison with experimental data and TDDFT calculations have demonstrated that this level of theory provides a reasonably accurate description of the absorption spectra of pyrene-BODIPY conjugates.[11]

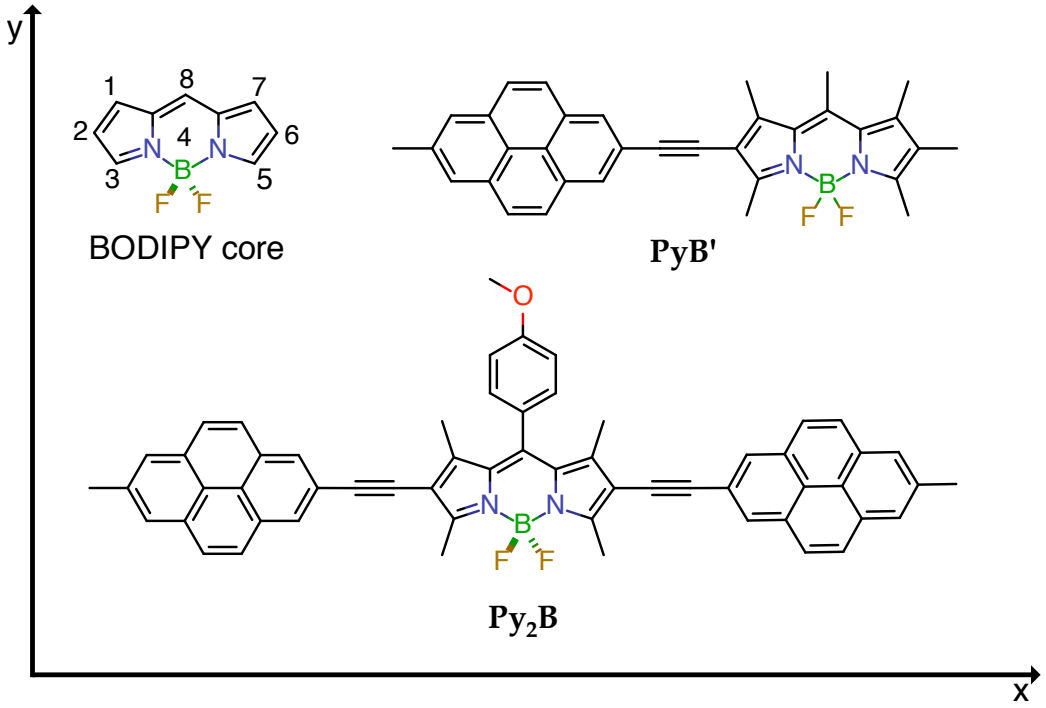

Figure 5.1: Structure of the **PyB'** and the **Py_2B** system.

5.2.2 Field-induced surface hopping dynamics simulations

The light-induced nonadiabatic dynamics simulations have been performed in the framework of the field-induced surface-hopping (FISH) methodology.[54] This allows for realistic modelling of the excitation process induced by an ultrashort laser pulse as well as the description of nonradiative transitions, which are mediated by the nonadiabatic couplings.[54,163] In the FISH simulations, an ensemble of classical trajectories representing a nuclear wavepacket is propagated in a manifold of several adiabatic electronic states, and the population transfer between these states is described by a stochastic hopping procedure, which is based on the change of the quantum electronic state populations. The ground-state phase distribution from which the initial conditions were sampled has been approximated by a harmonic Wigner distribution:[251,252]

$$\rho_{00}\left(\mathbf{q}_0, \mathbf{p}_0\right) = \prod_{n=1}^{N_{modes}} \frac{\alpha_n}{\pi\hbar} \exp\left[-\frac{\alpha_n}{\hbar\omega_n}\left(p_{0n}^2 + \omega^2 q_{0n}^2\right)\right] \tag{5.1}$$

where q_{0n} and p_{0n} denote the ground state normal coordinates and conjugate momenta, while $\alpha_n = \tanh\left(\hbar\omega_n / 2k_bT\right)$ is a temperature dependent quantity. 150 normal mode displacements and momenta were sampled at 300 K, converted into the cartesian coordinates and used as initial conditions for the trajectory simulations. In the FISH simulations, the Newtonian equations of motion have been solved in the framework of MD "on the fly" using the velocity Verlet[253] algorithm with a time step of 0.1 fs. Simultaneously, the electronic degrees of freedom were propagated along

the classical trajectories by solving the time-dependent Schrödinger equation in the manifold of the electronic ground and several excited states:

$$i\hbar\dot{c}_i(t) = E_i(\boldsymbol{R}(t))c_i(t) - i\hbar\sum_j \left[D_{ij}(\boldsymbol{R}(t)) + V_{ij})\right] c_j(t). \tag{5.2}$$

The integration was performed employing the fourth order Runge-Kutta procedure with a time step of 4 x 10^{-5} fs. The states are coupled by the laser field **E**(t) via an electric dipole coupling operator

$$V_{ij} = -\mu_{ij}\left[\mathbf{R}(t)\right] \cdot \mathbf{E}(t) \tag{5.3}$$

and the nonadiabatic coupling terms:

$$D_{ij}(\boldsymbol{R}(t)) = \langle \Psi_i(\boldsymbol{R}(t))|\frac{\mathrm{d}\Psi_j(\boldsymbol{R}(t))}{\mathrm{d}t}\rangle = \langle \Psi_i(\boldsymbol{R}(t))|\nabla_{\boldsymbol{R}}|\Psi_j(\boldsymbol{R}(t))\rangle \cdot \dot{\boldsymbol{R}}, \tag{5.4}$$

The latter can either be calculated using the scalar coupling of the electronic wavefunctions[53,56] or by the scalar product of the nonadiabatic coupling vectors with the nuclear velocities. In this manner, time-dependent electronic state populations are obtained, which are then used to calculate surface-hopping probabilities. For this purpose, the expansion coefficients of the electronic wave function in the adiabatic basis, $c(t)$, are used to calculate the density matrix elements as

$$\rho_{ij} = c_i^* c_j. \tag{5.5}$$

In order to decide when a state switch occurs, we determine the hopping probability in each nuclear time step by evaluating the change of the electronic state populations ρ_{ii} as follows[63]:

$$P_{i\to j} = \Theta(-\dot{\rho}_{ii})\Theta(\dot{\rho}_{jj})\frac{-\dot{\rho}_{ii}}{\rho_{ii}}\frac{\dot{\rho}_{jj}}{\sum_k \Theta(\dot{\rho}_{kk})\dot{\rho}_{kk}}\Delta t \tag{5.6}$$

where Θ is the Heaviside step function whose value is one for positive arguments and zero otherwise. If a jump from one state i to another state j occurs then it will result in change of the potential energy. To uphold the law of energy conservation the increase/decrease of the potential energy has to be compensated by a decrease/increase of the kinetic energy. Therefore the velocities are rescaled along the direction of the nonadiabatic coupling vector. It should be noted that during action of the laser pulse the energy is not conserved. Therefore, velocity rescaling after a surface-hopping event was only enabled for the time period after 80 fs, when the pulse had ceased. By averaging over an ensemble of independent trajectories, the real-time electronic-state population can be determined. The laser fields employed in the simulations were

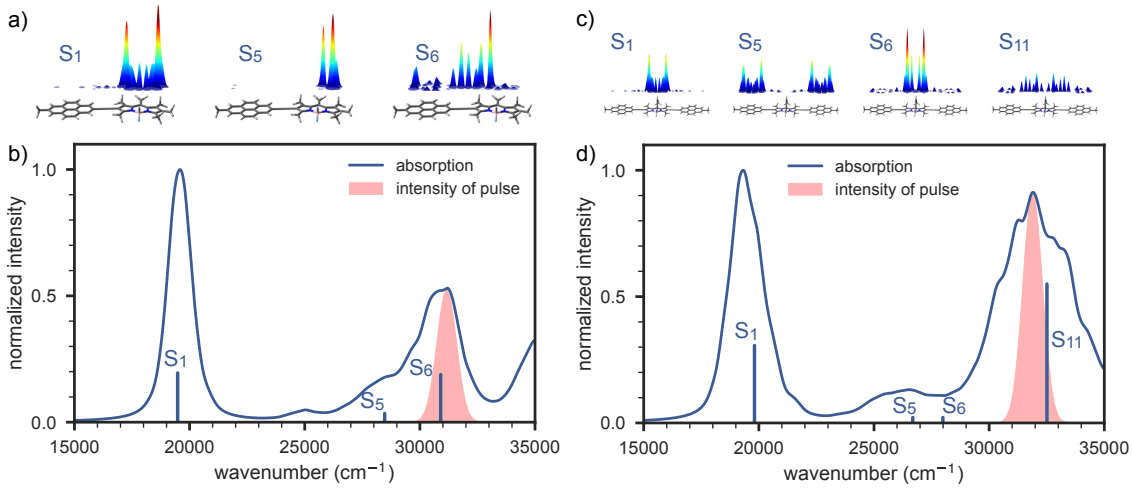

Figure 5.2: Simulation of optical ensemble spectra the AM1 CIS level of theory of the dyad (b) and triad (d). The most intense transition are depicted as sticks and the integrated square of the transition densities between the ground state and these transitions along the z-axis is shown in the top of each spectrum (a) and (c). The simulated individual transition have been convolved by a Lorentzian function with a width of 500 cm^{-1}. The spectral intensity bandwidth of the laser pulse is depicted by the red area.

parameterized in the time domain as Gaussian pulses of the form

$$\mathbf{E}(t) = E_0 \exp\left[-\frac{4\ln 2}{t_{1/2}^2}(t-t_0)^2\right]\cos\left[\omega(t-t_0)\right]. \tag{5.7}$$

The full width at half maximum (FWHM) $t_{1/2}$ for all applied pulses was 21 fs, and the field amplitude was maximal at $t_0 = 50$ fs, in correspondence with typical experimental parameters.[11]

5.2.3

Exciton analysis In order to analyze the exciton dynamics, the transition densities between the ground and the current electronic states were calculated for the whole ensemble at every 10th time step. We have monitored the motion of the excitation along the trajectories by integrating the square of the transition density (TD) for the adiabatic state which is populated at the given time step over the volume corresponding to each subunit and normalized the square of the whole TD to 1. After averaging over the whole ensemble, this delivers a function which shows the distribution of the excitation on the given subunit. However, this quantity provides no information about localisation/delocalisation on a single trajectory level due to the

fact that this is an ensemble average. Therefore, we defined a degree of localisation for the dyad system, $\eta(t)_{\mathrm{dyad}}$, and calculated this quantity on trajectory level along the FISH simulations with a timestep of 1 fs. The degree of localisation can be expressed as

$$\eta(t)_{\mathrm{dyad}} = \sum_{i=0}^{N^e_{\mathrm{traj}}(t)} 2 \cdot N^e_{\mathrm{traj}}(t)^{-1} \cdot \left| 0.5 - \frac{\int_{\mathbf{B'}} \mathrm{d}^3\mathbf{r} \left|\gamma^i_{\mathrm{eg}}(\mathbf{r},t)\right|^2}{\int \mathrm{d}^3\mathbf{r} \left|\gamma^i_{\mathrm{eg}}(\mathbf{r},t)\right|^2} \right|. \tag{5.8}$$

Here $N^e_{\mathrm{traj}}(t)$ is the number of trajectories in the excited state at time t and γ_{eg} is the transition density of trajectory i between ground state and the current state. The integration in the numerator is only performed over the spatial fragment of the **B'**-unit. The choice of the fragment, which is used for the integration, is arbitrary and the degree of localisation would yield the same result if the integration were performed over pyrene. As in the case of the dyad, we defined a degree of the localisation for the triad system as

$$\phi_X(t) = \frac{\int_X \mathrm{d}^3\mathbf{r} \left|\gamma^i_{\mathrm{eg}}(\mathbf{r},t)\right|^2}{\int \mathrm{d}^3\mathbf{r} \left|\gamma^i_{\mathrm{eg}}(\mathbf{r},t)\right|^2}, \; X \in \{A,B,C\}, \; \phi_A(t') > \phi_B(t') > \phi_C(t') \tag{5.9}$$

$$\eta(t)_{\mathrm{triad}} = \sum_{i=0}^{N^e_{\mathrm{traj}}(t)} \cdot N^e_{\mathrm{traj}}(t)^{-1} \cdot \left(\phi_A(t) - \frac{\phi_B(t) + \phi_C(t)}{2} \right). \tag{5.10}$$

The indices A, B and C denote the three spatial monomer fragments in descending order of magnitude. Thus, as in the case of the dyad, a value of 1 corresponds to the complete exciton localisation on the respective unit, while for the value of 0, the TD is equally distributed over the whole system. We have animated the exciton motion on an ensemble level to gain a deeper insight into energy transfer. In Fig. 5.5, we show four snapshots of the dynamics: To this end, we integrated the transition density γ_{eg} between the ground and the current electronic state of each trajectory along the z-axis, which is perpendicular to the molecular plane, as:

$$\gamma^{\mathrm{ensemble}}_{\mathrm{eg}}(x,y,t) = \sum_{i=0}^{N^e_{\mathrm{traj}}(t)} N^e_{\mathrm{traj}}(t)^{-1} \cdot \int \left|\gamma^i_{\mathrm{eg}}(x,y,z,t)\right|^2 dz \tag{5.11}$$

Here $N^e_{\mathrm{traj}}(t)$ and γ_{eq} are the same quantities as in Eq. 5.8.

5.2.4 Polarisation anisotropy

To link exciton motion of the field-induced surface hopping dynamics with experimentally accessible observables, we simulated the polarisation anisotropy in a similar way as done by S. Tretiak and coworkers.[239] Hence, the polarisation anisotropy is

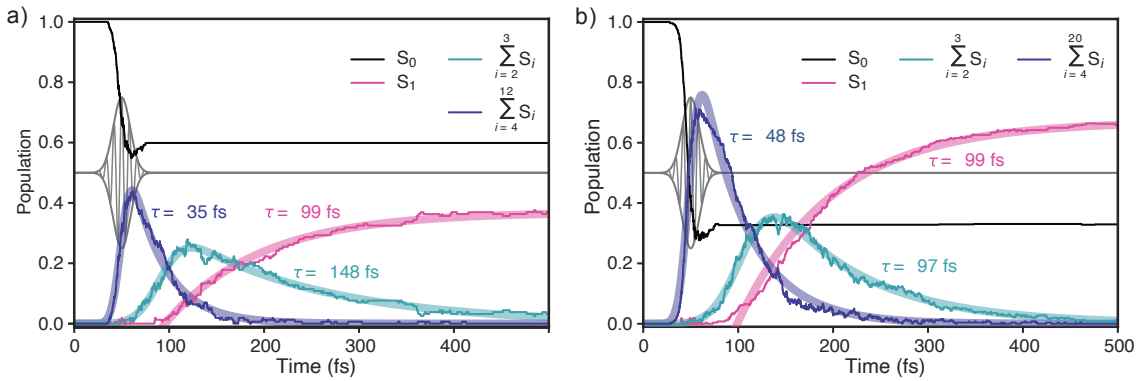

Figure 5.3: Population of an ensemble of 150 trajectories of the electronic states during the field-induced surface-hopping dynamics of **PyB'** (a) and **Py$_2$B** system (b). The bold red line shows the fit of the S_1 population to the following fit function: $F(t) = -A\exp\left(-\frac{t-t_0}{\tau}\right)+B$. The blue and green bold lines show the fit of the summed populations to the following fit function: $G(t) = A\cdot\exp\left(-\frac{t-t_0}{\tau}\right)\cdot\exp\left(\frac{b^2}{4\sigma^2}\right)\cdot\left[1+\mathrm{erf}\left(\frac{t-t_0-\frac{b^2}{2\sigma}}{b}\right)\right]$. In both functions τ is the time constant for the population decay/increase and t_0 is the center of the maximal field amplitude.

calculated by evaluating the autocorrelation function of the transition dipole moment during the dynamics,

$$R(t) = \frac{2}{5}N^e_{\mathrm{traj}}(t)^{-1}\sum_{i=0}^{N^e_{\mathrm{traj}}(t)} P_2\left(\langle\mu_{\mathrm{eg}}(0),\mu_{\mathrm{eg}}(t)\rangle\right), \tag{5.12}$$

where P_2 is the second order Legendre polynomial and the argument is the auto-correlation function of the transition dipole moment between the ground state and electronic excited state which is initially excited, $\mu_{\mathrm{eg}}(0)$, and the transition moment between the ground state and the actual electronic state at time t, $\mu_{\mathrm{eg}}(t)$.

5.3 Results and Discussion

5.3.1 Structural and electronic properties

In Figure 5.1, a schematic representation of the pyrene-**BODIPY** dyad and triad is presented. The pyrene and **BODIPY** subunits are coplanar in the ground state structure, lying in the xy-plane such that the longitudinal and transversal axes of the molecule are parallel to the x-axis and y-axis, respectively. The **PyB'**-system (dyad) contains only one pyrene unit, while the **Py$_2$B**-triad has two pyrene units and a 4-methoxyphenyl group which are linked to the **BODIPY** core on the 8-position. The simulated absorption spectra for the **PyB'** and **Py$_2$B** are shown in Fig. 5.2b and d, respectively. In order to simulate the spectra, a Wigner ensemble consisting

of 150 structures drawn from a T=300 K thermal ensemble has been used. The spectra have been calculated at the AM1-CIS level and were superposed in order to produce thermally broadened absorption profiles. In both conjugates, the spectrum consists of two dominant and one weak absorption bands. The first band is located at 19500 cm^{-1} and has a narrow band shape. The corresponding S_0-S_1 transition is strongly localized on the **BODIPY** unit (see upper part of 5.2a and b). The second band is located between 24000 cm^{-1} and 27000 cm^{-1} and is mainly localized on the outer pyrene units. The S_5-state (in the dyad) and the S_6-state (in the triad) are lying in between the second and the third absorption band, having some oscillator strengths and are mainly localized on the **BODIPY** unit. The third band, having a broad shape, is centered at around 31500 cm^{-1} and originates from a delocalized excitation in both system.

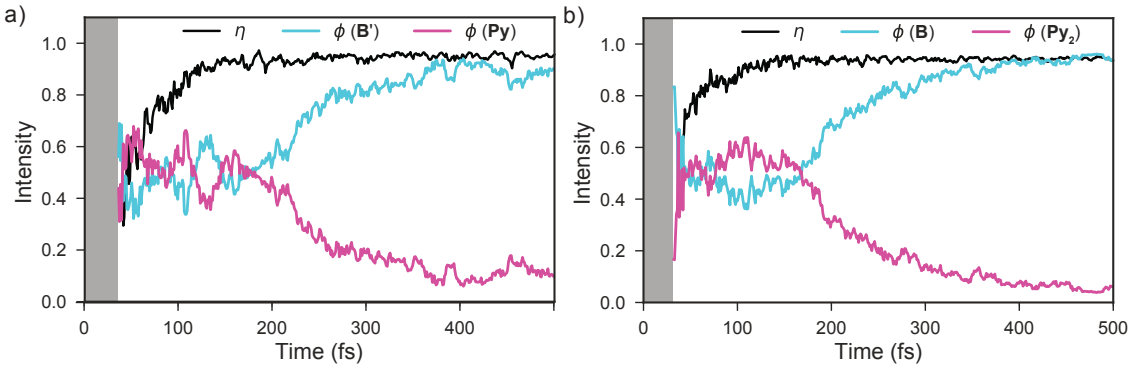

Figure 5.4: Integrated transition densities, between the ground state and the current state, on a given subunit (red: **BODIPY**; blue, pyrene) averaged over the whole ensemble of the **PyB'** (a) and **Py_2B** system (b). The degree of localisation (see Eq. 5.8) η is shown as a black curve. A value of 0 corresponds to a full delocalisation of every trajectory and a value of 1 to localisation of the excitation of every trajectory at a given time.

5.3.2 Light-Induced Dynamics

In order to reveal the mechanism of the exciton transfer from the pyrene to **BODIPY** units that take place following the excitation, we have performed simulations of the light-induced dynamics in the **PyB'** system by using the field-induced surface-hopping (FISH) methodology[54] as described above. The applied pump laser pulse of 31165 cm^{-1} central wavelength has been used. Given the high number of energetically close-lying excited states, the light pulse populates a manifold of electronic states rather than a single one. In order to facilitate the analysis, we present in Fig. 5.3a the populations for the three characteristic groups of states. Since the state populations from the S_4- up to the S_{12}-state show a very similar population decay, their populations have been summed up, giving rise to the blue traces in Fig. 5.3a. It is clearly visible that, within a short time of 35 fs, most of the trajectories leave

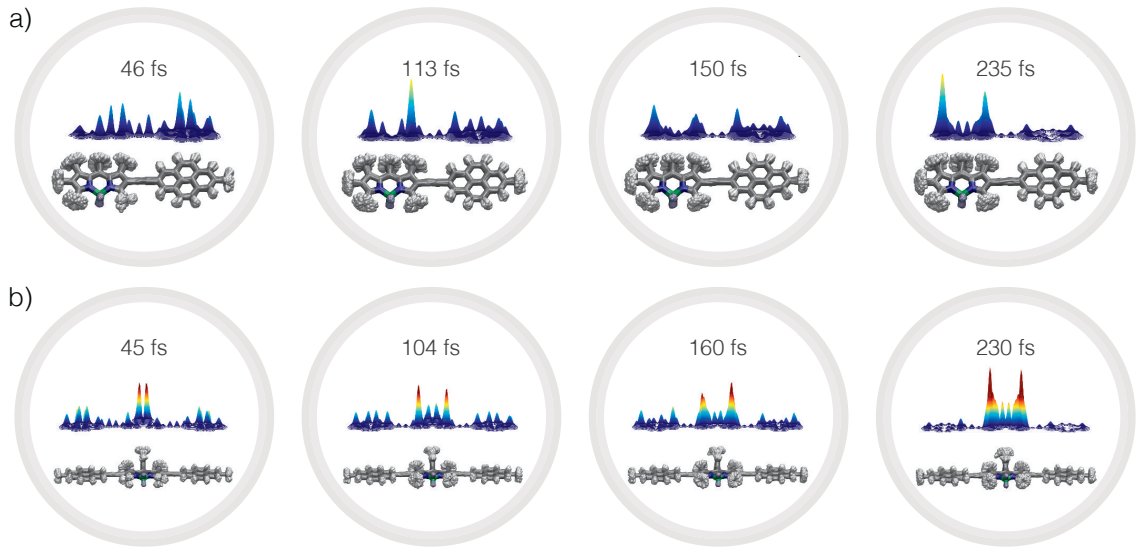

Figure 5.5: Integrated ensemble transition density along the z-axis as defined in Eq. 5.11 (middle of each figure) and superposition of the molecular structures of all trajectories (bottom of each figure) during the FISH dynamics of **PyB'** (a) and **Py_2B** (b)

the higher-lying states and the intermediate S_2- and S_3-states get populated. The joint population of these states is shown in green traces in Fig. 5.3a. On a time scale of about 150 fs, a second population transfer from the S_2 and S_3 to the S_1-state sets in. There are also some direct transitions from the higher lying states to the first excited state. The time constant for the population of the S_1-state is about 100 fs. The transfer of population from higher states to S_1 sets in after a time delay of 100 fs. In Fig. 5.3b we show the time-dependent electronic state populations of the **Py_2B**-triad. The laser pulse, which is resonant with the intense transition from the ground state to the second broad absorption band (see the red area in Fig. 5.2d), leads to significant population transfer to the higher lying states. The whole ensemble was propagated for 500 fs and the overall excitation efficiency is about 70%. We have summed the population of the S_4- up to the S_{20}-state, as in the case of the dyad, because these states show very similar population decay. Within a short time of about 50 fs, most of the trajectories leave the higher-lying states and the S_2- and S_3-states are populated (see the green line in Fig. 5.3b). The population of these states rises only up to 35 % because some of the trajectories relax directly into the first excited state. The decay of the second and third excited states is, with about 100 fs, on the same time scale as the population increase of the S_1-state. No transitions to the ground state take place within the simulation time of both systems, which is consistent with the experimental observations of luminescence in similar systems.[11,64,207]

5.3.3 Exciton dynamics

In order to analyze the exciton dynamic, we have monitored the monomeric state population along the trajectories by integrating the square of the transition density (TD) as described above. The two resulting functions are presented in Fig. 5.4, which show the distribution of the excitation on the given subunits.
The excitation of the **PyB'** at 32 fs is accompanied by a delocalized exciton motion over the whole system. The period in which the exciton oscillates during the first 200 fs between each monomer is about 60 fs. After 200 fs, the energy transfer sets in and the excitation gets strongly localized on the **B'**-subunit within 100 fs.
Whereas excitation in the $\mathbf{Py_2B}$-systems leads to very short localisation of the TD at 4-methoxyphenyl group, which is followed by an evenly distributed exciton at ensemble level. During the following 100 fs, the allocation of the excitation resides with a low maximum of localisation at the pyrene unit at around 110 fs. This is accompanied by a transfer to **BODIPY** within another 100 fs. The localisation at the **B** unit is above 90 % at the end of the dynamics simulation.
After excitation, the degree of localisation on an average trajectory level is about 30 % (60 %) in the dyad (triad), and almost immediately, it starts to increase (see the black curve in Fig. 5.4a). In less than 100 fs, the excitation is primarily localized on one of the monomers, as indicated by a degree of localisation of around 90 %. Hence we see a mainly localized exciton motion on a single trajectory level but going to an ensemble perspective translates to a delocalized dynamics of the particle-hole pair.
We have animated the exciton motion on an ensemble level to gain a deeper insight into energy transfer. In Fig. 5.5, we show four snapshots of the dynamics: These ensemble densities are shown together with a superposition of the molecular structures of all trajectories in each picture in Fig 5.5a. The interaction with the laser pulse leads to a "mixed" transition density, which is generally delocalized, but the main part is located on the **Py**-unit. This situation changes quickly so that most of the exciton stays at the **B'** molecule at 113 fs (see Fig. 5.5a). During the next 100 fs, the excitation is transiently localized/delocalized on a short timescale. This behaviour represents the oscillations of fully integrated transition densities that are shown in Fig. 5.4. After 200 to 250 fs, the energy transfer sets in and the excitation is exclusively located at the **B'**-unit and stays there for the rest of the simulation time. It is also visible from the bottom of each subfigure (in Fig. 5.4) that the aromatic system of the dyad remains planar, and only the hydrogens were distorted during the dynamics. The excitation of electronic states, whose character is dominated by the pyrene states, creates a coherent, delocalised wavepacket and it is subsequently transferred to the **B'** unit. We also calculated these ensemble densities for the triad system, as shown in Fig. 5.5b. Here the laser pulse leads to strong localisation of the TD at the 4-methoxyphenyl group and a substantial contribution on the pyrene units at the beginning of the excited state dynamics. Within 50 fs, the amplitude at the phenyl ring decreases and the exciton gets distributed over the whole system, with a significant amplitude on the **BODIPY** fragment. During this part of the simulation,

oscillations between the pyrene-subunits and the **BODIPY** occur (cf. Fig. 5.5b). At around 200 fs, the TD gets increasingly localised on the **BODIPY** molecule and resides there until the end of the FISH simulations.

5.3.4 Polarisation anisotropy

The polarisation anisotropy is an important observable that bridges the gap between experimental measurements and theoretical simulations, as it allows to directly track the population of electronic states if they differ in the transition dipole moment polarisation. In some instances, it allows the detection of exciton localisation or delocalisation[239,246], but this is not the general case in molecular aggregates, as this requires that the transition dipole moment between the ground state and the electronic state wavefunction and the localisation/delocalisation of the wave function are in direct correlation, which does not have to be the case. The dynamics of the polarisation anisotropy can be explained by a simple three state model, which corresponds to the three populations shown in Fig. 5.3. The initial and final states are polarized along the x-axis (longitudinal molecular axis), while the intermediate state is characterized by transition dipole moment with comparable x- and y-components. The relaxation from the initial state leads to a decrease in the polarisation anisotropy (cf. Fig 5.6), as the polarisation of the current excited state changes. The time constant for this anisotropy decay is therefore directly correlated to the blue population decay shown in Fig. 5.3. Afterwards, the relaxation to the first excited states leads to an increase in the anisotropy to a value between 0.3 and 0.38. Since the S_1 is strongly localised on the **BODIPY**-unit, this increase in the polarisation anisotropy can be directly linked to the exciton localisation (*cf.* Fig 5.4). But it should be noted that the signal in the anisotropy would be exactly the same if the S_1-state were delocalised. Therefore the experimental measurements of polarisation anisotropy should be linked with theoretical simulations to validate, on the one hand, the simulated rate constants, and on the other hand, to get a complete picture of the exciton motion.

5.4 Conclusions

In this work, the energy transfer dynamics in pyrene-**BODIPY** conjugates (dyad and triad) were studied by field-induced surface-hopping nonadiabatic dynamics simulations. The ensemble was propagated under the influence of a laser pulse resonant to the second bright absorption band for several hundred femtoseconds. The trajectories were promoted to a range of high-lying excited states, and after the pulse had ceased, a subsequent nonradiative relaxation process was observed, yielding a complete population transfer to the S_2- and S_3- excited state in both systems on a timescale of around 40 fs. This is accompanied by a change in orientation of the transition dipole moment between the ground state and the populated electronic state, from a longitudinal direction to an orientation between transversal and longitudinal.

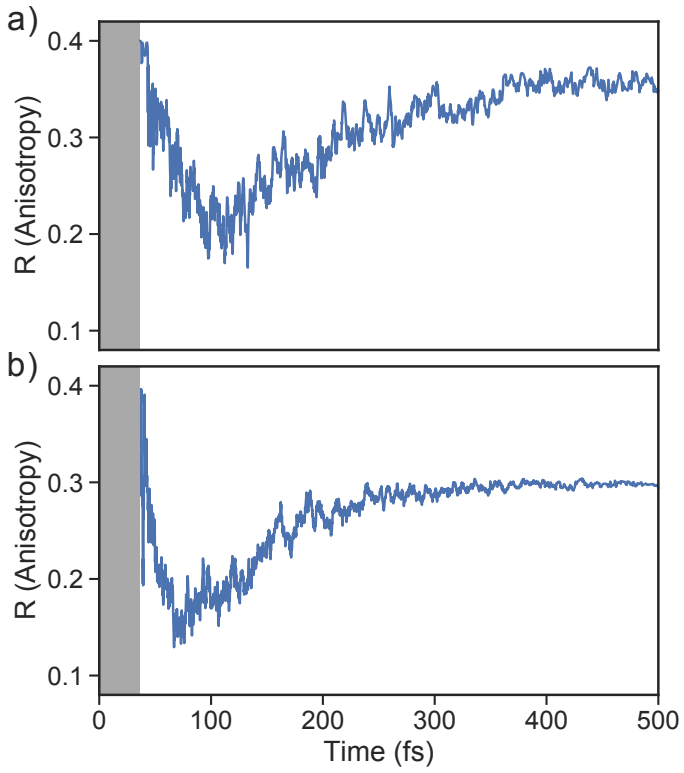

Figure 5.6: Simulated anisotropy curves for the **PyB'** (a) and **Py_2B** (b). The definition of R is given in Eq. 5.12.

Such changes in polarisation can be directly tracked by polarisation-anisotropy spectroscopy, as shown by the theoretical simulations. The electronic relaxation from the S_3/S_2-states to the lowest S_1 state finally localises the excitation almost completely on the **BODIPY** unit in both conjugates within 100 fs. This comes with a reorientation of the transition dipole moment along the longitudinal molecular axis. Therefore, the direct correlation between the S_1 population and exciton localisation degree makes it possible to track the ultrafast exciton localisation by time-resolved polarisation-anisotropy measurements. Finally, we note that exciton localisation on the **BODIPY** unit in the dyad and triad system takes place on an equal time scale and is thus neither delayed nor shortened by linking a second pyrene unit to the **BODIPY**. In both systems, the excitation energy transfer and exciton localisation is mediated by a cascade of nonradiative transitions induced by nonadiabatic coupling between the excited states.

Chapter 6

Excimer formation dynamics in the isolated tetracene dimer

The understanding of excimer formation and its interplay with the singlet-correlated triplet pair state ^{1}(TT) is of high significance for the development of efficient organic electronics. Here, we study the photoinduced dynamics of the tetracene dimer in the gas phase by time-resolved photoionisation and photoion imaging experiments as well as nonadiabatic dynamics simulations in order to obtain mechanistic insight into the excimer formation dynamics. The experiments are performed using a picosecond laser system for excitation into the S_2 state and reveal a biexponential time dependence. The time constants, obtained as a function of excess energy, lie in the range between ≈10 ps and 100 ps and are assigned to the relaxation of the excimer on the S_1 surface and to its deactivation to the ground state. Simulations of the quantum-classical photodynamics are carried out in the frame of the semi-empirical CISD and TD-lc-DFTB methods. Both theoretical approaches reveal a dominating relaxation pathway that is characterised by the formation of a perfectly stacked excimer. TD-lc-DFTB simulations have also uncovered a second relaxation channel into a less stable dimer conformation in the S_1 state. Both methods have consistently shown that the electronic and geometric relaxation to the excimer state is completed in less than 10 ps. The inclusion of doubly excited states in the CISD dynamics and their diabatisation further allowed to observe a transient population of the ^{1}(TT) state, which, however, gets depopulated on a timescale of 8 ps, leading finally to the trapping in the excimer minimum.

6.1 Introduction

Polyacenes are of interest in materials science, because they can act as hole conductors in organic devices. In particular tetracene and pentacene have been identified as candidates that fulfil the photophysical requirements for singlet fission (SF), a process in which an excited singlet state deactivates to two triplets located on neighbouring molecules. The underlying physics has been described in several reviews.[254–258] The major condition for SF is the existence of a low-lying triplet state at half the energy of the initially excited singlet state. SF has already been demonstrated to improve the efficiency of solar cells[259,260] and thus it receives considerable attention. In tetracene, the T_1 state is slightly too high for SF to occur from the S_1 origin, but already some vibrational excitation suffices to fulfil the energy condition. Due to its importance as a model for SF, various systems with tetracene chromophores have been studied. SF is envisioned to proceed in two steps, (a) formation of a pair of singlet-correlated triplets from the initially excited state, which then (b) decouples to two triplets on separate molecules.[257] However, a consistent picture of the dynamics has not yet emerged. The radiationless relaxation in the tetracene monomer was studied by Spiegelman *et al.* by employing nonadiabatic dynamics simulations.[261] Further nonadiabatic dynamics simulations on covalently linked tetracene dimers and tetracene clusters were conducted to study the exciton localisation process.[240,262] Studies by Burdett *et al.* compared the dynamics in solution with polycrystalline films and revealed an important role of defect states for the dynamics.[263] Thin films were investigated by transient absorption in the group of R. Friend and by Schmidt and coworkers, who both observed time-constants of around 80-90 ps. While Friend *et al.* attributed the time constant to the formation of triplet pairs from S_1, i.e. to singlet fission,[264] Schmidt and coworkers assigned the transient signal to a transition from S_1 to a multi-exciton state that possibly deactivates to separated triplets in a later step.[265] Numerous experiments dealt with tetracene units connected by linkers. Bradforth and coworkers recently reported the linker-dependence of SF in such assemblies dissolved in THF, applying a variety of time-resolved and steady-state spectroscopic techniques,[266] while Damrauer and coworkers explored structurally rigid dimers extensively.[267–270] In contrast, experiments on isolated dimers in a free jet permit a direct comparison with theory and offer an understanding of non-radiative relaxation processes on the molecular level without perturbations by the environment. Such experiments, which could give insight into the relationship between structural changes after excitation and subsequent non-radiative processes are however still scarce. In particular a description of excimer formation, which may compete with or precede the formation of a singlet-correlated triplet pair[40,257,271,272] is lacking. While some studies claimed that excimer formation constitutes an intermediate step in SF, Dover *et al.* investigated TIPS-tetracene in solution and found excimers to act as traps that hinder SF.[273] Very recently, comprehensive benchmarks on tetracene dimers, stacked and T-shaped, were performed by Cardozo *et al.* showing an overall good agreement between TD-lc-DFTB, TD-DFT, SOS-ADC(2) and DFT/MRCI.[274] A thorough in-

vestigation of excimer formation in tetracene thus seems to be mandated. Recently, the excimer formation of benzene was studied in detail experimentally by Fuji *et al.*[275] and by simulation by the groups of Krylov[276] and Cardozo[277]. The excimer formation dynamics were also studied in larger systems like bay-tethered perylene bisimides by Würthner *et al.*, where a single relaxation pathway to the excimer state was found.[39] We recently explored the excimer formation in isolated pyrene dimers in a joint computational and experimental study.[13] Upon photoexcitation, the parallel displaced dimer relaxed to a stacked geometry, which subsequently leads to excimer formation. The simulations led to the identification of two degrees of freedom associated with this process: (i) local relaxation along the stacking coordinate close to the FC window and (ii) large amplitude oscillations along the parallel shift coordinate accompanied by damped oscillations along the stacking direction. The combined motion leads to the stabilisation of the excimer on a time scale of around 5 ps. Here we address the tetracene system with the goal to understand the deactivation processes occurring in the photoexcited dimers, in particular excimer formation. In the experimental work the dynamics is monitored by time-resolved photoionisation. A picosecond (ps-) laser system is employed, which permits to study the dynamics as a function of excitation energy. The advantages of ps-lasers have been demonstrated in previous work on molecular dimers and clusters.[8,13,278,279] Nonadiabatic dynamics simulations are performed at the semi-empirical CISD level and in the frame of TD-lc-DFTB in order to explore the processes that set in after the electronic excitation and to identify the dominating relaxation channels.

6.2 Computational Details

6.2.1 Structural properties and absorption spectra

The electronic structure of the tetracene dimer has been described in the framework of density functional theory (DFT) employing the hybrid ωB97X-D functional[71] as implemented in the Gaussian16 software package[222] combined with the def2-SVP basis set[72]. The vibrationally resolved absorption spectra for the optically bright $S_2 \leftarrow S_0$ transition were simulated within the Franck–Condon approximation employing the adiabatic Hessian model (AH) and the vertical gradient method (VG), as implemented in the Santoro program of J. Cerezo and F. Santoro.[280,281]

6.2.2 Nonadiabatic dynamics simulations

The nonadiabatic dynamics simulations of the excimer formation process have been performed by employing Tully's surface hopping approach[55] in combination with a modified calculation scheme for the hopping probabilities[63] and using a local diabatisation method to propagate the electronic wavefunction[282,283]. A time step of 0.1 fs was used for the surface hopping simulations. Two sets of trajectories were

propagated by employing two different levels of theory. In the first set the efficient TD-lc-DFTB method which offers a good compromise between accuracy and computational cost[284–288] was used and 34 trajectories were simulated for 10 ps. A reduced active space composed of the highest 24 occupied and the lowest 24 virtual orbitals, denoted as (48e, 48o) in what follows, was used for the excited state calculations at the TD-lc-DFTB level. This space provides a good compromise between accuracy of excitation energies and the computational time needed for surface hopping calculations.
The second set of trajectories was propagated for up to 20 ps using semi-empirically parameterised configuration interaction with singles and doubles (CISD) with the PM6-D3H4 parameterisation[289–291]. Here, an active space of only 2 occupied and 2 virtual orbitals was selected, which shows qualitative agreement with TD-lc-DFTB and TD-DFT (ωB97X-D/def2-SVP) and requires a feasible amount of computational time. CISD allows to include the doubly excited states which are involved in the singlet-fission process (e. g. singlet-correlated triplet pair state). The TD-lc-DFTB calculations were performed using the software package DFTBaby[286] while MOPAC2016[292] was used for the semi-empirical CISD computations.
The ground-state phase-space distribution, from which the initial conditions were sampled, has been approximated by a canonical Wigner distribution calculated in the harmonic approximation.[251,252] For nonadiabatic dynamics simulations employing TD-lc-DFTB, 34 normal mode displacements and momenta were sampled at 50 K. Afterwards, these geometries were equilibrated to 20 K by performing ground-state dynamics at constant temperature using a Berendsen thermostat[293]. The Cartesian coordinates and velocities after equilibration were used as initial conditions for the nonadiabatic trajectory simulations. The equilibration step is needed in order to relax the high frequency modes, which tend to be too strongly excited if a harmonic distribution is sampled. For dynamics employing CISD, 100 of such initial conditions were generated. For all the sampled nuclear configurations the $S_2 \leftarrow S_0$ transition was found to be the most intense one. Therefore, all surface-hopping trajectories were launched from the S_2 state.

6.2.3 Analysis of nonadiabatic dynamics in diabatic picture

In order to analyse the electronic character of adiabatic states as computed along nonadiabatic CISD trajectories, one must at first localise the molecular orbitals (MOs) to each monomer. This was realised by using a localisation procedure based on a singular value decomposition (SVD) of the MO coefficients.[283,294,295] The basic idea is to divide the coefficient matrix for n occupied molecular orbitals into rectangular submatrices, each of which contains only AOs on one monomer. Principal component analysis (PCA) was then performed on all submatrices using SVD. The obtained right singular vectors with largest singular values were selected and assigned to the corresponding monomer. Since these vectors in general originate from different

submatrices, they were Löwdin orthogonalised[296] to form a unitary matrix $\mathbf{V}$, which transforms the original occupied MOs (φ_i) into localised occupied orbitals

$$\overline{\varphi}_k = \sum_{i=1}^{n} \varphi_i V_{ik} \quad k = 1, 2, ..., n. \tag{6.1}$$

The overline denotes transformed localised orbitals. The same procedure can be applied for the m virtual MOs in the active space, which results in localised virtual orbitals

$$\overline{\varphi}_c = \sum_{a=1}^{m} \varphi_a V_{ac} \quad c = 1, 2, ..., m. \tag{6.2}$$

The squared elements from the CI coefficient matrix for the d-th state $\left(C_{ia}^{d}\right)^2$ describe the contribution of a specific singly excited configuration. With the help of the unitary matrices V_{ik} and V_{ac}, one can transform the coefficient matrix from the MO basis into the basis of localised orbitals[297] giving rise to

$$\overline{C}_{kc}^{(\alpha_k,\alpha_c)} = \sum_{i,a} V_{ac} C_{ia}^{d} V_{ik}. \tag{6.3}$$

These elements can then be labelled with the initial monomer α_k, to which the localised orbital $\overline{\varphi}_k$ belongs, and the final monomer α_c, to which $\overline{\varphi}_c$ belongs. This way, one can define the contribution for local excitation (LE) p^{LE} by summing up all squared elements with $\alpha_k = \alpha_c$

$$p^{\mathrm{LE}} = \sum_{\substack{k,c \\ \alpha_k = \alpha_c}} \left(\overline{C}_{kc}^{(\alpha_k,\alpha_c)}\right)^2 \tag{6.4}$$

and the contribution for charge transfer (CT) p^{CT} by summing up all squared elements with $\alpha_k \neq \alpha_c$

$$p^{\mathrm{CT}} = \sum_{\substack{k,c \\ \alpha_k \neq \alpha_c}} \left(\overline{C}_{kc}^{(\alpha_k,\alpha_c)}\right)^2. \tag{6.5}$$

The coefficients for double excitations can be transformed into the basis of localised orbitals in a similar manner using

$$\overline{C}_{klcd}^{(\alpha_k,\alpha_l,\alpha_c,\alpha_d)} = \sum_{i,j,a,b} V_{bd} V_{ac} C_{ijab}^{d} V_{ik} V_{jl}. \tag{6.6}$$

The squared elements with $\alpha_k = \alpha_c$ and $\alpha_l = \alpha_d$, or $\alpha_k = \alpha_d$ and $\alpha_l = \alpha_c$ can be summed up to obtain the contribution of the multiexciton (two triplets coupled into

a singlet) state (^{1}(TT)) $p^{^1(\mathrm{TT})}$,

$$p^{^1(\mathrm{TT})} = \sum_{\substack{k,l,c,d \\ (\alpha_k=\alpha_c \wedge \alpha_l=\alpha_d) \\ \vee(\alpha_k=\alpha_d \wedge \alpha_l=\alpha_c)}} \left(\overline{C}_{klcd}^{(\alpha_k,\alpha_l,\alpha_c,\alpha_d)}\right)^2, \tag{6.7}$$

and all other squared elements sum up to the contribution of other doubly excited states p^{RST}.
The weight of a specific adiabatic state $X \in \{\mathrm{LE}, \mathrm{CT}, ^1(\mathrm{TT}), \mathrm{RST}\}$ can finally be obtained by normalising the contributions p^X

$$P^X = \frac{p^X}{\sum_Y p^Y}. \tag{6.8}$$

6.3 Experimental methods

All gas phase experiments were conducted in a differentially pumped vacuum chamber, which has been described in more detail in a previous publication[298]. Tetracene ($C_{18}H_{12}$, 228 g/mol) was purchased from Sigma-Aldrich and used without further purification. The sample was placed in a home-built oven, heated up to around 200 °C, seeded in argon or helium and expanded into vacuum *via* a pulsed valve with a 300 μm diameter nozzle. After around 2 cm, the produced supersonic jet passed a conical skimmer (aperture 2 mm) and reached the main chamber of the setup, where it was crossed by the laser beams. The presence of clusters in the molecular beam depended strongly on the expansion conditions. Experiments on monomeric tetracene were carried out at low argon or helium backing pressures ($p_0 \approx 1.2$ bar), temporally short molecular pulses (FWHM ≈ 150 μs) and at the leading edge of the gas pulse. In contrast, experiments on the dimer required higher backing pressures ($p_0 \approx 1.6$–1.8 bar) and longer molecular pulses (FWHM ≈ 400 μs) and the laser was synchronised closer to the centre of the pulses. As light source we used a system based on a picosecond Nd:YLF laser that was also described earlier[299]. The third harmonic of the 1053 nm fundamental (351 nm, 3.532 eV) was produced via frequency tripling (SHG and SFG) and used to pump an OPG, which generated tuneable laser pulses with a bandwidth of around 10 cm^{-1}. The OPG output pulses were used to excite the molecules, while the fourth harmonic of the setup (263.5 nm, 4.705 eV) was employed as probe wavelength in the two-colour [1+1'] REMPI experiments. The instrument response function (IRF) of the laser setup was found to be around 4 ps. Both pulses were overlapped with a dichroic mirror in front of the vacuum chamber and slightly focused into the molecular beam. For experiments aimed at the monomer, unfocused pump pulses were used, since no cluster fragmentation was visible under these conditions. Typically, both laser pulses were vertically polarised, however rotating one of the polarisations did not affect the experimental results.
A velocity map imaging ion optics[300] accelerated the photoions onto an imaging

detector, consisting of two microchannel plates (MCPs) in Chevron configuration and a P43 phosphor screen. In the TOF-MS experiments, the photoion signal was measured by a home-built current monitor. Typically, each data point was averaged over 50 laser shots. For the REMPI spectra, three scans with a step size of 0.2 nm were averaged, while the time-delay traces consist of ten scans with 50 time steps per trace. In the photoion VMI experiments, the light emitted from the phosphor screen was recorded with a CCD camera yielding 2D raw images, each averaged over 1800 laser shots. The images were reconstructed *via* the pBASEX method[301], employing Legendre Polynomials up to the 2nd order. To ensure mass selectivity in the VMI experiments, the voltage applied on the second MCP of the dual-stage detector was gated on the arrival time of the dimer species with a gate width of 150 ns employed by a push/pull switch.

6.4 Results

6.4.1 Structural properties.

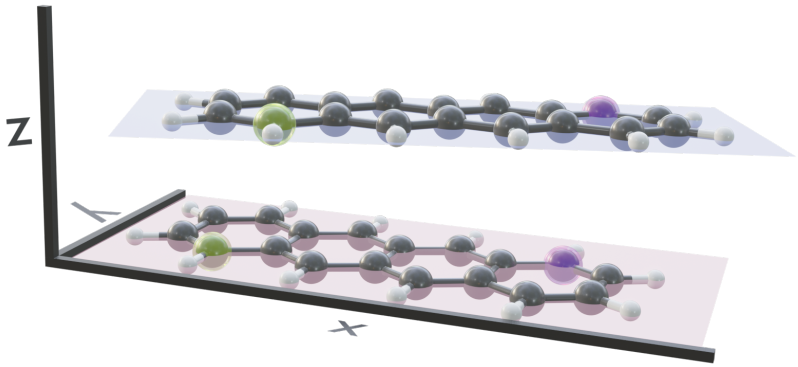

Figure 6.1: The optimised ground state geometry of the most stable tetracene dimer isomer. The longitudinal axes of the molecules close an angle of approximately 25°. The displacement in z-direction R_z is 3.27 Å and the distance between centres-of-mass 3.48 Å.

Several stable conformers of the tetracene dimer are described in the literature. Both experimentally and theoretically, a slightly rotated, stacked geometry was found to be the most stable arrangement.[274,302] Experimentally, the authors elucidated these structures from angular covariance maps recorded in a strong-field laser ionisation experiment of tetracene in helium nanodroplets. The optimised ground state geometry at the DFT(ωB97X-D/def2-SVP) level is shown in Fig. 6.1. The two longitudinal axes of the molecules close an angle of approximately 25°. The molecular planes are parallel and their centres are shifted slightly in x-direction. The displacement in x- and y-direction R_x and R_y, as well as the rotation about z-direction Rot_z, were evaluated with regard to the coordinate system of the first monomer as shown in Fig. 6.1. The axes were determined by performing a singular value decomposition (SVD)

on the coordinates of all carbon atoms of a single monomer with the centroid subtracted. The right singular vectors sorted by descending singular values were selected as x-, y- and z-axis, respectively. However, since the singular vectors do not possess a consistent direction, the vector spanning from the yellow carbon atom to the violet one in each monomer (as depicted in Fig. 6.1) was used to calibrate the positive direction of both x- and y-axis. The positive direction of z-axis follows from the right hand rule. The displacements in x- and y-directions were obtained by projecting the displacement vector between the centroids of both monomers on to x- and y-axis of the first monomer, respectively. The rotation about z-axis is obtained by evaluating the dihedral angle of both monomeric x-axes.

6.4.2 Potential energy curves

In order to investigate the energetic landscape of the interaction between both monomers, the energies of several electronic states were determined with respect to displacements in x- and z-directions using CISD(4e,4o, PM6-D3H4), TD-lc-DFTB and ωB97X-D/def2-SVP. Starting from a monomer structure that was optimised in its first excited singlet state (S_1), the potential energy curves (PECs) along x-displacement were generated by setting R_y to 0 and R_z to a specific value and shifting one monomer rigidly along the x-axis of the other. The value of R_z was chosen to be the distance for which the PEC of S_1 has a minimum for $R_x = R_y = 0$. Optimisations and single-point calculations were performed by using the same method. The PECs along z-displacement were generated by starting from the S_1 optimised dimer geometry at SOS-ADC(2) level obtained by Cardozo *et al.*[274] and shifting one monomer rigidly along the z-axis of the other monomer. The distances R_z were determined by measuring distances between the planes obtained using SVD as described above. Our results obtained with TD-lc-DFTB agree very well with the potential energy curves of Ref.[274] (see left side of Fig. 6.2). Despite employing the same method, the results differ slightly quantitatively because we use different Slater-Koster parameters and repulsive potentials in DFTBaby compared to DFTB+[303]. We have omitted a comparison to TD-DFT at this point, as we refer the reader to Ref.[274] for a more detailed comparison of the quantum chemical methods. There, it is observed that DFT/MRCI predicts a doubly excited state lying below the bright state at the optimised S_1 geometry that cannot be described by ordinary TD-DFT(B). In a comparison with the DFT/MRCI results of Ref.[274] it is evident that the semi-empirical CISD results agree qualitatively well. The right side of Fig. 6.2 depicts the potential energy curves at the CISD level, where the red curve shows the doubly excited 3^1A_g state. Since this double excited state could be important for the excimer relaxation as well as for the formation of the singlet-correlated triplet pair state, we simulated the nonadiabatic dynamics not only using TD-lc-DFTB but also at the semi-empirical CISD(4e,4o) level.

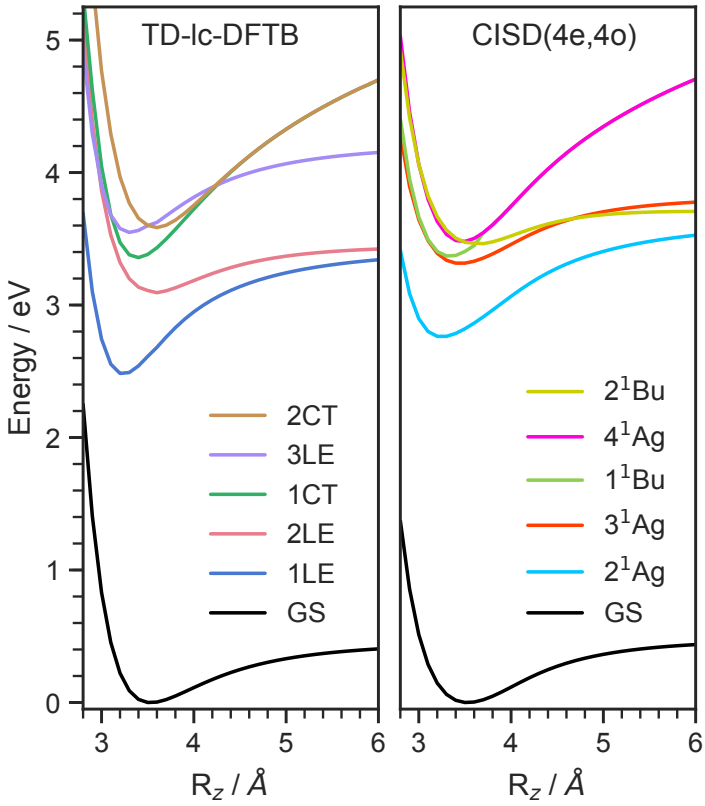

Figure 6.2: Potential energy curves along the intermolecular stacking coordinate (R_z) as defined in the text. The energies are relative to the minimal energy structure in the electronic ground state. The electronic excited states are diabatically connected in a similar way as done in Ref.[274] to to be able to readily compare the performance of the quantum chemical methods. In TD-lc-DFTB case, states are labelled based on their character, while for CISD, symmetry labels are used.

6.4.3 TOF-MS spectra

In a first experiment we recorded one-color REMPI spectra of the transitions into the S_1 (B_{2u}) and S_2 states in monomeric tetracene, which are depicted in the ESI of Ref. 5 (Fig. S1 and S2). It illustrates that at least at low excess energies individual vibronic bands can be resolved. Since the ionisation energy (IE) of the monomers is 6.97 eV[304] and the S_1 origin is located at 22397 cm^{-1} (2.78 eV),[305] a [1+2] REMPI process is required for ionisation via S_1. In good agreement with previous work,[305–307] the origin was found at 22406 cm^{-1} (446.3 nm). Furthermore, some well resolved vibronic modes were detected in the region up to +2000 cm^{-1}, with the most intense one at +1517 cm^{-1}.

At expansion conditions which favour the formation of multimeric species, even at excitation energies below the S_1 origin an intense signal is present in the mass spectrum at m/z = 228 (see Fig. 6.3, lower trace). The additional small peak at m/z = 456

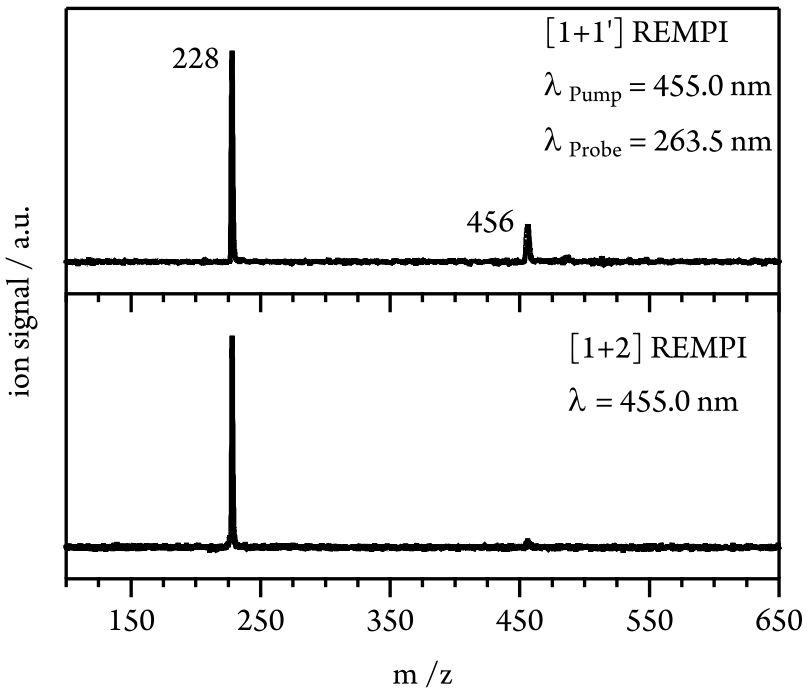

Figure 6.3: Mass spectra from [1+2] (lower trace) and [1+1'] (upper trace, $\lambda_{\mathrm{Probe}} = 263.5$ nm) ionisation at an excitation energy ($\lambda_{\mathrm{exc}} = 455.0$ nm, 2.73 eV) below the S_1 origin of monomeric tetracene (2.78 eV).

corresponds to the dimer and indicates strong fragmentation of the dimer cation due to the high excess energy provided in the [1+2] REMPI process (1.21 eV relative to the monomer IP at $\lambda = 455.0$ nm). To lower the excess energy and to suppress dissociative photoionisation (DPI), we therefore switched to [1+1'] REMPI experiments. Using a probe wavelength of $\lambda_{\mathrm{Probe}} = 263.5$ nm (4^{th} harmonic of Nd:YLF laser) gives a total photon energy of 7.43 eV (at $\lambda_{\mathrm{Pump}} = 455.0$ nm) and an excess energy of only 0.46 eV relative to the monomer IE. As can be seen in Fig. 6.3 (upper trace), the dimer signal is significantly enhanced compared to [1+2] ionisation. However, the monomer peak still dominates the spectrum and thus fragmentation of clusters has to be taken into account in the interpretation of the experimental data.

6.4.4 REMPI spectra and simulated absorption spectra

In the next step an absorption spectrum of the tetracene dimer was recorded. The pump-probe delay time was fixed to 20 ps and the dimer ion signal was recorded as a function of the excitation wavelength. The [1+1'] REMPI spectra ($\lambda_{\mathrm{Probe}} = 263.5$ nm) obtained in argon and helium as carrier gases are both presented in Fig. 6.4a). As can be seen, the spectra show three well defined maxima at 455.0, 427.0 and 403.5 nm. The band positions perfectly match in both spectra, however the higher energy bands are more pronounced in argon. In previous work an absorption

spectrum of the tetracene dimer in solution with an onset around ∼416 nm has been reported[308] which is in good agreement with our results.
In order to gain further information on the excited dimer species and to check quality of the quantum-chemical methods, the dimer absorption spectrum was calculated using TD-DFT (ωB97X-D/def2-SVP) and semi-empirically parameterised CISD(4e,4o). The vibrationally resolved absorption spectrum at the TD-DFT level is shown in Fig.

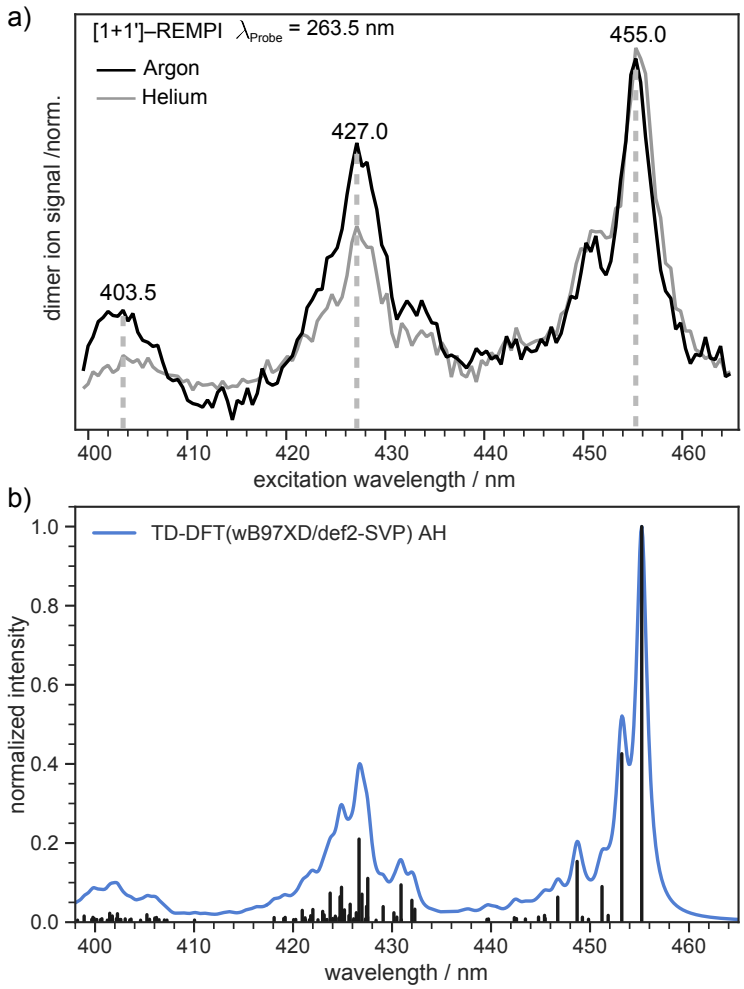

Figure 6.4: (a) [1+1'] REMPI spectrum (λ_{Probe} = 263.5 nm) of the tetracene dimer in argon and helium as carrier gas. Three distinct maxima can be seen at 455.0, 427.0 and 403.5 nm. (b) Simulated vibrationally resolved absorption spectrum of the most stable isomer at the TD-DFT level. The individual transitions (black sticks) were shifted by 0.67 eV for a better comparison with the experimental REMPI spectrum and convoluted with a Gaussian function (blue curve, HWHM = 4 meV).

6.4b). Note that the transition to the S_1 state is Franck–Condon forbidden for a dimer with a structure close to a H-aggregate, so the spectrum corresponds to excitation of the S_2 state. However, we also simulated the vibration-resolved absorption spectra of the S_1 taking into account Herzberg–Teller (HT) effect that is shown in Fig.

S6 of Ref. 5. The S_1 gains some intensity due to the HT coupling, but the overall intensity is negligible compared to the S_2 state. It should be noted, however, that the minimum of S_1 is significantly shifted compared to the ground state geometry. Therefore, it is questionable if the harmonic approximation is applicable at all in this case. The spectral envelopes and the relative energy differences between the three dominant peaks match the appearance of the experimental REMPI spectra almost perfectly in the AH model. The second (third) most intense transition is shifted by $\sim$1458 cm^{-1}($\sim$2916 cm^{-1}) with respect to the 0-0 transition and we denote these transitions as the "0–1" and "0–2" transition, respectively. For further comparison the vibrationally resolved absorption spectra were simulated in the frame of TD-DFT and CISD employing the vertical gradient model. These spectra are shown in Fig. S5 of Ref. 5 and agree very well with the experimental REMPI spectrum.
In addition to the dimer, a signal of the trimer is present in the mass spectrum with small intensity. Figure S3 of Ref. 5 shows its REMPI spectrum. As visible, dimer and trimer show separated bands, which allows to excite a given cluster size preferentially. This demonstrates the advantage of a ps-laser for cluster experiments.

6.4.5 Time-resolved photoionisation experiments

To gain insights into the dynamics of the tetracene dimer, we performed time-resolved photoionisation experiments. The dimers were excited at their absorption maxima (455.0, 427.0 and 403.5 nm) and ionised with a 263.5 nm probe photon. Note that Fig. S3 of Ref. 5 shows that selective excitation of the dimer is possible even in the presence of trimer. Recording the dimer ion signal as a function of the pump-probe delay yielded ion decay traces as depicted in Fig. 6.5 for excitation with 455.0 nm. Initially the time-dependence of the signal was fitted with a monoexponential decay function, but no satisfactory match was achieved. Instead, the biexponential fit with two time constants τ_1 and τ_2 is required for a proper description of the time-dependent signal. τ_1 possesses a negative amplitude and thus represents a population increase, while τ_2 describes a decay time. The contributions of both time constants to the total fit function in the case of 455.0 nm excitation are depicted in Fig. 6.5. Both time constants decrease with excitation energy and are slightly smaller in helium, due to the higher temperature of the molecular beam. τ_1 ranges from 62 ps in argon at 455.0 nm to 13 ps in helium at 403.5 nm, while the slower time constant τ_2 shows values from 123 ps (argon, $\lambda_{\mathrm{Pump}} = 455.0$ nm) to 50 ps (helium, $\lambda_{\mathrm{Pump}} = 403.5$ nm). A summary of all time constants obtained in both carrier gases is given in Tab. 6.1. Note that the transient signal does not decay to zero even at long delay times, but a constant signal offset remains. The origin of this feature will be discussed in more detail in the following section.

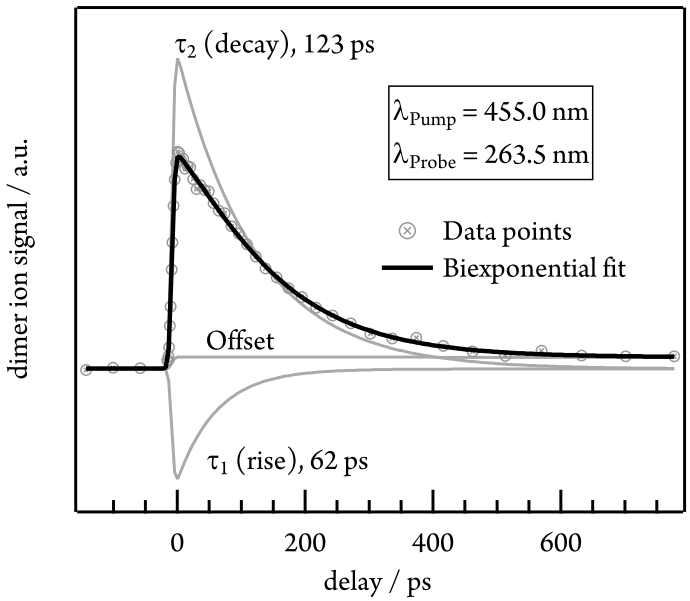

Figure 6.5: Time-dependent photoion signal of the tetracene dimer at an excitation wavelength of 455.0 nm. As shown in the plot, the data were fitted with a biexponential function including a rising (τ_1) and a decaying (τ_2) contribution.

6.4.6 Time-resolved VMI experiments

Dissociative photoionisation of larger clusters can contribute to the time-dependence in lower mass channels and thus obscure their dynamics.[279] To evaluate the influence of fragmentation processes on the dimer dynamics, we performed time-resolved velocity map imaging (VMI) experiments. While a cation produced through ionisation of a neutral dimer possesses negligible kinetic energy ($E_{\mathrm{kin}}(\mathrm{Ion}) \approx 0$), because the excess energy is carried away by the electron, fragment ions from dissociative photoionisation of larger clusters show a kinetic energy distributions with $E_{\mathrm{kin}}(\mathrm{Ion}) > 0$. As the VMI technique enables the determination of the photoion kinetic energy, it therefore allows us to distinguish between molecular ion and fragment ion signals, as demonstrated in Fig. 6.6. We ionised the dimer in a [1+1'] process with $\lambda_{\mathrm{Pump}} = 455.0$ nm and recorded the ion kinetic energy distribution as a function of the pump-probe delay. The inset in Fig. 6.6 represents the ion kinetic energy distribution integrated over the complete delay range. It can be seen that the spectrum is dominated by a Gaussian-shaped peak at E_{kin} (Ion) ≈ 0 meV, which is due to photoionised dimers. In addition, a small contribution is visible at higher kinetic energies up to around 150 meV, which originates from fragment ions. A comparison of the temporal evolution of the Gaussian and the higher energy component shows that the first one drops to zero at long delay times, while the latter one decays to a constant signal offset at long delay times. This leads us to conclude that the long-lived transient observed in the dimer decay traces (see Fig. 6.5) is due to fragmentation of higher order clusters and thus not related to photoinduced dynamics in tetracene dimers. As visible in

Table 6.1: Summary of the time constants obtained in the time-resolved [1+1'] REMPI experiments ($\lambda_{\mathrm{Probe}} = 263.5$ nm) at different excitation wavelengths. The dimer ion decay traces (Fig. 6.5) were fitted with a biexponential function including a rising (τ_1) and a decaying (τ_2) component.

	Argon		Helium	
	τ_1 [ps]	τ_2 [ps]	τ_1 [ps]	τ_2 [ps]
λ_{Pump} [nm]	(rise)	(decay)	(rise)	(decay)
455.0	62	123	49	97
427.0	34	69	38	58
403.5	18	54	13	50

Figure S3 of Ref. 5, dimer and trimer exhibit well separated bands, but nevertheless a small amount of trimer will be excited on the maxima of the dimer bands. The time dependence of the Gaussian contribution can again be described with a biexponential fit function with $\tau_1 = 57$ ps and $\tau_2 = 129$ ps (lower trace of Fig. 6.6) and thus agrees well with the results obtained in the TOF-MS experiments (see Tab. 6.1).

6.4.7 Nonadiabatic dynamics of excimer formation

In order to determine the mechanism that governs the excited state relaxation and leads to the subsequent excimer formation, we performed trajectory surface hopping dynamics simulations in the frame of TD-lc-DFTB as well as semi-empirical CISD. The two lowest excited states (S_1 and S_2) and the ground state have been included in the TD-lc-DFTB dynamics while in the CISD simulation we included the first six electronic states with a singlet multiplicity. The nonadiabatic couplings between all states have been calculated. The time-dependent excited state populations obtained from the CISD nonadiabatic dynamics (cf. Fig. 6.7) exhibit a decay within ~ 500 fs from the S_2 state to the S_1. The S_2 population falls drastically from 1 to about 0.2 in the first 100 fs and decreases gradually to 0 at around 8 ps in an oscillatory manner. This ultrafast population transfer results from the energetic proximity of the S_2 state to the higher lying excited states. Almost like its mirror image, the S_1 population increases from 0 to about 0.8 rapidly in about 400 fs and then slowly rises to 1 at around 8 ps. Higher excited states, especially the S_3 but also the S_4 do get populated up to 30 to 40 % in the initial decay of S_2. The populations however, are rather quickly funnelled to S_1 and are basically 0 after about 2.5 ps. The S_5 state hardly plays any role in the dynamics because of its very low population throughout the whole simulation. The diabatic states experience a very rapid change similar to the adiabatic ones. The local excitation (LE) falls from 1 to about 0.5 in the first 10 fs. It then raises oscillatorily to almost 0.9 at 4 ps. Afterwards, the populations of the LE states decrease to a value of 0.8. The charge transfer (CT) population behaves almost like the mirror image of LE. It reaches 0.5 in the first 10 fs starting from 0 and decreases to

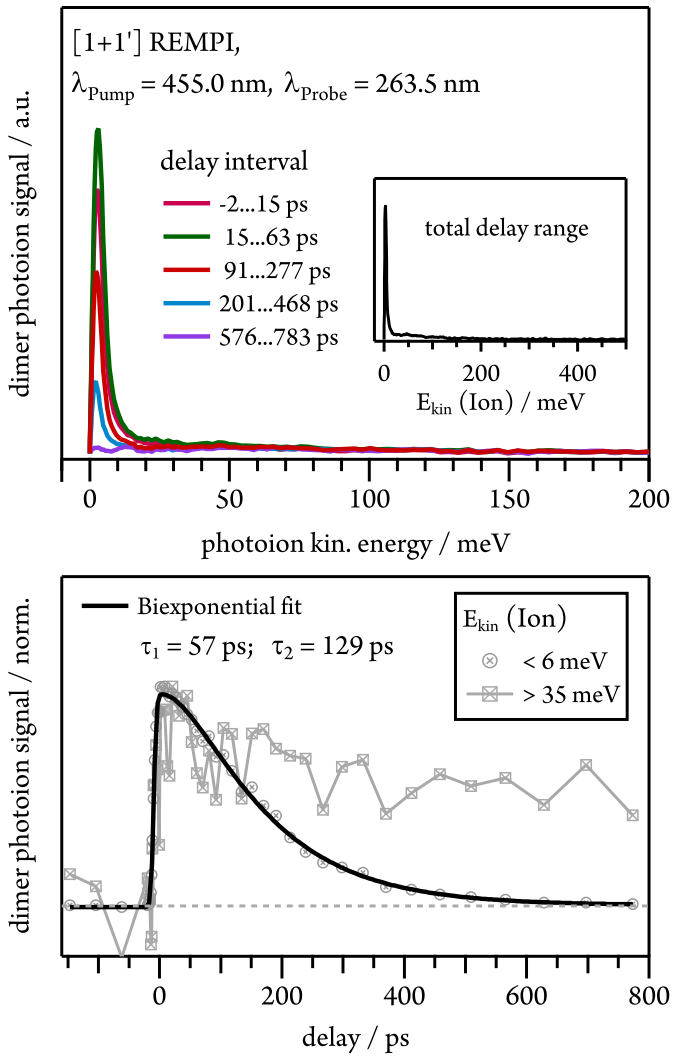

Figure 6.6: Upper panel: Ion kinetic energy distribution of the dimer ions after [1+1'] ionisation at different pump-probe delay intervals. Lower panel: Time-dependent behaviour of dimer ions with low (< 6 meV) and high (> 35 meV) translational energies.

about 0.1 at 2.5 ps. It then gradually increases to its final value 0.2 at the end of the simulation. The population of the singlet-correlated triplet pair state, ^{1}(TT), rises from 0 to about 0.13 in the first 250 fs. It then oscillates around this value, reaching a maximum of 0.2 at about 750 fs and starts to gradually fall at 2 ps. After about 8 ps, the population of the ^{1}(TT) has decreased to zero. The adiabatic state populations of the TD-lc-DFTB dynamics are shown in the ESI of Ref. 5 (see Figure S1) and exhibit a S_2 to S_1 population transfer on the same time scale as we observed in the CISD simulations. We did not transform the adiabatic TD-lc-DFTB states into a diabatic basis as this single-reference method cannot account for doubly excited states. The Fig. 6.8 shows scans of the potential energy curves along the longitudinal (x) axis.

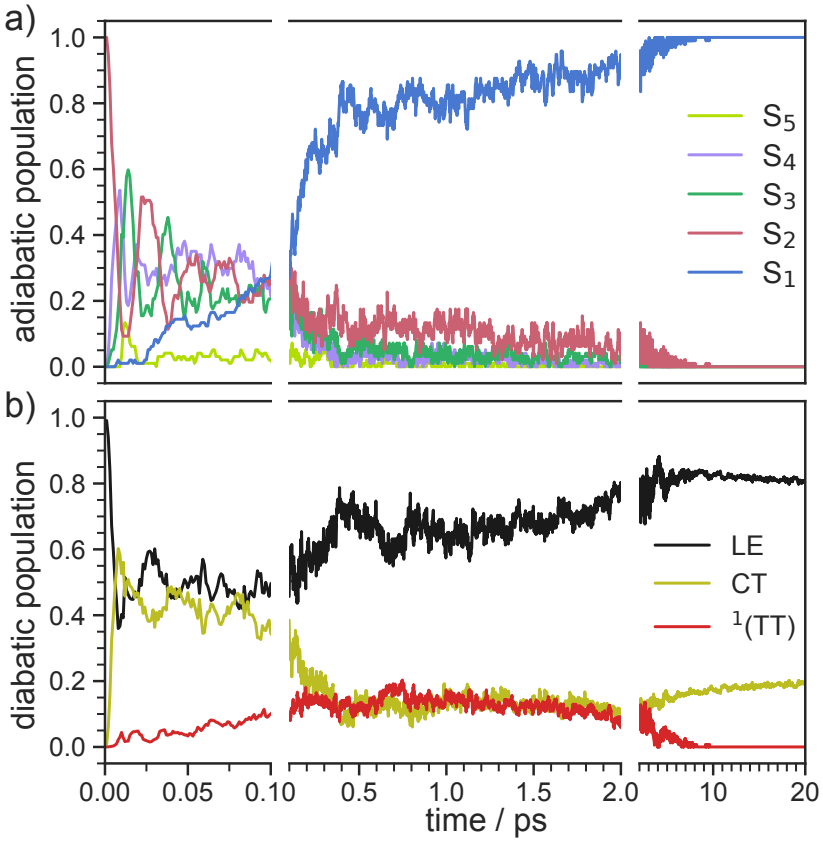

Figure 6.7: Time-dependent ensemble populations of the adiabatic excited states (a) and the diabatic states (b) obtained from the surface hopping nonadiabatic dynamics simulations at the semi-empirical CISD(4e,4o) level.

The upper part shows the curves for CISD(4e,4o), in the middle TD-lc-DFTB and at the bottom the results in the frame of TD-DFT(ωB97X-D/def2-SVP) are shown. It can be seen that the potential energy landscapes of all states are too flat with CISD (assuming the TD-DFT potentials are correct) and both the minimum of the excimer state at $R_x = 0$ and the other local minima at $R_x \approx 2.5$ Å are energetically underestimated. In TD-lc-DFTB, however, the agreement with the TD-DFT results is much better. For this reason, we also performed dynamics simulations with TD-lc-DFTB to check whether the geometric relaxations on the semi-empirical CISD are adequately described. Based on the results of the TD-lc-DFTB nonadiabatic dynamics simulations, two excimer formation channels have been identified in the gas phase: The trajectories either relax to a local minimum in the S_1-state close to the FC region and undergo vibrational dynamics mainly along the intermolecular rotation coordinate as the excimer state is formed (see green curve in Fig. 6.9), or they relax into the perfectly stacked global minimum in the first excited state along the parallel shift coordinate which is accompanied by a simultaneous decrease of the angle around the z-axis. Both relaxation channels can be qualitatively understood

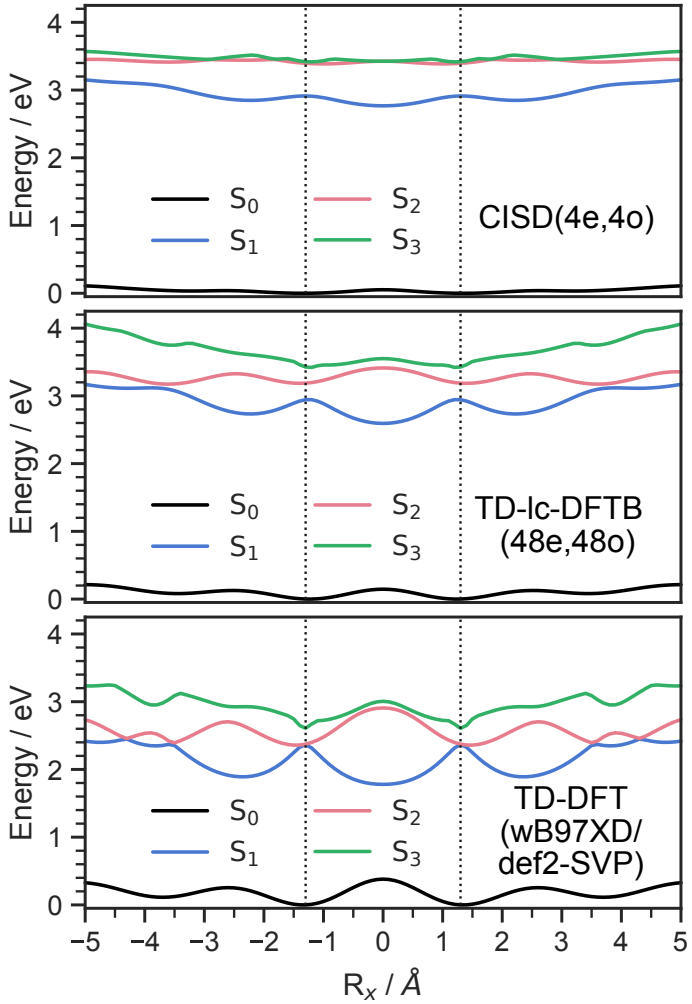

Figure 6.8: (a) Energies of the ground (S_0) and the three lowest (S_1, S_2, S_3) excited states of the tetracene dimer along the parallel shift coordinate (R_x) at an interplanar distance that corresponds to the S_1 minimum. The upper part shows the results from CISD(4e,4o/PM6-D3H4), the middle one the energy curves obtained by TD-lc-DFTB(48e,48o) and the lower part shows the TD-DFT(ωB97X-D/def2-SVP) values.

based on the shape of the potential energy curves shown in Fig. 6.8. The PECs exhibit a local minimum in the S_2 state close to the FC geometry and a local minimum in the S_1 state where $R_x \approx 2.4$. The global minimum in the S_1 state is characterised by a perfectly stacked geometry. In five trajectories dissociation within 10 ps was observed that was not assigned to one of the relaxation channels shown in Fig. 6.9. However, at the CISD level (see violet curves in Fig. 6.9) only one excimer formation channel could be identified. Furthermore, the displacement around the longitudinal coordinate and the rotation around the z-axis are much weaker in the CISD dynamics. These differences can be explained by the differences in the PECs. For one reason, the PECs at the CISD level are much flatter, which is why the large amplitude vibrations

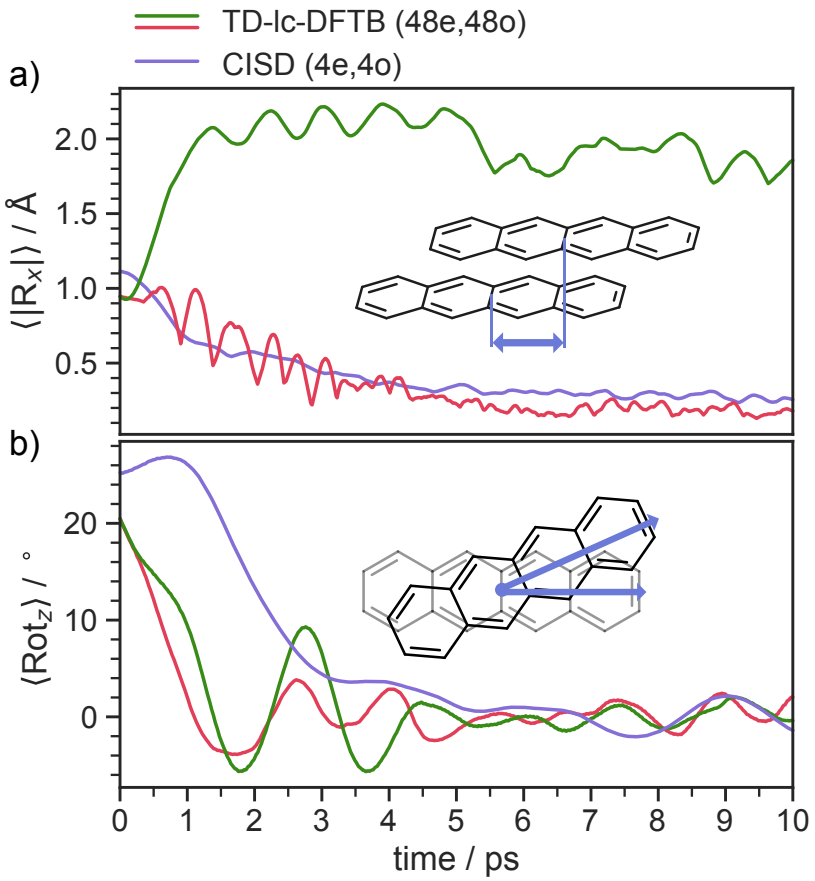

Figure 6.9: (a) Average value of the longitudinal shift coordinate (R_x) as defined in the text as a function of time. (b) Average value of the rotation around the z-axis, which is perpendicular to the molecular plane of a tetracene monomer. The TD-lc-DFTB values have been divided into two excimer forming channels, with the green line as the parallel slipped one (14 trajectories) and the red line as the stacked tetracene excimer (15 trajectories).

will be less pronounced, and for another, the local minima are less stable, so that the excimer cannot be trapped there.
After about 3 to 4 ps the excimer is formed and both the displacement along the x- and y-direction decrease to values representing an almost perfectly stacked geometry. Initially, the angle drops from about 24 degrees to around 0 degree within the first 3 to 4 ps and exhibits subsequently damped oscillations with a period of $\approx$ 2 ps that persist for the whole simulation period of 20 ps. The stabilisation of the excimer requires the removal of energy from the intermolecular coordinates and its internal redistribution over all available vibrational modes.

6.5 Discussion

Based on the computational and experimental results, a comprehensive picture of the dynamics can be deduced. The photoabsorption visible in the REMPI spectrum corresponds to the $S_2 \leftarrow S_0$ excitation of the tetracene dimer, as confirmed by computations. Simulations of the nonadiabatic dynamics starting in the S_2 state further reveal a fast deactivation to the S_1 state on the timescale of ∼500 fs. Such a fast relaxation process is not visible in the experimental data probably due to the limited temporal resolution of our ps laser setup (IRF ≈ 4 ps). Nevertheless, the time-resolved TOF-MS and VMI experiments reveal a biexponential time dependence of the dimer ion signal, with an increasing and a decaying component. Contributions from the photodissociation or dissociative photoionisation of the trimer can be ruled out, based on the different absorption bands and the analysis of the ion images. As the non-radiative deactivation of the optically excited state is not observed, the experimental transients reflect the dynamics on the S_1 surface, after it has been populated in a rapid non-radiative transition. Both time constants decrease with excitation energy, which suggests that the rates increase with the density of states. Generally speaking, the ion signal correlates with the ionisation probability at a given delay time. A rise in the transient signal thus can be related to a geometric relaxation into a more ion-like structure and therefore enhanced FC factors for the ionisation step. In contrast, electronic relaxation into vibrationally highly excited states typically leads to lower FC Factors and contributes a decay to the transient. We therefore assign τ_1 to geometric relaxation within the S_1 manifold, associated with excimer-formation and relaxation. Consequently, τ_2 is assigned to the deactivation of this excimer state. It is revealing to compare these time constants with data from previous work. In thin films time constants of 80-90 ps were observed in transient absorption spectra. Time-resolved fluorescence measurements on covalently bound stacked tetracene dimers yielded an excimer-emission lifetime of 230 ps.[309] These time constants are on the same order of magnitude as the decay time (τ_2) observed in the present experiments (123 ps at $\lambda_{\mathrm{Pump}} = 455.0$ nm in argon). Thus it is reasonable to assign τ_2 to the deactivation of the excimer.

As discussed above, tetracene is considered to be a model system for singlet fission. In our CISD dynamics simulations we observed that the ^{1}(TT) state, which is a precursor for singlet fission, is only transiently populated after excitation, before it deactivates to the excimer state. From the simulations we conclude that excimer formation prevents an efficient population of the ^{1}(TT) state in the gas phase. The latter is only an intermediate step between the optical excitation and excimer formation, which indicates an important role of the surrounding in the condensed phase. On the other hand, our interpretation is in accordance with the observations by Dover *et al.*, who conclude that the excimer acts as an excited state trap in TIPS-tetracene, which reduces the singlet-fission yield.[273] Experiments on isolated systems, as discussed in the present manuscript, permit to separate the intrinsic properties of the molecular aggregate from the influence of the environment and to validate the theoretical

methodology. Studies in solution or crystals will benefit from these investigations, because dynamics absent in the isolated dimer can more easily be assigned to the environment.

6.6 Conclusion

In this work we investigated excimer formation dynamics in tetracene dimer after optical excitation into the S_2 state, both by time-resolved spectroscopy and nonadiabatic dynamics simulations. The picosecond photoionisation experiments were performed in a supersonic jet. Due to the bandwidth of the laser system, dimers and trimers are excited separately and a vibrationally resolved spectrum of the dimer is recorded. Photoion imaging detection permits to distinguish between "true" dimer contributions and contributions from dissociative photoionisation. While the initial depopulation of the S_2 state is not resolved, two time constants are observed that are associated with relaxation and deactivation of the excimer state.
The nonadiabatic dynamics simulations were performed in the frame of semi-empirical CISD(4e,4o) as well as TD-lc-DFTB(48e,48o) in the gas phase. They led to the identification of a dominant excimer formation channel that is characterised by the relaxation to the global S_1 minimum at an almost perfectly stacked geometry. While the TD-lc-DFTB trajectories showed a second relaxation pathway to a geometry that is shifted along the longitudinal axis, this could not be observed in the semi-empirical CISD(4e,4o) simulations. This is explained by the resulting flat potential along this axis. On the other hand, the inclusion of doubly excited states allows to track the population of ^{1}(TT) state. During the electronic relaxation, we observe a population of a ^{1}(TT) state, that could in principle lead to singlet fission. However, this state was only transiently populated for 2 to 3 ps and was depopulated within the next 5 ps by the excimer formation process. In agreement with previous work on the pyrene dimer[13], we observe that large amplitude oscillations play an essential role in the relaxation process after excitation.
In conclusion, the singlet-correlated triplet state ^{1}(TT) is only transiently populated and excimer formation acts as an excited state trap.

Chapter 7

The Origin of the Solvent Dependence of Fluorescence Quantum Yields in Dipolar Merocyanine Dyes

---

Fluorophores with high quantum yields are desired for a variety of applications. Optimization of promising chromophores requires an understanding of the non-radiative decay channels that compete with the emission of photons. We synthesized a new derivative of the famous laser dye 4-dicyanomethylen-2-methyl-6-p-dimethylaminostyryl-4H-pyran (DCM), i.e., merocyanine 4-(dicyanomethylene)-2-*tert*-butyl-6-[3-(3-butyl-benzothiazol-2-ylidene)1-propenyl]-4H-pyran (**DCBT**). We measured fluorescence lifetimes and quantum yields in a variety of solvents and found a trend opposite to the energy gap law. This motivated a theoretical investigation into the possible non-radiative decay channels. We propose that a barrier to a conical intersection exists that is very sensitive to the solvent polarity. The conical intersection is characterized by a twisted geometry which allows a subsequent photoisomerization. Transient absorption measurements confirmed the formation of a photoisomer in unpolar solvents, while the measurements of fluorescence quantum yields at low temperature demonstrated the existence of an activation energy barrier.

7.1 Introduction

Understanding and predicting photophysical and electronic properties of fluorophores are a prerequisite for many applications including biomolecular imaging,[310] organic lasers,[311] and light-emitting molecular devices.[48,312] The usefulness of many organic fluorophores depends directly on the fluorescence quantum yield, which is defined by the competition of fluorescence to all other non-radiative relaxation channels. The ability to fluoresce is usually linked to a rigid, conjugated molecular structure which ensures that the excited state has a stable minimum.[47,313,314] If the emissive geometry differs only little from the ground-state geometry, sharp and structured absorption and emission spectra are observed, which are approximately mirror images of each other.[47] In contrast to that, non-fluorescent chromophores have reactive excited states and decompose or decay to the ground state non-radiatively before a photon can be emitted.[315] The non-radiative decay occurs via crossing potential energy surfaces (PES) and drastic deformations of the geometry.[49–51,316–318] Due to the fast nature of the decay, spectra are usually broad and featureless. This dichotomy of stable, fluorescent and reactive, non-fluorescent chromophores is also reflected in the theoretical modeling of those compounds: When fluorescence is dominant, the harmonic approximation is invoked and transitions (both radiative and non-radiative) between the harmonic potential energy surfaces of the initial and final electronic states are accounted for by perturbation theory.[319–322] On the other hand, photochemical reactions require different approaches such as non-adiabatic molecular dynamics simulations, where the nuclei are treated as classical particles rolling on and jumping between potential energy surfaces.[11–13,54,55,163] Such simulations, however, are limited to short timescales, not more than a few hundred femtoseconds, while typical experimental fluorescence lifetimes are in the order of nanoseconds. In recent years it has been noted that the distinction between stable and reactive chromophores is not that clear. Conical intersection can also play a role in non-ultrafast settings.[323–325] In a recent data survey on distyrylbenzene derivatives an inverted energy gap law for the non-radiative decay rate was attributed to access to a conical intersection.[326] Conical intersections in the vicinity of the Franck–Condon point may impact the fluorescence rate by opening an additional temperature-dependent channel for relatively slow non-radiative decay[52,327,328] and photoisomerization.[316,329–332] If a barrier separates a stable minimum close to the Franck–Condon point from a conical intersection, it is legitimate to assume that the reactions in the excited state are also governed by the rules of thermodynamics, so that one can apply transition-state theory for estimating the temperature-dependent rates of non-radiative decay.[323,333] The energetic position of the barrier and conical intersection can be tuned by substitutions as demonstrated for naphthalene derivatives.[325] Experimentally this situation is evidenced by the temperature dependence of the non-radiative rate.

In this contribution we study the photochemistry of a fluorescent merocyanine dye, 4-(dicyanomethylene)-2-*tert*-butyl-6-[3-(3-butyl-benzothiazol-2-ylidene)1-propenyl]-4H-pyran (**DCBT** , structure in Fig. 7.1), whose fluorescence quantum yield depends

markedly on the polarity of the solvent and temperature.
Merocyanines[334] are push–pull chromophores, which consist of a donor and an acceptor group that are covalently connected by a polymethine chain, which contains an odd number of –CH= groups.[335] The optical properties of merocyanines can be tuned by the length of the polymethine chain and the strength of the donor and acceptor groups.[141,336] Indeed, the choice of the donor/acceptor groups defines the electronic character that can span the range from neutral to zwitterionic.[233,336–343] These remarkable characteristics are of large technological interest for the development of organic photovoltaics, nonlinear optics, and electronics.[344–347]
With regard to applications depending on fluorescence, however, merocyanines are difficult chromophores. Thus, despite of a polymethine chain that can be tuned to the cyanine limit by proper choice of donor and acceptor groups,[339,346] the emissive properties of merocyanines are in general inferior to those of cyanine relatives. Thus, there are only a small number of merocyanine dyes such as the 4-dicyanomethylene-2-methyl-6-p-dimethylaminostyryl-4H-pyran laser dye DCM[348] that show high fluorescence quantum yields in well-chosen solvents.[349] In merocyanines as well as in cyanines solvent dependencies of the quantum yields were observed and possible relaxation channels were discussed.[316,328–330,349] In this work we aim to elucidate the reason for this behavior of merocyanines. Our hypothesis is that the structural relaxation that follows the displacement of the electron cloud in these push–pull chromophores after photoexcitation might be hindered by a barrier to a conical intersection that is very sensitive to the polarity of the solvent. The presence of an accessible conical intersection can thus be probed by the variation of the fluorescence quantum yield with the dielectric constant of the solvent. Tuning the dielectric constant allows to gradually turn off the non-radiative decay channel through the conical intersection.
To evaluate this hypothesis we measured fluorescence quantum yields and built a theoretical model to understand the different relaxation channels of the merocyanine **DCBT** for the following series of solvents ordered by increasing dielectric constant (ϵ_r): methylcyclohexane (MCH) < toluene (Tol) < chloroform ($CHCl_3$) < dichloromethane (CH_2Cl_2) < acetonitrile (MeCN) < dimethylsulfoxide (DMSO).

7.2 Results

7.2.1 Structural Properties

Figure 7.1 shows the molecular structure obtained from single-crystal X-ray analysis together with one of the optimized ground-state structures from DFT calculations of the merocyanine **DCBT** (for details on the chemical synthesis, ^{1}H NMR, ^{13}C and ROESY NMR as well as crystallographic data see Supporting Information, SI). It consists of a tertiary amine, which can donate a free electron pair, connected by a polymethine chain to a dicyanovinyl group, which can accept electrons. The acceptor half of the molecule is the same as in the DCM merocyanine laser dye while the donor

group is part of a strongly electron-donating benzothiazolidene methylene base.
In the solid state **DCBT** shows an all-trans polymethine chain which is also the configuration observed in solution according to our ROESY-NMR studies (cf. Fig. S4 in the SI). The C-C bond length alternation observed for the polymethine chain in the single crystal (Fig. 7.1b) indicates that the **DA** chromophore exhibits a more polyene-type structure with a dominating non-polar resonance structure (**DA** in Fig. 7.1a). This geometry also prevails in solution according to our electrooptical absorption measurements in methylcyclohexane (EOAM, see Fig. S6, Supporting Information). The merocyanine admits a neutral structure **DA** and a zwitterionic resonance structure $\mathbf{D}^{+}\mathbf{A}^{-}$ (depicted in Fig. 7.1a), which are responsible for the solvatochromism. The resonance structures are constructed by constraining an electron to either the donor or the acceptor region. The ground and excited states are linear combinations

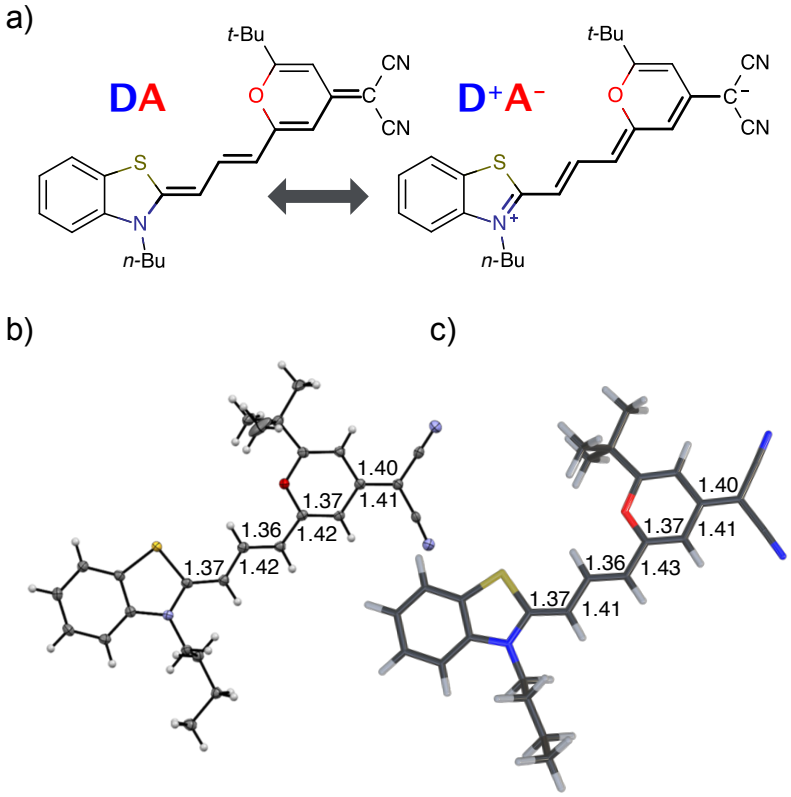

Figure 7.1: DCBT structure. (a) Neutral $|\mathbf{DA}\rangle$ and zwitterionic $|\mathbf{D}^{+}\mathbf{A}^{-}\rangle$ resonance structures of merocyanine dye **DCBT**. The polymethine chain connecting donor **D** and acceptor **A** is highlighted. (b) Molecular structure obtained from crystallographic analysis (thermal ellipsoids are set at 50 % probability) (c) DFT calculations using IEFPCM solvation (in DMSO). The bond distances (in Å) along the polymethine chain are shown next to each bond.

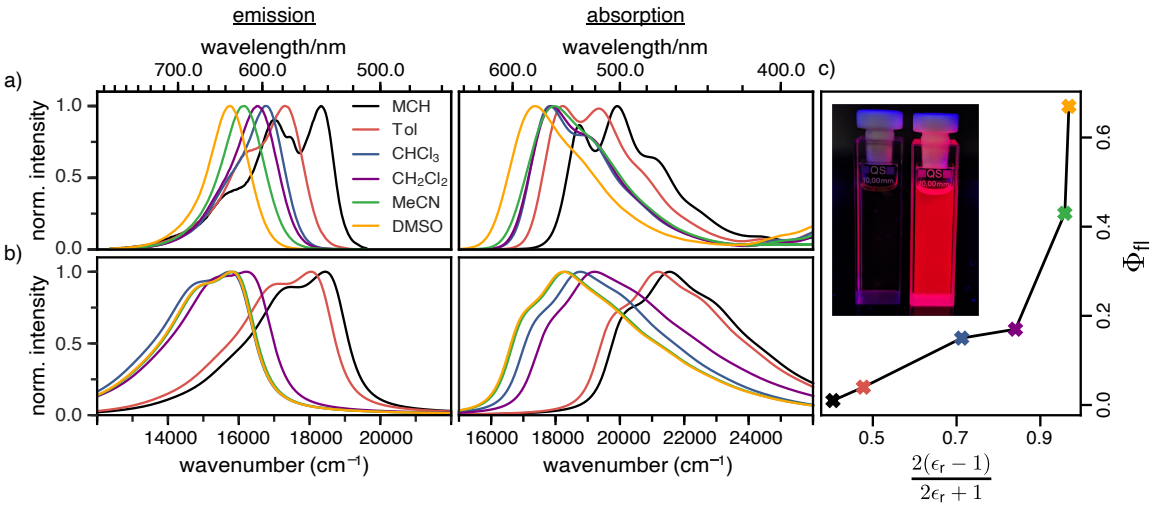

Figure 7.2: (a) Experimental absorption and emission spectra of **DCBT** in six different solvents. (b) Simulated vibrationally resolved absorption and emission spectra in the framework of TD-ωB97XD/def2-TZVP in combination with a polarizable continuum model using the integral equation formalism variant (IEFPCM). All simulated spectra were shifted by 0.3 eV to lower energies for better comparability to the experimental ones. (c) Dependence of the experimental fluorescence quantum yield on the dieletric screening factor of the solvent.The inset shows the optical photograph of samples ($c = 10^{-5}$ M) in MCH (left) and DMSO (right) under black light illumination.

of these two diabatic states,

$$\Psi_g = \sqrt{1-c^2}|\mathbf{DA}\rangle + c|\mathbf{D^+A^-}\rangle, \tag{7.1}$$

$$\Psi_e = c|\mathbf{DA}\rangle - \sqrt{1-c^2}|\mathbf{D^+A^-}\rangle. \tag{7.2}$$

The resonance parameter c^2 quantifies the character of the ground/excited-state wavefunction as neutral/zwitterionic ($c^2 = 0$) or zwitterionic/neutral ($c^2 = 1$).[339,344] In between lies the cyanine limit $c^2 = 0.5$ at which both diabatic states have equal weights. From electrooptical absorption measurements[350] we find that the ground-state dipole moment is $|\mu(S_0)| = 10.4 \pm 0.6$ D, suggesting that the neutral form dominates as expected in methylcyclohexane. In the first excited state the permanent dipole moment increases to $|\mu(S_1)| = 19.9 \pm 1.1$ D, so that this state can be described by the zwitterionic resonance structure ($\mathbf{D^+A^-}$). From the changes in the dipole moment it is possible to determine the weight of the zwitterionic configuration that is about $c^2 = 0.27 \pm 0.02$ for the ground state of **DCBT**.

7.2.2 Optical Properties

The steady-state absorption and fluorescence spectra of the **DCBT** merocyanine dye in the different solvents are depicted in Fig. 7.2a and the simulated spectra

are shown in Fig. 7.2b. The spectral features of the dyes exhibit a large positive solvatochromism, both in absorption and fluorescence spectra. Thus, the absorption maxima shift from 534 nm in MCH to 576 nm in DMSO which is in accordance with the increase in dipole moment upon optical excitation, i.e., stabilization of the more dipolar excited state by polar solvents. The bathochromic shift upon increasing solvent polarity is even larger in the fluorescence spectra, i.e., from 546 nm in MCH to 637 nm in DMSO, correlating to an increase in the Stokes shift from 400 to 1700 cm^{-1}. The most interesting result for this study is, however, the strong increase of fluorescence quantum yield upon increasing solvent polarity, i.e., from ≈ 1 % in MCH to 67 % in DMSO (see Fig. 7.2c and Table 7.1).

7.3 Discussion

The fluorescence quantum yield (Φ_{fl}) is defined as the ratio between the radiative rate (k_{r}) and all other rates including the non-radiative relaxation channels (k_{nr}):

$$\Phi_{\mathrm{fl}} = \frac{k_{\mathrm{r}}}{k_{\mathrm{r}} + k_{\mathrm{nr}}}. \tag{7.3}$$

Radiative and non-radiative rates show opposite trends with excitation energy, when initial and final states are approximated by harmonic potential energy surfaces. The radiative rate increases as the third power of the emission energy, while the non-radiative rate decreases faster than exponentially as the excitation energy increases. Accordingly the fluorescence quantum yield should go up with the emission energy. However this is not consistent with the observations for **DCBT**, where the lowering of the emission energy due to the solvatochromic shift is accompanied by an increase in the fluorescence quantum yield.
The missing piece is an additional non-radiative deactivation channel that leads to a conical intersection (CI). We have to amend our model by a temperature-dependent rate for leaving the metastable minimum over a barrier. The non-radiative rate is thus split into two parts,

$$k_{\mathrm{nr}} = k_{\mathrm{ic}}^{\mathrm{harm}} + k_{\mathrm{ic}}^{\mathrm{CI}}, \tag{7.4}$$

a temperature-independent rate that is calculated in the harmonic approximation with some additional simplifications ($k_{\mathrm{ic}}^{\mathrm{harm}}$) and a temperature-dependent rate based on Kramers' theory ($k_{\mathrm{ic}}^{\mathrm{CI}}$). The relaxation to triplet states is neglected in this work, as the experimental observation of fluorescence on the (sub)nanosecond timescale makes this relaxation pathway very unlikely. However, we cannot exclude that intersystem crossing contributes also to some degree to the relaxation channels.

7.3.1 Radiative Rate.

The radiative rate increases as the second power of the refractive index n (see Ref.[351] for a discussion of the refractive index correction), as the second power of the transition dipole moment μ_{eg}, and as the third power of the emission energy, $\Delta E - E_{\mathbf{m}}$:

$$k_{\mathrm{r}} = u_{\mathrm{rad}} n^2 |\mu_{\mathrm{eg}}|^2 \sum_{\mathbf{m}} (\Delta E - E_{\mathbf{m}})^3 F_{\mathbf{m}} \Theta (\Delta E - E_{\mathbf{m}}) . \tag{7.5}$$

Here, ΔE is the adiabatic excitation energy, $E_{\mathbf{m}}$ the energy of the final vibrational

Table 7.1: Theoretical (th.) and experimental (exp.) data for the characterization of the spectroscopic and electronic properties of the merocyanine **DCBT** in solvents of different polarity. See text for definitions of all quantities.

Solvent	ΔE /eV	$\lvert\mu_{\mathrm{eg}}\rvert$/D		C /eV	E_{A} /eV	γ^{b} /cm^{-1}	ω_a/cm^{-1}		ω_b/cm^{-1}		$k_{\mathrm{r}}/10^8$s^{-1}		$k_{\mathrm{nr}}/10^8$ s^{-1}			τ_{fl}/ns	Φ_{fl}/%	
		exp.	th.				TS$_1$	TS$_2$	TS$_1$	TS$_2$	exp.[c]	th.	exp.[c]	theory		exp.	exp.	th.
														$k_{\mathrm{ic}}^{\mathrm{harm}}$	$k_{\mathrm{ic}}^{\mathrm{CI}}$			
MCH	2.69	9.73	14.0	0.60	0.30	1047	117	210	344	401	>0.7[d]	10.5	>71[d]	0.0012	27600	< 0.2	1	0
Tol	2.65	9.04	14.2	0.66	0.32	845	117	228	359	395	1.8	11.4	44	0.0053	14000	0.22	4	0.1
$CHCl_3$	2.50	9.73	14.8	0.81	0.42	566	116	228	386	362	2.5	9.70	14	0.18	557	0.59	15	2
CH_2Cl_2	2.42	10.8	15.2	0.88	0.48	573	117	231	395	225	1.9	9.02	9.3	0.52	41.4	0.89	17	18
MeCN	2.34	9.78	15.5	0.98	0.58	886	116	230	363	181	2.4	7.56	3.2	5.38	0.80	1.78	43	55
DMSO	2.34	11.1	15.5	0.99	0.59	3641	116	230	333	175	2.9	9.18	1.4	6.05	0.22	2.32	67	60

[a]Values taken from Ref. 222; [b]details for the calculation of the friction coefficients are shown in SI; [c]obtained from TCSPC and fluorescence quantum yield measurements; [d]these radiative and non-radiative rate constants are only a lower limit, as the fluorescence lifetime is below the instrument response time of the TCSPC setup.

state $\mathbf{m}$ (without zero-point energy), $F_{\mathbf{m}} = |\langle \mathbf{0}' | \mathbf{m} \rangle|^2$ denotes the Franck–Condon factors and the Heaviside function $\Theta(\cdot)$ ensures that the energy difference between the initial state and final state is positive, so that a photon can be emitted. The factor $u_{\mathrm{rad}} = 2.142 \times 10^{10}$ s^{-1} converts the rates from atomic units to s^{-1}. For details about the prefactor and how the sum over all vibrational states is performed efficiently, see the SI.

7.3.2 Nonradiative Rates

For the harmonic part of the internal conversion rate we use a variant of the so-called energy gap law.[79] The detailed derivation from Fermi's Golden rule is given in the

SI and we limit us here to stating the final equation,

$$k_{\mathrm{ic}}^{\mathrm{harm}} \approx \frac{u_{\mathrm{ic}}}{2\sqrt{2\pi}} \left| \langle \Psi_i | \frac{\partial \Psi_f}{\partial \mathbf{Q}} \rangle \right|^2 \times e^{-NS} \times \left\{ I\left(\frac{\Delta E}{\omega_{\mathrm{eff}}} - 1 \right) + PS\ I''\left(\frac{\Delta E}{\omega_{\mathrm{eff}}} - 1 \right) \right\}, \tag{7.6}$$

with

$$I(x) = \sqrt{\frac{1}{x}} \exp\left(-x \left[\log\left(\frac{x}{NS} \right) - 1 \right] \right). \tag{7.7}$$

The factor $u_{\mathrm{ic}} = 2\pi E_h/\hbar = 2.598 \times 10^{17}\ \mathrm{s}^{-1}$ converts the rate to s^{-1} if all other quantities are given in atomic units, where E_{h} is the Hartree energy. $N = 168$ is the number of vibrational modes denoted by $\mathbf{Q}$, P is the number of promoting modes, i.e., those modes p carrying a large component of the non-adiabatic coupling vector $C_p = |\langle \Psi_i | \frac{\partial \Psi_f}{\partial Q_p} \rangle| \neq 0$, $\omega_{\mathrm{eff}} = \sum_{i=1}^{N} \omega_i \frac{C_i}{\sum_{j=1}^{N} C_j}$ is the effective vibrational mode, S the average Huang–Rhys factor and $I''(x)$ denotes the second derivative of $I(x)$. Averaging over the modes, so that the vibrational structure is described by a single effective mode ω_{eff}, is a drastic simplification that introduces some arbitrariness. The advantage is that it provides us with a closed expression for the internal conversion rate that brings out the dependence on the adiabatic excitation energy ΔE.

The second pathway with rate constant $k_{\mathrm{ic}}^{\mathrm{CI}}$ is the relaxation through conical intersections (CIs), which may lead back to the reactant well or to the formation of a photoproduct. Assuming that reaching the CI always leads to an internal conversion from the excited state to the electronic ground state, then the rate for depletion of S_1 is only dependent on the energetics of the barrier and the vibrational energy of the molecule.

This rate is calculated by Kramers' barrier-crossing theory,[58] where the decay process starts from an equilibrated initial state characterized by a well frequency ω_a and proceeds over a barrier of height E_{A} and frequency ω_b in the presence of a friction constant γ,

$$k_{\mathrm{ic}}^{\mathrm{CI}} = u_{\mathrm{ic}}^{\mathrm{CI}} \frac{\gamma}{4\pi} \frac{\omega_a}{\omega_b} \left\{ \left[1 + \left(\frac{2\omega_b}{\gamma} \right)^2 \right]^{1/2} - 1 \right\} \exp\left(\frac{-(E_{\mathrm{A}} - \alpha)}{k_{\mathrm{B}} T} \right), \tag{7.8}$$

where α is a global adjustable parameter as discussed in section 6 of the SI, $u_{\mathrm{ic}}^{\mathrm{CI}} = E_{\mathrm{h}}/\hbar = 4.134 \times 10^{16}\ \mathrm{s}^{-1}$ converts the rate to s^{-1} if all other quantities are given in atomic units and ω_b is the frequency of the mode with negative force constant at the lowest transition state leading to a conical intersection. Since Kramers' model is essentially one-dimensional, we had to select the corresponding mode a with frequency ω_a at the Franck–Condon point which is most similar to the mode b at the transition state. The detailed calculation of the friction constants γ is given in the SI. The

approach based on equations 7.5, 7.6, and 7.8 is one of the simplest models that can be used to rationalize the photoluminescence quantum yields and can predict qualitative trends based on temperature and solvent environment including the viscosity and solvatochromic shifts.

7.3.3 Barrier for Nonradiative Relaxation

The rate for internal conversion through the conical intersection is dependent on the energetics of the path to the CI from the Franck–Condon minimum. It has been shown by Maeda [323] and coworkers that if the internal conversion is the dominating relaxation pathway to the ground state, then the trend in the fluorescence quantum yields can be predicted very well by correlating these barrier heights to the experimentally obtained quantum yield. We observe an almost linear dependence between these quantities, suggesting that this is indeed the dominant relaxation pathway (Fig. 7.3). Since both the rotation of the double bond which is connected directly to the benzothiazolidene group, and the rotation about the next double bond lead to a conical intersection, there are also two different transition states (denoted as TS_1 and TS_2 in Fig. 7.3).
We have validated the whole reaction path at the CASSCF level, as linear-response TD-DFT has inherent problems in describing the S_0/S_1 conical intersection seam cor-

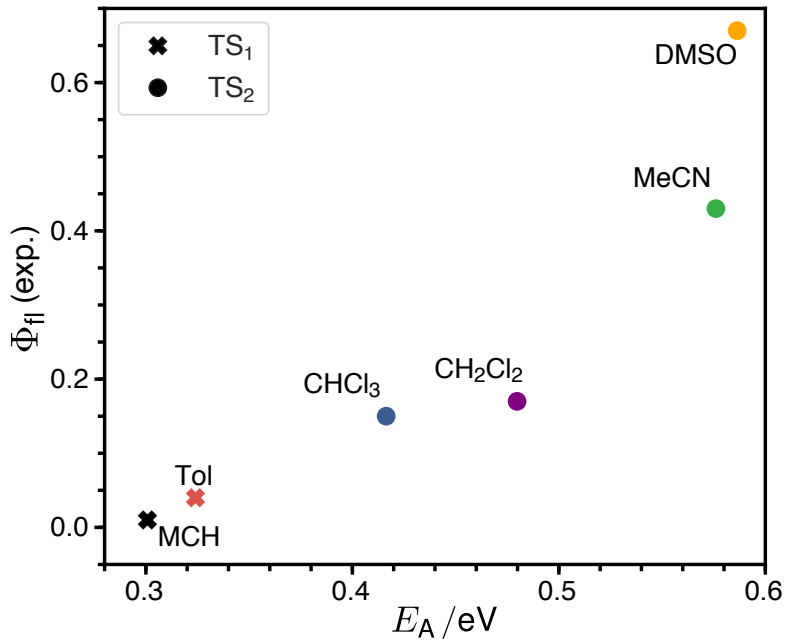

Figure 7.3: Correlation between the activation energy, E_A, in the S_1 state from the Franck–Condon minimum to the transition state and the experimental fluorescence quantum yield. For each solvent the transition state lowest in energy is selected.

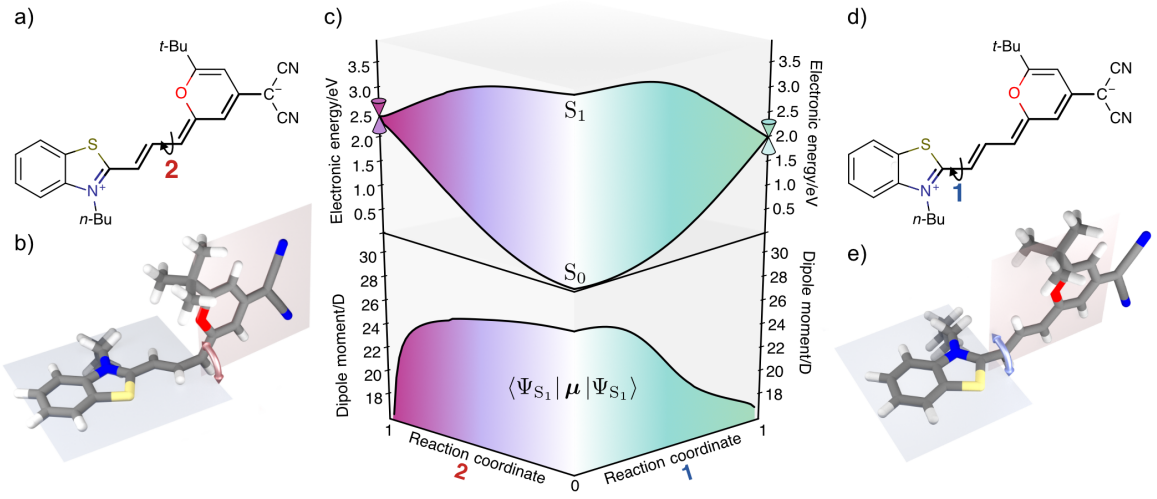

Figure 7.4: (a and d) In the zwitterionic resonance structure rotation around the former double bonds in the polymethine chain becomes possible leading to conical intersection 1 (e) or 2 (b). (c) CASSCF energies (top) and excited state dipole moments (bottom) in the gas phase along linearly interpolated geometries (in internal coordinates) between the Franck–Condon minimum and the two minimum energy conical intersection as indicated on the left and right hand sides.

rectly.[352] In Fig. 7.4 we illustrate the geometries at the conical intersection together with the energies and permanent dipole moments, from the Franck–Condon point to both conical intersections, of the S_1 state in the frame of CASSCF. In the gas phase the permanent dipole moment of the excited state decreases from ≈ 27 D at the Franck–Condon point to less than 16 D at the conical intersections. At the Franck–Condon point we can compare the change in the permanent dipole, $\Delta\mu$, between the ground and excited state with experiment, which is with a value of 10.5 D in good accordance to the experimental value of $\Delta\mu = 9.5 \pm 1.1$ D (as obtained from the EOA measurements shown in Fig. S6).

7.3.4 Fluorescence quantum yield

The calculated non-radiative decay rates are shown in Table 7.1 together with the simulated radiative rates and the resulting fluorescence quantum yields. The calculated adiabatic excitation energy ΔE decreases from 2.69 eV in the least polar solvent MCH to 2.34 eV in the most polar solvent DMSO. The harmonic radiative rates remain more or less constant for all solvents, since μ_{eg} increases from 14.0 D in MCH to 15.5 D in DMSO, so that the opposite trends of decreasing optical gap and increasing transition dipole moments cancel each other. Compared to experiment the radiative rate is overestimated by a factor of ≈ 3–6. This is partly due to the overestimation of the transition dipole moment by TDDFT relative to experiment (15.5 vs. 11.1 D in DMSO). The harmonic rate for internal conversion increases with

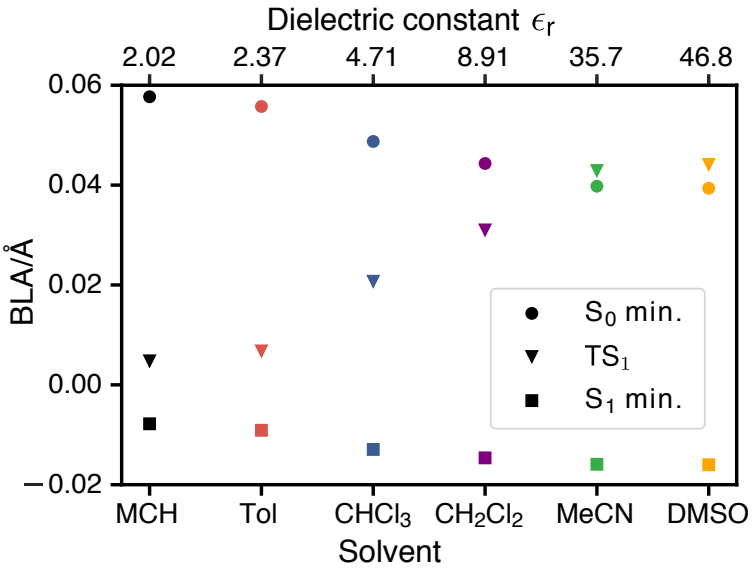

Figure 7.5: Bond length alternation of the polymethin chain of merocyanine **DCBT** at the ground-state minimum, the Franck–Condon S_1 minimum and the transition state between this minimum and the conical intersection 1.

the positive solvatochromic shift as expected from the energy gap law. This effect is enhanced by the increase of the electronic non-adiabatic coupling C from 0.60 eV in MCH to 0.99 eV in DMSO. The trend of the harmonic part of the IC rate alone is opposite to the experimental observation that the non-radiative rates decrease with decreasing emission energy: The experimental k_{nr} attains the largest value of 71×10^8 s^{-1} for MCH and the lowest value of 1.4×10^8 s^{-1} for DMSO.
The inclusion of the rate from Kramers' theory reverses the theoretical trend. k_{ic}^{CI} has its largest value of $\approx 3 \times 10^{12}$ s^{-1} for MCH and decreases with increasing polarity to 0.22×10^8 s^{-1} in DMSO. In MCH the theoretical rate is dominated by k_{ic}^{CI}, while in DMSO it is determined mostly by k_{ic}^{harm}. In the other solvents the dominant non-radiative decay channel changes gradually from being non-reactive (transition from the Franck–Condon point to the S_0 minimum) to being reactive (decay through a conical intersection). The solvent also determines which of the two conical intersections is accessed. In MCH and toluene the lowest transition state leads to conical intersection 1, while in the other more polar solvents the transition state to the conical intersection 2 is lower. Therefore one can expect *cis–trans* isomerization around the first double bond in solvents of low polarity and around the second double bond in solvents of high polarity. The branching ratios for returning to the ground state or *cis–trans* isomerization at the conical intersections could be very sensitive to the shape of the intersection seam. Making statements about the isomerization yield is therefore beyond the scope of our theoretical model.

Due to the fitting of the global parameter to $\alpha = 0.192$ eV the agreement between experimental and theoretical fluorescence quantum yields is quite good, although the

theoretical rates are off by multiples. In MCH the calculated fluorescence quantum yield is 0, because the barrier to one or the other conical intersection can be overcome easily, whereas this channel is inhibited in DMSO, thereby raising the fluorescence quantum yield to ≈ 60%. The fluorescence quantum yield does not go to 100% since the rate constant of the non-radiative decay from the Franck–Condon minimum to the ground state increases with the solvatochromic shift.
The single most important factor for explaining the trends in the fluorescence quantum yields is the activation energy. To elucidate how the height of the barrier to the conical intersections is affected by the solvent we characterize the polarity of the ground and excited state by constrained density functional theory followed by configuration interaction (CDFT-CI).

7.3.5 Qualitative Electronic Structure Analysis

CDFT-CI calculations in the gas phase put the weight of the zwitterionic configuration in the ground state at $c^2 = 0.267$ for the Franck–Condon geometry which is in accordance with an experimental value of $c^2 = 0.27 \pm 0.02$. The weight c^2 is approximately correlated with the pattern of bond length alternation (BLA), which is defined as the average difference in length of single and double bonds which are part of the polymethine chain (in the neutral resonance structure **DA**, see Fig. 7.1). When c^2 changes from 0 to 1 the double bonds in the polymethine turn into single bonds and vice versa. At the same time the BLA switches from positive to negative. Therefore the variations of the bond lengths are a sign of changes in the electronic character of the wavefunction. Figure 7.5 shows that the average length of the double bonds increases only slightly at the expense of the single bonds as the dielectric constant of the solvent increases from $\epsilon_r = 2.02$ (MCH) to $\epsilon_r = 46.83$ (DMSO). The calculated values at the TDDFT/IEFPCM level for the S_0 minimum (ranging from ≈ 0.06 Å for MCH to ≈ 0.04 Å for DMSO) agree very well with the experimental BLA value of 0.044 Å obtained from the crystal structure analysis. The ground state remains dominated by the neutral resonance structure and the excited state by the zwitterionic one for all solvents. However, we observe that the character of the wavefunction at the transition state has a strong dependence on the solvent. The BLA of almost zero in MCH for the TS and the S_1 minimum indicates that the electronic character is very similar at these geometries and this can be called an early transition state.[326] As the polarity of the solvent increases, the character of the transition state approaches that of the ground state. Thus, in solvents such as MeCN or DMSO, we are dealing with late transition states. The calculated barrier and experimentally observed trends in the relaxation rates agree well with the qualitative analysis based on the Hammond–Leffler postulate.

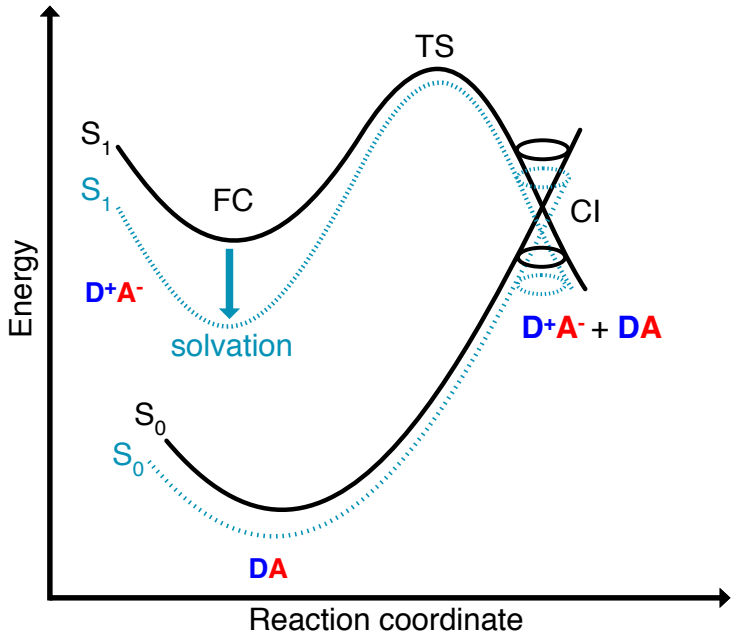

Figure 7.6: Energetics of thermally activated internal conversion through conical intersection for polyene-type merocyanines (with positive solvatochromism). The different stationary points in the ground and excited state are affected differently by the solvent depending on their polarity.

7.3.6 Excited-State Solvation

The Franck–Condon point on S_1 has the largest excited state dipole moment and its energy is therefore lowered most by a polar solvent (Fig. 7.6). Compared to this, the ground state with its small dipole moment is lowered much less by the same solvent. Therefore the optical gap decreases as the polarity of the solvent increases. This explains the positive solvatochromic shift observed in the absorption and emission spectrum. The transition state and the conical intersections, which have dipole moments in between the two extremes, are lowered less in energy by the polar solvent than the Franck–Condon point. Therefore the barrier to a conical intersection grows with increasing dielectric constant of the solvent. For the most polar solvents, MeCN and DMSO, the barrier becomes so high that the decay channel through a conical intersection is hardly accessible at room temperature resulting in the observed high fluorescence quantum yields for the most polar solvents. Furthermore, we provide a simple model based on CDFT-CI calculations and Onsager model that can explain why the polarity of the solvent affects different points along the reaction coordinate differently in the SI.
To test our hypothesis we conducted transient absorption spectroscopy which provides evidence for the presence of a decay channel through a conical intersection that can be turned on and off by changing the solvent.

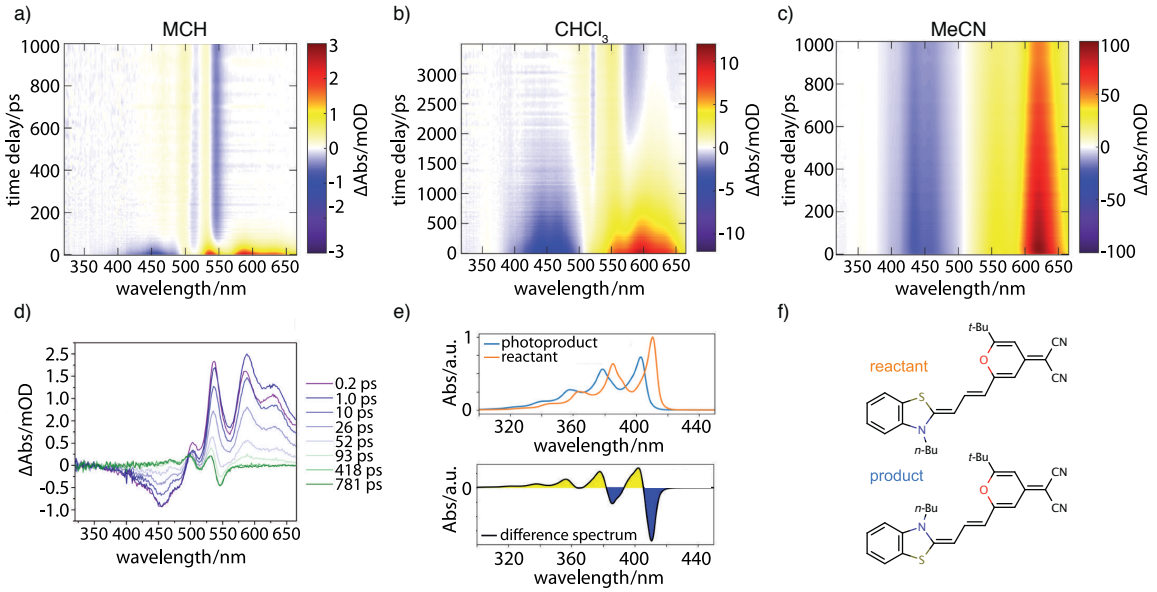

Figure 7.7: Transient absorption results. Maps are shown for the merocyanine dye **DCBT** in various solvents of increasing polarity using excitation wavelengths λ_{ex} tuned to the linear absorption maxima of 0-1 transition: (a) MCH at $\lambda_{ex} = 506$ nm, (b) $CHCl_3$ at $\lambda_{ex} = 518$ nm, and (c) MeCN at $\lambda_{ex} = 514$ nm. (d) Selected transient spectra for the case of MCH. The final shown trace at 781 ps (green) represents the absorption difference between the reactant and an isomerization product. (e) Top: Vibrationally resolved TDDFT absorption spectra in the gas phase of the reactant (red) and isomerization product (blue); bottom: linear difference spectrum between reactant and product that corresponds well to the green curve in d. (f) Corresponding chemical structures for reactant (red) and isomerization product (blue).

7.3.7 Transient Absorption Data

Figure 7.7 contains the results of the transient absorption experiment. Shown in Figs. 7.7a-c are transient absorption maps of the merocyanine dye in solvents with increasing polarity, namely methylcyclohexane (Fig. 7.7a), chloroform (Fig. 7.7b), and acetonitrile (Fig. 7.7c). Positive signals (yellow, red) around 500–660 nm correspond to excited-state absorption, negative signals (blue) in the region of 400–500 nm to ground-state bleach. Global analysis leads to decay-associated spectra as presented in the SI (Fig. S14). Obtained lifetimes for all solvents are summarized in Table S6. In the case of the nonpolar solvent MCH (Fig. 7.7a) global analysis reveals a time constant for the recovery of the ground-state bleach ($\tau_4 = 36.0$ ps) which is in agreement with the measured fluorescence lifetime of less than 120 ps. At long time delays a permanent change in absorption is observed in the range of 450–550 nm that is indicative of the formation of a photoproduct, to be discussed further below.

In the solvent with intermediate polarity (i.e., $CHCl_3$, Fig. 7.7b), the return of the population to the ground state is much slower than in the nonpolar solvent MCH (τ_4 = 834.0 ps) that is consistent with the experimentally determined fluorescence lifetime of 590 ps. We again observe a permanent change in absorption indicating the formation of a photoproduct.
In the most polar solvent MeCN (Fig. 7.7c) the return to the ground state is even slower than in $CHCl_3$ and the time constant for the relaxation back to the ground state (τ_5 = 1.44 ns) is in agreement with the experimentally determined fluorescence lifetime of $\tau_{\mathrm{fl}} = \Phi_{\mathrm{fl}}/k_r$ = 1.78 ns (see Table 7.1).
We now further analyze the photoproduct observed at long times in MCH and $CHCl_3$, shown exemplarily for the case of MCH in the transient spectrum at 781 ps (Fig. 7.7d, green curve). We observe characteristic positive and negative features corresponding, respectively, to the rise of product absorption and the permanent bleach of reactant. To identify the photoproduct, we calculated vibrationally resolved TDDFT absorption spectra (Fig. 7.7e, top) for the reactant (red) and a tentative photoproduct (blue) following *cis–trans* isomerization around the first double bond in the polymethine chain, with chemical structures displayed in Fig. 7.7f. The photoproduct is connected to the initially excited Franck–Condon region by a path over the transition state and a conical intersection at a twisted double bond. The geometry of the isomer is sterically hindered and less stable than the reactant by ΔG = 19.96 kJ/mol. The vibrational substructure can be assigned to a progression of the C–C stretch vibration in the polymethine bridge. Since the spectrum of the photoproduct is blue shifted by approximately half the vibrational frequency, the resulting difference spectrum (Fig. 7.7e, bottom) consists of alternating troughs and peaks. It agrees very well with the experimental difference spectrum at long time delay (Fig. 7.7d, green).
In summary, the experimental transient absorption data confirms the observed trend of increasing lifetimes with increasing solvent polarity. Furthermore, a permanent change in absorption indicating the formation of a photoproduct can be observed in case of MCH and $CHCl_3$. In MeCN such a change was not seen within the maximum delay time of 1 ns. This is in line with the proposed increase of the barrier to the conical intersection with increasing solvent polarity.

7.3.8 Temperature Dependence of Fluorescence Quantum Yields

Measurements of fluorescence quantum yields at lower temperatures ($T \approx$ 250 K and 200 K) provide additional evidence for our theoretical model. Thus, they are in accord with the temperature dependence implied in Eq. (7.3) due to $k_{\mathrm{ic}}^{\mathrm{CI}} \propto e^{-E_{\mathrm{A}}/(k_{\mathrm{B}}T)}$ (shown in Fig. S15 in the SI). In all solvents for which experimental data are available over a larger temperature range (limitations are imposed by the melting point of the solvent and dye aggregation at lower temperatures in MCH), the fluorescence quantum yield increases at lower temperatures. Importantly, also the inflection point, where the fluorescence quantum yield increases most, moves to higher temperatures

as the polarity of the solvent increases.

7.4 Conclusion

We have synthesized a new dipolar merocyanine dye and measured its fluorescence quantum yield as a function of the solvent polarity and temperature. A positive solvatochromic shift is accompanied by an increase in the fluorescence lifetime which is at odds with the predictions of the energy gap law. An additional decay channel through conical intersections was found by extensive quantum chemical exploration of the potential energy surfaces of the solvated merocyanine and resolved this apparent contradiction. We have presented theoretical and experimental evidence for the presence of conical intersections that are thermally activated and lead to a non-radiative decay involving either return to the reactant minimum or *cis–trans* isomerization. The temperature dependence of the non-radiative decay rates proves the existence of a barrier. The activation energy increases with solvent polarity which is explained by the better stabilization of the very dipolar excited state by the polar solvents as illustrated in Fig. 7.6.
These results are not only of importance for our fundamental understanding of the photophysics of donor–acceptor dyes. Merocyanines like **DCBT** may also open up interesting opportunities as fluorescent probes in biomolecular studies because both the increase of the barrier in the polar solvent water as well as the inhibition of the torsional decay channel by coordination of the dye to proteins or RNA/DNA macromolecules are expected to enable high fluorescence quantum yields.[353–355]

7.5 Appendix

7.5.1 Rates based on Kramers's Theory

For the evaluation of the Kramers's equation (see eqn. 8 in the main article) the electronic energy gap between the S_1 minimum and transition state, which connects the FC minimum and the conical intersection, is used to calculate the nonradiative rate k_{ic}^{CI}. However, our calculated activation barriers E_A are too high and if plugged unadulterated into Kramers's equation would lead to negligibly small internal conversion rates. Furthermore, also the prefactor might be prone to errors and therefore this fitting to the experimental values corrects both for the systematic errors in the barrier heights as well for the errors in the frequency prefactor. In view of the clear correlation between activation barriers and quantum yields, we introduce a parameter α for shifting the activation energies to a reasonable magnitude. α is fitted to minimize the difference between experimental and simulated quantum yields. The optimal value of α is obtained by finding the maximum of the sample Pearson corre-

lation coefficient[356],

$$r_{xy} = \frac{n\sum_{i=1}^{n} x_i y_i - \sum_{i=1}^{n} x_i \sum_{i=1}^{n} y_i}{\sqrt{n\sum_{i=1}^{n} x_i^2 - \left(\sum_{i=1}^{n} x_i^2\right)^2}\sqrt{n\sum_{i=1}^{n} y_i^2 - \left(\sum_{i=1}^{n} y_i^2\right)^2}}, \tag{7.9}$$

between the two data sets. Here x_i, y_i are the experimental and simulated quantum yields in the different solvents and n is the number of solvents. This gives $\alpha = 0.192$ eV.

Calculation of Friction Coefficients

The microscopic friction coefficients, γ, were calculated using Stokes law:

$$\gamma = \frac{6 \cdot \pi \cdot \eta \cdot r}{m} \tag{7.10}$$

Here η is the dynamic viscosity of the solvent, r the radius of a single solvent molecule and m the molar mass. The radii were calculated from the macroscopic density and the molar mass by assuming that the geometry of the solvent molecule corresponds to a hard sphere. The used data in combination with the reference are given in Tab. S2 of Ref. 10.

7.5.2 Onsager Solvation Model

Having established by the CDFT-CI calculations and the BLA criterion that the weight c^2 changes along the path FC $\rightarrow$ TS $\rightarrow$ MECI, we can interpret c^2 as a reaction coordinate. CDFT-CI also provides qualitative matrix elements of the x-component (along the principal axis of the molecule) of the dipole operator for the diabatic wavefunctions (in Debye):

$$\mu_{\text{neutral}} = \langle \mathbf{DA}|ex|\mathbf{DA}\rangle = 6.1 \text{ D} \tag{7.11}$$
$$\mu_{\text{zwitter}} = \langle \mathbf{D^+A^-}|ex|\mathbf{D^+A^-}\rangle = 40.5 \text{ D} \tag{7.12}$$
$$\mu_{\text{cross}} = \langle \mathbf{DA}|ex|\mathbf{D^+A^-}\rangle = -3.7 \text{ D} \tag{7.13}$$

With the help of the diabatic to adiabatic transformation

$$\Psi_{\text{g}} = \sqrt{1-c^2}|\mathbf{DA}\rangle + c|\mathbf{D^+A^-}\rangle \tag{7.14}$$
$$\Psi_{\text{e}} = c|\mathbf{DA}\rangle - \sqrt{1-c^2}|\mathbf{D^+A^-}\rangle, \tag{7.15}$$

the permanent dipole moments of the adiabatic ground and excited state may be expressed as functions of the parameter c:

$$\mu_{\mathrm{g}}(c) = \sqrt{1-c^2}\mu_{\mathrm{neutral}} + c^2\mu_{\mathrm{zwitter}} + 2c\sqrt{1-c^2}\mu_{\mathrm{cross}} \tag{7.16}$$

$$\mu_{\mathrm{e}}(c) = c^2\mu_{\mathrm{neutral}} + (1-c^2)\mu_{\mathrm{zwitter}} - 2c\sqrt{1-c^2}\mu_{\mathrm{cross}} \tag{7.17}$$

These qualitative dipole moments are plotted in the upper part of Fig. 7.8. The similarity of the curves with the quantitative dipole moments from CASSCF calculations in Fig. 4 justifies the choice of c as a reaction coordinate, but it is also obvious that the amplitude of these dipole moments is overestimated.
Now we are in a position to build a simple model that explains why the polarity of the solvent affects different points along the reaction coordinate differently. In the Onsager model[357,358], the solute is approximated by a dipole in a spherical cavity of radius a surrounded by a homogeneous dielectric medium of the relative dielectric constant ϵ_{r} (to vacuum). The dipole moment induces a polarization in the dielectric which gives rise to a reaction field $\boldsymbol{R}$, the strength of which depends on ϵ_r:

$$\boldsymbol{R} = \frac{2(\epsilon_{\mathrm{r}}-1)}{2\epsilon_{\mathrm{r}}+1}\frac{\mu}{a^3} \tag{7.18}$$

If the excited state is long-lived, the reaction field has time to adjust to the excited state dipole moment. The state-specific solvation energy is given by the interaction of the dipole moment of the ground or excited state with the respective reaction field:

$$U_{\mathrm{sol}}(c) = -\frac{1}{2}\mu\cdot\boldsymbol{R} = -\frac{\epsilon_{\mathrm{r}}-1}{2\epsilon_{\mathrm{r}}+1}\frac{\mu^2(c)}{a^3} \tag{7.19}$$

The Onsager model is only able to predict qualitative trends. For elongated planar molecules the assumption of a spherical cavity is questionable and it is not clear which value should be chosen for the cavity radius – we use a value of $a \approx 10$ Å.
The solvation energies along the reaction path according to eqn. 7.19 are shown on the right in Fig. 7.8b. For $c \approx 0$ the excited state is largely zwitterionic and strongly stabilized by polar solvents, whereas the stabilization is only small for $c \approx 1$. This leads to an increase in the activation energy and consequently a reduction in the rate for non-radiative decay through the CI.

7.5.3 Temperature Dependence of Quantum Yields

In Fig. 7.9 the predicted and experimental fluorescence quantum yields as functions of the temperature are plotted as lines and crosses, respectively. In all solvents for which experimental data are available at more than one point, the quantum yield increases at lower temperatures. The largest temperature range could be investigated for CH_2Cl_2. For this solvent of intermediate polarity a quite good agreement between experiment and theory is found with an increase of the fluorescence quantum yield

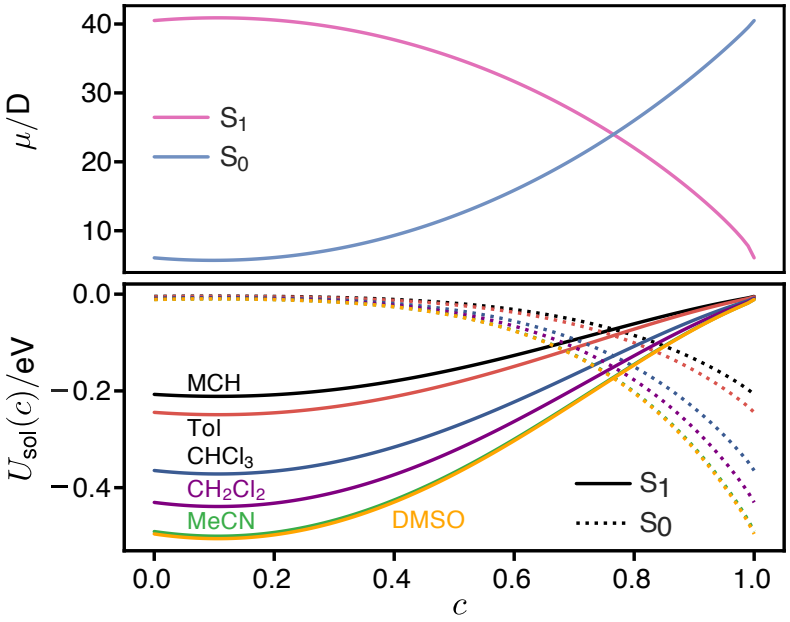

Figure 7.8: (top) Permanent dipole moments in the ground and excited state along the reaction coordinate c. (bottom) State-specific solvation energy from Onsager's model for solvents of increasing polarity. The Franck-Condon point ($c \approx 0.52$) is stabilized more by a polar solvent than the transition state and the MECI ($c \approx 0.71$).

from 17 % at 293 K to 54% at 195 K. For the least polar solvent MCH a small increase from QY=1 % at T=293 K to 4 % at 248 K can be discerned in the experimental data. For the unpolar solvent MCH (where the dye aggregation precludes measuremnts below 248 K) and the polar solvent DMSO (where no measurements below 291 K are possible due to the solidification of the solvent) the inflection points lie below or above the temperature range that can be measured. Based on the position of the inflection point relative to room temperature, the solvents can be divided into three groups: the unpolar solvents MCH (and Tol) which suppress the fluorescence, the polar solvents DMSO (and MeCN) which enable fluorescence and the solvents CH_2Cl_2 (and $CHCl_3$), which allow to tune the fluorescence quantum yield of **DCBT** over a relatively narrow temperature interval close to room temperature.

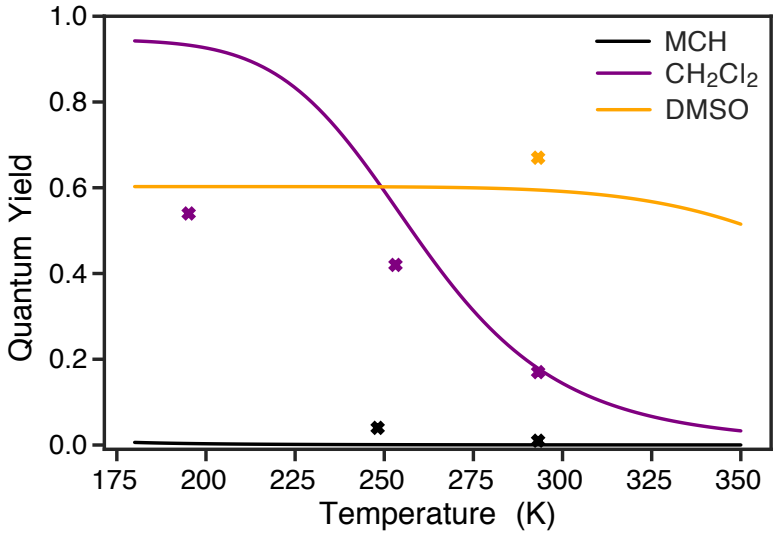

Figure 7.9: Temperature dependence of the quantum yield in different solvents. Solid curves correspond to the predictions, crosses are measurements.

Chapter 8

Transforming Dyes into Fluorophores

Herein we present a systematic study demonstrating to which extent exciton formation can amplify fluorescence based on a series of ethylene-bridged oligo-BODIPYs. A set of non- and weakly fluorescent BODIPY motifs was selected and transformed into discrete, chain-like oligomers by linkage via a flexible ethylene tether. The prepared superstructures constitute excitonically active entities with non-conjugated, Coulomb-coupled oscillators. The non-radiative deactivation channels of Internal Conversion (IC), also combined with an upstream reductive Photoelectron Transfer (rPET) and Intersystem Crossing (ISC) were addressed at the monomeric state and the evolution of fluorescence and (non-)radiative decay rates studied along the oligomeric series. We demonstrate that a "masked" fluorescence can be fully reactivated irrespective of the imposed conformational rigidity. This work challenges the paradigm that a collective fluorescence enhancement is limited to sterically induced motional restrictions.

8.1 Introduction

In the mid 1930s Jelley and Scheibe independently discovered the influence of dye aggregation on the spectral response and described a phenomenon that was later termed J-aggregation.[66,67] A red-shifted, usually strongly amplified absorption, often accompanied by narrowed bandwidths,[135] was recognized as the distinctive spectral signature. Photophysically it originates from a collective or coherent excitation event of an ensemble of π-chromophores, which evokes either a red-shifted excitation energy (J-type coupling) as observed by its discoverers or an analogous blue-shifted absorption band (H-type coupling) depending on the geometrical parameters of the aggregation.[24,26,88,359,360] After Davydov[361] and Frenkel[362,363] introduced quantum-mechanical descriptions of the process scientific progress finally disclosed that defined dye aggregation with resulting exciton formation is not just an artificial lab curiosity but widely abundant in nature's unique strategy to harvest light and transform photon energy into charge gradients as exploited by the photosynthetic apparatus.[20,85,86] Although the photophysical outcome of an aggregation can be concertedly modulated,[364–367] it remains a challenging, multicausal process. Increasing effort is therefore invested to enable J-aggregation also within an intramolecularly constrained

conformational space.[106,132,368] To this end various dye scaffolds were linked in a J-type fashion directly at their core moiety ($sp^2 - sp^2$)[351,369–372] or via alkynyl tethers[162,211,373–376] to furnish homo and hetero-oligomeric superchromophores[64] with characteristic properties, such as exceptionally high extinction coefficients, narrowed absorption[132] and/or emission[211] bandwidths, solvent-dependent intramolecular excitation energy transfers (EET),[96] but also an enhanced quantum yield of fluorescence.[64,162,372,373,377] Although this effect might appear to contradict Englman and Jortner's energy gap law[79] it can be in fact rationalized by combining the latter with Kasha's exciton theory.[70,87,164] However, photoinduced distortive relaxations and intramolecular charge transfer processes can easily overrule a radiative decay of a J-aggregate resulting in decreased emissions[371,375,376,378–381] or even a complete loss of fluorescence at the oligomerized state.[382,383] For instance, while Lambert et al. reported an amplified fluorescence with a squaraine-homodimer from $\Phi_F = 0.62$ to 0.80[162] J-type arranged BODIPY polymers (linked via the β-position) show lower emission intensities.[369,376,378,379] In most of the studies a fluorescence property has been improved based on intermolecular or superstructural rigidifications either with an already strong emitter and/or with rather low amplifications,[132,162,377] while correlations to excited state dynamics have often not been investigated or remained elusive. As an extension to our previous investigation on strongly fluorescent BODIPY monomers that we integrated into ethylene-bridged superchromophores,[132] we now expound how non- or weakly fluorescent species ($\Phi_F \approx 0.05$) that forfeit their emission due to an IC-, ISC- or a preceding rPET-process are able to fully regain their fluorescence property ($\Phi_F \approx 0.90$) when linked by the same ethylene spacer unit. This intramolecular linkage widely preserves the autonomy of the integrated π-systems and conceptually resembles an intermolecular approach based on the conformational instability and the missing π-conjugation.[64,96,162,211,351,369–377] For this purpose, we have transformed a set of tailor-made BODIPY monomers into a series of oligo-BODIPYs and investigated the photophysical outcome by optical spectroscopy and computations. Figure 8.1 presents an overview of the BODIPY species studied in this work and relates the structures to the corresponding prevailing non-radiative decay processes.

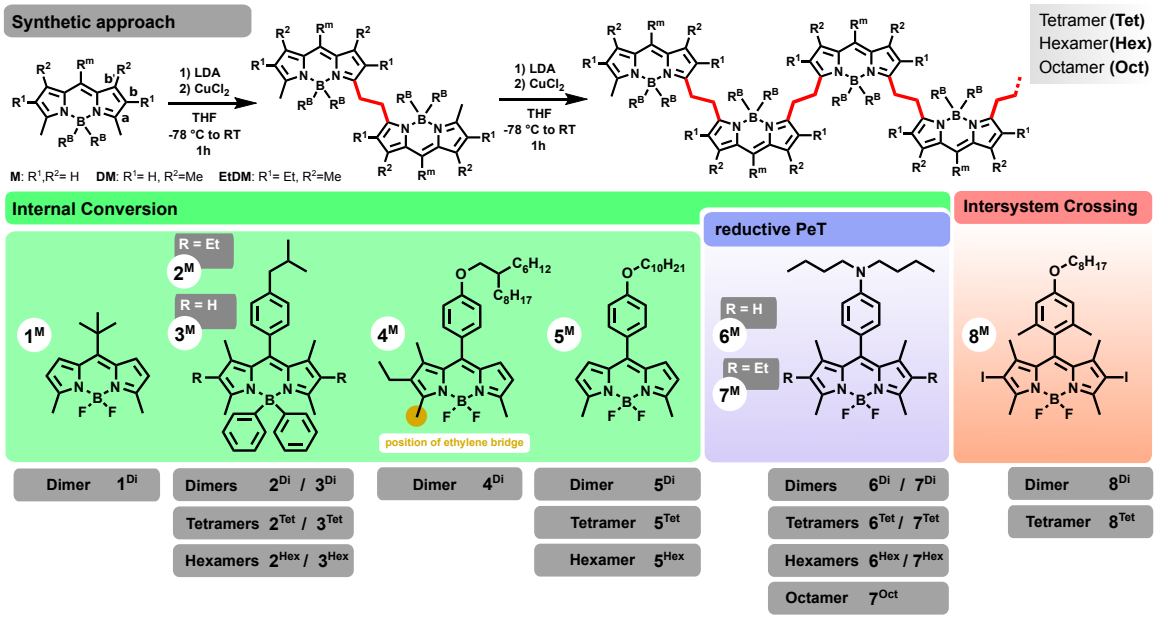

Figure 8.1: Synthetic scheme with the engaged pyrrole substitution patterns M, DM and EtDM and obtained compound range with assignment of synthesized BODIPY monomers to corresponding deactivation pathways responsible for the suppressed emission at the monomeric state. The Internal Conversion (IC) section encompasses also the rPET mechanism which happens prior to the decay to S_0.

8.2 Theoretical Background

The quantum yield of fluorescence Φ_F can be generally expressed as an interplay of excited state decay rates via Equation 8.1:

$$\Phi_F = \frac{k_r}{k_r + k_{nr}} = \frac{k_r}{k_r + k_{IC} + k_{ISC}} \tag{8.1}$$

High values of Φ_F can be either achieved by increasing the radiative decay rate k_r, by mitigation of its non-radiative counterpart k_{nr} or, most efficiently, by influencing both rates in a beneficial direction. The non-radiative decay process can furthermore be expanded according to the involved multiplicity giving k_{IC} for a transfer in between states of equal multiplicity (Internal Conversion or IC) and k_{ISC} in case of different multiplicities (Intersystem Crossing or ISC). Prior to these decay pathways, however, molecular moieties can also induce a charge separation and form charge-transfer states that are typically dark. If the excited π-system (dye unit) accepts an electron this process is called reductive photoelectron transfer (rPET).
In an excitonically active J-aggregate[384] all these terms can undergo significant variations. First, for the radiative decay process, it has been theoretically predicted that the radiative decay rate $k_{r,N}$ increases proportionally with number of integrated dye

units N:[385]

$$k_{\mathrm{r},N} \approx |\mu_{eg,N}|^2 \left(\frac{4n}{3c^3}\Delta E^3\right) \approx N\,|\mu_{eg,1}|^2 \left(\frac{4n}{3c^3}\Delta E^3\right) \approx N k_{\mathrm{r},1} \tag{8.2}$$

ΔE and n denote the energy gap/emission energy and the refractive index of the medium, respectively. Owing to the relatively small red-shift of a J-aggregate ΔE_N and ΔE_1 can be approximated with $\Delta E = \Delta E_N \approx \Delta E_1$. The resulting linear dependency between $k_{\mathrm{r},N}$ and $k_{\mathrm{r},1}$ then originates in an amplified electronic coupling between ground and excited state, which is determined by the transition dipole moment μ_{eg}. For a bright state of a J-aggregate with N units it follows, that the squared transition dipole moment of the J-aggregate $|\mu_{\mathrm{eg},N}|^2$ is a sum of the squared transition dipole moments of the single interacting units $|\mu_{\mathrm{eg},N}|^2 = N\,|\mu_{\mathrm{eg},1}|^2$. The uniform de-excitation then results in a superradiant emission[386] with decreased fluorescence lifetimes.

For delocalized excitons[12] the scaling of the nonradiative decay rate k_{IC} with the number of coupled dye units can also be derived.[385,387] In the case of weakly displaced potential energy surfaces, where the harmonic approximation is valid, the most common approach to estimate the internal conversion rate is based on the energy gap law (EGL) by Englman and Jortner.[79] We will adopt the notation of the EGL from ref.[385] that reads:

$$k_{\mathrm{IC}}^{\mathrm{EGL}} \approx \frac{u_{\mathrm{IC}}}{2\sqrt{2\pi}} C^2 e^{-S\cdot d} \sqrt{\frac{1}{x}} \exp\left(-x\left[\log\left(\frac{x}{S\cdot d}\right) - 1\right]\right) \tag{8.3}$$

The normal mode frequencies and Huang-Rhys factors are replaced by the number of effective promoting modes d that carry an average Huang-Rhys factor S. The length of the non-adiabatic coupling vector between the initial and final state is denoted as C. If all quantities are given in atomic units, the factor $u_{\mathrm{IC}} = 4.134\times10^{16}\ \mathrm{s}^{-1}$ converts the rate to s^{-1}. The quantity $x = \Delta E/\hbar\omega_{\mathrm{eff}}$ is the number of quanta in the effective modes that is required to match the energy gap between the electronic states. Some of us have recently derived the following scaling relations.[385] The number of promoting modes scales linearly with the number of monomers $d_N = N d_1$. Using the second Hellmann-Feynman theorem it follows that the length of the non-adiabatic coupling vector stays approximately constant ($C_N \approx C_1$) and the Huang-Rhys factors follow a scaling with N^{-2}. In addition, some further approximations can be introduced: If the influence of the excitonic coupling on the electronic energy gap is small, then $\Delta E_N \approx \Delta E_1$ and $x_N \approx x_1$ stay approximately constant. Furthermore, the scaling relations strongly dominate the number of quanta to match the energy gap so that their impact on the prefactor ($\exp(-Sd)$) is negligible. Using these approximations we get the following scaling of the internal conversion rate:

$$k_{\mathrm{IC},N}^{\mathrm{EGL}} \approx \left(\frac{1}{N}\right)^x k_{\mathrm{IC},1} \tag{8.4}$$

However, we observed that the scaling of the Huang–Rhys factor is only valid in the limit of large oligomers/polymers. In rather small aggregates, such as the ones studied in this work, the displacement of the promoting modes stays approximately constant or decreases only slightly with the number of monomers.[385] As a result, the exponent might be much smaller than x for the comparison of monomers ($N = 1$) to aggregates with $N \leq 8$. Thus, an inverse linear scaling might be considered as an upper bound for the internal conversion rate that is mediated by vibronic coupling:

$$k_{\mathrm{IC},N}^{\mathrm{EGL}} < \frac{1}{N} k_{\mathrm{IC},1} \tag{8.5}$$

It can be seen that in growing aggregates, for which the harmonic approximation is valid (e.g. no presence of conical intersections), a strong reduction of the non-radiative decay rate k_{IC} should be observed. Together with the amplification of k_{r} according to Equation 8.1 J-aggregates have the potential to develop strong emissions even in the nearinfrared region[388] despite their typically red-shifted main absorptions. In the following, we will present experimental data for the decay rates k_{r} and k_{nr} as functions of N.

8.3 Results and Discussion

8.3.1 Synthesis and Conformational Analysis

BODIPY scaffolds[117,118,194,389–395] bearing an α-methyl group are suitable substrates for an oxidative coupling strategy to furnish a series of ethylene-bridged oligomers in a straightforward two-step approach (see Figure 8.1, top), a general method that is applicable to various building blocks.[396,397] While the first step leads to dimeric species exclusively with yields up to 75 %, a subsequent oligomerization gives a range of n (dimeric) oligomers ($n = 1, 2, 3, 4$).[132] Owing to the transition dipole moment of S_1 that is oriented along the long axis of the BODIPY motif the linkage results in a geometrical predisposition for J-type coupling. Since a conformational exchange at the ethylene bridge occurs in the picosecond regime standard NMR spectroscopy is illsuited to detect possible conformational distributions. We thus decided for a computational approach. First, we envisaged finding ground-state global minimum geometries of simple dimeric structures assuming that resulting lowest energy geometries should then be transferable to higher homologs with reasonable accuracy. Owing to the large structural diversity of our compound range we decided for a representative dimeric BODIPY prototype with a *meso* substituent R^{m} = Phenyl as an adequate, geometrical approximation to account for most series in Figure 8.1 (for series **2** and **3** with phenyl-equipped boron centers an additional study with similar results is presented in the Supporting Information of Ref. 4). We furthermore modified the dipyrrin substitution pattern according to our set of compounds: 2-methyl (M) in the series **1**, **5** and **4**; 2, 4-dimethyl (DM) in series **3** and **6** and finally 3-ethyl-2,4-dimethyl

(EtDM) as present in the series **2**, **4** and **7**. After an initial conformational analysis with a force-field-based Monte Carlo sampling resulting dominant geometries were furthermore optimized at the DFT-level and refined with a final single-point calculation using a robust double-hybrid functional (DSD-BLYP/TZVPP) with D3 dispersion correction.[133] Figure 8.2 depicts the conformational space at the ethylene bridge and contrasts dominant microstructures with free Gibbs energies to outline an estimated ranking. While the energetic discrimination in EtDM-derived series is highest as a result of the steric repulsion of β-ethyl residues that favor the saddle2 arrangement, dimers with M and DM dipyrrin cores exhibit a wider conformational space and might adopt staggered, saddle or even the gauche conformation SC-*cis* with similar preference. A nearly equivalent ranking has been found by some of us in Ref. 132. Thus, we conclude with some caution that saddle2 in case of the EtDM-derived series and a potential coexistence of various geometries for M- and DM-derived congeners are the structural equivalents in accordance with the obtained spectroscopic results below, also for higher homologs with multiple ethylene bridges.

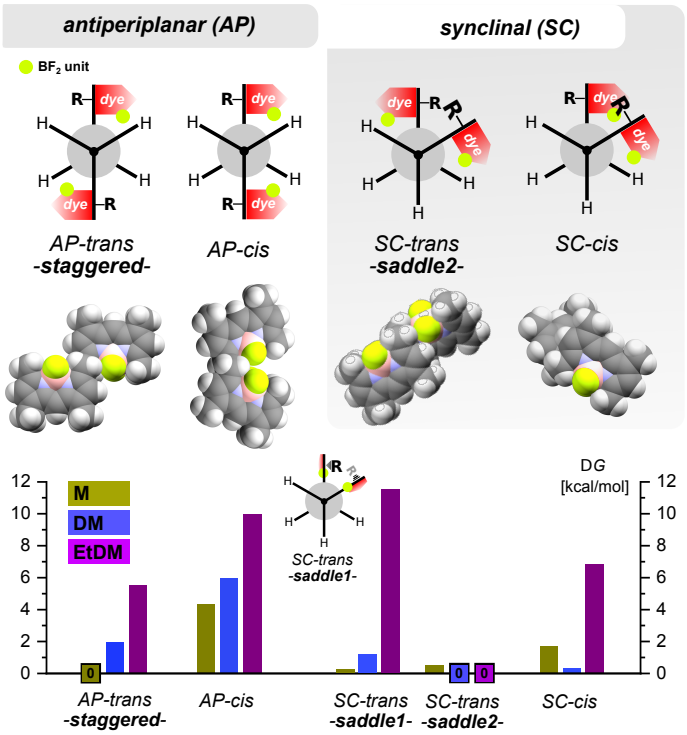

Figure 8.2: Conformational space of the ethylene bridge (Newman projections) with microstructures of a representative dimer platform (*meso* substituent: R^m = Ph). Computationally derived relative free Gibbs energies as a function of M-, DM- and EtDM derived dipyrrin core structures, respectively. Depicted microstructures refer to the DM case exemplarily (R^m = Ph is replaced by R^m = H for better visualization.)

8.3.2 Spectroscopy

Steady-state absorption and emission spectra, which we recorded in DCM, THF and toluene, support the conformational selection of our computational study. All oligo-BODIPY series develop a consistent increase of extinction coefficients with growing chain-lengths accompanied by a strong red-shift of absorption and emission independent of solvent polarity, which supports the global linear morphology arranged by the ethylene tether. To exclude contributions of intermolecular aggregation effects, all spectra were additionally recorded at different dilutions without observing changes in the spectral characteristics in all cases. The range distribution of spectrally derived excitonic coupling constants V is quite homogeneous (ca. -600 cm^{-1} to -800 cm^{-1}) indicating prevailing J-type coupling conditions for all series. A pronounced excitonic splitting[380,398] which would arise from bright H-type coupling contributions specifically at geometries that enforce a deviation from the global structural linearity (*AP-cis* and *SC-cis*) was not observed explicitly in shape of distinct high-energy peaks but contributes to the tailing of the absorption bands especially in case of the M- and DM-derived series with unshielded ethylene linkers and conformational instabilities. Figure 8.3 illustrates the spectral evolution of two series with different BODIPY substitution patterns and deactivation channels (series **3** and series **7**). Both examples are depicted as two extreme cases of the compound range presented (for more spectra see Supporting Information of Ref. 4, chap. 4.1). In case of series **3**, absorption and emission widely appear as mirror images, corresponding bands, however, are broad and seem to be an overlay of at least two distinct absorption events, especially for $\mathbf{3}^{\mathrm{Di}}$. This might indicate an excitonically intensified vibronic progression, the aforementioned coexistence of virtually isoenergetic geometries or the interplay of both. Such complex spectra were observed for many compounds of this study affecting also emission profiles (see series $\mathbf{3}/\mathbf{3}^{\mathrm{Di}}$ and $\mathbf{5}/\mathbf{5}^{\mathrm{Di}}$, see Supporting Information of Ref. 4). This is different for series **7**, where β- groups (EtDM core) impose additional steric restrictions and enable a fixation of adjacent BODIPY units in the saddle2 conformation. The exciton delocalization thus becomes spectroscopically evident and is manifested in narrowed absorption and emission bandshapes, which are compressed (fwhm) from 850/880 cm^{-1} (7^{M}) to 270 cm^{-1} (7^{Oct}), corresponding to an effective coherence length of:

$$N_{\mathrm{eff}} \approx 10 \quad \text{according to} \quad \sqrt{N_{\mathrm{eff}}} = \frac{\Delta\tilde{\upsilon}_{2/3}^{\mathrm{monomer}}}{\Delta\tilde{\upsilon}_{2/3}^{\mathrm{oligomer}}} \tag{8.6}$$

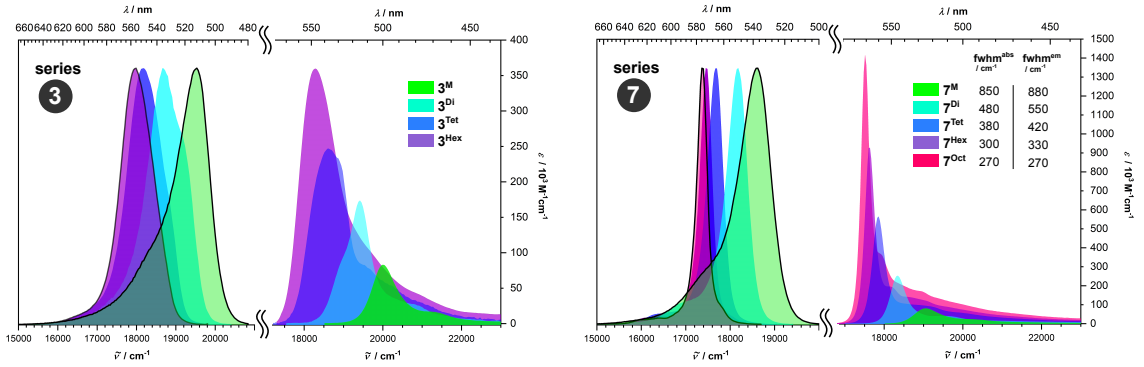

Figure 8.3: Series **3** and series **7** with absorption spectra (right) and emission spectra (left), respectively, in toluene at room temperature (RT). Emission is normalized. For series **7** full width at half maximum values (fwhm) are given for main absorption and emission bands.

We next examined the impact of the oligomerization on radiative decay rates k_r, as well as quantum yields of fluorescence Φ_F and rationalized a correlation with the deactivation channel involved. Except for series **8** (all solvents) and series **6** (DCM, THF) k_r trends widely proportionally with the number of integrated dye units N (Figure 8.4A) as predicted by theory for strongly coupled dye aggregates [see Eq. 8.4]. An exception is made for series **6** and **7** (rPET channel) where k_r increases disproportionally (**6**^{M} to **6**^{Di}, 10-fold; **7**^{Di} to **7**^{Tet}, 5-fold, see normalized plot). The tendency for a weak flattening of the curves at higher homologs might indicate the statistical increase of conformational disorder with higher contributions of heterogeneous coupling conditions or might be traced back to the decreasing emission energy ΔE_N, which was ignored in the approximation of Equation 8.2. Non-radiative rates k_{nr} show a more disparate evolution along the series (Figure 8.4B). A consistent decrease is only present in series **2** and **3** and cannot be specified for series **1** and **4** owing to the short oligomeric compound range in these cases. Despite this variety of excited state scenarios, the quantum yield of fluorescence Φ_F (Figure 8.4C) increases strongly upon oligomerization in all series, except for the ISC case. In series **1**, **2**, **3** and **5** (IC decay mechanism) as well as in series **6** and **7** (toluene) the fluorescence is virtually maximized at the highest homolog. The absorption and emission spectra for most series (except series **4** and **7**) show no clear band narrowing, although the radiative rates detected prove high delocalization lengths. However, this can be explained by the specific conformational stability within the BODIPY series (see Figure 8.5). As demonstrated by the energetic ranking in Figure 8.2, the rigidification of the ethylene linker units by β-ethyl groups (EtDM core) and the exclusive saddle2 microstructure in this case leads to consistently defined superstructures at higher homologs disclosing the well-known exchange narrowing effect.

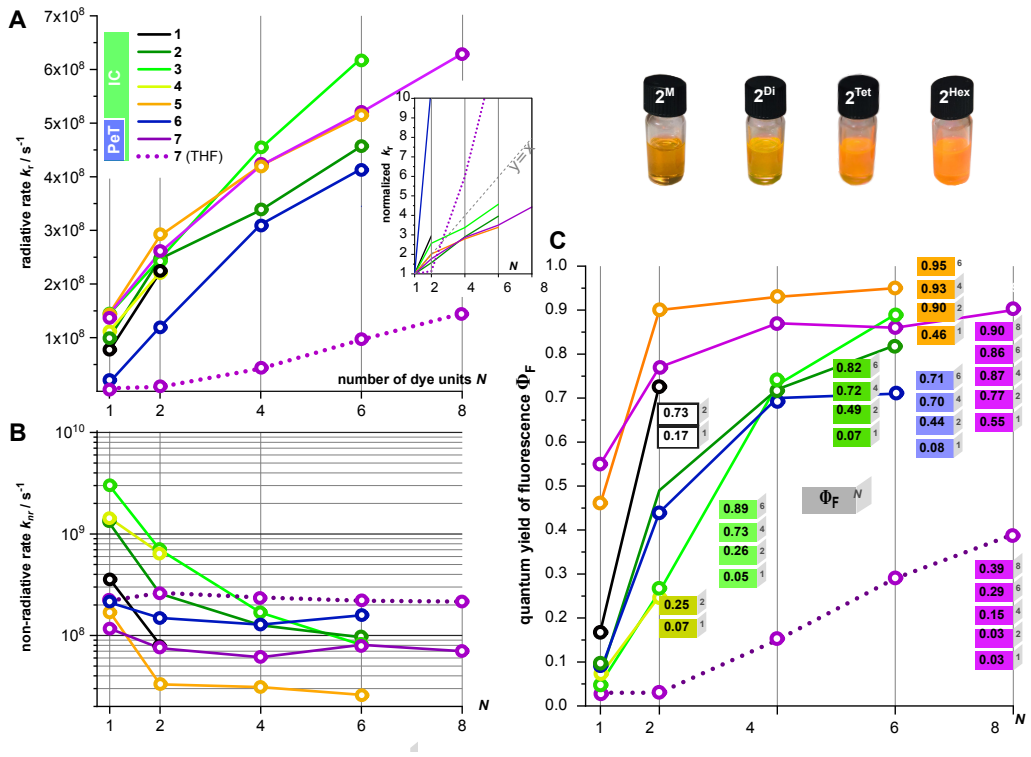

Figure 8.4: A) Evolution of (normalized) radiative decay rates k_r according to ($k_r = \Phi_F/\tau_F$. B) Evolution of non-radiative decay rates k_{nr} according to $k_{nr} = (1 - \Phi_F)/\tau_F$ in logarithmic scale. C) Quantum yields of fluorescence Φ_F along the growing oligomers in toluene. Φ_F values are given in boxes starting from the monomer at the bottom.

In cases where the ethylene bridge is less shielded (series **1**, **3**, **5**, **6** and **8**) or distorted by remote interactions (BPh_2 groups in series **2** and **3**), the presence of multiple microstructures within one superstructure leads to strongly differing excitonic couplings (off-diagonal disorder) and a redistribution of oscillator strengths within the exciton manifold.[399] Based on this microstructural diversity, a manifold of coexisting superstructures emerges in addition. In order to address this effect, we have simulated absorption spectra and excitonic couplings V of all representative dimer microstructures (see Figure 8.2) at the TDDFT-level (see Table S3 of Ref. 4) and used Boltzmann populations (see donut charts in Figure 8.5, and Figure S149 in Ref. 4) for simulation of absorption spectra (outlined graphs in Figure 8.5, Figure S150 in Ref. 4). Assuming that the H-type arrangement *AP-cis* is thermally inaccessible for M-, DM- and EtDM-derived series, V values are negative, yet quite homogeneous for *AP*-trans, saddle1 and saddle2 (-600 to -1000 cm^{-1}) but positive in case of the H-type microstructure *SC-cis* ($800 - 1600$ cm^{-1}). Since a *SC-cis* contribution thus results in higher excitonic couplings (up to 1600 cm^{-1}) the degree of exciton delocalization according to $\left|\frac{V}{\Delta E_{AB}}\right|$ is unaffected by the sign of V and even tolerates a higher site energy disorder ΔE_{AB}. These heterogeneous coupling contributions within one superstructure clearly show that a superstructure manifold will lead to a superpo-

sition of individual absorption spectra that effectively hide the exchange narrowing effect. Analogous to the absorption, the emission originates also in a manifold of coexisting, excited superstructures. The complexity of the absorption profiles is thus partially mirrored on the emission side except for the higher excited states that will mostly equilibrate to S_1 according to Kasha's rule. We found evidence for the coexistence of multiple emissive geometries in complex lifetime compositions of fluorescence decay curves and emission-wavelength-dependent lifetime measurements (see Figures S34 and S59 in Ref. 4). In the following we will discuss each series separately and review the specific decay mechanisms involved.

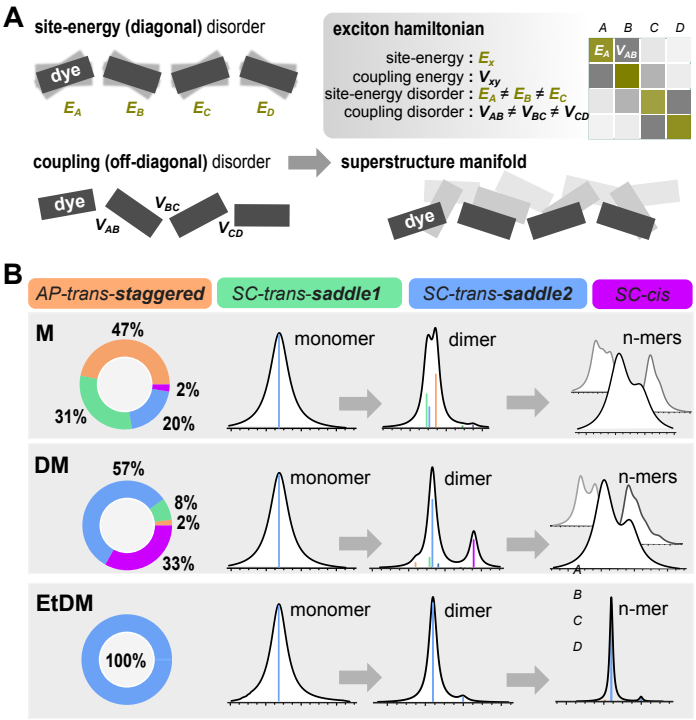

Figure 8.5: A) Illustrated disorder contributions and B) evolution of dimer (oligomer) bandshapes based on the microstructural compositions (Boltzmann population) derived from Gibbs free energies (representative M-, DM- and EDM-dimer platform / Figure 2).

8.3.3 BODIPY Series 1

BODIPY $\mathbf{1^M}$ bearing a sterically demanding *tert*-butyl group at the *meso* position is weakly fluorescent in DCM, THF and toluene ($\Phi_F \approx 0.16 - 0.22$). In addition, the emission band appears unusually broad for a BODIPY motif pointing towards a dominant excited state relaxation channel. A similar species without α-methyl groups has been computationally investigated by Jiao and Corminboeuf,[24,394] who found a conical intersection at a puckered dipyrrin geometry with an out-of-plane distorted *tert*-butyl group as the responsible decay channel. We found minimum energy conical intersections (MECI's), which structurally correspond very well to

those presented previously.[400] The excited state barrier between the Franck–Condon geometry and the MECI are quite small in the monomer (see Figure 8.6D) as well as in the dimer (see Figure S151 in Ref. 4) with values of 0.09 eV and 0.16 eV, respectively, clearly indicating a conical intersection as a prevailing relaxation pathway in S_1. The dimer $\mathbf{1}^{\mathrm{Di}}$ shows a strongly amplified emission ($\Phi_{\mathrm{F}} \approx 0.58 - 0.73$) accompanied by a doubled radiative rate constant k_{r} in all three solvent systems as predicted by theory (Eq. 8.2). The oligomerization, however, could not be extended further because of a limited solubility. Albeit of complex shape the emission band of $\mathbf{1}^{\mathrm{Di}}$ is narrowed ($\mathrm{fwhm}^{\mathrm{E}} \approx 1200 - 1300\ \mathrm{cm}^{-1}$) compared to its monomeric precursor $\mathbf{1}^{M}$ ($\mathrm{fwhm}^{\mathrm{E}} \approx 2100 - 2300\ \mathrm{cm}^{-1}$), which reflects a mitigated relaxation process as a result of delocalized excitation energy.

8.3.4 BODIPY Series 2 and 3

The non-radiative deactivation in the monomers $\mathbf{2^M}$ (EtDM core) and $\mathbf{3^M}$ (DM core) incorporating a central $\mathrm{B(Ph)_2}$ group[368,401] is even more pronounced, which results in a very weak, solvent-independent fluorescence at the monomeric state ($\Phi_{\mathrm{F}} \approx 0.07$ $\mathbf{2^M}$), $\Phi_{\mathrm{F}} \approx 0.05$ ($\mathbf{3^M}$). The mechanism for the quenching process has not been revealed yet, but additional high frequency C−H bonds[401–405] of the installed phenyl residues at the boron center as well as photoinduced interactions between the phenyl residues and the *meso* aryl group are likely to play a key role. In contrast to $\mathbf{1^M}$ we found MECI's for both monomers that are thermally not accessible since they exceed the Franck-Condon minimum by 0.66 $\left(\mathbf{2}^{\mathrm{M}}\right)$ and 1.00 $\left(\mathbf{3}^{\mathrm{M}}\right)$ eV (see Figure 6D). The non-radiative relaxation process should thus be dominated by an internal conversion mediated by vibronic coupling and can be understood qualitatively by using Englman & Jortner's energy gap law. Using the scaling relations derived in Equation 8.5 for the upper bound of k_{IC}, Figure 8.6E illustrates a good correlation with experimentally obtained nonradiative decay rates, which supports the theoretically derived decrease according to $1/N$ as the upper limit.
Upon oligomerization the fluorescence quantum yield is substantially enhanced in both series and in all solvent systems up to $\Phi_{\mathrm{F}} \approx 0.8 - 0.9$. Comparing the similar fluorescence enhancements in both series (DM and EtDM core) indicates that the effect is less restricted to a rigid alignment of the coupled dye units but tolerates a certain degree of conformational disorder. However, in case of the structurally rigidified series **2**, the β-ethyl substituents lead to a continuous narrowing of emission bands ($\mathrm{fwhm}^{\mathrm{E}} \approx 1000\ \mathrm{cm}^{-1}$ ($\mathbf{2}^{\mathrm{M}}$), $\mathrm{fwhm}^{\mathrm{E}} \approx 500\ \mathrm{cm}^{-1}$ $\mathbf{2}^{\mathrm{Hex}}$)), similar to but not as pronounced as that in series **7**.

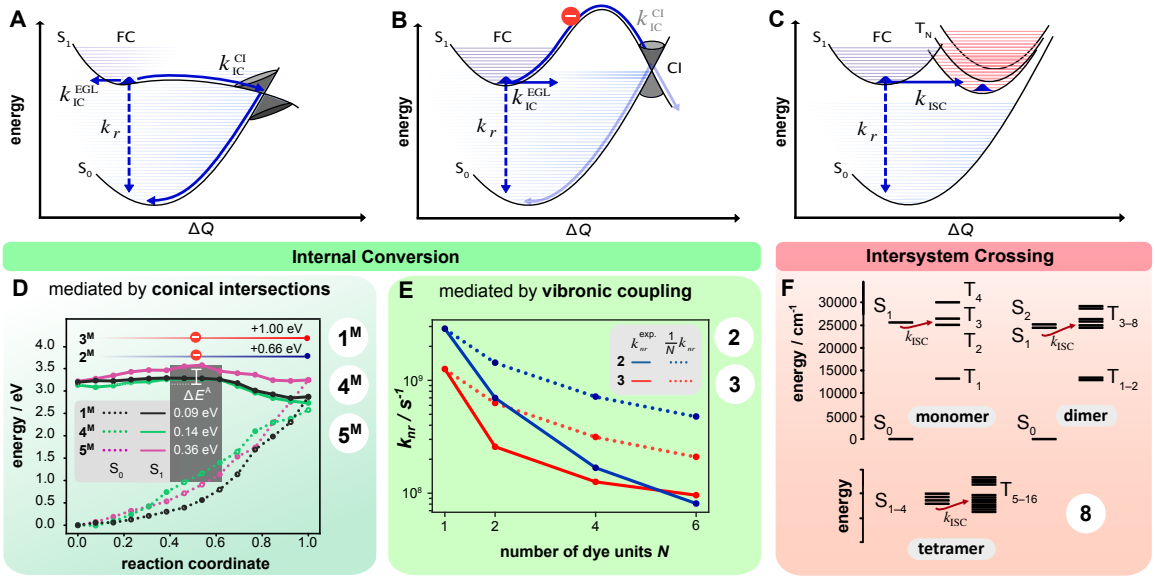

Figure 8.6: A-C) Energetics and relaxation pathways after excitation into the bright exciton state of a J-aggregate with illustrations of the conical intersection pathway I^{Cl}(A), the vibrationally controlled IC mechanism $\mathrm{IC}^{\mathrm{vib}}$ (B) and the ISC decay (C). D) Minimum energy pathways between the Franck-Condon minimum and the conical intersection for BODIPY monomers $\mathbf{1}^{\mathrm{M}}$, $\mathbf{4}^{\mathrm{M}}$ and $\mathbf{5}^{\mathrm{M}}$ as well as the inaccessible MECI's of $\mathbf{2}^{\mathrm{M}}$, $\mathbf{3}^{\mathrm{M}}$ for comparison. E) Graphical juxtaposition of experimental, non-radiative decay rates and theoretical counterparts according to the scaling relation derived in Equation 8.6 for series **2** and **3**. F) Energy diagram of the singlet and triplet states for monomer, dimer and tetramer of series **8**

8.3.5 BODIPY Series 4 and 5

BODIPYs $\mathbf{4}^{\mathbf{M}}$ and $\mathbf{5}^{\mathbf{M}}$ with torsional freedom at their unsaturated meso position are known to generally exhibit a diminished fluorescence.[406,407] A structural congener of $\mathbf{5}^{\mathbf{M}}$ (no α-methyl groups, underivatized *meso* phenyl group) has been computationally studied[400] and a torsional motion of its phenyl ring disclosed as a probable relaxation pathway for a conical intersection mechanism ($\Phi_{\mathrm{F}} \approx 0.05$). In fact, BODIPYs with an unrestricted aryl group at the meso position can induce non-directional, rotational motions around the meso bond[193,408,409] a process which was recently implemented in a rotaxane-BODIPY conjugate by Stoddard *et al.*[410] Hence, we optimized the MECIs and the corresponding minimum energy paths for $\mathbf{4}^{\mathrm{M}}$ and $\mathbf{5}^{\mathrm{M}}$ and obtained low barriers of 0.14 and 0.36 eV, respectively, which underlines a strong contribution of non-radiative relaxation mechanism through a conical intersection (see Figure 8.6D). While $\mathbf{4}^{\mathbf{M}}$ was only dimerized owing to its unsymmetrical core structure, its emission could be increased up to fourfold ($\mathbf{4}^{\mathrm{Di}}\Phi_{\mathrm{F}} \approx 0.14 - 0.25$). Starting from a reasonably strong fluorescence at $\mathbf{5}^{\mathbf{M}}$ the oligomerization up to a hexamer leads to Φ_{F} values that steadily approach unity. Even though Φ_{F} is thus quickly maximized already at the dimer $\mathbf{5}^{\mathrm{Di}}$ k_{r} still increases due to consistently lowered superradiant lifetimes (see

Figure 8.4A). In contrast to related BODIPY rotors, whose motional relaxation can be suppressed e.g. by sterics,[410] aggregation[371] or viscosity[371,410–414] resulting in reactivated emissions, the enhanced fluorescence of series **4** and **5** is not governed by an interchromophoric stacking process or an imposed steric hindrance that is rationalized nowadays in the frames of restricted intramolecular motion (RIM)[415,416] or restricted access to a conical intersection (RACI).[415,416] Instead, the weakly predefined spatial proximity of the ethylene tether generates excitons of sufficient delocalization and stability to maximize a masked fluorescence property. For distinction of this mechanism, also within the concepts of aggregationinduced emissio[25,417–419] and folding-induced fluorescence enhancement (FIFE)[365], we thus propose the term exciton-induced emission (EIE) as a qualified expression for such cases.

8.3.6 BODIPY Series 6 and 7

Series **6** and **7** are equipped with an electron-rich aniline *meso* residue that is known to trigger a dark charge-transfer (CT) state as a consequence of a preceding solvent-dependent, rPET process.[420,421] For the DM-derived series **6**, only a very weak emission in all three solvents was detected with low-energy CT emission bands in polar DCM and THF. In non-polar toluene, this band is blue-shifted and superimposed with the main emission band. We computed particle and hole densities between ground and excited states for $\mathbf{6^M}$ and $\mathbf{7^M}$ (see Figure S152 in Ref. 4) that unambiguously prove the existence of a charge transfer state for $\mathbf{6}^{\mathrm{M}}$ and $\mathbf{7}^{\mathrm{M}}$, respectively. While the oligomerization has no impact on the emission in DCM and THF regarding series **6**, the fluorescence efficiency is strongly increased from $\Phi_{\mathrm{F}} = 0.05$ $\left(\mathbf{6}^{\mathrm{M}}\right)$ to $\Phi_{\mathrm{F}} = 0.71$ $\left(\mathbf{6}^{\mathrm{Hex}}\right)$ in toluene. The β-ethyl substituted congener $\mathbf{7}^{\mathrm{M}}$ shows similar spectroscopic features in DCM and THF as $\mathbf{6}^{\mathrm{M}}$ ($\Phi_{\mathrm{F}} \approx 0.01 - 0.03$), however, in toluene a reasonably strong fluorescence ($\Phi_{\mathrm{F}} \approx 0.55$) is already present. The lack of a pronounced CT emission band thus questions the impact of a rPET process in case of this nonpolar solvent. Differently to series **6**, however, the emission can now also be gradually increased in DCM and THF ($7^{\mathrm{oct}}\Phi_{\mathrm{F}} \approx 0.20 - 0.39$). While the non-radiative rate stays widely constant the radiative rate k_{r} shows a disproportional step in both series (see Figure 8.4A, normalized plot), which reflects the energetic variation of localized donor and acceptor orbitals responsible for the rPET process. We plotted frontier orbital energies of series **6** and **7** up to the tetramer and found a higher energy gap between the aniline- (donor) and the BODIPY-core-centered orbitals (acceptor) in series **7**[422] which explains the inhibited rPET mechanism (see Figure S153 in Ref. 4). The higher energy gap can be clearly attributed to the enhanced electron-richness of the ethyl-equipped EtDM core and, associated therewith, an energetically upshifted exciton manifold. Even though the very weak fluorescence of the monomer $\mathbf{7^M}$ in DCM and THF is hard to determine accurately, we assume that the amplification of emission in this case is the largest in our study and to the best of our knowledge unprecedented in literature for a CT-defined decay channel.

8.3.7 BODIPY Series 8

Diiodinated BODIPY motifs[423] are widely non-emissive owing to a rapid ISC process populating a low-energy triplet state. The intersystem crossing efficiency of a very similar diiodinated BODIPY dye has been studied very recently by Grusenmeyer *et al.* and determined in the range of 10^9 s^{-1}, which is roughly one magnitude higher than the radiative rate constant obtained and verified by us rationalizing the pronounced loss of emission.[424] Even though the β-iodine residues in series **8** seem to promote an ordered aggregation sphere at the ethylene bridges (see Figure S138 in Ref. 4), the emission efficiency is hard to determine accurately ($\Phi_F \approx 0.01 - 0.04$) and not amplified upon oligomerization. In contrast to the IC rate, the ISC rate is expected to increase with the number of monomeric units because the number of triplet acceptor states expand linearly and in addition to the extended singlet exciton manifold upon oligomerization (see Figure 8.6f and Table S4 in Ref. 4). According to Fermi's Golden Rule the coupling between singlet and triplet states is thus enhanced leading to a more efficient intersystem crossing process. Albeit not quantifiable, yet present in the background the increase of the radiative rate cannot overcompensate this effect that is sometimes described in the literature as aggregation-induced intersystem crossing.[425] However, in contrast to the very long known phenomenon of aggregation-induced emission, this effect is achieved purely by the electronic interaction of the monomers.

8.3.8 Weak coupling limit

After having studied the impact of EIE on several nonradiative deactivation channels, we sought for clarifying the role of the ethylene bridge and the proximity and alignment it provides between the dye units. Thus, we prepared two analogs of dimers $\mathbf{3}^{Di}$ and $\mathbf{5}^{Di}$ where the BODIPY motifs are linked at the *meso* position via a flexible alkyl ($\mathbf{9}^{mDi}$) or an alkoxyaryl ($\mathbf{10}^{mDi}$) tether unit (Figure 8.7). While $\mathbf{9}^{mDi}$ addresses the vibronically mediated internal conversion channel, $\mathbf{10}^{mDi}$ represents the case of the relaxation through a conical intersection in analogy to $\mathbf{3}^{Di}$ and $\mathbf{5}^{Di}$.

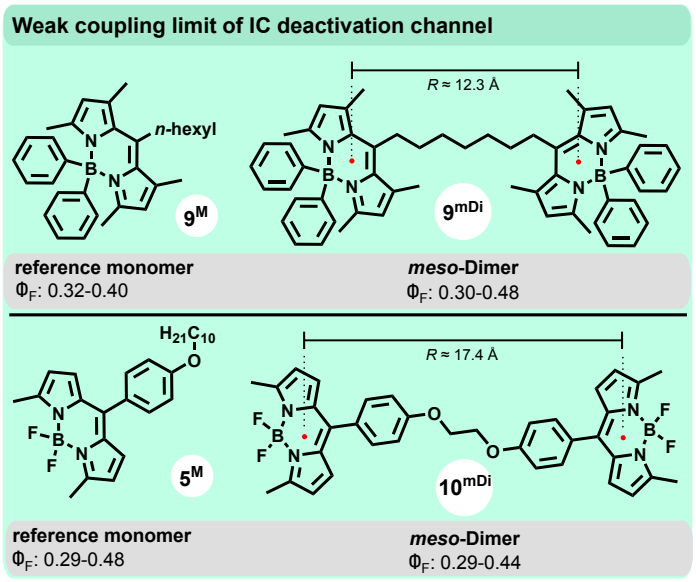

Figure 8.7: Meso-tethered BODIPY dimers as model scaffolds to study the weak coupling limit. Φ_F value range results from different solvent systems. Distance R assumes a stretched, all-anti conformation. For synthetic details, see Supporting Information of Ref. 4.

Assuming stretched geometries as global minimum structures, both dye units are aligned face-to-face in an H-type fashion but are still able to exchange their excitation energy via resonance energy transfer (RET).[361] We performed ground-state semiempirical molecular dynamic simulations (see Figure S154 and S155 in Ref. 4) to estimate the average interchromophoric distance R and obtained values of 10.4 Å ($\mathbf{9}^{\mathrm{mDi}}$) and 13.4 Å($\mathbf{10}^{\mathrm{mDi}}$). UV and emission spectra give no hints for a coexistence of photophysically differing conformers, which underlines a rapid inter-conformational exchange. The distance relations in these dimer structures resemble the ones found for instance in light-harvesting frameworks,[426] MOFs[427–429] and dye-containing nanostructures.[430,431] Comparing now the *meso*-linked dimer $\mathbf{9}^{\mathrm{mDi}}$ with its monomeric reference $\mathbf{9}^{\mathrm{M}}$ reveals very similar spectral properties except for the trivial doubling of the extinction coefficient. Radiative decay rates and Φ_F values, however, do not increase for $\mathbf{9}^{\mathrm{mDi}}$ and are widely identical with values obtained for $\mathbf{9}^{\mathbf{M}}$ within the instrumental error. An even higher spectral and photophysical accordance was found for the compound pair $\mathbf{5}^{\mathbf{M}}$ and $\mathbf{10}^{\mathrm{mDi}}$ with an extended interchromophoric distance and an even smaller excitonic coupling energy indicating the absence of a delocalized exciton. The exchange of excitation energy of a two-level quantum system can be approximated as a coherent oscillation with the frequency $\omega_R = \frac{E_2 - E_1}{\hbar} = \frac{2V}{\hbar}$, also known as Rabi oscillation. Excitonic coupling constants V derived either from TDDFT computations or explicitly (see Supporting Information and Table S5 in Ref. 4) give respective frequencies in the range of ca. $1700 - 6800$ ns^{-1} ($\mathbf{9}^{\mathrm{mDi}}$) and $1200 - 4400$ ns^{-1} ($\mathbf{10}^{\mathrm{mDi}}$) depending on the level of theory. Assuming a (Homo-)FRET approach[425] and using Equation S5 in Ref. 4 as another rough approximation gave

corresponding rates of $500 - 800$ ns^{-1} for $\mathbf{9}^{\mathrm{mDi}}$ and $500 - 600$ ns^{-1} for $\mathbf{10}^{\mathrm{mDi}}$. Thus, with the small coupling energies of ca. $20 - 110$ cm^{-1}, both dimeric systems are still able to transfer excitation energy back and forth several hundred times within the fluorescence lifetime of ca. $2 - 4$ ns. However, an evident impact on excited state relaxations and Φ_{F} values cannot be observed. From these results we conclude that such a symmetric and bidirectional RET process is neither sufficient to slowdown a non-radiative decay process related to energy barriers of a conical intersection process, nor for a vibronically mediated internal conversion. Instead, sufficient exciton delocalization based on a close, yet less defined proximity, as provided for example by an ethylene bridge, seems to be key to enable an efficient decoupling of nuclear and photoinduced electronic oscillations and unveil an inherent fluorescence property.

8.4 Conclusion

Within a mechanistic concept that we practically term exciton-induced emission (EIE) we presented a systematic study of the molecular parameters necessary to enhance or reactivate a structurally disguised emission capacity with exemplary BODIPY scaffolds. In contrast to previous molecular setups that rely on aggregation processes (AIE), molecular rigidifications and π-conjugational connectivities we could engage a flexible ethylene tether unit to achieve maximum enhancements of fluorescence based on exciton delocalization. A certain amount of conformational instability within the chain structures, as present in M and DM derived species, does not seem to be detrimental to the amplification effect, suggesting a tolerance to higher (off)-diagonal disorders or even a transient trapping of excitonic energy on single sites. Along this strategy we demonstrated that non-radiative deactivation processes based on an IC mechanism, from the conical intersection limit to vibronically mediated cases, can be fully suppressed. Especially in the case of the very weak emitters with phenyl-substituted boron centers ($\Phi_{\mathrm{F}} \approx 0.04 - 0.08$) the fluorescence was virtually maximized at the hexameric state ($\Phi_{\mathrm{F}} \approx 0.79 - 0.89$). To the best of our knowledge, such extreme amplifications based on a widely unconstrained spatial proximity have not yet been reported for discrete fluorescent entities. Within the frame of IC we additionally proved the attenuation of weakly emissive CT states triggered by an upstream rPET process at conformationally more rigidified EtDM-derived oligo-BODIPYs. In this case the fluorescence of a virtually non-emissive aniline-equipped BODIPY monomer $\mathbf{7}^{\mathbf{M}}$ was amplified by a factor of ca. 20. Since BODIPY motifs are not characterized by a unique photophysical signature, alternative chromophores, preferentially without ISC deactivation, should also transform into fluorescent counterparts if an ethylene bridge is installed with appropriate regioselectivity. Building upon the high amplifications detected already at the dimeric state, we believe that an EIE mechanism might also evolve in case of an intermolecular encounter of designated, yet identical dye scaffolds. If so, this concept holds promise to refrain from the common donor-acceptor setup and serve as a simplified tool for detection and visualization of spatial, molecular recognition processes, similar to the FRET assay,

but with modified, functional parameters.
We finally hope that this work can help to further elaborate the paradigms of fluorescence enhancement and support future endeavours in the prosperous field of AIE.

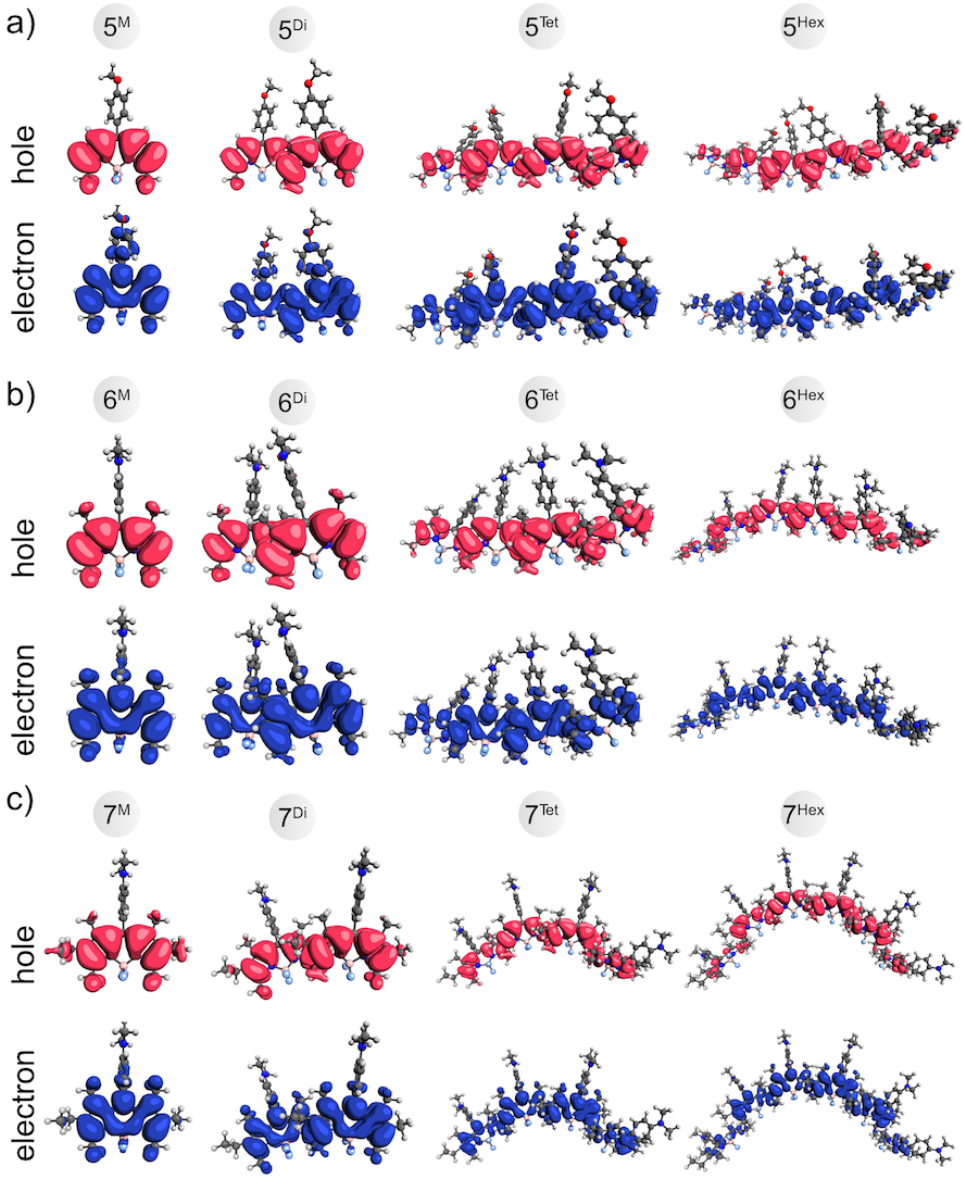

Figure 8.8: Electron and hole density between the electronic ground-state and the first excited state at the TD- DFT (wB97XD/def2-SVP) level. The respective *para*-substituents of the *meso* moieties were truncated to methoxy (series **5**) and dimethylamino (series **6** and **7**) to reduce computational costs. The ground state geometries of the monomers and dimers were optimized at the same level of theory, while the tetramer and hexamers were optmized using the GFN1-xTB method.

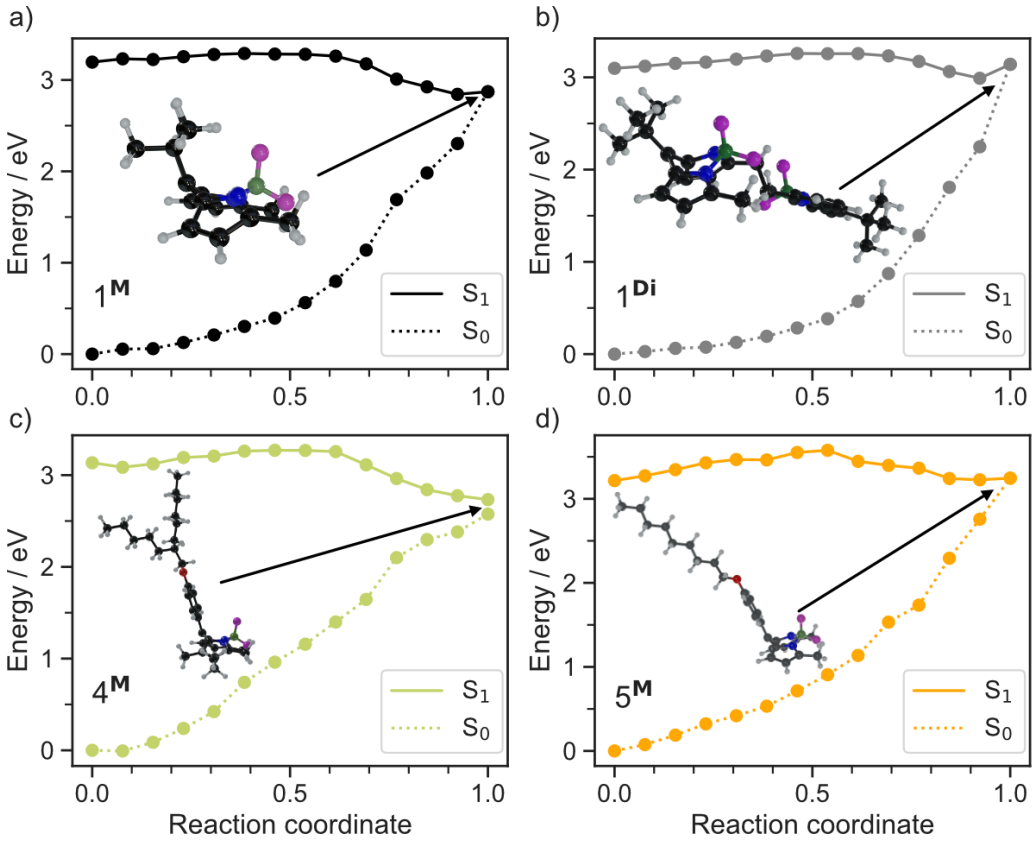

Figure 8.9: Ground- and excited-state energies along the excited-state minimum energy path from the Franck–Condon minimum to the conical intersection. The path was optimized using the nudged elastic band method. The MECI geometry is shown in each graph.

8.5 Appendix

8.5.1 Minimum energy paths to conical intersections

For the calculation of the energy along the relaxation path to the minimum energy conical intersection (MECI), the Franck-Condon structure in the S_1-state and the MECI were first optimized. These calculations were performed in the framework of TDA-TD-DFT using the ωB97XD functional and the def2-SVP[221] basis set as implemented in the Q-Chem 5.1.2 software package. The branching plane algorithm was employed for the optimization of the conical intersection. Although TD-DFT does not provide the correct dimensionality of the crossing seam for the of S_0 and S_1-state it often leads to reasonable predictions for MECl geometries.[323,324] The initial path between both minima was interpolated in internal coordinates and minimized using the nudged elastic band algorithm (NEB). In Fig. 8.12 the resulting relaxations paths in the first excited state and the corresponding ground state energies are shown. In the case of BODIPY 2^{M} and 3^{M} the MECls were only optimized but no minimum energy path was calculated. The energy of the MECl geometry was in these cases 0.66

eV $\left(2^{\mathrm{M}}\right)$ and 1.00 eV $\left(3^{\mathrm{M}}\right)$ above the Franck-Condon minimum. Since this is almost one order of magnitude higher than the barriers in the other BODIPY systems, we assume that this pathway does not play a significant role in the radiationless relaxation.

8.5.2 Charge-transfer states of BODIPYs 6^{M} and 7^{M}

To characterize the charge-transfer state in the monomers of BODIPY **6** and **7** the particle and hole densities between the electronic ground state and the excited states were computed at the same level of theory as the NEB calculations were done. In both systems, we found a low lying CT state which has the same character in both systems where the electron is located on the BODIPY moiety and the hole resides on the aniline unit (see Figure 8.10).

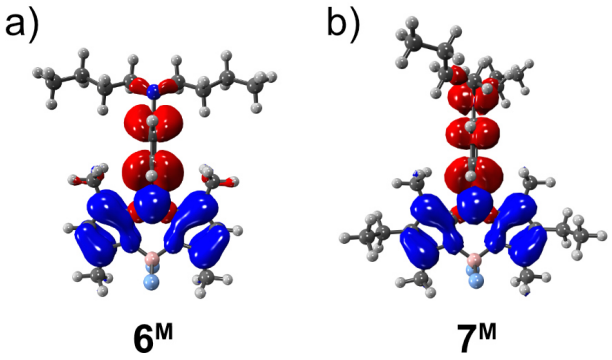

Figure 8.10: Particle (blue) and hole (red) densities of the CT state (S_4 in $\mathbf{6}^{\mathrm{M}}$/S_2 in $\mathbf{7}^{\mathrm{M}}$).

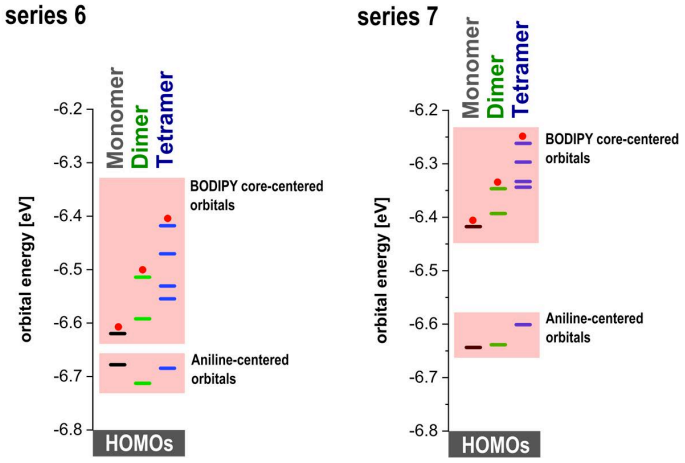

Figure 8.11: Frontier orbital energies of series **6** and **7** up to the tetramers as well as their localizations, *meso* moiety (aniline unit) or BODIPY core unit. HOMO is marked with a red dot.

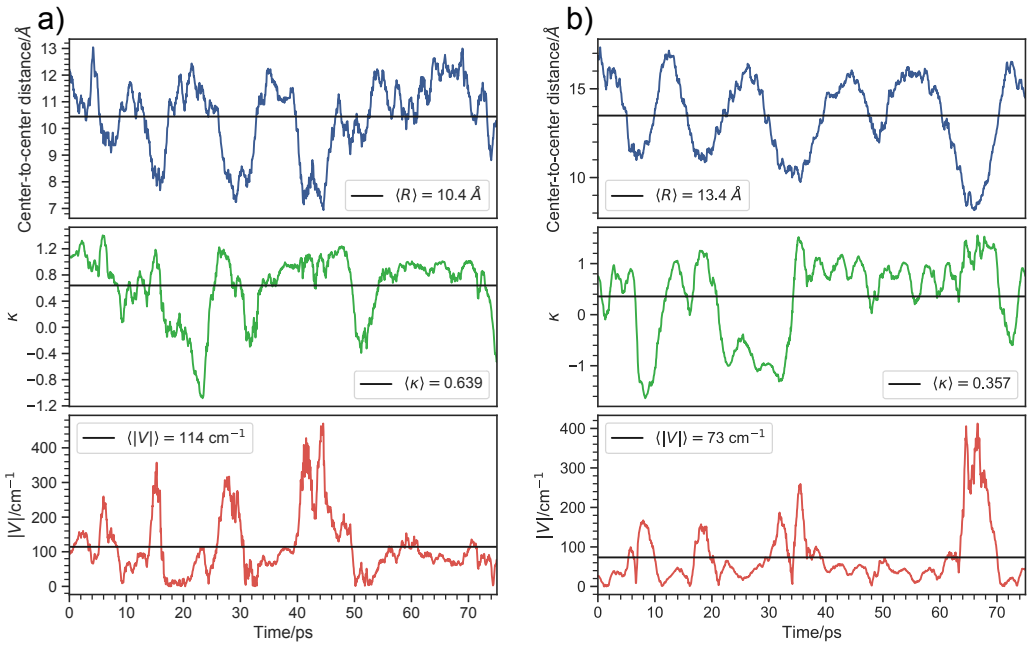

Figure 8.12: Interchromophoric distance R, orientation factor κ and resulting excitonic coupling energy V during the molecular dynamic simulation for $\mathbf{9}^{\mathrm{mDi}}$ (a) and $\mathbf{10}^{\mathrm{mDi}}$ (b)

8.5.3 Molecular Dynamics Simulations

The molecular dynamics simulations of 9^{mDi} and 10^{mDi} have been performed at the semi-empirical PM6 level using the MOPAC2016 software package.[217] A time step of 1.0 fs was used for a simulation time of 75 ps. The trajectories were coupled to heat-bath by employing the Berendsen thermostat at 298.15 K with a time constant of 500 fs.

Chapter 9

Conclusion

This dissertation has presented new approaches and methods for the simulation and investigation of optical properties of organic chromophores and their supramolecular aggregates. The motivation was to comprehensively understand which processes occur after excitation of a molecular system and influence its emission properties. Not only the ultrafast dynamics of electronic and geometric relaxation within femto- or picoseconds were studied but also the radiative and non-radiative processes on the nano- to microsecond time scale.
Based on these processes and time scales, the obtained findings can be grouped into the following three areas:

(A) Ultrafast energy transfer and exciton localization dynamics

- Chromophores in a weak excitonic coupling regime have shown that the internal conversion from higher excited electronic states to the first excited singlet state is accompanied by an energy transfer process. In the case of squaraine triads, simulations could reveal the exciton dynamics over several subunits. Here, it was possible to show that transient localizations and delocalizations of the excitations occur during the dynamics until the exciton localizes to one of the subunits within a few hundred femtoseconds in all systems studied.

- Simulations of the two different BODIPY series, which differ only by an ethyl group, elucidated strong differences in the energy transfer dynamics. Although both series' absorption and emission properties did not show significant differences, a 35 % faster energy transfer from green to red BODIPY units was seen in the β-ethyl bridged series. By combining light-induced dynamics simulations with newly developed analysis methods, it was possible to predict excitation energy and exciton coupling disorder directly. Using the BODIPY series as an example, it was thus shown that the ethyl group significantly reduced these disorders. This reduction leads to lower internal conversion rates and slows down the energy transfer.

- Time-resolved polarization anisotropy spectroscopy (also called fluorescence anisotropy spectroscopy) allows following the change of the transition dipole moment of populated excited states in time. Here, building on light-induced dynamics simulations, a method could be developed to simulate time-resolved polarization anisotropy spectra. Using the example of the BODIPY pyrene dyad

and triad, these spectra could be successfully simulated, allowing the different energy transfer phases to be precisely mapped. Thus, this method forms an essential bridge for the future between experimental polarization anisotropy measurements and theoretical tracing of the energy transfer dynamics.

(B) Excimer formation and its interaction with triplet-correlated singlet states (^{1}TT)

- Since excimer formation plays a vital role as a loss channel in emission, the dynamics of this process was simulated using the tetracene dimer as an example. Here, it was first shown that semi-empirical quantum chemistry methods show good agreement with DFT-MRCI in the calculation of potential energy surfaces of the relevant electronic states. This made it possible to simulate non-adiabatic dynamics for 20 picoseconds in this system for the first time. Here, excimer formation occurred in about 5-6 ps, and half of the dimers studied formed an excimer. In addition, by diabatizing the populated singly- and doubly-excited states, it was possible to classify the character according to locally-excited (LE), charge-transfer (CT), and triplet-correlated singlet (^{1}TT) states. In this way, diabatic time-dependent state populations could be calculated, and the involvement of the (^{1}TT) state in the excimer formation process could be elucidated. During the excimer formation dynamics, a transient occupation of the (^{1}TT) state could thus be observed for about 2-3 ps. However, after about 5 ps the state was wholly depopulated again. Furthermore, it was observed that strong vibrational excitations of the molecules play an essential role in the excimer formation.

(C) Simulations of photoluminescence quantum yields (PLQYs)

- Building on Englman & Jortner's energy gap law and Kramers' Rate Theory, a new model was developed to predict internal conversion rates. With this approach, the polarity and viscosity effects of the solvent, as well as relaxation via conical intersections, can be taken into account. Using this model, it was possible to fully elucidate the relaxation processes of a merocyanine dye in different solvents and to simulate the rates quantitatively. In combination with transient absorption spectroscopy, it was also possible to understand the photoisomerization mechanism, and temperature-dependent PLQY measurements showed that the developed model also correctly predicts the temperature dependence of the relaxation rates.

- Based on the previously developed model, the relaxation processes were investigated in a large series of BODIPY oligomers, with a total of more than 25 different molecular systems. For this purpose, intersystem crossings and reductive photoelectron transfer processes were also taken into account, and it was possible to elucidate the dominant relaxation channel for all eight different se-

ries. However, not only the dominant channels were identified, but also how the rates scale with the number of monomer units. The radiative and intersystem crossing rates increase with the number of monomers. In contrast, the rate for relaxation across a conical intersection is nearly constant. The part of the internal conversion rate that can be described in a harmonic approximation again shows a substantial decrease with increasing number of monomers. This is not obvious, especially for J-aggregates, since an increase in the rate would be expected by lowering the excitation energy. However, oligomerization leads to a decrease in the Huang-Rhys factors, which strongly predominates in this case. This motivated experimental studies in which the PLQY could be increased from 7 % to over 80 % by targeted oligomerization.

Overall, this dissertation introduced and applied new approaches and methods for simulating optical properties in organic systems. The results presented here show that, on the one hand, it is possible to describe the ultrafast relaxation dynamics after excitation using these methods. Here, exciton dynamics and energy transfer between chromophore units as well as excimer formation could be simulated explicitly. On the other hand, it was possible to identify the radiative and non-radiative processes in different fluorophores and to describe their rates quantitatively. Thus, these results provide an important basis for the development of new materials for organic electronics, such as organic light-emitting diodes, photovoltaics or wearable technologies, guided by simulations.

Chapter 10

Zusammenfassung

Im Rahmen dieser Dissertation wurden neue Ansätze und Methoden für die Simulation und Untersuchung von optischen Eigenschaften organischer Chromophore und deren supramolekularer Aggregate entwickelt. Die Motivation lag dabei darin umfassend zu verstehen, welche Prozesse nach der Anregung eines molekularen Systems stattfinden und dessen Emissionseigenschaften beeinflussen. Dabei wurde nicht nur die ultraschnelle Dynamik der elektronischen und geometrischen Relaxation innerhalb von Femto- oder Pikosekunden berücksichtigt sondern auch die radiativen und nicht-radiativen Prozesse auf der Nano- bis Mikrosekunden-Zeitskala.
Die gewonnenen Erkenntnisse lassen sich anhand dieser Prozesse und Zeitskalen in die folgenden drei Bereiche gruppieren:

(A) Ultraschnelle Energietransfer- und Exzitonlokalisierungdynamik

- Bei Chromophoren, die sich in einem schwachen exzitonischen Kopplungsregime befinden, konnte gezeigt werden, dass die interne Konversion von höher angeregten elektronischen Zuständen zum ersten angeregten Singulettzustand durch einen Energietransferprozess begleitet wird. Im Fall der Squarain-Triaden war es möglich, durch Simulationen die Exzitonendynamik über mehrere Untereinheiten aufzudecken. Hierbei gelang es zu zeigen, dass es während der Dynamik zu transienten Lokalisierungen und Delokalisierungen der Anregungen kommt, bis sich das Exziton in allen untersuchten Systemen innerhalb von wenigen hundert Femtosekunden auf einer der Untereinheiten lokalisiert.

- Für die zwei verschiedenen BODIPY-Serien, die sich nur durch eine Ethylgruppe unterscheiden, gelang es die deutlichen Unterschiede in der Energietransferdynamik durch die Simulationen eindeutig aufzuklären. Obwohl die Absorptions- und Emissionseigenschaften beider Serien keine wesentlichen Unterschiede aufwiesen, sah man in der β-ethyl verbrückten Serie einen 35 % schnelleren Energietransfer von grünen zu roten BODIPY-Einheiten. Durch Kombination von lichtinduzierten Dynamiksimulationen mit neu entwickelten Analysemethoden gelang es, die Anregungsenergie- und Exzitonkopplungsunordnung direkt vorherzusagen. Am Beispiel der BODIPY-Serien konnte so gezeigt werden, dass die Ethylgruppe zu einer signifikanten Reduzierung dieser Unordnungen führt. Dies führt zu kleineren internen Konversionraten und verlangsamt auf diese Weise den Energietransfer.

- Die zeitaufgelöste Polarisationsanisotropie-Spektroskopie (auch Fluoreszenzanisotropie-Spektroskopie genannt) ermöglicht es, die Änderung des Übergangsdipolmoments von populierten angeregten Zuständen zeitlich zu verfolgen. Hier konnte aufbauend auf lichtinduzierten Dynamiksimulationen eine Methode entwickelt werden, die die Simulation von zeitaufgelösten Polarisationsanisotropie-Spektren ermöglicht. Am Beispiel der BODIPY-Pyren-Dyade und -Triade konnten diese Spektren erfolgreich simuliert werden und dies ermöglichte es, die verschiedenen Phasen des Energietransfers präzise abzubilden. Damit bildet diese Methode für die Zukunft eine wichtige Brücke zwischen experimentellen Polarisationsanisotropie-Messungen und der theoretischen Nachverfolgung der Energietransferdynamik.

(B) Exzimerbildung und deren Wechselwirkung mit triplett-korrelierten Singulettzuständen (^{1}TT)

- Da die Exzimerbildung eine wichtige Rolle als Verlustkanal bei der Emission spielt, wurde am Beispiel des Tetracen-Dimers die Dynamik dieses Prozesses simuliert. Hierbei konnte zunächst gezeigt werden, dass semi-empirische Quantenchemiemethoden eine gute Übereinstimmung mit DFT-MRCI bei der Berechnung von Potentialenergieflächen der elektronischen Zustände zeigen. Dies ermöglichte es, erstmals nicht-adiabatische Dynamik für 20 Pikosekunden in diesem System zu simulieren. Die Exzimerbildung fand hierbei in etwa 5-6 ps statt und die Hälfte der untersuchten Dimere bildete ein Exzimer. Zusätzlich war es möglich durch Diabatisierung der populierten einfach- und doppelangeregten Zustände den Charakter nach lokal-angeregten (LE), Ladungstransfer- (CT) und triplett-korrelierten Singulettzuständen (^{1}TT) zu klassifizieren. Auf diese Weise konnten diabatische zeitabhängige Zustandspopulationen berechnet und die Beteiligung des (^{1}TT)-Zustands an der Exzimerbildung aufgeklärt werden. Während der Exzimerbildungsdynamik konnte so eine transiente Besetzung des (^{1}TT)-Zustands für etwa 2-3 ps beobachtet werden. Allerdings wurde nach etwa 5 ps der Zustand wieder vollständig depopuliert. Gleichzeitig konnte beobachtet werden, dass starke Schwingungsanregungen der Moleküle eine wesentliche Rolle in der Exzimerbildung spielen.

(C) Simulation von Photolumineszenz-Quanteneffizienzen (PLQEs)

- Aufbauend auf Englmans & Jortners *Energy-Gap-Law* und der Kramers'schen Ratentheorie wurde ein neues Modell entwickelt, um interne Konversionsraten vorherzusagen. Mit diesem Modell können sowohl Polaritäts- und Viskositätseffekte des Lösungsmittels als auch die Relaxation über konische Durchschneidungen berücksichtigt werden. Hiermit war es möglich, die Relaxationsprozesse eines Merocyanin-Farbstoffs in unterschiedlichen Lösungsmitteln vollständig aufzuklären und die Raten quantitativ zu simulieren. In Kombination mit transienter Absorptionsspektroskopie konnte zudem die Photoisomerisierung ver-

standen werden und temperaturabhängige PLQE-Messungen konnten zeigen, dass das entwickelte Modell auch die Temperaturabhängigkeit der Relaxationsraten richtig vorhersagt.

- Auf Basis des zuvor entwickelten Modells wurden in einer großen Serie von BODIPY-Oligomeren, mit insgesamt mehr als 25 verschiedenen molekularen Systemen, die Relaxationsprozesse untersucht. Dafür wurden hierbei auch die Intersystem-Crossing-Übergänge und der reduktive Photoelektronentransfer berücksichtigt und es gelang für alle acht verschiedenen Grundeinheiten den dominanten Relaxationskanal aufzuklären. Jedoch wurden nicht nur die dominanten Kanäle identifiziert, sondern auch die Skalierungsrelation der Raten in Abhägnigkeit der Zahl der Monomereinheiten. Dabei wächst die radiative und die intersystem Crossing Rate mit der Zahl der Monomere an. Die Rate für die Relaxation über eine konische Durchschneidung hingegen ist nahezu konstant. Der Teil der internen Konversionrate, der sich in harmonischer Näherung beschreiben lässt, zeigt wiederum einen starken Abfall mit zunehmender Anzahl an Monomeren. Dies ist insbesondere bei J-Aggregaten nicht offensichtlich, da eine Erhöhung der Rate durch die Absenkung der Anregungsenergie erwartbar wäre. Jedoch führt die Oligomerisierung zu einer Abnahme der Huang-Rhys Faktoren, die hierbei stark überwiegt. Diese Ergebnisse haben experimentelle Untersuchungen angestoßen, in denen durch gezielte Oligomerisierung die PLQE von 7 % auf über 80 % erhöht werden konnte.

Insgesamt wurden in dieser Dissertation neue Ansätze und Methoden für die Simulation von optischen Eigenschaften in organischen Systemen eingeführt und angewandt. Die hier vorgestellten Ergebnisse zeigen, dass es mit diesen Methoden zum einen möglich ist die ultraschnelle Relaxationsdynamik nach der Anregung zu beschreiben. Hierbei konnte sowohl die Exzitonendynamik und der Energietransfer zwischen Chromophoreinheiten als auch die Exzimerbildung explizit simuliert werden. Zum anderen gelang es die radiativen und nicht-radiativen Prozesse in verschiedenen Fluorophoren zu identifizieren und deren Raten quantitativ zu beschreiben. Damit stellen diese Ergebnisse eine wichtige Grundlage für die Entwicklung neuer Materialien für die organische Elektronik, wie zum Beispiel organische Leuchtdioden, Photovoltaik oder tragbare Technologien, dar.

Acknowledgements

- Prof. Dr. Roland Mitric, my supervisor and mentor, for giving me the opportunity for PhD studies in his group. I am grateful for his competent supervision, his constant support and approachable character. I am especially thankful for the freedom and support he has given me in designing research projects. Additionally, he provided me with the possibilities to attend international conferences and lead collaborations with external partners.

- Dr. Merle Insa Silja Röhr, Dr. Jens Petersen, Dr. Alexander Humeniuk, Dr. Evgenii Titov, Dr. Joachim Lindner, Dr. Matthias Wohlgemuth, Dr. Polina Lisinetskaya, Michael Wenzel, Kevin Issler, Richard Einsele, Xincheng Miao, Luca Nils Philipp, Michi Bühler, Lasse Kreimendahl, Nikita Kavka, David Fischermeier and Anurag Singh for the many scientific discussion, the friendly atmosphere and their support.

- Dr. Jens Petersen, Dr. Alexander Humeniuk, Richard Einsele, Xincheng Miao and Luca Nils Philipp for attentive proof-reading.

- Dr. Charlotte Walter, Dr. Philipp Stößel, Dr. Martin Engel, Dr. Alexander Schubert, Dr. Falk May and Jens Pfalzgraf for the fruitful collaboration, stimulating discussions and especially Charlotte and Philipp for their strong support.

- Prof. Dr. Ingo Fischer, Dr. Hans-Christian Schmitt and Dr. Marco Flock for the nice collaborations and atmosphere on the pyrene and tetracene project.

- Prof. Dr. Frank Würthner, Prof. Dr. Tobias Brixner, Dr. Matthias Stolte, Alexander Schulz, and Lysanne Dietrich for the great collaboration on the merocyanine project.

- Prof. Dr. Christoph Lambert for the many sucessfull scientific collaborations and discussions.

- Prof. Dr. Vlasta Bonacic-Koutecky, Dr. Fabrizio Santoro and Prof. Dr. Javier Cerezo for the collaboration on the internal conversion rate project and Vlasta especially for inviting me various times to her institute in Split.

- Dr. Lukas Patalag and Prof. Dr. Daniel Werz for great collaborations and Lukas especially for the many scientific discussions.

- My family and my friends for their invaluable support through all these years.

Bibliography

[1] R. Einsele, J. Hoche, and R. Mitric.
Long-range corrected fragment molecular orbital density-functional tight- binding method for excited states in large molecular systems.
J. Chem. Phys. **158**, 044121 (2023).

[2] J. Hoche, M. I. S. Röhr, C. Lambert, and R. Mitric.
Polarisation-anisotropy and nonadiabatic dynamics simulations in pyrene-bodipy conjugates.
in preparation (2023).

[3] E. Titov, T. Kopp, J. Hoche, A. Humeniuk, and R. Mitrić.
(de)localization dynamics of molecular excitons: comparison of mixed quantum-classical and fully quantum treatments.
Phys. Chem. Chem. Phys. **24**, 12136–12148 (2022).

[4] L. J. Patalag, J. Hoche, R. Mitric, D. B. Werz, and B. L. Feringa.
Transforming dyes into fluorophores: Exciton-induced emission with chain-like oligo-bodipy superstructures.
Angew. Chem. Int. Ed. (2022).

[5] J. Hoche, M. Flock, X. Miao, L. N. Philipp, M. Wenzel, I. Fischer, and R. Mitric.
Excimer formation dynamics in the isolated tetracene dimer.
Chem. Sci. **12**, 11965–11975 (2021).

[6] L. J. Patalag, J. Hoche, M. Holzapfel, A. Schmiedel, R. Mitric, C. Lambert, and D. B. Werz.
Ultrafast resonance energy transfer in ethylene-bridged bodipy heterooligomers: From frenkel to förster coupling limit.
J. Am. Chem. Soc. **143**, 7414–7425 (2021). PMID: 33956430.

[7] C. Lambert, J. Hoche, M. H. Schreck, M. Holzapfel, A. Schmiedel, J. Selby, A. Turkin, and R. Mitric.
Ultrafast energy transfer dynamics in a squaraine heterotriad.
J. Phys. Chem. A **125**, 2504–2511 (2021).

[8] H.-C. Schmitt, I. Fischer, L. Ji, J. Merz, T. B. Marder, J. Hoche, M. I. S. Röhr, and R. Mitric.
Isolated 2-hydroxypyrene and its dimer: a frequency- and time-resolved spectroscopic study.
New. J. Chem. **45**, 14949–14956 (2020).

[9] A. Humeniuk, M. Bužančić, J. Hoche, J. Cerezo, R. Mitrić, F. Santoro, and V. Bonačić-Koutecký.
Predicting fluorescence quantum yields for molecules in solution: A critical assessment of the harmonic approximation and the choice of the lineshape function.
J. Chem. Phys. **152**, 054107 (2020).

[10] J. Hoche, A. Schulz, L. M. Dietrich, A. Humeniuk, M. Stolte, D. Schmidt, T. Brixner, F. Würthner, and R. Mitric.
The origin of the solvent dependence of fluorescence quantum yields in dipolar merocyanine dyes.
Chem. Sci. **10**, 11013–11022 (2019).

[11] N. Auerhammer, A. Schulz, A. Schmiedel, M. Holzapfel, J. Hoche, M. Röhr, R. Mitrić, and C. Lambert.
Dynamic exciton localisation in a pyrene-bodipy-pyrene dye conjugate.
Phys. Chem. Chem. Phys. **21**, 9013–9025 (2019).

[12] M. Röhr, H. Marciniak, J. Hoche, M. H. Schreck, H. Ceymann, R. Mitrić, and C. Lambert.
Exciton dynamics from strong to weak coupling limit illustrated on a series of squaraine dimers.
J. Phys. Chem. C **122**, 8082–8093 (2018).

[13] J. Hoche, H.-C. Schmitt, A. Humeniuk, I. Fischer, R. Mitrić, and M. Röhr.
The mechanism of excimer formation: an experimental and theoretical study on the pyrene dimer.
Phys. Chem. Chem. Phys. **19**, 25002–25015 (2017).

[14] B. Geffroy, P. le Roy, and C. Prat.
Organic light-emitting diode (oled) technology: materials, devices and display technologies.
Polym. Intern. **55**, 572–582 (2006).

[15] Y.-S. Tyan.
Organic light-emitting-diode lighting overview.
J. Phot. Energy **1**, 011009 (2011).

[16] M. C. Gather, A. Köhnen, and K. Meerholz.
White organic light-emitting diodes.
Adv. Mat. **23**, 233–248 (2011).

[17] A. Hagfeldt and M. Grätzel.
Molecular photovoltaics.
Acc. Chem. Res. **33**, 269–277 (2000).

[18] B. Kippelen and J.-L. Brédas.
Organic photovoltaics.
Energy Environ. Sci. **2**, 251–261 (2009).

[19] M. Fahlman, S. Fabiano, V. Gueskine, D. Simon, M. Berggren, and X. Crispin.
Interfaces in organic electronics.
Nat. Rev. Mat. **4**, 627–650 (2019).

[20] F. Fassioli, R. Dinshaw, P. C. Arpin, and G. D. Scholes.
Photosynthetic light harvesting: excitons and coherence.
J. R. Soc. Interface **11**, 20130901 (2014).

[21] G. D. Scholes and G. Rumbles.
Excitons in nanoscale systems.
Nat. Mater. **5**, 683–696 (2006).

[22] G. D. Scholes and G. R. Fleming.
On the mechanism of light harvesting in photosynthetic purple bacteria: B800 to b850 energy transfer.
J. Phys. Chem. B **104**, 1854–1868 (2000).

[23] H. van Amerongen, R. van Grondelle, and L. Valkunas. *Photosynthetic excitons.* in *Photosynthetic excitations; world scientific pub co: Singapore*, p. 122. World Scientific, (2000).

[24] F. Würthner, T. E. Kaiser, and C. R. Saha-Möller.
J-aggregates: From serendipitous discovery to supramolecular engineering of functional dye materials.
Angew. Chem. Int. Ed **50**, 3376–3410 (2011).

[25] F. Würthner.
Aggregation-induced emission (AIE): A historical perspective.
Angew. Chem. Int. Ed **59**, 14192–14196 (2020).

[26] N. J. Hestand and F. C. Spano.
Expanded theory of h- and j-molecular aggregates: The effects of vibronic coupling and intermolecular charge transfer.
Chem. Rev. **118**, 7069–7163 (2018).

[27] N. J. Hestand and F. C. Spano.
Molecular aggregate photophysics beyond the kasha model: Novel design principles for organic materials.
Acc. Chem. Res. **50**, 341–350 (2017). PMID: 28145688.

[28] M. J. Kamlet, J. L. M. Abboud, M. H. Abraham, and R. W. Taft.

Linear solvation energy relationships. 23. a comprehensive collection of the solvatochromic parameters, .pi., .alpha., and .beta., and some methods for simplifying the generalized solvatochromic equation.*
J. Org. Chem. **48**, 2877–2887 (1983).

[29] B. Sanchez-Lengeling and A. Aspuru-Guzik.
Inverse molecular design using machine learning: Generative models for matter engineering.
Science **361**, 360–365 (2018).

[30] B. P. MacLeod, F. G. L. Parlane, T. D. Morrissey, F. Häse, L. M. Roch, K. E. Dettelbach, R. Moreira, L. P. E. Yunker, M. B. Rooney, J. R. Deeth, V. Lai, G. J. Ng, H. Situ, R. H. Zhang, M. S. Elliott, T. H. Haley, D. J. Dvorak, A. Aspuru-Guzik, J. E. Hein, and C. P. Berlinguette.
Self-driving laboratory for accelerated discovery of thin-film materials.
Science Adv. **6**, eaaz8867 (2020).

[31] E. O. Pyzer-Knapp, C. Suh, R. Gómez-Bombarelli, J. Aguilera-Iparraguirre, and A. Aspuru-Guzik.
What is high-throughput virtual screening? a perspective from organic materials discovery.
Annu. Rev. Mater. Res. (2015).

[32] A. Aspuru-Guzik and K. Persson.
Materials acceleration platform: Accelerating advanced energy materials discovery by integrating high-throughput methods and artificial intelligence.
Mission Innovation (2018).

[33] C. Bernini, L. Zani, M. Calamante, G. Reginato, A. Mordini, M. Taddei, R. Basosi, and A. Sinicropi.
Excited state geometries and vertical emission energies of solvated dyes for dssc: A pcm/td-dft benchmark study.
Journal of Chemical Theory and Computation **10**, 3925–3933 (2014). PMID: 26588536.

[34] T. Förster.
Energiewanderung und fluoreszenz.
Die Naturwissenschaften **33**, 166–175 (1946).

[35] F. Laquai, Y.-S. Park, J.-J. Kim, and T. Basché.
Excitation energy transfer in organic materials: From fundamentals to optoelectronic devices.
Macromol. Rapid. Comm. **30**, 1203–1231 (2009).

[36] G. D. Scholes.
Long-range resonance energy transfer in molecular systems.
Annu. Rev. Phys. Chem. **54**, 57–87 (2003).

[37] B. P. Krueger, G. D. Scholes, and G. R. Fleming.
Calculation of couplings and energy-transfer pathways between the pigments of LH2 by the ab initio transition density cube method.
J. Phys. Chem. B **102**, 5378–5386 (1998).

[38] G. D. Scholes, C. Curutchet, B. Mennucci, R. Cammi, and J. Tomasi.
How solvent controls electronic energy transfer and light harvesting.
J. Phys. Chem. B **111**, 6978–6982 (2007).

[39] C. Kaufmann, W. Kim, A. Nowak-Król, Y. Hong, D. Kim, and F. Würthner.
Ultrafast exciton delocalization, localization, and excimer formation dynamics in a highly defined perylene bisimide quadruple π-stack.
J. Am. Chem. Soc. **140**, 4253–4258 (2018). PMID: 29502406.

[40] X. Feng and A. I. Krylov.
On couplings and excimers: lessons from studies of singlet fission in covalently linked tetracene dimers.
Phys. Chem. Chem. Phys. **18**, 7751–7761 (2016).

[41] J. Birks and L. Christophorou.
Excimer fluorescence of aromatic hydrocarbons in solution.
Nature **194**, 442–444 (1962).

[42] R. Singh, M. Kim, J.-J. Lee, T. Ye, P. E. Keivanidis, and K. Cho.
Excimer formation effects and trap-assisted charge recombination loss channels in organic solar cells of perylene diimide dimer acceptors.
J. Mater. Chem. C **8**, 1686–1696 (2020).

[43] S. Samanta, S. K. Ray, S. Deolka, S. Saha, P. K. R., R. Bhowal, N. Ghosh, and D. Chaudhuri.
Safeguarding long-lived excitons from excimer traps in h-aggregated dye-assemblies.
Chem. Sci. **11**, 5710–5715 (2020).

[44] C. Ye, V. Gray, J. Mårtensson, and K. Börjesson.
Annihilation versus excimer formation by the triplet pair in triplet–triplet annihilation photon upconversion.
Journal of the American Chemical Society **141**, 9578–9584 (2019).

[45] Y. Appiarius, P. J. Gliese, S. A. W. Segler, P. Rusch, J. Zhang, P. J. Gates, R. Pal, L. A. Malaspina, K. Sugimoto, T. Neudecker, N. C. Bigall, S. Grabowsky, A. A. Bakulin, and A. Staubitz.
Bn-substitution in dithienylpyrenes prevents excimer formation in solution and in the solid state.
The Journal of Physical Chemistry C **126**, 4563–4576 (2022).

[46] M. B. Smith and J. Michl.
Singlet fission.
Chemical Reviews **110**, 6891–6936 (2010).

[47] S. J. Strickler and R. A. Berg.
Relationship between absorption intensity and fluorescence lifetime of molecules.
J. Chem. Phys. **37**, 814–822 (1962).

[48] J. Gierschner and S. Y. Park.
Luminescent distyrylbenzenes: tailoring molecular structure and crystalline morphology.
J. Mater. Chem. C. **1**, 5818–5832 (2013).

[49] A. Weigel, M. Pfaffe, M. Sajadi, R. Mahrwald, R. Improta, V. Barone, D. Polli, G. Cerullo, N. P. Ernsting, and F. Santoro.
Barrierless photoisomerisation of the "simplest cyanine": Joining computational and femtosecond optical spectroscopies to trace the full reaction path.
Phys. Chem. Chem. Phys. **14**, 13350 (2012).

[50] P. A. Hunt and M. A. Robb.
Systematic Control of Photochemistry: The Dynamics of Photoisomerization of a Model Cyanine Dye.
J. Am. Chem. Soc. **127**, 5720–5726 (2005).

[51] B. G. Levine and T. J. Martínez.
Isomerization Through Conical Intersections.
Ann. Rev. Phys. Chem. **58**, 613–634 (2007).

[52] X. Zhang, D. Jacquemin, Q. Peng, Z. Shuai, and D. Escudero.
General Approach To Compute Phosphorescent OLED Efficiency.
J. Phys. Chem. C **122**, 6340–6347 (2018).

[53] U. Werner, R. Mitric, T. Suzuki, and V. Bonacic-Koutecky.
Nonadiabatic dynamics within the time dependent density functional theory: Ultrafast photodynamics in pyrazine.
Chem. Phys. **349**, 319–324 (2008).

[54] R. Mitric, U. Werner, M. Wohlgemuth, G. Seifert, and V. Bonacic-Koutecky.
Nonadiabatic dynamics within time-dependent density functional tight binding method.
J. Phys. Chem. A **113**, 12700–12705 (2009).

[55] J. C. Tully.
Molecular dynamics with electronic transitions.
J. Chem. Phys. **93**, 1061–1071 (1990).

[56] R. Mitric, J. Petersen, and V. Bonacic-Koutecky.
Laser-field induced surface-hopping method for the simulation and control of ultrafast photodynamics.
Phys. Rev. A **79**, 053416 (2009).

[57] R. Englman and J. Jortner.
The energy gap law for radiationless transitions in large molecules.
Mol. Phys. **18**, 145–164 (1970).

[58] T. S. Blacker, R. J. Marsh, M. R. Duchen, and A. J. Bain.
Activated barrier crossing dynamics in the non-radiative decay of NADH and NADPH.
Chem. Phys. **422**, 184–194 (2013).

[59] M. Born and R. Oppenheimer.
Zur quantentheorie der molekeln.
Annalen der Physik **389**, 457–484 (1927).

[60] L. Verlet.
Computer "experiments" on classical fluids. i. thermodynamical properties of lennard-jones molecules.
Phys. Rev. **159**, 98–103 (1967).

[61] W. C. Swope, H. C. Andersen, P. H. Berens, and K. R. Wilson.
A computer simulation method for the calculation of equilibrium constants for the formation of physical clusters of molecules: Application to small water clusters.
The Journal of Chemical Physics **76**, 637–649 (1982).

[62] X. Li, J. C. Tully, H. B. Schlegel, and M. J. Frisch.
Ab initio ehrenfest dynamics.
The Journal of Chemical Physics **123**, 084106 (2005).

[63] P. G. Lisinetskaya and R. Mitrić.
Simulation of laser-induced coupled electron-nuclear dynamics and time-resolved harmonic spectra in complex systems.
Phys. Rev. A **83**, 033408 (2011).

[64] C. Lambert, T. Scherpf, H. Ceymann, A. Schmiedel, and M. Holzapfel.
Coupled oscillators for tuning fluorescence properties of squaraine dyes.
J. Am. Chem. Soc. **137**, 3547–3557 (2015).

[65] T. Brixner, R. Hildner, J. Köhler, C. Lambert, and F. Würthner.
Exciton transport in molecular aggregates - from natural antennas to synthetic chromophore systems.
Adv. Energ. Mater. **7**, 1700236 (2017).

[66] E. Jelley.
Spectral absorption and fluorescence of dyes in the molecular state.
Nature **138**, 1009–1010 (1936).

[67] G. Scheibe.
Über die veränderlichkeit der absorptionsspektren in lösungen und die nebenvalenzen als ihre ursache.
Angew. Chem. **50**, 212–219 (1937).

[68] M. E. Madjet, A. Abdurahman, and T. Renger.
Intermolecular coulomb couplings from ab initio electrostatic potentials: application to optical transitions of strongly coupled pigments in photosynthetic antennae and reaction centers.
J. Phys. Chem. B **110**, 17268–17281 (2006).

[69] D. J. Griffiths,
Introduction to electrodynamics.
Pearson. (2013).

[70] M. Kasha.
Energy transfer mechanisms and the molecular exciton model for molecular aggregates.
Radiat. Res. **20**, 55–70 (1963).

[71] J.-D. Chai and M. Head-Gordon.
Long-range corrected hybrid density functionals with damped atom–atom dispersion corrections.
Phys. Chem. Chem. Phys. **10**, 6615–6620 (2008).

[72] F. Weigend, M. Häser, H. Patzelt, and R. Ahlrichs.
Optimized auxiliary basis sets and demonstration of efficiency.
Chem. Phys. Lett. **294**, 143 (1988).

[73] A. Corney,
Atomic and Laser Spectroscopy. Oxford Classic Texts in the Physical Sciences. Clarendon Press, Oxford. (2006).

[74] F. Santoro, R. Improta, A. Lami, J. Bloino, and V. Barone.
Effective method to compute Franck-Condon integrals for optical spectra of large molecules in solution.
J. Chem. Phys. **126**, 084509 (2007).

[75] S. H. Lin.
Spectral band shape of absorption and emission of molecules in dense media.
Theor. Chem. Act. **10**, 301–310 (1968).

[76] Q. Peng, Y. Yi, Z. Shuai, and J. Shao.
Toward Quantitative Prediction of Molecular Fluorescence Quantum Efficiency: Role of Duschinsky Rotation.
J. Am. Chem. Soc. **129**, 9333–9339 (2007).

[77] S. Banerjee, A. Baiardi, J. Bloino, and V. Barone.
Temperature Dependence of Radiative and Nonradiative Rates from Time-Dependent Correlation Function Methods.
J. Chem. Theor. Comput. **12**, 774–786 (2016).

[78] G. Schatz and M. Ratner,
Quantum Mechanics in Chemistry.
Dover. (1993).

[79] R. Englman and J. Jortner.
The energy gap law for radiationless transitions in large molecules.
Mol. Phys. **18**, 145–164 (1970).

[80] K. Huang and A. Rhys.
Theory of light absorption and non-radiative transitions in f-centres.
Proc. Roy. Soc. Lond **A204**, 406–423 (1950).

[81] R. O'Rourke.
Absorption of light by trapped electrons.
Phys. Rev. **91**, 265 (1953).

[82] C. Cohen-Tannoudji, B. Diu, and F. Laloë,
Quantenmechanik. volume 2 of *Quantum Mechanics.*
Wiley-VCH. (1991).

[83] T. Förster.
Zwischenmolekulare energiewanderung und fluoreszenz.
Ann. Phys. (Berl.) **437**, 55–75 (1948).

[84] M. Şener, J. Strümpfer, J. Hsin, D. Chandler, S. Scheuring, C. N. Hunter, and K. Schulten.
Förster energy transfer theory as reflected in the structures of photosynthetic light-harvesting systems.
ChemPhysChem **12**, 518–531 (2011).

[85] G. D. Scholes, G. R. Fleming, A. Olaya-Castro, and R. van Grondelle.
Lessons from nature about solar light harvesting.
Nat. Chem. **3**, 763–774 (2011).

[86] H. Lee, Y.-C. Cheng, and G. R. Fleming.
Coherence dynamics in photosynthesis: Protein protection of excitonic coherence.

Science **316**, 1462–1465 (2007).

[87] M. Kasha, H. R. Rawls, and M. A. El-Bayoumi.
The exciton model in molecular spectroscopy.
Pure Appl. Chem. **11**, 371–392 (1965).

[88] F. C. Spano.
The spectral signatures of frenkel polarons in h- and j-aggregates.
Acc. Chem. Res. **43**, 429–439 (2009).

[89] V. A. Montes, G. V. Zyryanov, E. Danilov, N. Agarwal, M. A. Palacios, and P. Anzenbacher.
Ultrafast energy transfer in oligofluorene-aluminum bis(8-hydroxyquinoline)acetylacetone coordination polymers.
J. Am. Chem. Soc. **131**, 1787–1795 (2009).

[90] O. Ostroverkhova.
Organic optoelectronic materials: Mechanisms and applications.
Chem. Rev. **116**, 13279–13412 (2016).

[91] M. H. Schreck, L. Breitschwerdt, H. Marciniak, M. Holzapfel, D. Schmidt, F. Würthner, and C. Lambert.
fs–ps exciton dynamics in a stretched tetraphenylsquaraine polymer.
Phys. Chem. Chem. Phys. **21**, 15346–15355 (2019).

[92] J. C. Nelson, J. G. Saven, J. S. Moore, and P. G. Wolynes.
Solvophobically driven folding of nonbiological oligomers.
Science **277**, 1793–1796 (1997).

[93] B. A. Ikkanda and B. L. Iverson.
Exploiting the interactions of aromatic units for folding and assembly in aqueous environments.
Chem. Commun. **52**, 7752–7759 (2016).

[94] X. Hu, J. O. Lindner, and F. Würthner.
Stepwise folding and self-assembly of a merocyanine folda-pentamer.
J. Am. Chem. Soc. **142**, 3321–3325 (2020).

[95] E. Collini and G. D. Scholes.
Coherent intrachain energy migration in a conjugated polymer at room temperature.
Science **323**, 369–373 (2009).

[96] C. Lambert, F. Koch, S. F. Völker, A. Schmiedel, M. Holzapfel, A. Humeniuk, M. I. S. Röhr, R. Mitric, and T. Brixner.
Energy transfer between squaraine polymer sections: From helix to zigzag and all the way back.

J. Am. Chem. Soc. **137**, 7851–7861 (2015).

[97] L. Lüer, J. Crochet, T. Hertel, G. Cerullo, and G. Lanzani.
Ultrafast excitation energy transfer in small semiconducting carbon nanotube aggregates.
ACS Nano **4**, 4265–4273 (2010).

[98] D. Badgurjar, K. Sudhakar, K. Jain, V. Kalantri, Y. Venkatesh, N. Duvva, S. Prasanthkumar, A. K. Sharma, P. R. Bangal, R. Chitta, and L. Giribabu.
Ultrafast intramolecular photoinduced energy transfer events in benzothiazole–borondipyrromethene donor–acceptor dyads.
J. Phys. Chem. C **120**, 16305–16321 (2016).

[99] R. Ziessel, P. Stachelek, A. Harriman, G. J. Hedley, T. Roland, A. Ruseckas, and I. D. W. Samuel.
Ultrafast through-space electronic energy transfer in molecular dyads built around dynamic spacer units.
J. Phys. Chem. A **122**, 4437–4447 (2018).

[100] J. E. A. Webb, K. Chen, S. K. K. Prasad, J. P. Wojciechowski, A. Falber, P. Thordarson, and J. M. Hodgkiss.
Quantifying highly efficient incoherent energy transfer in perylene-based multichromophore arrays.
Phys. Chem. Chem. Phys. **18**, 1712–1719 (2016).

[101] K. Kilså, J. Kajanus, J. Mårtensson, and B. Albinsson.
Mediated electronic coupling: Singlet energy transfer in porphyrin dimers enhanced by the bridging chromophore.
J. Phys. Chem. B **103**, 7329–7339 (1999).

[102] T. G. Kim, J. C. Castro, A. Loudet, J. G.-S. Jiao, R. M. Hochstrasser, K. Burgess, and M. R. Topp.
Correlations of structure and rates of energy transfer for through-bond energy-transfer cassettes.
J. Phys. Chem. A **110**, 20–27 (2005).

[103] S. Athanasopoulos, L. A. Hernandez, D. Beljonne, S. Fernandez-Alberti, and S. Tretiak.
Ultrafast non-förster intramolecular donor–acceptor excitation energy transfer.
J. Phys. Chem. Lett. **8**, 1688–1694 (2017).

[104] G. Hinze, R. Métivier, F. Nolde, K. Müllen, and T. Basché.
Intramolecular electronic excitation energy transfer in donor/acceptor dyads studied by time and frequency resolved single molecule spectroscopy.
J. Chem. Phys. **128**, 124516 (2008).

[105] J. Oh, J. Sung, M. Kitano, Y. Inokuma, A. Osuka, and D. Kim.
Unique ultrafast energy transfer in a series of phenylene-bridged subporphyrin–porphyrin hybrids.
Chem. Commun. **50**, 10424–10426 (2014).

[106] H. Marciniak, N. Auerhammer, S. Ricker, A. Schmiedel, M. Holzapfel, and C. Lambert.
Reduction of the fluorescence transition dipole moment by excitation localization in a vibronically coupled squaraine dimer.
J. Phys. Chem. C **123**, 3426–3432 (2019).

[107] H. Dekkiche, A. Buisson, A. Langlois, P.-L. Karsenti, L. Ruhlmann, R. Ruppert, and P. Harvey.
Metal linkage effects on ultrafast energy transfer.
Chem. - Eur. J. **22**, 10484–10493 (2016).

[108] G. J. Hedley, A. Ruseckas, A. C. Benniston, A. Harriman, and I. D. W. Samuel.
Ultrafast electronic energy transfer beyond the weak coupling limit in a proximal but orthogonal molecular dyad.
J. Phys. Chem. A **119**, 12665–12671 (2015).

[109] H. Langhals, A. J. Esterbauer, A. Walter, E. Riedle, and I. Pugliesi.
Förster resonant energy transfer in orthogonally arranged chromophores.
J. Am. Chem. Soc. **132**, 16777–16782 (2010).

[110] C. Wiebeler, F. Plasser, G. J. Hedley, A. Ruseckas, I. D. W. Samuel, and S. Schumacher.
Ultrafast electronic energy transfer in an orthogonal molecular dyad.
J. Phys. Chem. Lett. **8**, 1086–1092 (2017).

[111] E. Hennebicq, D. Beljonne, C. Curutchet, G. D. Scholes, and R. J. Silbey.
Shared-mode assisted resonant energy transfer in the weak coupling regime.
J. Chem. Phys. **130**, 214505 (2009).

[112] A. Harriman, L. J. Mallon, K. J. Elliot, A. Haefele, G. Ulrich, and R. Ziessel.
Length dependence for intramolecular energy transfer in three- and four-color donor-spacer-acceptor arrays.
J. Am. Chem. Soc. **131**, 13375–13386 (2009).

[113] G. S. Engel, T. R. Calhoun, E. L. Read, T.-K. Ahn, T. Mančal, Y.-C. Cheng, R. E. Blankenship, and G. R. Fleming.
Evidence for wavelike energy transfer through quantum coherence in photosynthetic systems.
Nature **446**, 782–786 (2007).

[114] D. Hayes, G. B. Griffin, and G. S. Engel.

Engineering coherence among excited states in synthetic heterodimer systems.
Science **340**, 1431–1434 (2013).

[115] A. Ishizaki and G. R. Fleming.
Unified treatment of quantum coherent and incoherent hopping dynamics in electronic energy transfer: Reduced hierarchy equation approach.
J. Chem. Phys. **130**, 234111 (2009).

[116] S. Jang, Y.-C. Cheng, D. R. Reichman, and J. D. Eaves.
Theory of coherent resonance energy transfer.
J. Chem. Phys. **129**, 101104 (2008).

[117] A. Loudet and K. Burgess.
BODIPY dyes and their derivatives: Syntheses and spectroscopic properties.
Chem. Rev. **107**, 4891–4932 (2007).

[118] G. Ulrich, R. Ziessel, and A. Harriman.
The chemistry of fluorescent bodipy dyes: Versatility unsurpassed.
Angew. Chem. - Int. Ed. **47**, 1184–1201 (2008).

[119] T. Kowada, H. Maeda, and K. Kikuchi.
BODIPY-based probes for the fluorescence imaging of biomolecules in living cells.
Chem. Soc. Rev. **44**, 4953–4972 (2015).

[120] H. Lu, J. Mack, Y. Yang, and Z. Shen.
Structural modification strategies for the rational design of red/NIR region BODIPYs.
Chem. Soc. Rev. **43**, 4778–4823 (2014).

[121] P. Shrestha, K. C. Dissanayake, E. J. Gehrmann, C. S. Wijesooriya, A. Mukhopadhyay, E. A. Smith, and A. H. Winter.
Efficient far-red/near-IR absorbing BODIPY photocages by blocking unproductive conical intersections.
J. Am. Chem. Soc. **142**, 15505–15512 (2020).

[122] N. Boens, B. Verbelen, and W. Dehaen.
Postfunctionalization of the BODIPY core: Synthesis and spectroscopy.
Eur. J. Org. Chem. **2015**, 6577–6595 (2015).

[123] L. J. Patalag, J. A. Ulrichs, P. G. Jones, and D. B. Werz.
Decorated BODIPY fluorophores and thiol-reactive fluorescence probes by an aldol addition.
Org. Lett. **19**, 2090–2093 (2017).

[124] D. Wang, C. Cheng, Q. Wu, J. Wang, Z. Kang, X. Guo, H. Wu, E. Hao, and L. Jiao.

Visible-light excitation of BODIPYs enables self-promoted radical arylation at their 3,5-positions with diazonium salts.
Org. Lett. **21**, 5121–5125 (2019).

[125] S. Jeon, T.-I. Kim, H. Jin, U. Lee, J. Bae, J. Bouffard, and Y. Kim.
Amine-reactive activated esters of meso-carboxybodipy: Fluorogenic assays and labeling of amines, amino acids, and proteins.
J. Am. Chem. Soc. **142**, 9231–9239 (2020).

[126] J. Ahrens, B. Cordes, R. Wicht, B. Wolfram, and M. Bröring.
Acidic condensation of bodipys with aldehydes: A quick and versatile route to alkenyl-bodipys and c(sp(3))-connected dyemers.
Chem. - Eur. J. **22**, 10320–10325 (2016).

[127] Q. Wu, G. Jia, B. Tang, X. Guo, H. Wu, C. Yu, E. Hao, and L. Jiao.
Conformationally restricted α, α directly linked BisBODIPYs as highly fluorescent near-infrared absorbing dyes.
Org. Lett. **22**, 9239–9243 (2020).

[128] A. B. Nepomnyashchii, M. Bröring, J. Ahrens, and A. J. Bard.
Synthesis, photophysical, electrochemical, and electrogenerated chemiluminescence studies. multiple sequential electron transfers in BODIPY monomers, dimers, trimers, and polymer.
J. Am. Chem. Soc. **133**, 8633–8645 (2011).

[129] A. B. Nepomnyashchii, M. Bröring, J. Ahrens, and A. J. Bard.
Chemical and electrochemical dimerization of BODIPY compounds: Electrogenerated chemiluminescent detection of dimer formation.
J. Am. Chem. Soc. **133**, 19498–19504 (2011).

[130] Y. Cakmak and E. U. Akkaya.
Phenylethynyl-BODIPY oligomers: Bright dyes and fluorescent building blocks.
Org. Lett. **11**, 85–88 (2008).

[131] W. Zhang, W. Sheng, C. Yu, Y. Wei, H. Wang, E. Hao, and L. Jiao.
One-pot synthesis and properties of well-defined butadiynylene-BODIPY oligomers.
Chem. Commun. **53**, 5318–5321 (2017).

[132] L. J. Patalag, L. P. Ho, P. G. Jones, and D. B. Werz.
Ethylene-bridged oligo-BODIPYs: Access to intramolecular j-aggregates and superfluorophores.
J. Am. Chem. Soc. **139**, 15104–15113 (2017).

[133] L. Goerigk, A. Hansen, C. Bauer, S. Ehrlich, A. Najibi, and S. Grimme.

A look at the density functional theory zoo with the advanced GMTKN55 database for general main group thermochemistry, kinetics and noncovalent interactions.
Phys. Chem. Chem. Phys. **19**, 32184–32215 (2017).

[134] E. Knapp.
Lineshapes of molecular aggregates, exchange narrowing and intersite correlation.
Chem. Phys. **85**, 73–82 (1984).

[135] P. B. Walczak, A. Eisfeld, and J. S. Briggs.
Exchange narrowing of the j band of molecular dye aggregates.
J. Chem. Phys. **128**, 044505 (2008).

[136] J. J. Snellenburg, S. P. Laptenok, R. Seger, K. M. Mullen, and I. H. M. van Stokkum.
Glotaran: A java-based graphical user interface for the r package timp.
J. Stat. Softw. **49**, 1–22 (2012).

[137] M. L. Horng, J. A. Gardecki, A. Papazyan, and M. Maroncelli.
Subpicosecond measurements of polar solvation dynamics: Coumarin 153 revisited.
J. Phys. Chem. **99**, 17311–17337 (1995).

[138] G. D. Scholes, I. R. Gould, R. J. Cogdell, and G. R. Fleming.
Ab initio molecular orbital calculations of electronic couplings in the lh2 bacterial light-harvesting complex of rps. acidophila.
J. Phys. Chem. B **103**, 2543–2553 (1999).

[139] F. Würthner, T. Kaiser, and C. Saha-Möller.
J-aggregates: From serendipitous discovery to supramolecular engineering of function.
Angew. Chem. Int. Ed. **50**, 3376 – 3410 (2011).

[140] T.-A. Kobayashi.
J-aggregates in spectral sensitization of photographic materials.
World Scientific: Singapore (1996).

[141] F. Würthner.
Dipole-dipole interaction driven self-assembly of merocyanine dyes: From dimers to nanoscale objects and supramolecular materials.
Acc. Chem. Res. **49**, 868–876 (2016).

[142] B. Heyne.
Self-assembly of organic dyes in supramolecular aggregates.
Photochem. Photobiol. Sci **15**, 1103–1114 (2016).

[143] J. Bricks, Y. Slominskii, I. Panas, and A. Demchenko.
Fluorescent j-aggregates of cyanine dyes: basic research and applications review.
Methods Appl. Fluoresc. **6**, 012001 (2018).

[144] D. Bialas, A. Zitzler-Kunkel, E. Kirchner, D. Schmidt, and F. Würthner.
Structural and quantum chemical analysis of exciton coupling in homo- and heteroaggregate stacks of merocyanines.
Nat. Comm. **7**, 12949 (2016).

[145] C. Lambert, T. Scherpf, H. Ceymann, A. Schmiedel, and M. Holzapfel.
Coupled oscillators for tuning fluorescence properties of squaraine dyes.
J. Am. Chem. Soc. **137**, 3547–3557 (2015).

[146] S. Völker, A. Schmiedel, M. Holzapfel, K. Renziehausen, V. Engel, and C. Lambert.
Singlet-singlet exciton annihilation in an exciton-coupled squaraine-squaraine copolymer: A model toward hetero-j-aggregates.
J. Phys. Chem. C **118**, 17467–17482 (2014).

[147] P. Maly, J. Lüttig, A. Turkin, J. Dostal, C. Lambert, and T. Brixner.
From wavelike to sub-diffusive motion: exciton dynamics and interaction in squaraine copolymers of varying length.
Chem. Sci. (2020).

[148] D. Scherer, R. Dörfler, A. Feldner, T. Vogtmann, M. Schwörer, U. Lawrentz, W. Grahn, and C. Lambert.
Two-photon states in squaraine monomers and oligomers.
Chem. Phys. **279**, 179– (2002).

[149] S. F. Völker, S. Uemura, L. M., M. Mingebach, C. Deibel, V. Dyakonov, and C. Lambert.
Polymeric squaraine dyes as electron donors in bulk heterojunction solar cells.
Macromol. Chem. Phys. **211**, 1098–1108 (2010).

[150] S. Sreejith, P. Carol, P. Chithra, and A. Ajayaghosh.
Squaraine dyes: a mine of molecular materials.
J. Mater. Chem. **18**, 264 274 (2008).

[151] F.-P. Gao, Y.-X. Lin, L.-L. Li, Y. Liu, U. Mayerhöffer, P. Spenst, J.-G. Su, J.-Y. Li, F. Würthner, and H. Wang.
Supramolecular adducts of squaraine and protein for noninvasive tumor imaging and photothermal therapy in vivo.
Biomat. **35**, 1004–1014 (2014).

[152] K. Belfield, M. Bondar, H. Haniff, I. Mikhailov, G. Luchita, and O. Przhonska.

Superfluorescent squaraine with efficient two-photon absorption and high photostability.
ChemPhysChem **14**, 3532–3542 (2013).

[153] T. Maeda, T. Tsukamoto, A. Seto, S. Yagi, and H. Nakazumi.
Synthesis and characterization of squaraine-based conjugated polymers with phenylene linkers for bulk heterojunction solar cells.
Macromol. Chem. Phys. **213**, 2590–2597 (2012).

[154] T. Maeda, Y. Hamamura, K. Miyanaga, N. Shima, S. Yagi, and H. Nakazumi.
Near-infrared absorbing squarylium dyes with linearly extended π-conjugated structure for dye-sensitized solar cell applications.
Org. Lett. **13**, 5994–5997 (2011).

[155] H. Ceymann, A. Rosspeintner, M. Schreck, C. Mützel, A. Stoy, E. Vauthey, and C. Lambert.
Cooperative enhancement versus additivity of two-photon-absorption cross sections in linear and branched squaraine superchromophores.
Phys. Chem. Chem. Phys. **18**, 16404–16413 (2016).

[156] A. Ajayaghosh.
Chemistry of squaraine-derived materials: Nearir dyes, low band gap systems, and cation sensors.
Acc. Chem. Res. **38**, 449–459 (2005).

[157] L. Beverina and P. Salice.
Squaraine compounds: Tailored design and synthesis towards a variety of material science applications.
Eur. J. Org. Chem. p. 1207–1225 (2010).

[158] D. Harkin, K. Broch, M. Schreck, H. Ceymann, A. Stoy, C. Yong, M. Nikolka, I. McCulloch, N. Stingelin, C. Lambert, and H. Sirringhaus.
Decoupling charge transport and electroluminescence in a high mobility polymer semiconductor.
Adv. Mater. pp. 28,6378–6385 (2016).

[159] T. Maeda, N. V. T., Y. Kuwano, C. J., X. Miyanaga, N. K., Y. H., S. S., and A. Ajayaghosh.
Intramolecular exciton-coupled squaraine dyes for dye-sensitized solar cells.
J. Phys. Chem. C **122**, 21745–21754 (2018).

[160] G. W. Wei, S. Sun, T. K., M. E., and S. Forrest.
Solvent-annealed crystalline squaraine: Pc70bm (1:6) solar cells.
Adv. Energ. Mater. **1**, 184–187 (2011).

[161] U. Mayerhöffer, K. Deing, K. Gruss, H. Braunschweig, K. Meerholz, and F. Würthner.
Outstanding short-circuit currents in bhj solar cells based on nir-absorbing acceptor-substituted squaraines.
Angew. Chem. Int. Ed **48**, 8776–8779 (2009).

[162] E. Michail, M. Schreck, M. Holzapfel, and C. Lambert.
Exciton coupling effects on the two-photon absorption of squaraine homodimers with varying bridge units.
Phys. Chem. Chem. Phys. **22**, 18340–18350 (2020).

[163] M. Röhr, P. J., W. M., B.-K. V., and M. R.
Nonlinear absorption dynamics using field-induced surface hopping: Zinc porphyrin in water.
ChemPhysChem **14**, 1377–1386 (2013).

[164] E. McRae and M. Kasha.
The molecular exciton model.
Phys. Process. Radiation Biol. p. 23–42 (1964).

[165] T. Holstein.
Studies of polaron motion: Part i. the molecular-crystal model.
Ann. Phys. **8**, 325–342 (1959).

[166] R. Fulton and M. Gouterman.
Vibronic coupling. i. mathematical treatment for two electronic states.
J. Chem. Phys. **35**, 1059–1071 (1961).

[167] A. Witkowski and W. Moffitt.
Electronic spectra of dimers: derivation of the fundamental vibronic equation.
J. Chem. Phys. pp. 33,872–875 (1960).

[168] A. Sillen and Y. Engelborghs.
The correct use of "average" fluorescence parameters.
Photochem. Photobiol. **67**, 475–486 (1998).

[169] G. M. Paterno, N. Barbero, G. S., B. C., L. G., S. F., and B. R.
Excited state photophysics of squaraine dyes for photovoltaic applications: an alternative deactivation scenario.
J. Mater. Chem. C **6**, 2778–2785 (2018).

[170] X. Chen and T. Kobayashi.
The effect of two-exciton states on the linear absorption of the third molecular level in linear molecular aggregates.
J. Chem. Phys. **117**, 11347–11351 (2002).

[171] P. Maly, S. Müller, J. Lüttig, C. Lambert, and T. Brixner.
Signatures of exciton dynamics and interaction in coherently and fluorescence-detected four- and six-wave-mixing two-dimensional electronic spectroscopy.
J. Chem. Phys. **153**, 144204 (2020).

[172] P. Maly, J. Lüttig, S. Müller, M. Schreck, C. Lambert, and T. Brixner.
Coherently and fluorescence-detected two-dimensional electronic spectroscopy: direct comparison on squaraine dimers.
Phys. Chem. Chem. Phys. **22**, 21222–21237 (2020).

[173] A. Harriman.
Artificial light-harvesting arrays for solar energy conversion.
Chem. Commun. **51**, 11745–11756 (2015).

[174] B. Albinsson and J. Mårtensson.
Excitation energy transfer in donor–bridge–acceptor systems.
Phys. Chem. Chem. Phys. **12**, 7338 (2010).

[175] V. May.
Beyond the förster theory of excitation energy transfer: importance of higher-order processes in supramolecular antenna systems.
Dalton Trans. p. 10086 (2009).

[176] S. Speiser.
Photophysics and mechanisms of intramolecular electronic energy transfer in bichromophoric molecular systems: solution and supersonic jet studies.
Chem. Rev. **96**, 1953–1976 (1996).

[177] I. Hwang and G. D. Scholes.
Electronic energy transfer and quantum-coherence in π-conjugated polymers.
Chem. Mater. **23**, 610–620 (2010).

[178] J.-L. Brédas, D. Beljonne, V. Coropceanu, and J. Cornil.
Charge-transfer and energy-transfer processes in π-conjugated oligomers and polymers: a molecular picture.
Chem. Rev. **104**, 4971–5004 (2004).

[179] C. J. Bardeen.
The structure and dynamics of molecular excitons.
Ann. Rev. Phys. Chem. **65**, 127–148 (2014).

[180] O. Kühn and S. Lochbrunner.
Quantum dynamics and spectroscopy of excitons in molecular aggregates pp. 47–81 (2011).

[181] J. Knoester.
Optical properties of molecular aggregates.

Proc. Int. Sch. Phys. Enrico Fermi **149**, 149–186 (2002).

[182] A. Chenu and G. D. Scholes.
Coherence in energy transfer and photosynthesis.
Ann. Rev. Phys. Chem. **66**, 69–96 (2015).

[183] C. Lambert, J. Ehbets, D. Rausch, and M. Steeger.
Charge-transfer interactions in a multichromophoric hexaarylbenzene containing pyrene and triarylamines.
J. Org. Chem. **77**, 6147–6154 (2012).

[184] J. Merz, J. Fink, A. Friedrich, I. Krummenacher, H. H. Al Mamari, S. Lorenzen, M. Haehnel, A. Eichhorn, M. Moos, M. Holzapfel, H. Braunschweig, C. Lambert, A. Steffen, L. Ji, and T. B. Marder.
Pyrene molecular orbital shuffle-controlling excited state and redox properties by changing the nature of the frontier orbitals.
Chem. - Eur. J. **23**, 13164–13180 (2017).

[185] M. Raytchev, E. Pandurski, I. Buchvarov, C. Modrakowski, and T. Fiebig.
Bichromophoric interactions and time-dependent excited state mixing in pyrene derivatives. a femtosecond broad-band pump-probe study.
J. Phys. Chem. A **107**, 4592–4600 (2003).

[186] N. Krebs, I. Pugliesi, J. Hauer, and E. Riedle.
Two-dimensional fourier transform spectroscopy in the ultraviolet with sub-20 fs pump pulses and 250–720 nm supercontinuum probe.
New. J. Phys. **15**, 085016 (2013).

[187] W. Rodriguez-Córdoba, C. A. Sierra, C. O. Puentes, P. M. Lahti, and J. Peon.
Photoinduced energy transfer in bichromophoric pyrene–PPV oligomer systems: The role of flexible donor–acceptor bridges.
J. Phys. Chem. B **116**, 3490–3503 (2012).

[188] T. M. Figueira-Duarte and K. Müllen.
Pyrene-based materials for organic electronics.
Chem. Rev. **111**, 7260–7314 (2011).

[189] A. G. Crawford, A. D. Dwyer, Z. Liu, A. Steffen, A. Beeby, L.-O. Pålsson, D. J. Tozer, and T. B. Marder.
Experimental and theoretical studies of the photophysical properties of 2- and 2,7-functionalized pyrene derivatives.
J. Am. Chem. Soc. **133**, 13349–13362 (2011).

[190] A. G. Crawford, Z. Liu, I. A. I. Mkhalid, M.-H. Thibault, N. Schwarz, G. Alcaraz, A. Steffen, J. C. Collings, A. S. Batsanov, J. A. K. Howard, and T. B. Marder.

Synthesis of 2- and 2,7-functionalized pyrene derivatives: An application of selective c-h borylation.
Chem. - Eur. J. **18**, 5022–5035 (2012).

[191] R. Ziessel, C. Goze, and G. Ulrich.
Design and synthesis of alkyne-substituted boron in dipyrromethene frameworks.
Synthesis **2007**, 936–949 (2007).

[192] J. Karolin, L. B.-A. Johansson, L. Strandberg, and T. Ny.
Fluorescence and absorption spectroscopic properties of dipyrromethene boron difluoride (BODIPY) derivatives in liquids, lipid membranes, and proteins.
J. Am. Chem. Soc. **116**, 7801–7806 (1994).

[193] H. L. Kee, C. Kirmaier, L. Yu, P. Thamyongkit, W. J. Youngblood, M. E. Calder, L. Ramos, B. C. Noll, D. F. Bocian, W. R. Scheidt, R. R. Birge, J. S. Lindsey, and D. Holten.
Structural control of the photodynamics of boron-dipyrrin complexes.
J. Phys. Chem. B **109**, 20433–20443 (2005).

[194] R. Ziessel and A. Harriman.
Artificial light-harvesting antennae: electronic energy transfer by way of molecular funnels.
Chem. Commun. **47**, 611–631 (2011).

[195] R. Ziessel, G. Ulrich, A. Haefele, and A. Harriman.
An artificial light-harvesting array constructed from multiple bodipy dyes.
J. Am. Chem. Soc. **135**, 11330–11344 (2013).

[196] M. A. H. Alamiry, J. P. Hagon, A. Harriman, T. Bura, and R. Ziessel.
Resolving the contribution due to förster-type intramolecular electronic energy transfer in closely coupled molecular dyads.
Chem. Sci. **3**, 1041–1048 (2012).

[197] A. Harriman, G. Izzet, and R. Ziessel.
Rapid energy transfer in cascade-type bodipy dyes.
J. Am. Chem. Soc. **128**, 10868–10875 (2006).

[198] A. Harriman, L. Mallon, and R. Ziessel.
Energy flow in a purpose-built cascade molecule bearing three distinct chromophores attached to the terminal acceptor.
Chem. - Eur. J. **14**, 11461–11473 (2008).

[199] A. Harriman, L. Mallon, S. Goeb, G. Ulrich, and R. Ziessel.
Electronic energy transfer to the s2 level of the acceptor in functionalised boron dipyrromethene dyes.
Chem. - Eur. J. **15**, 4553–4564 (2009).

[200] R. Ziessel, C. Goze, G. Ulrich, M. Césario, P. Retailleau, A. Harriman, and J. P. Rostron.
Intramolecular energy transfer in pyrene–bodipy molecular dyads and triads.
Chem. - Eur. J. **11**, 7366–7378 (2005).

[201] C. Goze, G. Ulrich, and R. Ziessel.
Tetrahedral boron chemistry for the preparation of highly efficient "cascatelle" devices.
J. Org. Chem. **72**, 313–322 (2006).

[202] C. Goze, G. Ulrich, and R. Ziessel.
Unusual fluorescent monomeric and dimeric dialkynyl dipyrromethene-borane complexes.
Org. Lett. **8**, 4445–4448 (2006).

[203] G. Ulrich, R. Ziessel, S. Goeb, A. D. Nicola, and P. Retailleau.
Synthesis of bisisoindolomethene dyes bearing anisole or ethylthiophene residues for red and near-IR fluorescence.
Synlett **2007**, 1517–1520 (2007).

[204] L. Bonardi, G. Ulrich, and R. Ziessel.
Tailoring the properties of boron-dipyrromethene dyes with acetylenic functions at the 2,6,8 and 4-b substitution positions.
Org. Lett. **10**, 2183–2186 (2008).

[205] A. Haefele, G. Ulrich, P. Retailleau, and R. Ziessel.
Synthesis of multi-branched dipyrromethene dyes with soluble diethynylphenyl links.
Tetrah. Lett. **49**, 3716–3721 (2008).

[206] D. Bai, A. C. Benniston, J. Hagon, H. Lemmetyinen, N. V. Tkachenko, and R. W. Harrington.
Tuning the förster overlap integral: energy transfer over 20 Ångstroms from a pyrene-based donor to borondipyrromethene (bodipy).
Phys. Chem. Chem. Phys. **15**, 9854–9861 (2013).

[207] M. Fakis, J. S. Beckwith, K. Seintis, E. Martinou, C. Nançoz, N. Karakostas, I. Petsalakis, G. Pistolis, and E. Vauthey.
Energy transfer and charge separation dynamics in photoexcited pyrene–bodipy molecular dyads.
Phys. Chem. Chem. Phys. **20**, 837–849 (2018).

[208] R. Ziessel, G. Ulrich, and A. Harriman.
The chemistry of bodipy: A new el dorado for fluorescence tools.
New. J. Chem. **31**, 496 (2007).

[209] C.-W. Wan, A. Burghart, J. Chen, F. Bergström, L. B.-Å. Johansson, M. F. Wolford, T. G. Kim, M. R. Topp, R. M. Hochstrasser, and K. Burgess.
Anthracene–BODIPY cassettes: Syntheses and energy transfer.
Chem. - Eur. J. **9**, 4430–4441 (2003).

[210] J. Gierschner, J. Cornil, and H.-J. Egelhaaf.
Optical bandgaps of π-conjugated organic materials at the polymer limit: Experiment and theory.
Adv. Mater. **19**, 173–191 (2007).

[211] N. Auerhammer, A. Schmiedel, M. Holzapfel, and C. Lambert.
Exciton coupling enhancement in the relaxed excited state.
J. Phys. Chem. C **122**, 11720–11729 (2018).

[212] J. S. Beckwith, A. Rosspeintner, G. Licari, M. Lunzer, B. Holzer, J. Fröhlich, and E. Vauthey.
Specific monitoring of excited-state symmetry breaking by femtosecond broadband fluorescence upconversion spectroscopy.
J. Phys. Chem. Lett. **8**, 5878–5883 (2017).

[213] E. Vauthey.
Photoinduced symmetry-breaking charge separation.
ChemPhysChem **13**, 2001–2011 (2012).

[214] S. Amthor, C. Lambert, S. Dümmler, I. Fischer, and J. Schelter.
Excited mixed-valence states of symmetrical donor-acceptor-donor π systems.
J. Phys. Chem. A **110**, 5204–5214 (2006).

[215] T.-S. Ahn, R. O. Al-Kaysi, A. M. Müller, K. M. Wentz, and C. J. Bardeen.
Self-absorption correction for solid-state photoluminescence quantum yields obtained from integrating sphere measurements.
Rev. Sci. Instrum. **78**, 086105 (2007).

[216] I. H. van Stokkum, D. S. Larsen, and R. van Grondelle.
Erratum to "global and target analysis of time-resolved spectra" [biochimica et biophysica acta 1658/2–3 (2004) 82–104].
Biochimica et Biophysica Acta (BBA) - Bioenergetics **1658**, 262 (2004).

[217] J. J. P. Stewart.
Optimization of parameters for semiempirical methods i. method.
J. Comput. Chem. **10**, 209–220 (1989).

[218] J. J. P. Stewart.
Optimization of parameters for semiempirical methods II. applications.
J. Comput. Chem. **10**, 221–264 (1989).

[219] R. L. Martin.
Natural transition orbitals.
J. Chem. Phys. **118**, 4775–4777 (2003).

[220] T. Yanai, D. P. Tew, and N. C. Handy.
A new hybrid exchange–correlation functional using the coulomb-attenuating method (CAM-b3lyp).
Chem. Phys. Lett. **393**, 51–57 (2004).

[221] F. Weigend, M. Häser, H. Patzelt, and R. Ahlrichs.
RI-MP2: optimized auxiliary basis sets and demonstration of efficiency.
Chem. Phys. Lett. **294**, 143–152 (1998).

[222] M. J. Frisch, G. W. Trucks, H. B. Schlegel, G. E. Scuseria, M. A. Robb, J. R. Cheeseman, G. Scalmani, V. Barone, G. A. Petersson, H. Nakatsuji, X. Li, M. Caricato, A. V. Marenich, J. Bloino, B. G. Janesko, R. Gomperts, B. Mennucci, H. P. Hratchian, J. V. Ortiz, A. F. Izmaylov, J. L. Sonnenberg, D. Williams-Young, F. Ding, F. Lipparini, F. Egidi, J. Goings, B. Peng, A. Petrone, T. Henderson, D. Ranasinghe, V. G. Zakrzewski, J. Gao, N. Rega, G. Zheng, W. Liang, M. Hada, M. Ehara, K. Toyota, R. Fukuda, J. Hasegawa, M. Ishida, T. Nakajima, Y. Honda, O. Kitao, H. Nakai, T. Vreven, K. Throssell, J. A. Montgomery, Jr., J. E. Peralta, F. Ogliaro, M. J. Bearpark, J. J. Heyd, E. N. Brothers, K. N. Kudin, V. N. Staroverov, T. A. Keith, R. Kobayashi, J. Normand, K. Raghavachari, A. P. Rendell, J. C. Burant, S. S. Iyengar, J. Tomasi, M. Cossi, J. M. Millam, M. Klene, C. Adamo, R. Cammi, J. W. Ochterski, R. L. Martin, K. Morokuma, O. Farkas, J. B. Foresman, and D. J. Fox.
Gaussian16 Revision C.01. (2016). Gaussian Inc. Wallingford CT.

[223] J.-L. Brédas, J. E. Norton, J. Cornil, and V. Coropceanu.
Molecular understanding of organic solar cells: The challenges.
Acc. Chem. Res. **42**, 1691–1699 (2009).

[224] N. Boens, V. Leen, and W. Dehaen.
Fluorescent indicators based on BODIPY.
Chem. Soc. Rev. **41**, 1130–1172 (2012).

[225] Y. Hong, J. W. Y. Lam, and B. Zhong Tang.
Aggregation-induced emission: phenomenon, mechanism and applications.
Chem. Comm. **0**, 4332–4353 (2009).

[226] T. Renger, M. Dankl, A. Klinger, T. Schlücker, H. Langhals, and F. Müh.
Structure-based theory of fluctuation-induced energy transfer in a molecular dyad.
J. Phys. Chem. Lett. **9**, 5940–5947 (2018).

[227] H. Lin, R. Camacho, Y. Tian, T. E. Kaiser, F. Würthner, and I. G. Scheblykin.
Collective fluorescence blinking in linear j-aggregates assisted by long-distance exciton migration.
Nano Lett. **10**, 620–626 (2010).

[228] J. Megow, M. I. S. Roehr, M. Schmidt am Busch, T. Renger, R. Mitric, S. Kirstein, J. P. Rabe, and V. May.
Site-dependence of van der waals interaction explains exciton spectra of double-walled tubular j-aggregates.
Phys. Chem. Chem. Phys. **17**, 6741–6747 (2015).

[229] M. Di Donato, A. Iagatti, A. Lapini, P. Foggi, S. Cicchi, L. Lascialfari, S. Fedeli, S. Caprasecca, and B. Mennucci.
Combined experimental and theoretical study of efficient and ultrafast energy transfer in a molecular dyad.
J. Phys. Chem. C **118**, 23476–23486 (2014).

[230] C. Curutchet, A. Muñoz-Losa, S. Monti, J. Kongsted, G. D. Scholes, and B. Mennucci.
Electronic energy transfer in condensed phase studied by a polarizable qm/mm model.
J. Chem. Theor. Comput. **5**, 1838–1848 (2009). PMID: 26610008.

[231] F. Würthner.
Perylene bisimide dyes as versatile building blocks for functional supramolecular architectures.
Chem. Commun. pp. 1564–1579 (2004).

[232] V. M. Freixas, D. Ondarse-Alvarez, S. Tretiak, D. V. Makhov, D. V. Shalashilin, and S. Fernandez-Alberti.
Photoinduced non-adiabatic energy transfer pathways in dendrimer building blocks.
J. Chem. Phys. **150**, 124301 (2019).

[233] D. Bialas, C. Zhong, F. Würthner, and F. C. Spano.
Essential States Model for Merocyanine Dye Stacks: Bridging Electronic and Optical Absorption Properties.
J. Phys. Chem. C **123**, 18654–18664 (2019).

[234] R. Hildner, D. Brinks, J. B. Nieder, R. J. Cogdell, and N. F. van Hulst.
Quantum coherent energy transfer over varying pathways in single light-harvesting complexes.
Science **340**, 1448–1451 (2013).

[235] S. M. Falke, C. A. Rozzi, D. Brida, M. Maiuri, M. Amato, E. Sommer, G. Cerullo, E. Molinari, and C. Lienau.

Coherent ultrafast charge transfer in an organic photovoltaic blend.
Science **344**, 1001–1005 (2014).

[236] G. D. Scholes, G. R. Fleming, L. X. Chen, A. Aspuru-Guzik, A. Buchleitner, D. F. Coker, G. S. Engel, R. van Grondelle, A. Ishizaki, D. M. Jonas, J. S. Lundeen, J. K. McCusker, S. Mukamel, J. P. Ogilvie, A. Olaya-Castro, M. A. Ratner, F. C. Spano, K. B. Whaley, and X. Zhu.
Using coherence to enhance function in chemical and biophysical systems.
Nature **543**, 647–656 (2017).

[237] S. Guo, L. Ma, J. Zhao, B. Küçüköz, A. Karatay, M. Hayvali, H. G. Yaglioglu, and A. Elmali.
BODIPY triads triplet photosensitizers enhanced with intramolecular resonance energy transfer (RET): broadband visible light absorption and application in photooxidation.
Chem. Sci. **5**, 489–500 (2014).

[238] S. Kilina, D. Kilin, and S. Tretiak.
Light-driven and phonon-assisted dynamics in organic and semiconductor nanostructures.
Chem. Rev. **115**, 5929–5978 (2015).

[239] T. Nelson, S. Fernandez-Alberti, A. E. Roitberg, and S. Tretiak.
Electronic delocalization, vibrational dynamics, and energy transfer in organic chromophores.
J. Phys. Chem. Lett. **8**, 3020–3031 (2017).

[240] E. Titov, A. Humeniuk, and R. Mitric.
Exciton localization in excited-state dynamics of a tetracene trimer: A surface hopping LC-TDDFTB study.
Phys. Chem. Chem. Phys. **20**, 25995–26007 (2018).

[241] R. Mitrić, J. Petersen, M. Wohlgemuth, U. Werner, V. Bonačić-Koutecký, L. Wöste, and J. Jortner.
Time-resolved femtosecond photoelectron spectroscopy by field-induced surface hopping.
J. Phys. Chem. A **115**, 3755–3765 (2011).

[242] T. E. Dykstra, E. Hennebicq, D. Beljonne, J. Gierschner, G. Claudio, E. R. Bittner, J. Knoester, and G. D. Scholes.
Conformational disorder and ultrafast exciton relaxation in ppv-family conjugated polymers.
J. Phys. Chem. B **113**, 656–667 (2009). PMID: 19105646.

[243] D. Ondarse-Alvarez, S. Kömürlü, A. E. Roitberg, G. Pierdominici-Sottile, S. Tretiak, S. Fernandez-Alberti, and V. D. Kleiman.

Ultrafast electronic energy relaxation in a conjugated dendrimer leading to inter-branch energy redistribution.
Phys. Chem. Chem. Phys. **18**, 25080–25089 (2016).

[244] M. M.-L. Grage, Y. Zaushitsyn, A. Yartsev, M. Chachisvilis, V. Sundström, and T. o. Pullerits.
Ultrafast excitation transfer and trapping in a thin polymer film.
Phys. Rev. B **67**, 205207 (2003).

[245] M. M.-L. Grage, P. W. Wood, A. Ruseckas, T. Pullerits, W. Mitchell, P. L. Burn, I. D. W. Samuel, and V. Sundström.
Conformational disorder and energy migration in meh-ppv with partially broken conjugation.
J. Chem. Phys. **118**, 7644–7650 (2003).

[246] Y. Li, G. He, X. Wang, Q. Guo, Y. Niu, and A. Xia.
A study of excitation delocalization/localization in multibranched chromophores by using fluorescence excitation anisotropy spectroscopy.
ChemPhysChem **17**, 406–411 (2016).

[247] R. Binder, D. Lauvergnat, and I. Burghardt.
Conformational dynamics guides coherent exciton migration in conjugated polymer materials: First-principles quantum dynamical study.
Phys. Rev. Lett. **120**, 227401 (2018).

[248] J. R. Mannouch, W. Barford, and S. Al-Assam.
Ultra-fast relaxation, decoherence, and localization of photoexcited states in -conjugated polymers.
J. Chem. Phys. **148**, 034901 (2018).

[249] W. Barford, J. L. A. Gardner, and J. Mannouch.
Using two-dimensional spectroscopy to probe relaxation, decoherence, and localization of photoexcited states in pi-conjugated polymers.
Faraday Discuss. **221**, 281–298 (2019).

[250] M. J. S. Dewar, E. G. Zoebisch, E. F. Healy, and J. J. P. Stewart.
Development and use of quantum mechanical molecular models. 76. AM1: a new general purpose quantum mechanical molecular model.
J. Am. Chem. Soc. **107**, 3902–3909 (1985).

[251] E. Wigner.
On the quantum correction for thermodynamic equilibrium.
Phys. Rev. **40**, 749–759 (1932).

[252] V. Bonačić-Koutecký and R. Mitrić.
Theoretical exploration of ultrafast dynamics in atomic clusters: Analysis and control.

Chem. Rev. **105**, 11–65 (2005).

[253] W. C. Swope, H. C. Andersen, H. P. Berens, and K. R. Wilson.
A computer simulation method for the calculation of equilibrium constants for the formation of physical clusters of molecules: Application to small water clusters.
J. Chem. Phys. **76**, 637 (1982).

[254] M. B. Smith and J. Michl.
Singlet Fission.
Chem. Rev. **110**, 6891–6936 (2010).

[255] M. B. Smith and J. Michl. *Recent Advances in Singlet Fission.* in Johnson, MA and Martinez, TJ (Ed.), *Annu. Rev. Phys. Chem.*, volume 64 of *Annu. Rev. Phys. Chem.*, pp. 361–386. Annual Reviews, (2013).

[256] J. C. Johnson, A. J. Nozik, and J. Michl.
The Role of Chromophore Coupling in Singlet Fission.
Acc. Chem. Res. **46**, 1290–1299 (2013).

[257] N. V. Korovina, N. F. Pompetti, and J. C. Johnson.
Lessons from intramolecular singlet fission with covalently bound chromophores.
J. Chem. Phys. **152**, 040904 (2020).

[258] D. Casanova.
Theoretical modeling of singlet fission.
Chem. Rev. **118**, 7164–7207 (2018). PMID: 29648797.

[259] M. Einzinger, T. Wu, J. F. Kompalla, H. L. Smith, C. F. Perkinson, L. Nienhaus, S. Wieghold, D. N. Congreve, A. Kahn, M. G. Bawendi, et al.
Sensitization of silicon by singlet exciton fission in tetracene.
Nature **571**, 90–94 (2019).

[260] R. W. MacQueen, M. Liebhaber, J. Niederhausen, M. Mews, C. Gersmann, S. Jäckle, K. Jäger, M. J. Y. Tayebjee, T. W. Schmidt, B. Rech, and K. Lips.
Crystalline silicon solar cells with tetracene interlayers: the path to silicon-singlet fission heterojunction devices.
Mater. Horiz. **5**, 1065–1075 (2018).

[261] E. Posenitskiy, M. Rapacioli, B. Lepetit, D. Lemoine, and F. Spiegelman.
Non-adiabatic molecular dynamics investigation of the size dependence of the electronic relaxation in polyacenes.
Phys. Chem. Chem. Phys. **21**, 12139–12149 (2019).

[262] G. Tao.
Nonadiabatic simulation of singlet fission dynamics in tetracene clusters: The topology of quantum coherence in a global view.

J. Chem. Phys. **151**, 054308 (2019).

[263] J. J. Burdett, A. M. Müller, D. Gosztola, and C. J. Bardeen.
Excited state dynamics in solid and monomeric tetracene: The roles of superradiance and exciton fission.
J.Chem. Phys. **133**, 144506 (2010).

[264] M. W. B. Wilson, A. Rao, K. Johnson, S. Gelinas, R. di Pietro, J. Clark, and R. H. Friend.
Temperature-Independent Singlet Exciton Fission in Tetracene.
J. Am. Chem.Soc. **135**, 16680–16688 (2013).

[265] M. J. Y. Tayebjee, R. G. C. R. Clady, and T. W. Schmidt.
The exciton dynamics in tetracene thin films.
Phys. Chem. Chem. Phys. **15**, 14797–14805 (2013).

[266] N. V. Korovina, J. Joy, X. Feng, C. Feltenberger, A. I. Krylov, S. E. Bradforth, and M. E. Thompson.
Linker-Dependent Singlet Fission in Tetracene Dimers.
J. Am. Chem. Soc. **140**, 10179–10190 (2018).

[267] P. J. Vallett, J. L. Snyder, and N. H. Damrauer.
Tunable Electronic Coupling and Driving Force in Structurally Well-Defined Tetracene Dimers for Molecular Singlet Fission: A Computational Exploration Using Density Functional Theory.
J. Phys. Chem. A **117**, 10824–10838 (2013).

[268] J. D. Cook, T. J. Carey, and N. H. Damrauer.
Solution-Phase Singlet Fission in a Structurally Well-Defined Norbornyl-Bridged Tetracene Dimer.
J. Phys. Chem. A **120**, 4473–4481 (2016).

[269] J. D. Cook, T. J. Carey, D. H. Arias, J. C. Johnson, and N. H. Damrauer.
Solvent-Controlled Branching of Localized versus Delocalized Singlet Exciton States and Equilibration with Charge Transfer in a Structurally Well-Defined Tetracene Dimer.
J. Phys. Chem. A **121**, 9229–9242 (2017).

[270] C. J. Imperiale, P. B. Green, E. G. Miller, N. H. Damrauer, and M. W. B. Wilson.
Triplet-Fusion Upconversion Using a Rigid Tetracene Homodimer.
J. Phys. Chem. Lett. **10**, 7463–7469 (2019).

[271] P. M. Zimmerman, F. Bell, D. Casanova, and M. Head-Gordon.
Mechanism for singlet fission in pentacene and tetracene: From single exciton to two triplets.
J. Am. Chem. Soc. **133**, 19944–19952 (2011).

[272] P. M. Zimmerman, C. B. Musgrave, and M. Head-Gordon.
A correlated electron view of singlet fission.
Acc. Chem. Res. **46**, 1339–1347 (2013).

[273] C. B. Dover, J. K. Gallaher, L. Frazer, P. C. Tapping, A. J. Petty, II, M. J. Crossley, J. E. Anthony, T. W. Kee, and T. W. Schmidt.
Endothermic singlet fission is hindered by excimer formation.
Nat. Chem. **10**, 305–310 (2018).

[274] D. C. A. Valente, M. T. do Casal, M. Barbatti, T. A. Niehaus, A. J. A. Aquino, H. Lischka, and T. M. Cardozo.
Excitonic and charge transfer interactions in tetracene stacked and t-shaped dimers.
J. Chem. Phys. **154**, 044306 (2021).

[275] M. Miyazaki and M. Fujii.
Real time observation of the excimer formation dynamics of a gas phase benzene dimer by picosecond pump–probe spectroscopy.
Phys. Chem. Chem. Phys. **17**, 25989–25997 (2015).

[276] E. S. S. Iyer, A. Sadybekov, O. Lioubashevski, A. I. Krylov, and S. Ruhman.
Rewriting the story of excimer formation in liquid benzene.
J. Phys. Chem. A **121**, 1962–1975 (2017). PMID: 28182435.

[277] T. M. Cardozo, A. P. Galliez, I. Borges, F. Plasser, A. J. A. Aquino, M. Barbatti, and H. Lischka.
Dynamics of benzene excimer formation from the parallel-displaced dimer.
Phys. Chem. Chem. Phys. **21**, 13916–13924 (2019).

[278] R. Knochenmuss, I. Fischer, D. Luhrs, and Q. Lin.
Intermolecular excited-state proton transfer in clusters of 1-naphthol with water and with ammonia.
Isr. J. Chem. **39**, 221–230 (1999). Reserch Workshop on Proton Solvation and Proton Mobility, NEVE ILAN, ISRAEL, 1998.

[279] D. C. Lührs, R. Knochenmuss, and I. Fischer.
Excited-state proton transfer in 1-naphthol (nh 3) n clusters: Wavelength-dependence of the picosecond pump–probe spectra.
Phys. Chem. Chem. Phys. **2**, 4335–4340 (2000).

[280] F. Santoro, R. Improta, A. Lami, J. Bloino, and V. Barone.
Effective method to compute franck-condon integrals for optical spectra of large molecules in solution.
J. Chem. Phys. **126**, 084509 (2007).

[281] F. Santoro.

Fcclasses: A fortran 77 code; 2008. (available via the internet at www.pi.iccom.cnr.it/fcclasses; last accessed 27/04/2022).

[282] D. Accomasso, G. Granucci, M. Wibowo, and M. Persico.
Delocalization effects in singlet fission: Comparing models with two and three interacting molecules.
J. Chem. Phys. **152**, 244125 (2020).

[283] D. Accomasso, G. Granucci, and M. Persico.
Diabatization by localization in the framework of configuration interaction based on floating occupation molecular orbitals (fomo-ci).
ChemPhotoChem (2019).

[284] M. Elstner, D. Porezag, G. Jungnickel, J. Elsner, M. Haugk, T. Frauenheim, S. Suhai, and G. Seifert.
Self-consistent-charge density-functional tight-binding method for simulations of complex materials properties.
Phys. Rev. B **58**, 7260–7268 (1998).

[285] A. Humeniuk and R. Mitrić.
Long-range correction for tight-binding td-dft.
J. Chem. Phys. **143**, 134120 (2015).

[286] A. Humeniuk and R. Mitrić.
Dftbaby: A software package for non-adiabatic molecular dynamics simulations based on long-range corrected tight-binding td-dft(b).
Comput. Phys. Commun. **221**, 174 – 202 (2017).

[287] J. J. Kranz, M. Elstner, B. Aradi, T. Frauenheim, V. Lutsker, A. D. Garcia, and T. A. Niehaus.
Time-dependent extension of the long-range corrected density functional based tight-binding method.
J. Chem. Theory Comput. **13**, 1737–1747 (2017). PMID: 28272887.

[288] F. Spiegelman, N. Tarrat, J. Cuny, L. Dontot, E. Posenitskiy, C. Martí, A. Simon, and M. Rapacioli.
Density-functional tight-binding: basic concepts and applications to molecules and clusters.
Adv. Phys. X **5**, 1710252 (2020). PMID: 33154977.

[289] J. J. Stewart.
Optimization of parameters for semiempirical methods v: modification of nddo approximations and application to 70 elements.
J. Mol. Model. **13**, 1173–1213 (2007).

[290] J. Rezac and P. Hobza.

Advanced corrections of hydrogen bonding and dispersion for semiempirical quantum mechanical methods.
J. Chem. Theory Comput. **8**, 141–151 (2012).

[291] S. Grimme, J. Antony, S. Ehrlich, and H. Krieg.
A consistent and accurate ab initio parametrization of density functional dispersion correction (dft-d) for the 94 elements h-pu.
J. Chem. Phys. **132**, 154104 (2010).

[292] J. J. P. Stewart.
Mopac2016 (2016).

[293] H. J. Berendsen, J. v. Postma, W. F. van Gunsteren, A. DiNola, and J. R. Haak.
Molecular dynamics with coupling to an external bath.
J. Chem. Phys. **81**, 3684–3690 (1984).

[294] A. Luzanov, A. Sukhorukov, and V. Umanskii.
Application of transition density matrix for analysis of excited states.
Theor. Exp. Chem. **10**, 354–361 (1976).

[295] A. Luzanov and V. Pedash.
Interpretation of excited states using charge-transfer numbers.
Theor. Exp. Chem. **15**, 338–341 (1980).

[296] P.-O. Löwdin. *On the nonorthogonality problem.* in *Advances in quantum chemistry*, volume 5, pp. 185–199. Elsevier, (1970).

[297] W. Liu, B. Lunkenheimer, V. Settels, B. Engels, R. F. Fink, and A. Köhn.
A general ansatz for constructing quasi-diabatic states in electronically excited aggregated systems.
J. Chem. Phys. **143**, 084106 (2015).

[298] M. Flock, L. Bosse, D. Kaiser, B. Engels, and I. Fischer.
A time-resolved photoelectron imaging study on isolated tolane: observation of the biradicalic 1au state.
Phys. Chem. Chem. Phys. **21**, 13157–13164 (2019).

[299] J. Auerswald, B. Engels, I. Fischer, T. Gerbich, J. Herterich, A. Krueger, M. Lang, H.-C. Schmitt, C. Schon, and C. Walter.
The electronic structure of pyracene: a spectroscopic and computational study.
Phys. Chem. Chem. Phys. **15**, 8151 (2013).

[300] A. T. J. B. Eppink and D. H. Parker.
Velocity map imaging of ions and electrons using electrostatic lenses: Application in photoelectron and photofragment ion imaging of molecular oxygen.
Rev. Sci. Instrum. **68**, 3477–3484 (1997).

[301] G. A. Garcia, L. Nahon, and I. Powis.
Two-dimensional charged particle image inversion using a polar basis function expansion.
Rev. Sci. Instrum. **75**, 4989–4996 (2004).

[302] C. Schouder, A. S. Chatterley, F. Calvo, L. Christiansen, and H. Stapelfeldt.
Structure determination of the tetracene dimer in helium nanodroplets using femtosecond strong-field ionization.
Struct. Dyn. **6**, 044301 (2019).

[303] B. Hourahine, B. Aradi, V. Blum, F. Bonafé, A. Buccheri, C. Camacho, C. Cevallos, M. Y. Deshaye, T. Dumitrică, A. Dominguez, S. Ehlert, M. Elstner, T. van der Heide, J. Hermann, S. Irle, J. J. Kranz, C. Köhler, T. Kowalczyk, T. Kubař, I. S. Lee, V. Lutsker, R. J. Maurer, S. K. Min, I. Mitchell, C. Negre, T. A. Niehaus, A. M. N. Niklasson, A. J. Page, A. Pecchia, G. Penazzi, M. P. Persson, J. Řezáč, C. G. Sánchez, M. Sternberg, M. Stöhr, F. Stuckenberg, A. Tkatchenko, V. W.-z. Yu, and T. Frauenheim.
Dftb+, a software package for efficient approximate density functional theory based atomistic simulations.
J. Chem. Phys. **152**, 124101 (2020).

[304] W. Schmidt.
Photoelectron spectra of polynuclear aromatics. v. correlations with ultraviolet absorption spectra in the catacondensed series.
J. Chem. Phys. **66**, 828–845 (1977).

[305] B. Dick, E. Zinghar, and Y. Haas.
Spectral hole-burning of tetracene and tetracene-argon complexes in a supersonic jet.
Chem. Phys. Lett. **187**, 571 – 578 (1991).

[306] A. Amirav, U. Even, and J. Jortner.
Energetics and intramolecular dynamics of the isolated ultracold tetracene molecule in its first excited singlet state.
J. Chem. Phys. **75**, 3770–3793 (1981).

[307] A. M. Griffiths and P. A. Freedman.
Out-of-plane vibrations of isolated tetracene and pentacene molecules.
J. Chem. Soc., Faraday Trans. 2 **78**, 391–398 (1982).

[308] J. A. Katul and A. B. Zahlan.
Tetracene dimer.
J. Chem. Phys. **47**, 1012–1014 (1967).

[309] H. Liu, V. M. Nichols, L. Shen, S. Jahansouz, Y. Chen, K. M. Hanson, C. J. Bardeen, and X. Li.

Synthesis and photophysical properties of a "face-to-face" stacked tetracene dimer.
Phys. Chem. Chem. Phys. **17**, 6523–6531 (2015).

[310] L. D. Lavis and R. T. Raines.
Bright ideas for chemical biology.
ACS Chem. Biol. **3**, 142–155 (2008).

[311] I. D. W. Samuel and G. A. Turnbull.
Organic semiconductor lasers.
Chem. Rev. **107**, 1272–1295 (2007).

[312] S. R. Forrest and M. E. Thompson.
Introduction: Organic electronics and optoelectronics.
Chem. Rev. **107**, 923–925 (2007).

[313] R. Richter, M. I. S. Röhr, T. Zimmermann, J. Petersen, C. Heidrich, R. Rahner, T. Moeller, J. E. Dahl, R. M. K. Carlson, R. Mitric, T. Rander, and A. Merli.
Laser-induced fluorescence of free diamondoid molecules.
Phys. Chem. Chem. Phys. **17**, 4739–4749 (2015).

[314] J. Gierschner, L. Lüer, B. Milián-Medina, D. Oelkrug, and H.-J. Egelhaaf.
Highly emissive h-aggregates or aggregation-induced emission quenching? the photophysics of all-trans para-distyrylbenzene.
J. Phys. Chem. Lett. **4**, 2686–2697 (2013).

[315] D. Polli, P. Altoè, O. Weingart, K. M. Spillane, C. Manzoni, D. Brida, G. Tomasello, G. Orlandi, P. Kukura, R. A. Mathies, M. Garavelli, and G. Cerullo.
Conical intersection dynamics of the primary photoisomerization event in vision.
Nature **467**, 440–443 (2010).

[316] S. Upadhyayula, V. Nuñez, E. M. Espinoza, J. M. Larsen, D. Bao, D. Shi, J. T. Mac, B. Anvari, and V. I. Vullev.
Photoinduced dynamics of a cyanine dye: parallel pathways of non-radiative deactivation involving multiple excited-state twisted transients.
Chem. Sci. **6**, 2237–2251 (2015).

[317] V. Karunakaran, J. L. Pérez Lustres, L. Zhao, N. P. Ernsting, and O. Seitz.
Large Dynamic Stokes Shift of DNA Intercalation Dye Thiazole Orange has Contribution from a High-Frequency Mode.
J. Am. Chem. Soc. **128**, 2954–2962 (2006).

[318] N. Amdursky, Y. Erez, and D. Huppert.
Molecular Rotors: What Lies Behind the High Sensitivity of the Thioflavin-T Fluorescent Marker.

Acc. Chem. Res. **45**, 1548–1557 (2012).

[319] R. R. Valiev, V. N. Cherepanov, G. V. Baryshnikov, and D. Sundholm.
First-principles method for calculating the rate constants of internal-conversion and intersystem-crossing transitions.
Phys. Chem. Chem. Phys. **20**, 6121–6133 (2018).

[320] S. Banerjee, A. Baiardi, J. Bloino, and V. Barone.
Temperature Dependence of Radiative and Nonradiative Rates from Time-Dependent Correlation Function Methods.
J. Chem. Theor. Comput. **12**, 774–786 (2016).

[321] B. de Souza, F. Neese, and R. Izsák.
On the theoretical prediction of fluorescence rates from first principles using the path integral approach.
J. Chem. Phys. **148**, 034104 (2018).

[322] B. de Souza, G. Farias, F. Neese, and R. Izsák.
Predicting Phosphorescence Rates of Light Organic Molecules Using Time-Dependent Density Functional Theory and the Path Integral Approach to Dynamics.
J. Chem. Theor. Comput. **15**, 1896–1904 (2019).

[323] Y. Harabuchi, T. Taketsugu, and S. Maeda.
Exploration of minimum energy conical intersection structures of small polycyclic aromatic hydrocarbons: toward an understanding of the size dependence of fluorescence quantum yields.
Phys. Chem. Chem. Phys. **17**, 22561–22565 (2015).

[324] Y. Harabuchi, M. Hatanaka, and S. Maeda.
Exploring approximate geometries of minimum energy conical intersections by TDDFT calculations.
Chem. Phys. Lett: X **2**, 100007 (2019).

[325] A. W. Kohn, Z. Lin, and T. V. Voorhis.
Towards Prediction of Non-Radiative Decay Pathways in Organic Compounds I: The Case of Naphthalene Quantum Yields.
J. Phys. Chem. C **123**, 15394–15402 (2019).

[326] J. Shi, M. A. Izquierdo, S. Oh, S. Y. Park, B. Milián-Medina, D. Roca-Sanjuán, and J. Gierschner.
Inverted energy gap law for the nonradiative decay in fluorescent floppy molecules: larger fluorescence quantum yields for smaller energy gaps.
Org. Chem. Front. **6**, 1948–1954 (2019).

[327] D. Escudero.

Quantitative prediction of photoluminescence quantum yields of phosphors from first principles.
Chem. Sci. **7**, 1262–1267 (2016).

[328] S. Wang, W. Chen, M. Syue, K. Tan, and I. Chen.
Rapid relaxation pathway of the excited state of linear merocyanines in solutions.
J. Chin. Chem. Soc. pp. 1–14 (2019).

[329] X. F. Xu, A. Kahan, S. Zilberg, and Y. Haas.
Photoreactivity of a push-pull merocyanine in static electric fields: A three-state model of isomerization reactions involving conical intersections.
J. Phys. Chem. A **113**, 9779–9791 (2009). PMID: 19725583.

[330] A. Kahan, A. Wand, S. Ruhman, S. Zilberg, and Y. Haas.
Solvent tuning of a conical intersection: Direct experimental verification of a theoretical prediction.
J. Phys. Chem. A **115**, 10854–10861 (2011).

[331] C. Petermayer and H. Dube.
Indigoid Photoswitches: Visible Light Responsive Molecular Tools.
Acc. Chem. Res. **51**, 1153–1163 (2018).

[332] S. Wiedbrauk, B. Maerz, E. Samoylova, A. Reiner, F. Trommer, P. Mayer, W. Zinth, and H. Dube.
Twisted Hemithioindigo Photoswitches: Solvent Polarity Determines the Type of Light-Induced Rotations.
J. Am. Chem. Soc. **138**, 12219–12227 (2016).

[333] M. Kondo, X. Li, and M. Maroncelli.
Characterization of trans -2-[4-[(Dimethylamino)styryl]benzothiazole as an Ultrafast Isomerization Probe and a Modifed Kramers Theory Analysis.
J. Phys. Chem. B **117**, 12224–12233 (2013).

[334] A. Mishra, R. K. Behera, P. K. Behera, B. K. Mishra, and G. B. Behera.
Cyanines during the 1990s: A review.
Chem. Rev. **100**, 1973–2012 (2000).

[335] A. V. Kulinich and A. A. Ishchenko.
Merocyanine dyes: Synthesis, structure, properties and applications.
Russ. Chem. Rev. **78**, 141–164 (2009).

[336] V. Parthasarathy, R. Pandey, M. Stolte, S. Ghosh, F. Castet, F. Würthner, P. K. Das, and M. Blanchard-Desce.
Combination of Cyanine Behaviour and Giant Hyperpolarisability in Novel Merocyanine Dyes: Beyond the Bond Length Alternation (BLA) Paradigm.
Chem. Eur. J. **21**, 14211–14217 (2015).

[337] F. Liu and K. Morokuma.
Multiple Pathways for the Primary Step of the Spiropyran Photochromic Reaction: A CASPT2//CASSCF Study.
J. Am. Chem. Soc. **135**, 10693–10702 (2013).

[338] S. Dähne.
Color and constitution: One hundred years of research.
Science **199**, 1163–1167 (1978).

[339] F. Würthner, G. Archetti, R. Schmidt, and H.-G. Kuball.
Solvent Effect on Color, Band Shape, and Charge-Density Distribution for Merocyanine Dyes Close to the Cyanine Limit.
Angew. Chem. Int. Ed. **47**, 4529–4532 (2008).

[340] C. Brückner, C. Walter, M. Stolte, B. Braïda, K. Meerholz, F. Würthner, and B. Engels.
Structure–Property Relationships for Exciton and Charge Reorganization Energies of Dipolar Organic Semiconductors: A Combined Valence Bond Self-Consistent Field and Time-Dependent Hartree-Fock and DFT Study of Merocyanine Dyes.
J. Phys. Chem. C **119**, 17602–17611 (2015).

[341] F. Koch, A. Steinbacher, C. Consani, A. Zitzler-Kunkel, M. Stolte, F. Würthner, and T. Brixner.
The role of the dipolar neighborhood on the relaxation dynamics of multichromophoric merocyanines.
Phys. Chem. Chem. Phys. **18**, 19820–19831 (2016).

[342] S. R. Marder, C. B. Gorman, B. G. Tiemann, J. W. Perry, G. Bourhill, and K. Mansour.
Relation between bond-length alternation and second electronic hyperpolarizability of conjugated organic molecules.
Science **261**, 186–189 (2009).

[343] A. V. Kulinich, A. A. Ishchenko, and U. M. Groth.
Electronic structure and solvatochromism of merocyanines.
Spectrochim. Acta **68**, 6–14 (2007).

[344] F. Würthner, S. Yao, J. Schilling, R. Wortmann, M. Redi-Abshiro, E. Mecher, F. Gallego-Gomez, and K. Meerholz.
Atop dyes. optimization of a multifunctional merocyanine chromophore for high refractive index modulation in photorefractive materials.
J. Am. Chem. Soc. **123**, 2810–2824 (2001). PMID: 11456967.

[345] A. Arjona-Esteban, J. Krumrain, A. Liess, M. Stolte, L. Huang, D. Schmidt, V. Stepanenko, M. Gsänger, D. Hertel, and K. Meerholz.

Influence of solid-state packing of dipolar merocyanine dyes on transistor and solar cell performances.
J. Am. Chem. Soc. **137**, 13524–13534 (2015).

[346] S. R. Marder, J. E. Sohn, and G. D. Stucky,
Materials for nonlinear optics chemical perspectives.
American Chemical Society Washington DC. (1991).

[347] H. Mustroph, J. Mistol, B. Senns, D. Keil, M. Findeisen, and L. Hennig.
Relationship between the molecular structure of merocyanine dyes and the vibrational fine structure of their electronic absorption spectra.
Angew. Chem., Int. Ed. **48**, 8773–8775 (2009).

[348] P. R. Hammond.
Laser dye DCM, its spectral properties, synthesis and comparison with other dyes in the red.
Opt. Comm. **29**, 331 – 333 (1979).

[349] J. Massin, A. Charaf-Eddin, F. Appaix, Y. Bretonnière, D. Jacquemin, B. van der Sanden, C. Monnereau, and C. Andraud.
A water soluble probe with near infrared two-photon absorption and polarity-induced fluorescence for cerebral vascular imaging.
Chem. Sci. **4**, 2833 (2013).

[350] W. Liptay,
Dipole Moments and Polarizabilities of Molecules in Excited States.
Academic Press. (1974).

[351] S. Hirayama and D. Phillips.
Correction for refractive index in the comparison of radiative lifetimes in vapour and solution phases.
J. Photochem. **12**, 139–145 (1980).

[352] B. G. Levine, C. Ko, J. Quenneville, and T. J. Martinez.
Conical intersections and double excitations in time-dependent density functional theory.
Mol. Phys. **104**, 1039–1051 (2006).

[353] A. Fürstenberg, M. D. Julliard, T. G. Deligeorgiev, N. I. Gadjev, A. A. Vasilev, and E. Vauthey.
Ultrafast Excited-State Dynamics of DNA Fluorescent Intercalators: New Insight into the Fluorescence Enhancement Mechanism.
J. Am. Chem. Soc. **128**, 7661–7669 (2006).

[354] A. Glazer and H. S. Rye.
Stable dye-dna intercalation complexes as reagents for high-sensitivity fluorescence detection.

Nature **359**, 859–861 (1992).

[355] G. Hirons, J. Fawcett, and H. Crissman.
Toto and yoyo: New very bright fluorochromes for dna content analyses by flow cytometry'.
Cytometry **15**, 129–140 (1994).

[356] K. Pearson.
Note on Regression and Inheritance in the Case of Two Parents.
Proc. R. Soc. Lond. A **58**, 240–242 (1895).

[357] L. Onsager.
Electric moments of molecules in liquids.
J. Am. Chem. Soc. **58**, 1486–1493 (1936).

[358] A. Milischuk and D. V. Matyushov.
Dipole solvation: Nonlinear effects, density reorganization, and the breakdown of the onsager saturation limit.
J. Phys. Chem. A **106**, 2146–2157 (2002).

[359] S. Choi, J. Bouffard, and Y. Kim.
Aggregation-induced emission enhancement of a meso-trifluoromethyl BODIPY via j-aggregation.
Chem. Sci. **5**, 751–755 (2014).

[360] A. C. Benniston, G. Copley, A. Harriman, D. Howgego, R. W. Harrington, and W. Clegg.
Cofacial boron dipyrromethene (bodipy) dimers: Synthesis, charge delocalization, and exciton coupling.
J. Org. Chem. **75**, 2018–2027 (2010).

[361] A. S. Davydov.
The theory of molecular excitons.
Sov. Phys. Uspekhi **7**, 145–178 (1964).

[362] J. Frenkel.
On the transformation of light into heat in solids. i.
Phys. Rev. **37**, 17–44 (1931).

[363] J. Frenkel.
On the transformation of light into heat in solids. II.
Phys. Rev. **37**, 1276–1294 (1931).

[364] A. Cravcenco, Y. Yu, F. Edhborg, J. F. Goebel, Z. Takacs, Y. Yang, B. Albinsson, and K. Börjesson.
Exciton delocalization counteracts the energy gap: A new pathway toward NIR-emissive dyes.

J. Am. Chem. Soc. **143**, 19232–19239 (2021).

[365] A. Schulz and F. Würthner.
Folding-induced fluorescence enhancement in a series of merocyanine hetero-folda-trimers.
Angew. Chem. **134**, e202114667 (2021).

[366] M. Hecht, P. Leowanawat, T. Gerlach, V. Stepanenko, M. Stolte, M. Lehmann, and F. Würthner.
Self-sorting supramolecular polymerization: Helical and lamellar aggregates of tetra-bay-acyloxy perylene bisimide.
Angew. Chem. Int. Ed. **59**, 17084–17090 (2020).

[367] W. Wagner, M. Wehner, V. Stepanenko, S. Ogi, and F. Würthner.
Living supramolecular polymerization of a perylene bisimide dye into fluorescent j-aggregates.
Angew. Chem. **129**, 16224–16228 (2017).

[368] A. Bozdemir, H. H. T. Al-Sharif, W. McFarlane, P. G. Waddell, A. C. Benniston, and A. Harriman.
Solid-state emission from mono- and bichromophoric boron dipyrromethene (BODIPY) derivatives and comparison with fluid solution.
Chem. Eur. J. **25**, 15634–15645 (2019).

[369] A. B. Nepomnyashchii and A. J. Bard.
Electrochemistry and electrogenerated chemiluminescence of BODIPY dyes.
Acc. Chem. Res. **45**, 1844–1853 (2012).

[370] S. F. Völker and C. Lambert.
Exciton coupling effects in polymeric cis-indolenine squaraine dyes.
Chem. Mat. **24**, 2541–2553 (2012).

[371] Z. Liu, Z. Jiang, M. Yan, and X. Wang.
Recent progress of BODIPY dyes with aggregation-induced emission.
Front. Chem. **7**, 712 (2019).

[372] N. Aratani, A. Osuka, Y. H. Kim, D. H. Jeong, and D. Kim.
Extremely long, discrete meso – meso-coupled porphyrin arrays.
Angew. Chem. Int. Ed. **39**, 1458–1462 (2000).

[373] Y. H. Kim, D. H. Jeong, D. Kim, S. C. Jeoung, H. S. Cho, S. K. Kim, N. Aratani, and A. Osuka.
Photophysical properties of long rodlik meso-meso-linked zinc(II) porphyrins investigated by time-resolved laser spectroscopic methods.
J. Am. Chem. Soc. **123**, 76–86 (2000).

[374] V. S.-Y. Lin, S. G. DiMagno, and M. J. Therien.
Highly conjugated, acetylenyl bridged porphyrins: New models for light-harvesting antenna systems.
Science **264**, 1105–1111 (1994).

[375] H. Shimizu, K. Fujimoto, M. Furusyo, H. Maeda, Y. Nanai, K. Mizuno, and M. Inouye.
Highly emissive π-conjugated alkynylpyrene oligomers: their synthesis and photophysical properties.
J. Org. Chem. **72**, 1530–1533 (2007).

[376] J. Ahrens, B. Haberlag, A. Scheja, M. Tamm, and M. Bröring.
Conjugated BODIPY DYEmers by metathesis reactions.
Chem. Eur. J **20**, 2901–2912 (2014).

[377] X. Qiu, R. Lu, H. Zhou, X. Zhang, T. Xu, X. Liu, and Y. Zhao.
Synthesis of linear monodisperse vinylene-linked phenothiazine oligomers.
Tetrah. Lett. **48**, 7582–7585 (2007).

[378] S. Rihn, M. Erdem, A. D. Nicola, P. Retailleau, and R. Ziessel.
Phenyliodine(III) bis(trifluoroacetate) (PIFA)-promoted synthesis of bodipy dimers displaying unusual redox properties.
Org. Lett. **13**, 1916–1919 (2011).

[379] Y. Hayashi, S. Yamaguchi, W. Y. Cha, D. Kim, and H. Shinokubo.
Synthesis of directly connected BODIPY oligomers through suzuki–miyaura coupling.
Org. Lett. **13**, 2992–2995 (2011).

[380] M. Bröring, R. Krüger, S. Link, C. Kleeberg, S. Köhler, X. Xie, B. Ventura, and L. Flamigni.
Bis(BF2)-2,2′-bidipyrrins (BisBODIPYs): Highly fluorescent BODIPY dimers with large stokes shifts.
Chem. Eur. J. **14**, 2976–2983 (2008).

[381] B. Ventura, G. Marconi, M. Bröring, R. Krüger, and L. Flamigni.
Bis(BF_2-2,2′-bidipyrrins, a class of BODIPY dyes with new spectroscopic and photophysical properties.
New J. Chem. **33**, 428–438 (2009).

[382] J. Ahrens, B. Böker, K. Brandhorst, M. Funk, and M. Bröring.
Sulfur-bridged BODIPY DYEmers.
Chem. Eur. J. **19**, 11382–11395 (2013).

[383] H. Yokoi, S. Hiroto, and H. Shinokubo.
Synthesis of diazo-bridged BODIPY dimer and tetramer by oxidative coupling of β-amino-substituted BODIPYs.

Org. Lett. **16**, 3004–3007 (2014).

[384] J. Knoester.
Modeling the optical properties of excitons in linear and tubular j-aggregates.
Int. J. Photoenerg. **2006**, 1–10 (2006).

[385] A. Humeniuk, R. Mitrić, and V. Bonačić-Koutecký.
Size dependence of non-radiative decay rates in j-aggregates.
J. Phys. Chem. A **124**, 10143–10151 (2020).

[386] H. Fidder, J. Knoester, and D. A. Wiersma.
Superradiant emission and optical dephasing in j-aggregates.
Chem. Phys. Lett. **171**, 529–536 (1990).

[387] B. Scharf and U. Dinur.
Striking dependence of the rate of electronic radiationless transitions on the size of the molecular system.
Chem. Phys. Lett. **105**, 78–82 (1984).

[388] Y.-C. Wei, S. F. Wang, Y. Hu, L.-S. Liao, D.-G. Chen, K.-H. Chang, C.-W. Wang, S.-H. Liu, W.-H. Chan, J.-L. Liao, W.-Y. Hung, T.-H. Wang, P.-T. Chen, H.-F. Hsu, Y. Chi, and P.-T. Chou.
Overcoming the energy gap law in near-infrared OLEDs by exciton–vibration decoupling.
Nat. Phot. **14**, 570–577 (2020).

[389] Z. Shi, X. Han, W. Hu, H. Bai, B. Peng, L. Ji, Q. Fan, L. Li, and W. Huang.
Bioapplications of small molecule aza-BODIPY: from rational structural design to in vivo investigations.
Chem. Soc. Rev. **49**, 7533–7567 (2020).

[390] O. A. Bozdemir, S. Erbas-Cakmak, O. O. Ekiz, A. Dana, and E. Akkaya.
Towards unimolecular luminescent solar concentrators: Bodipy-based dendritic energy-transfer cascade with panchromatic absorption and monochromatized emission.
Angew. Chem. Int. Ed **50**, 10907–10912 (2011).

[391] L. J. Patalag, S. Ahadi, O. Lashchuk, P. G. Jones, S. Ebbinghaus, and D. B. Werz.
GlycoBODIPYs: Sugars serving as a natural stock for water-soluble fluorescent probes of complex chiral morphology.
Angew. Chem. Int. Ed **133**, 60,8766–8771 (2021).

[392] A. Patra, L. Patalag, P. Jones, and D. Werz.
Extended benzene-fused oligo-BODIPYs: In three steps to a series of large, arc-shaped, near-infrared dyes.
Angew. Chem. Int. Ed **60**, 747–752 (2021).

[393] K. Sitkowska, M. F. Hoes, M. M. Lerch, L. N. Lameijer, P. Meer, W. Szymanski, and B. L. Feringa.
Red-light-sensitive BODIPY photoprotecting groups for amines and their biological application in controlling heart rhythm.
Chem. Commun. **56**, 5480–5483 (2020).

[394] K. Sitkowska, B. L. Feringa, and W. Szymański.
Green-light-sensitive BODIPY photoprotecting groups for amines.
J. Org. Chem. **83**, 1819–1827 (2018).

[395] G. Das, S. Cherumukkil, A. Padmakumar, V. B. Banakar, V. K. Praveen, and A. Ajayaghosh.
Tweaking a BODIPY spherical self-assembly to 2d supramolecular polymers facilitates excited-state cascade energy transfer.
Angew. Chem. Int. Ed **60**, 7851–7859 (2021).

[396] Y. Ito, T. Konoike, and T. Saegusa.
Reaction of ketone enolates with copper dichloride. synthesis of 1,4-diketones.
J. Am. Chem. Soc. **97**, 2912–2914 (1975).

[397] M. Blangetti, P. Fleming, and D. F. O'Shea.
Homo- and hetero-oxidative coupling of benzyl anions.
J. Org. Chem. **77**, 2870–2877 (2012).

[398] C. Zhong, D. Bialas, C. J. Collison, and F. C. Spano.
Davydov splitting in squaraine dimers.
J. Phys. Chem. C **123**, 18734–18745 (2019).

[399] A. Turkin, P. Malý, and C. Lambert.
Fluorescence band exchange narrowing in a series of squaraine oligomers: energetic vs. structural disorder.
Phys. Chem. Chem. Phys. **23**, 18393–18403 (2021).

[400] A. Prlj, L. Vannay, and C. Corminboeuf.
Fluorescence quenching in BODIPY dyes: The role of intramolecular interactions and charge transfer.
Helv. Chim. Acta **100**, e1700093 (2017). E 1700093 .

[401] C. Goze, G. Ulrich, L. J. Mallon, B. D. Allen, A. Harriman, and R. Ziessel.
Synthesis and photophysical properties of borondipyrromethene dyes bearing aryl substituents at the boron center.
J. Am. Chem. Soc. **128**, 10231–10239 (2006).

[402] M. Kusinski, J. Nagesh, M. Gladkikh, A. F. Izmaylov, and R. A. Jockusch.
Deuterium isotope effect in fluorescence of gaseous oxazine dyes.
Phys. Chem. Chem. Phys. **21**, 5759–5770 (2019).

[403] T. Abe, A. Miyazawa, H. Konno, and Y. Kawanishi.
Deuteration isotope effect on nonradiative transition of fac-tris (2-phenylpyridinato) iridium (III) complexes.
Chem. Phys. Lett. **491**, 199–202 (2010).

[404] U. Mayerhöffer, B. Fimmel, and F. Würthner.
Bright near-infrared fluorophores based on squaraines by unexpected halogen effects.
Angew. Chem. Int. Ed **51**, 164–167 (2012).

[405] U. Mayerhöffer, M. Gsänger, M. Stolte, B. Fimmel, and F. Würthner.
Synthesis and molecular properties of acceptor-substituted squaraine dyes.
Chem. Eur. J. **19**, 218–232 (2013).

[406] R. Lincoln, L. E. Greene, C. Bain, J. O. Flores-Rizo, D. S. Bohle, and G. Cosa.
When push comes to shove: Unravelling the mechanism and scope of nonemissive meso-unsaturated BODIPY dyes.
J. Phys. Chem. B **119**, 4758–4765 (2015).

[407] A. Prlj, A. Fabrizio, and C. Corminboeuf.
Rationalizing fluorescence quenching in meso-BODIPY dyes.
Phys. Chem. Chem. Phys. **18**, 32668–32672 (2016).

[408] F. Li, S. I. Yang, Y. Ciringh, J. Seth, C. H. Martin, D. L. Singh, D. Kim, R. R. Birge, D. F. Bocian, D. Holten, and J. S. Lindsey.
Design, synthesis, and photodynamics of light-harvesting arrays comprised of a porphyrin and one, two, or eight boron-dipyrrin accessory pigments.
J. Amer. Chem. Soc. **120**, 10001–10017 (1998).

[409] J. A. Levitt, P.-H. Chung, M. K. Kuimova, G. Yahioglu, Y. Wang, J. Qu, and K. Suhling.
Fluorescence anisotropy of molecular rotors.
ChemPhysChem **12**, 662–672 (2011).

[410] Y. Wu, M. Frasconi, W.-G. Liu, R. M. Young, W. A. Goddard, M. R. Wasielewski, and J. F. Stoddart.
Electrochemical switching of a fluorescent molecular rotor embedded within a bistable rotaxane.
J. Am. Chem. Soc. **142**, 11835–11846 (2020).

[411] M. K. Kuimova, G. Yahioglu, J. A. Levitt, and K. Suhling.
Molecular rotor measures viscosity of live cells via fluorescence lifetime imaging.
J. Am. Chem. Soc. **130**, 6672–6673 (2008).

[412] I. López-Duarte, T. T. Vu, M. A. Izquierdo, J. A. Bull, and M. K. Kuimova.

A molecular rotor for measuring viscosity in plasma membranes of live cells.
Chem. Commun. **50**, 5282–5284 (2014).

[413] Y. Wu, M. Štefl, A. Olzyńska, M. Hof, G. Yahioglu, P. Yip, D. R. Casey, O. Ces, J. Humpoličková, and M. K. Kuimova.
Molecular rheometry: direct determination of viscosity in lo and ld lipid phases via fluorescence lifetime imaging.
Phys. Chem. Chem. Phys. **15**, 14986 (2013).

[414] T. Suhina, S. Amirjalayer, S. Woutersen, D. Bonn, and A. M. Brouwer.
Ultrafast dynamics and solvent-dependent deactivation kinetics of BODIPY molecular rotors.
Phys. Chem. Chem. Phys. **19**, 19998–20007 (2017).

[415] N. L. C. Leung, N. Xie, W. Yuan, Y. Liu, Q. Wu, Q. Peng, Q. Miao, J. W. Y. Lam, and B. Z. Tang.
Restriction of intramolecular motions: The general mechanism behind aggregation-induced emission.
Chem. Eur. J. **20**, 15349–15353 (2014).

[416] Y. Tu, J. Liu, H. Zhang, Q. Peng, J. W. Y. Lam, and B. Z. Tang.
Restriction of access to the dark state: A new mechanistic model for heteroatom-containing AIE systems.
Angew. Chem. Int. Ed. **58**, 14911–14914 (2019).

[417] Z. Zhao, H. Zhang, J. Lam, and B. Tang.
Aggregation-induced emission: New vistas at the aggregate level.
Angew. Chem. Int. Ed. **59**, 9888–9907 (2020).

[418] J. Mei, N. L. C. Leung, R. T. K. Kwok, J. W. Y. Lam, and B. Z. Tang.
Aggregation-induced emission: Together we shine, united we soar!
Chem. Rev. **115**, 11718–11940 (2015).

[419] K. Kokado and K. Sada.
Consideration of molecular structure in the excited state to design new luminogens with aggregation-induced emission.
Angew. Chem. Int. Ed **58**, 8632 (2019).

[420] H. Sunahara, Y. Urano, H. Kojima, and T. Nagano.
Design and synthesis of a library of BODIPY-based environmental polarity sensors utilizing photoinduced electron-transfer-controlled fluorescence ON/OFF switching.
J. Am. Chem. Soc. **129**, 5597–5604 (2007).

[421] W. Qin, M. Baruah, M. V. der Auweraer, F. C. D. Schryver, and N. Boens.
Photophysical properties of borondipyrromethene analogues in solution.
J. Phys. Chem. A **109**, 7371–7384 (2005).

[422] *Owing to the rapidly growing amount of (ct)-excited states at the oligomers, a valid quantification of their influences on (non-)radiative decay channels revealed to be too complex and goes beyond the scope of this study.* Owing to the rapidly growing amount of (CT)-excited states at the oligomers, a valid quantification of their influences on (non-)radiative decay channels revealed to be too complex and goes beyond the scope of this study.

[423] W. Li, L. Li, H. Xiao, R. Qi, Y. Huang, Z. Xie, X. Jing, and H. Zhang.
Iodo-BODIPY: a visible-light-driven, highly efficient and photostable metal-free organic photocatalyst.
RSC Adv. **3**, 13417 (2013).

[424] J. T. Ly, K. F. Presley, T. M. Cooper, L. A. Baldwin, M. J. Dalton, and T. A. Grusenmeyer.
Impact of iodine loading and substitution position on intersystem crossing efficiency in a series of ten methylated-meso-phenyl-BODIPY dyes.
Phys. Chem. Chem. Phys. **23**, 12033–12044 (2021).

[425] L. Yang, X. Wang, G. Zhang, X. Chen, G. Zhang, and J. Jiang.
Aggregation-induced intersystem crossing: a novel strategy for efficient molecular phosphorescence.
Nanoscale **8**, 17422–17426 (2016).

[426] J. G. Woller, J. K. Hannestad, and B. Albinsson.
Self-assembled nanoscale DNA–porphyrin complex for artificial light harvesting.
J. Am. Chem. Soc. **135**, 2759–2768 (2013).

[427] J.-D. Yi, D.-H. Si, R. Xie, Q. Yin, M.-D. Zhang, Q. Wu, G.-L. Chai, Y.-B. Huang, and R. Cao.
Conductive two-dimensional phthalocyanine-based metal–organic framework nanosheets for efficient electroreduction of CO_2.
Angew. Chem. Int. Ed **60**, 17108–17114 (2021).

[428] L. Zhang, G. Ng, N. Kapoor-Kaushik, X. Shi, N. Corrigan, R. Webster, K. Jung, C. Andre, and J. Boyer.
2d porphyrinic metal–organic framework nanosheets as multidimensional photocatalysts for functional materials.
Angew. Chem. Int. Ed **60**, 22664–22671 (2021).

[429] S. Garg, H. Schwartz, M. Kozlowska, A. B. Kanj, K. Müller, W. Wenzel, U. Ruschewitz, and L. Heinke.
Conductance photoswitching of metal–organic frameworks with embedded spiropyran.
Angew. Chem. Int. Ed. **58**, 1193–1197 (2019).

[430] K. Trofymchuk, A. Reisch, P. Didier, F. Fras, P. Gilliot, Y. Mely, and A. S. Klymchenko.
Giant light-harvesting nanoantenna for single-molecule detection in ambient light.
Nat. Phot. **11**, 657–663 (2017).

[431] G. P. Acuna, F. M. Möller, P. Holzmeister, S. Beater, B. Lalkens, and P. Tinnefeld.
Fluorescence enhancement at docking sites of DNA-directed self-assembled nanoantennas.
Science **338**, 506–510 (2012).

Chapter 11

Individual Contributions

All co-authors of the publications below have been informed about the specified own contributions, as stated below, and they agree to them.

Ultrafast Resonance Energy Transfer in Ethylene-Bridged BODIPY Heterooligomers: From Frenkel to Förster Coupling Limit

L. J. Patalag, J. Hoche, M. Holzapfel, A. Schmiedel, R. Mitric, C. Lambert, D. B. Werz, *J. Am. Chem. Soc.*, **143**, 7414–7425 (2021)

Author	**LJP**	**JH**	**MH**	**AS**	**RM**	**CL**	**DBW**	**Sum**
Design of research	3 %				3 %	3 %	3 %	12 %
Synthesis and characterization	10 %							10 %
Absorption & fluorescence spectroscopy	7 %							7 %
Transient absorption spectroscopy			6 %	8 %		4 %		18 %
Calculation and analysis of EET rates and excitonic coupling	1 %	5 %						6 %
Analysis of diagonal and off-diagonal disorder		8 %						8 %
Light-induced dynamics simulations		10 %						10 %
Publication writing	6 %	4 %			1 %	4 %	1 %	16 %
Publication correction	2 %	2 %			1 %	2 %	1 %	8 %
Publication coordination	1 %	1 %			1 %	1 %	1 %	5 %
Sum	30 %	30 %	6 %	8 %	6 %	14 %	6 %	100 %

Ultrafast Energy Transfer Dynamics in a Squaraine Hetero-Triad

C. Lambert, J. Hoche, M. H. Schreck, M. Holzapfel, A. Schmiedel, J. Selby, A. Turkin, R. Mitric, *J. Phys. Chem. A*, **125**, 2504–2511, (2021)

Author	**CL**	**JH**	**MHS**	**MH**	**AS**	**JS**	**AT**	**RM**	**Sum**
Design of research	5 %							5 %	10 %
Synthesis and characterization			16 %			2 %	2 %		20 %
Exp. & sim. absorption and fluorescence spectra		4 %	10 %						14 %
Transient absorption spectroscopy	1 %			2 %	4 %				7 %
Light-induced dynamics simulations		10 %							10 %
Analysis of dynamic exciton localization		8 %							8 %
Publication writing	11 %	6 %						3 %	20 %
Publication correction	2 %	2 %		1				1 %	6 %
Publication coordination	3 %	1 %						1 %	5 %
Sum	22 %	31 %	26 %	3 %	4 %	2 %	2 %	10 %	100 %

Dynamic Exciton Localisation in a pyrene-BODIPY-pyrene dye conjugate

N. Auerhammer, A. Schulz, A. Schmiedel, M. Holzapfel, J. Hoche, M.I.S. Röhr, R. Mitric, C. Lambert, *Phys. Chem. Chem. Phys.* **21**, 9013–9025 (2019)

Author	**NA**	**ASz**	**ASl**	**MH**	**JH**	**MISR**	**RM**	**CL**	**Sum**
Design of research						4 %	4 %	4 %	12 %
Synthesis and characterization	18 %	2 %							20 %
Exp. & sim. absorption and fluorescence spectra	5 %				4 %				9 %
Transient absorption spectroscopy			5 %	3 %				2 %	10 %
Light-induced dynamics simulations					10 %				10 %
Analysis of dynamic exciton localization					7 %				7 %
Publication writing	2 %			1 %	6 %	2 %	2 %	9 %	22 %
Publication correction					1 %	1 %	1 %	2 %	5 %
Publication coordination						1 %	2 %	2 %	5 %
Sum	25 %	2 %	5 %	4 %	28 %	8 %	9 %	15 %	100 %

Excimer formation in the isolated tetracene dimer

J. Hoche, M. Flock, X. Miao, L. N. Philipp, M. Wenzel, I. Fischer, R. Mitric, *Chem. Sci.*, **10**, 11965–11975, (2021)

Author	**JH**	**MF**	**XM**	**LNP**	**MW**	**IF**	**RM**	**Sum**
Design of research						5 %	5 %	10 %
TOF-MS Spectra		8 %						10 %
Time-resolved experiments		10 %						10 %
Exp. & sim. absorption spectra	3 %	4 %		1 %	2 %			10 %
Sim. of potential energy curves	3 %		3 %	2 %				8 %
TD-DFTB nonadiabatic dynamics	6 %			4 %				10 %
CISD nonadiabatic dynamics	4 %		5 %					9 %
Writing first version of the manuscript	6 %	2 %	2 %		1 %	5 %	5 %	21 %
Correction of the manuscript	2 %					2 %	2 %	6 %
Publication coordination	2 %					2 %	2 %	6 %
Sum	26 %	24 %	11 %	7 %	3 %	14 %	14 %	100%

The Origin of the Solvent Dependence of Fluorescence Quantum Yields in Dipolar Merocyanine Dyes

J. Hoche, A. Schulz, L. Dietrich, A. Humeniuk, M. Stolte, D. Schmidt, T. Brixner, F. Würthner, R. Mitric, *Chem. Sci.*, **10**, 11013–11022 (2019)

Author	**JH**	**AS**	**LD**	**AH**	**MS**	**DS**	**TB**	**FW**	**RM**	**Sum**
Design of research							4 %	4 %	4 %	12 %
Synthesis and characterization		8 %				4 %				12 %
Exp. & sim. absorption and fluorescence spectra	3 %	4 %			3 %					10 %
Development of theoretical model for calculation of QYs	3 %			7 %						10 %
Characterization of conical intersections	6 %									6 %
Analysis of QY dependence on polarity & temperature	3.5 %	2 %		1.5 %	1 %					8 %
Transient absorption spectroscopy			12 %							12 %
Writing first version of the manuscript	6 %	2 %	2 %	4 %			2 %	2 %	2 %	20 %
Correction of the manuscript	1 %				1 %		1 %	1 %	1 %	5 %
Publication coordination	2 %	0.5 %	0.5 %					2 %		5 %
Sum	24.5 %	16.5 %	14.5 %	12.5 %	5 %	4 %	7 %	9 %	7 %	100%

Transforming Dyes Into Fluorophores: Exciton-Induced Emission with Ethylene-Bridged Oligo-BODIPYs

L. J. Patalag, J. Hoche, R. Mitric, D. B. Werz, B. L. Feringa, *Angew. Chem.*, **61**, e202116834 (2022)

Author	**LJP**	**JH**	**RM**	**DBW**	**BLF**	**Sum**
Design of research	4 %		2 %	2 %	4 %	12 %
Synthesis and characterization	10 %					10 %
Spectroscopy	12 %					12 %
Electronic structure calculations		10 %				10 %
Theoretical model of quantum yields		10 %				10 %
Writing first version of the manuscript	10 %	6 %	2 %	2 %	2 %	22 %
Correction of the manuscript	4 %	4 %	2 %	2 %	2 %	14 %
Publication coordination	5 %				5 %	10 %
Sum	45 %	30 %	6 %	6 %	13 %	100 %